A THREE-AXIS ACCELEROMETER FOR MEASURING HEART WALL MOTION

Craig Lowrie

A Dissertation Submitted for the Degree of Doctor of Philosophy

Heriot-Watt University

School of Engineering and Physical Sciences

November 2010

Abstract

This thesis presents the work carried out in the design, simulation, fabrication and testing of miniaturised three-axis accelerometers. The work was carried out at the Faculty of Science and Engineering at Vestfold University College (Tønsberg, Norway), the MIcroSystems Engineering Centre (MISEC) at Heriot-Watt University and in collaboration with the Interventional Centre at Rikshospitalet University Hospital (Oslo, Norway). The accelerometers presented in this thesis were produced to be stitched to the surface of human hearts. In doing so they are used to measure the heart wall motion of patients that have just undergone heart bypass surgery. Results from studies carried out are presented and prove the concept of using such sensors for the detection of problems that can lead to the failure of heart bypasses. These studies were made possible using commercially available MEMS (MicroElectroMechanical Systems) three-axis accelerometers. However, the overall size of these sensors does not meet the requirements deemed necessary by the medical team (2(W)×2(H)×5(L) mm^3) and fabrication activities were necessary to produce custom-made sensors. Design verification and performance modelling were carried out using Finite Element Analysis (FEA) and these results are presented alongside relevant analytical calculations. For fabrication, accelerometer designs were submitted to three foundry processes during the course of the work. The designs utilise the piezoresistive effect for the acceleration sensing and fabrication was carried out by bulk micromachining. Results of the characterisaton of the sensors are presented.

“Cha do dhùin doras nach
do d’fhosgail doras.”

Acknowledgements

I have many people to acknowledge who have all played a part during this journey of which an important part has been my stay in the beautiful Norway. I do not have room to mention everyone but I will do my best to get most people in!

I would firstly like to give my gratitude to the person that made me aware of this opportunity and made it all possible as well as accompanying me to the interview in Norway. I would also like to thank him for his advice, motivation and support in his capacity as my supervisor but also as a friend. Many thanks to you, Professor Marc Desmulliez.

It was a slight wrench for me to move to Norway and leave Scotland behind for a time but it was an even greater one to leave my family behind. My love goes to my Mum and Dad, my sisters Susan and Rachael as well as the new arrival along the way, my nephew Ryan. Shortly before I was made aware of me being successful with the Norway interview, my Grandpa passed away. I miss him dearly and I know that he would have had great advice for me during this development of my career and as a person.

In Norway I would like to begin by thanking the people from Vestfold University College: Lars Hoff, Christopher Grinde, Lars Fleischer, Kristin Imenes, Henrik Jakobsen, Per Øhlckers, Hans-Jørgen Alcker, Morten Grimnes, Einar Halvorsen, Oddvin Arne, and Thomas Halvorsen. In addition I would like to thank Dag Wang, Preben Storås, Kari Schjølberg-Henriksen, Sigurd Moe, Andreas Vogl, Maaike Taklo (all of Sintef) as well as Daniel Lapadatu of SensoNor.

A mention to some of my Norwegian friends outwith work: Paul Enes, Martin Reiten, Sindre Martinsen, Henning Gloersen, Mikael Dirholt, Frederik Nystrom and Elisabeth Edvardsen.

In Scotland, thanks firstly go to my colleagues at Heriot-Watt University: David Flynn, Suzanne Millar, Keith Sinclair, Douglas Colliar, Mark Leonard, Markus Luetzelschwab, Dominik Weiland, Brian Moffat, Jack Ng, the Secretaries, the IT guys, the Electronic Workshop guys, Al Houstin, Stevie Selkirk, Jun Zeng, Kun Zhao, Yves Lacrotte, Neil Ross, Resh Dhariwal, Robert Maier and Rob Watson.

To my Scottish friends outwith work: Andy Jackson, Richie Davison, Michael Pollock, Tommy Kelly, Robbie Cook, Dale Prentice, Neil Thomson, Gary Young, Allan Connolly, Lynne-Marie Thom and Karen Cornwall.

Some other mentions are Peter Lomax, Alec Ruthven, Anthony Walton (all of SMC); Laurence Brice, Mark Stewart, Richard Leach (all of NPL) and Frank Bellion (Extec).

Thank you to all of you (including the ones I have missed) for making this experience what it was!!!

Table of Contents

List of Figures

List of Tables

Glossary

α_{nwell} Sidewall angle of MultiMEMS seismic masses

ϵ Permittivity

ω_n Natural resonant frequency

π_L Longitudinal piezoresistive coefficient

π_T Transversal piezoresistive coefficient

ρ Density

σ Stress

σ_{IP} In-plane stress

σ_{OP} Out-of-plane stress

A Area

a Acceleration

$AHRS$ Attitude and Heading Reference System

$APDL$ ANSYS Parametric Design Language

$ASIC$ Application Specific Integrated Circuit

b Damping coefficient

BCB BenzoCycloButene

BOX Buried OXide

$BSPM$ Body Surface Potential Mapping

BW_{LPF} BandWidth of Low-Pass Filter

$CABG$ Coronary Artery Bypass Surgery

CHD Coronary Heart Disease

$CMOS$ Complimentary Metal-Oxide-Semiconductor

CSP Chip Scale Package

CVD CardioVascular Disease

d Distance

DFN Dual Flat No-lead

DIP Dual In-line Package

DOF Degrees Of Freedom

$DRIE$ Deep Reactive Ion Etch

ECG ElectroCardioGram

EMI ElectroMagnetic Interference

ESC Electronic Stability Control

F Force

FEA Finite Element Analysis

FEM Finite Element Modelling

FFT Fast Fourier Transform

FSO Full-Scale Output

g Acceleration due to gravity at the Earth's surface

GPS Global Positioning System

GUI Graphical User Interface

H Height

H_b Height of a cantilever beam

H_m Height of a seismic mass

I Moment of inertia

IC Integrated Circuit

ICP Inductively Coupled Plasma

k Spring constant

L Length

L_b Length of a cantilever beam

L_m Length of a seismic mass

LAD Left Anterior Descending

LCC Leadless Ceramic Carrier

LD_{full} Lateral displacement of backside etch

$LFCSP$ Lead Frame Chip Scale Package

LGA Land Grid Array

M Bending moment

m Mass

m_{epi} Mass of the epi layer

m_{handle} Mass of the SOI handle layer

M_{IP} Bending moment for in-plane accelerations

m_{mass} Mass of the seismic mass

m_{nwell} Mass of the n-well

M_{OP} Total bending moment for out-of-plane acceleration

MCG MagnetoCardioGraphy

$MEMS$ MicroElectroMechanical Systems

$MISEC$ MIcroSystems Engineering Centre, Heriot-Watt University

MO Mask opening

MPW Multi Project Wafer

MSA MicroSystem Analyser

N Power spectral density noise

NCA Non-Conductive Adhesive

NEG Non-Evaporated Getter

NPL National Physical Laboratories

PCB Printed Circuit Board

$POST1$ ANSYS general postprocessor

$PREP7$ ANSYS general preprocessor

PSD Power Spectral Density

PZE PieZoElectric

PZT Lead Zirconate Titanate

Q Quality factor

QFN Quad Flat No-leads

R Resistance

$r0$ Distance from the neutral axis of a cantilever beam to the vertical centre of gravity of a seismic mass

S Mechanical sensitivity

SMC Scottish Microelectronic Centre, Edinburgh University

SNR Signal-to-Noise Ratio

SOI Silicon-On-Insulator

$SOLUTION$ ANSYS solution processor

TCS Temperature Coefficient of Sensitivity

$TMAH$ TetraMethylAmmonium Hydroxide

TSV Through Silicon Via

UE Under Etch of oxide mask

V Voltage

V_s Voltage supply

V_{out} Voltage output

W Width

W_b Width of a cantilever beam

W_m Width of a seismic mass

x Displacement

y Distance along the length of the beam from the base

z_c Distance from the neutral axis to the surface of a beam

z_{cm} Vertical centre of mass of a seismic mass

ZnO Zinc Oxide

List of Author's Publications

Journals

- C. Lowrie, M.P.Y. Desmulliez, L. Hoff, O.J. Elle, and E. Fosse, "Fabrication of a MEMS accelerometer to detect heart bypass surgery complications," Sensor Review, 29/4, pp. 319-324, 2009. This paper was chosen as a Highly Commended Award Winner at the Literati Network Awards for Excellence 2010.

- C. Lowrie, M.P.Y. Desmulliez, L. Hoff, K. Imenes, O.J. Elle, and E. Fosse, "Progress towards real time monitoring of cardiac wall motion using inertial sensors," Submitted to the Journal of Micromechanics and Microengineering.

Conferences

- C. Lowrie, C. Grinde, L. Hoff, and M. Desmulliez, "Piezoresistive three-axis accelerometer for monitoring heart wall motion," Poster presented and paper published in the Proceedings of DTIP of MEMS & MOEMS 2005, 01-03 June 2005, Montreux, Switzerland.

- C. Lowrie, C. Grinde, L. Hoff, M. Desmulliez, O.J. Elle, and E. Fosse, "Design of a three-axis accelerometer for heart motion studies," Poster presented and paper published in the Proceedings of IMAPS Nordic 2005, 11-14 September 2005, Tønsberg, Norway.

- C. Lowrie, C. Grinde, L. Hoff, M. Desmulliez, O.J. Elle, and E. Fosse, "Design of a miniature three-axis accelerometer for the study of heart wall motion," Paper presented and published in the Proceedings of Micro Structure Workshop 2006, 09-10 May 2006, Västerås, Sweden.

- C. Lowrie, M. Desmulliez, L. Hoff, O.J. Elle, and E. Fosse, "Design and fabrication of a miniaturized three-axis accelerometer for measuring heart wall motion," Paper presented and published in the Proceedings of the 15^{th} IEEE International Conference on Electronics, Circuits, and Systems, ICECS 2008, 31 August-3 September 2008, St Julians, Malta.

- C. Lowrie, M. Desmulliez, L. Hoff, O.J. Elle, and E. Fosse, "Design and fabrication of an implantable three-axis accelerometer for post-surgery monitoring of heart wall motion," Paper presented and published in the Proceedings of the 2^{nd} Electronics System-Integration Technology Conference, 1-4 September 2008, London, UK.

- C. Lowrie, M. Desmulliez, L. Hoff, O.J. Elle, and E. Fosse, "Design and fabrication of a miniaturized three-axis accelerometer for measuring heart wall motion," Poster presented and paper published in the Proceedings of the 38^{th} European Solid-State Device Research Conference (ESSDERC) and the 34^{th} European Solid-State Circuits Conference (ESSCIRC), 15-19 September 2008, Edinburgh, UK.

- C. Lowrie, C. Grinde, L. Hoff, and M. Desmulliez, "MEMS three-axis accelerometer: design, fabrication and application of measuring heart wall motion," Poster presented and paper published in the Proceedings of DTIP of MEMS & MOEMS 2009, 01-03 April 2009, Rome, Italy.

- C. Lowrie, M.P.Y. Desmulliez, L. Hoff, O.J. Elle, and E. Fosse, "The application of a micromachined three-axis accelerometer in heart bypass surgery," Paper presented and published in the Proceedings of MicroTech 2009, 02-03 March 2009, Edinburgh, Scotland.

Chapter 1

Introduction and Thesis Outline

1.1 Motivation

Micromachined accelerometers have been driving the MEMS market for many years now. They represent one of the most common types of silicon sensors, largely due to their use in the automotive industry and airbag sensors in particular. As a result, extensive development has resulted in high performance accelerometers capable of measuring acceleration along three axes with reduced footprints. For further increase of market share, these sensors have to branch out into different industrial sectors and offer solutions to different applications. The biomedical industry is one such industry and the MicroHeart Project is one such example of research [1].

The MicroHeart Project is a collaboration between Heriot-Watt University, Vestfold University College and the Interventional Centre at Rikshospitalet University Hospital. In 2003, clinicians at Rikshospitalet Hospital proposed the idea of using miniaturised three-axis accelerometers to measure the heart wall motion of patients who have undergone CABG surgery. Such measurements would allow medical staff to detect any perioperative complications with the bypass procedure. Moreover "real-time" monitoring is potentially feasible so that any detected complications can potentially be remedied before the patient leaves the hospital.

The contribution to the project, for which the results are presented in this thesis, consists of the design, fabrication and characterisation of a three-axis accelerometer that measures approximately 2 mm in width and up to 5 mm in length. These values were quoted as a requirement by the medical team. The small width is required for

the sensor to be pulled free from its sutures on the surface of the heart and out through a hole left in the patient's chest. The lack of availability of a suitable commercial accelerometer meant that it was necessary for the group to design their own heart sensor.

1.2 Thesis outline

A breakdown of the thesis is shown in Figure 1.1 at the end of this chapter. This thesis consists of eight chapters:

Chapter 2: The MicroHeart Project. The intended biomedical application of the three-axis accelerometer is introduced in this chapter. The benefits of the proposed diagnosis method are presented against the shortfalls of other available methods. The approach followed for clinical experimentation is introduced as well as the results from these experiments. The case for the in-house design of a micromachined three-axis accelerometer is presented.

Chapter 3: Review of Micromachined Three-Axis Accelerometers. A literature review of three-axis accelerometers available commercially and also published in the research field is presented in this chapter. A variety of three-axis accelerometers with different sensing techniques are introduced. In addition, the different approaches in silicon micromachining applied to the realisation of these accelerometers are included to further the knowledge of the options available and structures possible for the designer of MEMS accelerometers.

Chapter 4: Design of a Micromachined Three-Axis Accelerometer. This chapter introduces the different designs that were produced. A discussion is presented on the approaches taken for each of these designs alongside their advantages and disadvantages.

Chapter 5: ANSYS Simulation of a Micromachined Three-Axis Accelerometer. This chapter consists of a description of the FEA carried out using the simulation software package ANSYS. Stress, deflection and resonant frequencies are simulated to aid in the design and optimisation of the sensors.

Chapter 6: Fabrication of a Micromachined Three-Axis Accelerometer. Here, the fabrication processes used at various foundries for the different designs are presented and discussed in detail. Manufacturing limitations and problems experienced during manufacturing are discussed. The packaging of the sensors is also introduced.

Chapter 7: Characterisation of a Micromachined Three-Axis Accelerometer. Using a specialised commercially available setup, the out-of-plane and in-plane motions of the fabricated accelerometers are studied. This approach gives a better understanding of the behaviour of the free-standing structures when subjected to different accelerations. This characterisation technique can be used for prototyping purposes as well as verification of the analytical and FEA approaches.

In addition to this the electrical outputs due to the piezoresistive effect and the stress introduced from displacements of the cantilever beams are also investigated in this chapter. These displacements are introduced using a shaker and the outputs are studied using waveforms displayed and recorded by means of an oscilloscope.

Chapter 8: Conclusions and Future Work. This chapter concludes the work described in the previous chapters. Issues with the production of these sensors and lessons learnt are discussed. Future work is presented to enhance the performance of the sensors, increase the manufacturing yield and improve the packaging of the sensor.

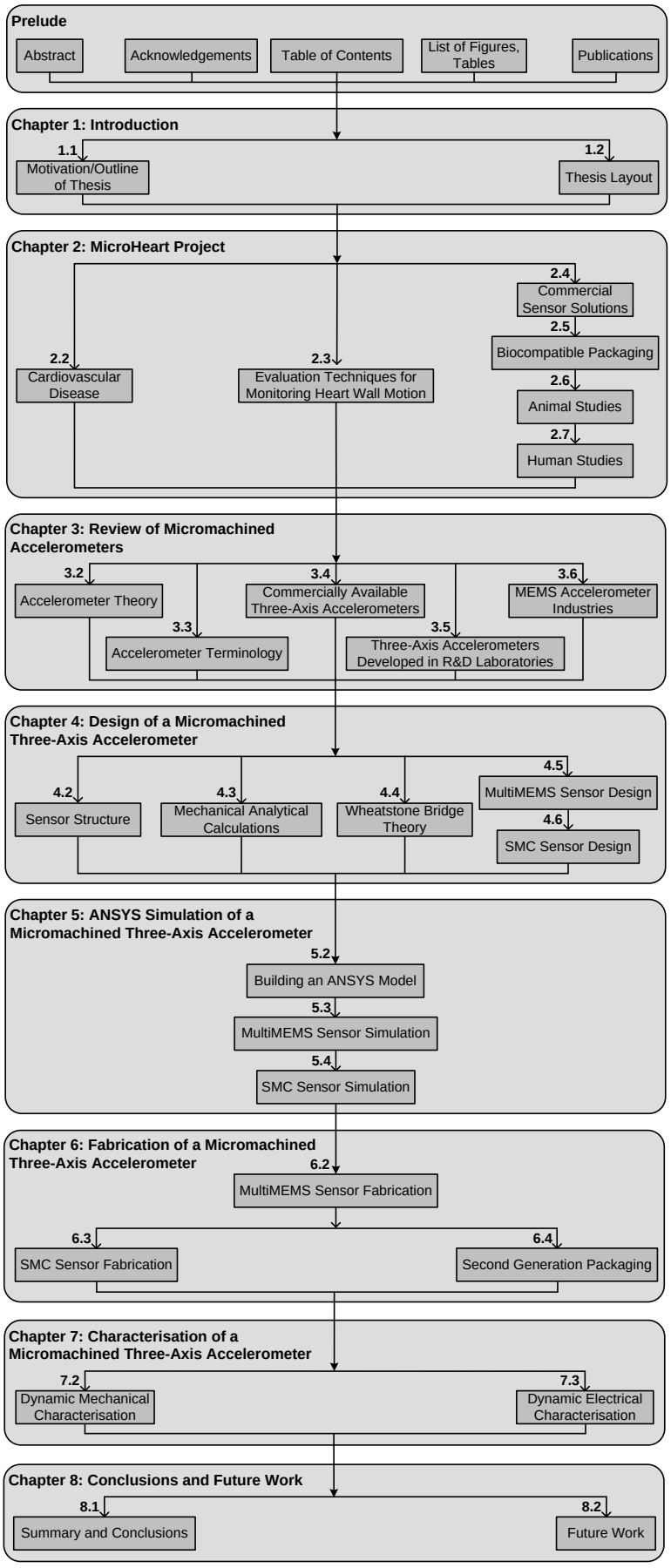

Figure 1.1: Synopsis of the thesis.

References

[1] O.J. Elle, E. Fosse, and M.G. Gulbrandsen. Patent: (WO/2003/061473) Use of Sensor and System for Monitoring Heart Movements.

Chapter 2

The MicroHeart Project

2.1 Introduction

Accelerometers have found a place in the emerging biomedical field and the MicroHeart project is an example of such a research activity in this field. The MicroHeart project was a collaboration with Heriot-Watt University, Vestfold University College, and the Interventional Centre at Rikshospitalet University Hospital. The clinicians at Rikshospitalet Hospital decided to investigate the possibility of using miniaturised three-axis accelerometers to measure the heart wall motion of patients who had undergone Coronary Artery Bypass Graft (CABG) surgery. A visualisation of the proposed setup can be seen in Figure 2.1. Such measurements would allow medical staff to detect any complications with the bypass during surgery and for a short period following the surgery. In addition the monitoring of the heart condition could be done in "real-time" so that any detected complications could potentially be remedied before the patient leaves the care of the hospital. The purpose of the authors' involvement in the MicroHeart project was to develop a miniaturised three-axis accelerometer to be attached to the cardiac wall to monitor the movement of the heart.

A considerable amount of academic work has been carried out over the last 20 years to assess the benefits of using accelerometers as a means to gain more information about heart motion in general and the detection of heart failure in particular [1–3]. In these studies, large single-axis accelerometers were placed on both the epicardial and endocardial surfaces. The research into this area has demonstrated the usefulness of employing such sensors for monitoring heart motion and function.

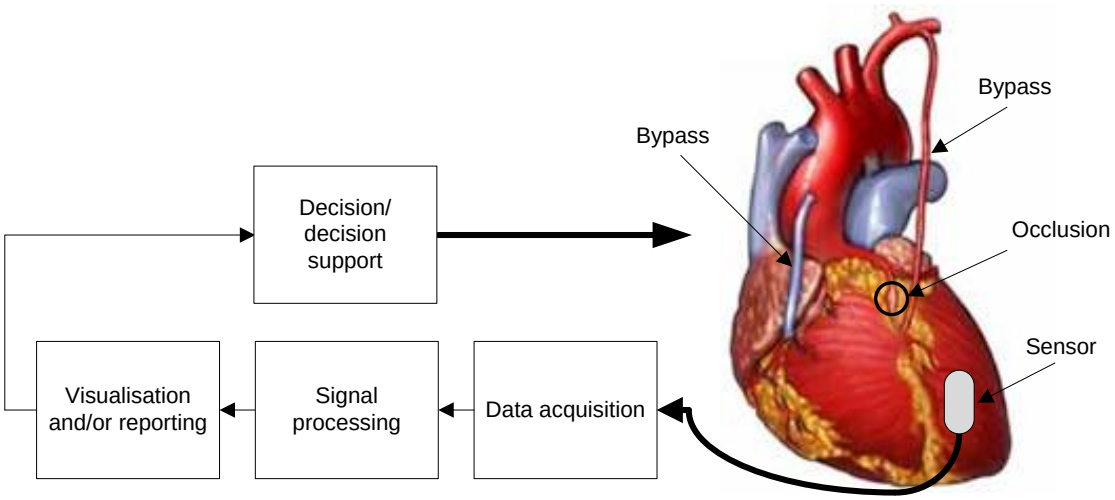

Figure 2.1: Visualisation of a heart bypass, placement of a miniaturised sensor, and associated data processing [4].

The use of a micro-accelerometer opens up the possibility of implanting the sensor. The sensor permits continuous real-time assessment of the heart wall motion and is not dependent on the operator skill. The reasoning for using a three-axis accelerometer is twofold: (1) the medical team do not know which of the heart axes are the best for detecting ischemia and (2) it removes the need for the surgeon to place the accelerometer at a fixed and identical angle in every patient and thus complicating the use of the sensor. The use of a three-axis sensor also means that three-dimensional movement of the heart can be recorded in real-time allowing the production of more detailed data sets and also accurate monitoring of the heart movement.

For this application, the sensors are to be designed to sense acceleration in three axes and meet the following indicative specifications [5–7]:

- Size $(W \times L \times H)$ (mm): 2×5×2 - designed with a view to integrating with a temporary pacemaker lead.
- Sensing Axes: 3 - makes the orientation of the chip arbitrary.

- Bandwidth (Hz): <40 - to be able to resolve details in heart motion which has a frequency of 1-3 Hz.
- Range (g): $\pm$ 4.
- Resolution (g): 0.05 - required for sensitivity and specificity.
- Accuracy (%): $\pm$ 10.
- DC Stability (s): $\approx$ 10 - to allow for respiration and patient motion.
- Temperature ($^{\circ}C$): 35-45 - human body temperature.
- Power Dissipation (mW): 0.5.
- Sterilization: γ rays - designed for single use.
- Electrical: 50 cm cable - to pre-amplifier positioned close to the patient.

2.2 Cardiovascular disease

CardioVascular Disease (CVD) is the most common cause of death in most Western countries and is a major cause of hospital admissions. The main form of CVD, Coronary Heart Disease (CHD), was responsible for over 446,000 deaths in America in 2005 [8]. In the United Kingdom, 94,000 CVD-related deaths were recorded in 2006 [9].

One of the most common surgical procedures to treat CHD is CABG surgery. Arteries or veins taken from elsewhere in the patient's body are grafted to the coronary arteries to bypass atherosclerotic narrowings in the arteries and improve the blood supply to the coronary circulation which supplies the myocardium. The success rate of this surgery is very high but complications, albeit rare, do sometimes occur. An external image showing the location of the main arteries of a human heart can be seen in Figure 2.2(a) whilst in Figure 2.2(b) it is possible to see two grafts bypassing blocked arteries.

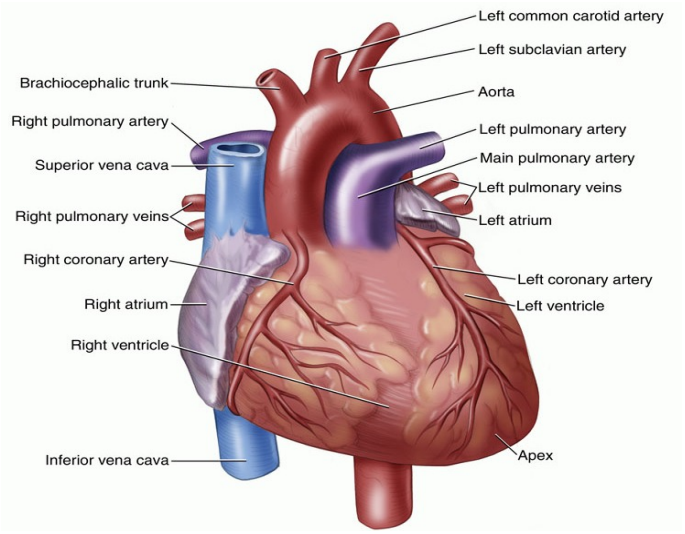

(a)

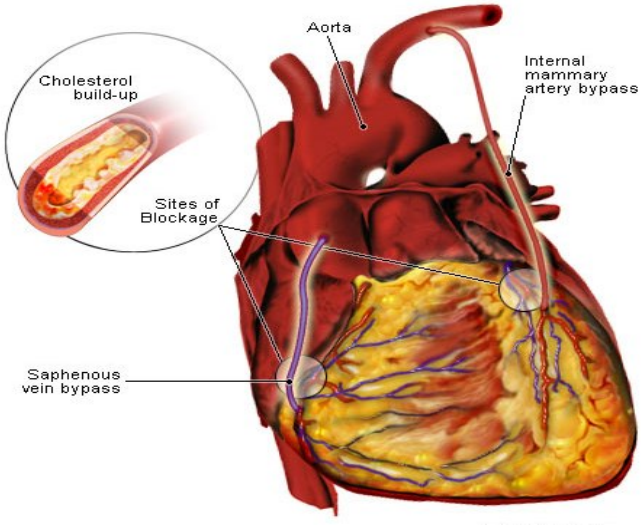

(b)

Figure 2.2: (a) External view of a Heart. (b) Example of a coronary heart bypass [10, 11].

Perioperative mortality in CABG is usually caused by reduced left ventricular function due to regional myocardial ischemia or infarction. Post-operative graft occlusion is a well-known problem in coronary surgery with 2-6% of arterial and 10-20% of venous grafts occluded after a period of 1 year. In a clinical study, 4% of grafts were identified as malfunctioning once the operation wound was closed in the operation theatre [12]. If this is not detected quickly enough, the onset of myocardial infarction may occur with serious risk to the health of the patient. It is therefore paramount for the medical staff to have a sensitive tool that is capable of detecting

graft occlusion and monitoring myocardial function during and following the surgical procedure so that the opportunity is given to review malfunctioning grafts before the patient's departure from the hospital [5].

2.3 Evaluation techniques for monitoring heart wall motion

A number of techniques exist that can be used in evaluating heart wall motion and can be applied to detecting abnormalities. For each method listed below, the possibility of using the technique for continuously monitoring for myocardial ischemia before and after cardiac surgery is considered.

An ElectroCardioGram (ECG) is a non-invasive test that records the electrical activity of the heart. The electrical activity is related to the rate and rhythm of the impulses that travel through the heart. The recording electrodes are placed on the chest, arms and legs.

Myocardial ischemia after CABG can be detected by ECG changes, and eventually by reduction in the cardiac pump function as measured by invasive hemodynamic monitoring of the heart. ECG is the only existing method for continuous monitoring of the heart with the potential to diagnose postoperative ischemia. However, this technique suffers from low specificity and sensitivity even with 12-channel monitoring and results are often inconsistent [13–16].

Angiography is an imaging technique to visualise the inside of arteries, veins and heart chambers and is commonly used to identify stenotic and occluded coronary arteries. Using a system of guiding wires and catheters, a type of contrast agent (which shows up by absorbing the X-rays) is added to the blood to make it visible on X-ray images. Angiography can be used to verify graft patency but this method is not suitable for continuous monitoring and is not typically integrated in the operating theatre.

Echocardiography uses standard ultrasound techniques to image 2-D slices of the heart. The latest ultrasound systems now employ 3-D real-time imaging. This method is used in the diagnostics of cardiac contractility, hemodynamic performance and valve function. Measurements of the strain and tissue velocity are new echocardiographic methods for the estimation of the viability and the contractility of the myocardium. Transesophageal echocardiography can detect myocardial ischemia, because ischemia is followed by an immediate decrease in regional myocardial contraction. Currently, echocardiography is considered to be the best method to quantify the heart function [17]. However, the method is user-dependent and is unsuitable for continuous post-operative monitoring due to the need for a cardiologist to hold the probe and analyse the visual output [18–20].

MagnetoCardioGraphy (MCG) is the measurement of the magnetic fields emitted by the human heart which result from small currents in the electrically active cells of the heart muscle. The measurement of these fields over the torso provides information which is complementary to that provided by electrocardiography, used especially in the diagnosis of abnormalities of heart function. Multichannel MCG enables the simultaneous recording of the signal over a large area without the need for time consuming electrode attachment encountered in ECG. However, with presently available technology the measurements still have to be performed in a shielded room, which excludes it as a quick bed-side test [21].

Body Surface Potential Mapping (BSPM) is the recording of the regional electrophysiological information obtained by the analysis of surface potentials to give a complete picture of the effects of the currents from the heart on the body surface. It covers an extensive area of the thorax offering better spatial scope and resolution than the standard ECG due to sampling in areas of the thoracic surface not covered by the conventional six precordial leads. The method has been reported to be more sensitive in the detection of myocardial infarction commpared to the 12-lead ECG. Combining BSPM and multichannel MCG allows a comprehensive study of

the electromagnetic fields generated by the heart in different clinical settings. These multichannel mapping techniques have also made it possible to look at the ischemia-induced spatial changes both in the magnetic and electric fields over the thorax. The time consuming placement of electrodes is a major disadvantage of the BSPM method [22, 23].

Another approach is the measurement of cardiac output which is an indirect measurement of heart function. Measurements taken here include thermodilution cardiac output, descending thoracic aortic flow velocity, mean arterial pressure, mean pulmonary artery pressure and heart rate. This method has no immediate response and has no selectivity for ischemia [24].

Using the strain Doppler technique, the patient undergoes an ultrasound examination. The examination requires qualified personnel and expensive equipment. It provides no direct warning but diagnosis after complication is possible.

Enzymes such as troponin and myoglobin which are specific to cell damage can be detected and monitored. This is an experimental method and could potentially become a future product. However, no immediate detection of re-occlusion is provided with this technique.

Myocard metabolism measurements offer a continuous measurement of the partial pressure (tension) of carbon dioxide (pCO2) or other metabolic parameters in the myocardium. It is an experimental technique which looks likely to be adequate but gives later warning of occlusion. The sensor is required to be placed in the myocardium unlike other sensors which are placed on the epicardium [5–7, 25].

2.4 Commercial sensor solutions

For the purposes of carrying out some feasibility studies at the beginning of the project, it was decided to employ a commercially available three-axis accelerometer.

However, at the start of this research project there were no suitable monolithic three-axis accelerometers readily available. As a substitute, two commercially available two-axis accelerometers from Analog Devices Inc. (ADXL311, Norwood, MA) were mounted at 90 degrees to one another, as shown in Figure 2.3(a), to provide sensing in three axes [26]. This assembly however resulted in a sensor solution of considerable size ($6\times12\times6$ mm^3).

Having used this sensor solution for a number of animal experiments, smaller monolithic three-axis capacitive accelerometers from Kionix Inc. (KXM52-1050, Ithaca, NY) became available and these were subsequently utilised in these studies forthwith, Figure 2.3(b). For this solution the sensor measured $5\times5\times1.8$ mm^3 and the substrate that this sensor was mounted to measured 5 mm in width and 11.5 mm in length.

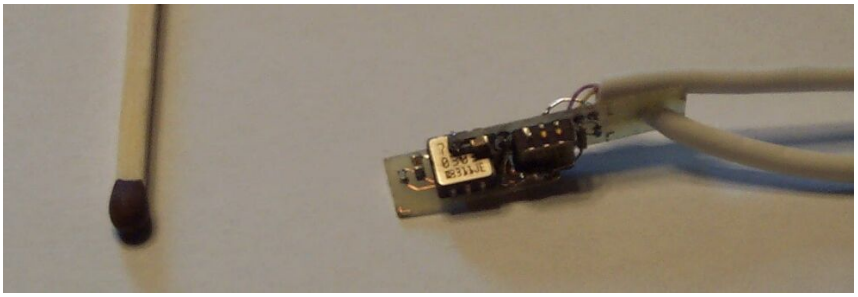

(a)

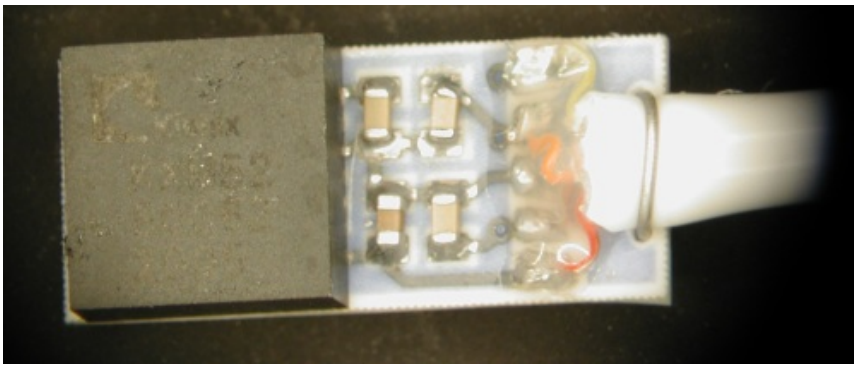

(b)

Figure 2.3: (a) Two dual-axis accelerometers from Analog Devices mounted at 90° to one another. (b) Kionix three-axis accelerometer (KXM52) mounted on substrate with associated passive electronics.

2.5 Biocompatible packaging

As the sensor is to be used *in vivo*, biocompatible encapsulation was undertaken using medical grade silicone. A biocompatibly packaged Kionix accelerometer can be seen in Figure 2.4. The resulting size of this biocompatibly-packaged sensor measured 11×14.5×5.2 mm^3. This encapsulation had to be suitable for sterilisation and be implantable for at least 29 days (USP Class VI). The use of silicone as the biocompatible encapsulation material is a well established approach for invasive medical devices [6]. Such a material also has the advantage of being suitable for prototyping and moulding. For rapid sterilisation, a low-temperature hydrogen peroxide gas plasma method was used.

Figure 2.4: Biocompatibly packaged Kionix accelerometer.

2.6 Animal studies

Feasibility studies were first carried out on porcine animals according to a protocol approved by the Institutional Animal Care and Use Committee [27]. During the procedure, the thorax of anesthetised pigs was opened to provide access to the heart; a procedure which is common in open heart surgery. The sensor is sutured onto the left ventricular free wall in the region of blood supply of the Left Anterior Descending (LAD) coronary artery as can be visualised in Figure 2.5. The suture

was made possible by four holes included in the silicone mould at each corner of the sensor which can partly be seen in Figure 2.4. To induce myocardial ischemia, the LAD was occluded for different periods of time.

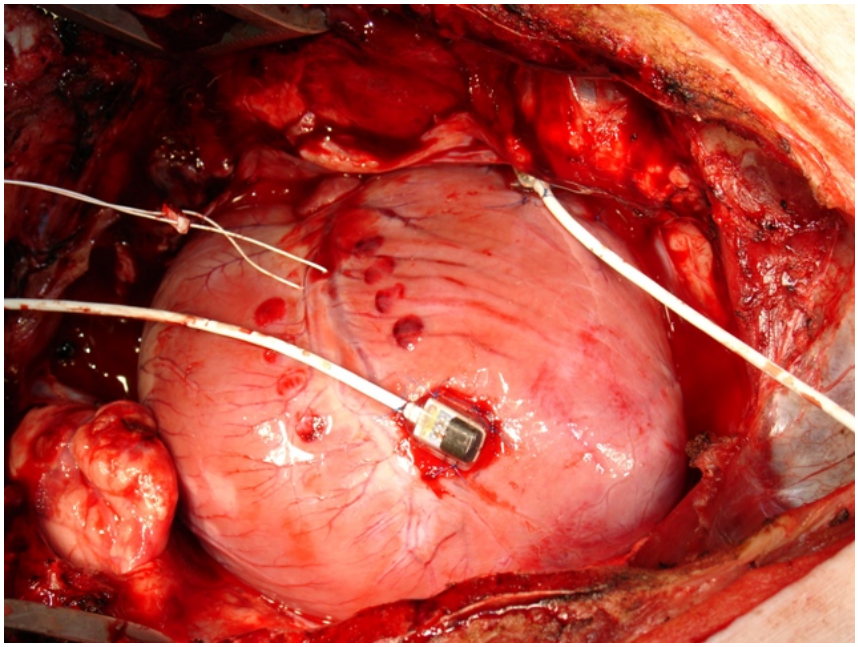

Figure 2.5: Placement of commercial three-axis accelerometer during open heart surgery.

Data from the sensor was logged using a NI-USB 6009 data acquisition board and was interfaced using a software program written in LabView (both from National Instruments Inc, Austin, TX). As a reference, an ECG signal was sampled synchronously. The results were stored on a computer and processed using Matlab (The MathWorks, Inc., MA). These animal studies demonstrated that it was possible to obtain continuous real-time assessments of heart wall motion and to detect regional cardiac ischemia [5]. An example of the output of such an experiment can be seen in Figure 2.6 where the periodic output from the accelerometer of a healthy beating heart can be seen in the upper signal. This is clearly interrupted by arrhythmias at 638 s and 643 s. The lower signal in Figure 2.6 is from ECG and the accelerometer output is in perfect synchronisation with this signal. The distortion due to the arrhythmias is also mirrored in this signal.

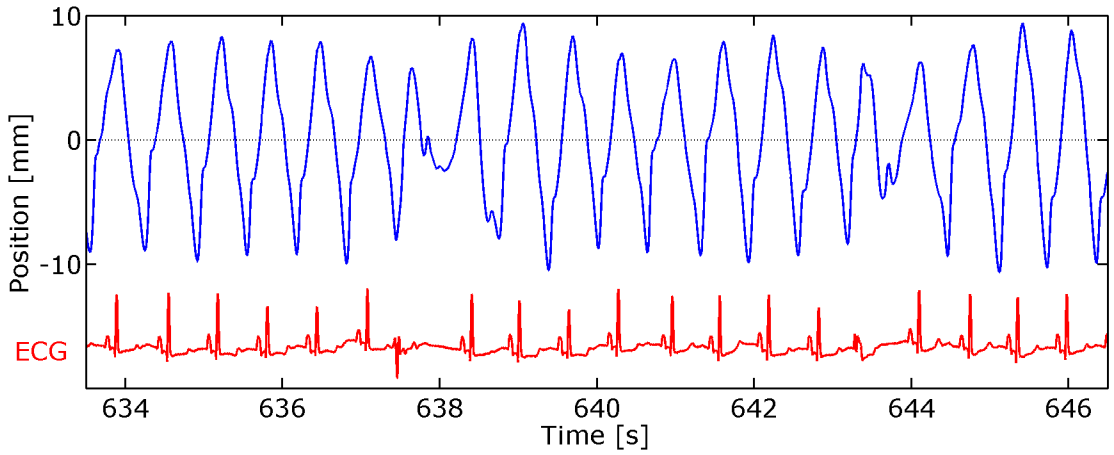

Figure 2.6: Output signal from sutured accelerometer together with ECG signal recorded during animal studies.

Results such as these indicate that early recognition of regional cardiac ischemia is possible by analysing accelerometer data acquired from animal trials using commercial three-axis accelerometer sensors.

2.7 Human studies

Further clinical studies were carried out on consenting human patients in accordance with the IEC 60601 standard. These patients, suffering from significant LAD coronary artery stenosis, were due to undergo off-pump CABG. These studies further confirmed that the epicardial accelerometer can detect myocardial ischemia with great accuracy. This novel technique has therefore the potential to be implemented in clinical practice to improve monitoring of myocardial ischemia during and after cardiac surgery [7].

2.8 Summary and conclusions

An investigation was performed by the team to demonstrate that a three-axis accelerometer could be implemented to detect perioperative complications resulting

from CABG surgery. Other techniques that are associated with the monitoring of heart wall motion are introduced and the shortfalls of these methods for continuous, non-invasive implementation are discussed.

The suitability of a miniaturised micromachined accelerometer for *in vivo* operation opens the possibility of continuously monitoring the heart movement, both during the open heart surgery and during the first critical post-operative days. The sensor is sutured directly to the epicardium of the patient. With a three-axis accelerometer, simultaneous assessment of wall motion in the longitudinal, circumferential, and radial directions can be performed. To make the sensor suitable for implantation the packaging of the sensor was biocompatible for the patient's safety. Silicone moulding was introduced which is also suitable for suturing the sensor to the surface of the heart as well as for sterilisation.

With application of the commercial sensor solutions, it was shown that an epicardial three-axis accelerometer is capable of sensing abnormal motions of the heart wall and be used as a tool to report such anomalies to the cardiac surgeon. However, these commercial sensor solutions were still deemed to be too large and it was necessary to design and fabricate a smaller sensor solution in-house. Further progress in the integration of the sensor is also possible in the form of temporary epicardial pacemaker leads.

References

[1] J.C. Wood, A.J. Buda, and D.T. Barry. Time-frequency transforms: a new approach to first heart sound frequency dynamics. *IEEE. Trans. Biomed. Eng.*, 39(7):730–740, 1992.

[2] J.C. Wood, M.P. Festen, M.J. Lim, A.J. Buda, and D.T. Barry. Regional effects of myocardial ischemia on epicardially recorded canine first heart sounds. *J. Appl. Physiol.*, 76(1):291–302, 1994.

[3] H.P. Theres, D.R. Kaiser, S.D. Nelson, M. Glos, T. Leuthold, G. Baumann, S. Sowelam, T.J. Sheldon, and L. Stylos. Detection of acute myocardial ischemia during percutaneous transluminal coronary angioplasty by endocardial acceleration. *Pace.*, 27(5):621–625, 2004.

[4] EBSCO Publishing. Coronary artery bypass grafting (CABG), 2006. `http://www.beliefnet.com/healthandhealing/getcontent.aspx?cid=14782` (Accessed: 07 Oct 10).

[5] O.J. Elle, S. Halvorsen, M.G. Gulbrandsen, L. Aurdal, A. Bakken, E. Samset, H. Dugstad, and E. Fosse. Early recognition of regional cardiac ischemia using a 3-axis accelerometer sensor. *Physiol. Meas.*, 26:429–440, April 2005.

[6] K. Imenes, K. Aasmundtveit, E.M. Husa, J.O. Hogetveit, S. Halvorsen, O.J. Elle, P. Mirtaheri, E. Fosse, and L. Hoff. Assembly and packaging of a three-axis micro accelerometer used for detection of heart infarction. *Biomedical Microdevices*, 9(6):951–957, December 2007.

[7] S. Halvorsen, A. Espinoza, L.A. Fleischer, O.J. Elle, L. Hoff, R. Lundblad, H. Skulstad, T. Edvardsen, H. Ihlen, and E. Fosse. Feasibility of a three-axis epicardial accelerometer in detecting myocardial ischemia in cardiac surgical patients. *J. Thorac. Cardiovasc. Surg.*, 136:1496–1502, 2008.

[8] Heart disease & stroke statistics 2009. http://www.americanheart.org/.

[9] Coronary heart disease statistics. http://www.heartstats.org/.

[10] Summit Medical Group. Coronary artery disease. `http://www.summitmedicalgroup.com/library/heart_health/coronary_artery_disease/` (Accessed: 07 Oct 10).

[11] MedicineNet.com. Coronary artery bypass graft. `http://www.medicinenet.com/coronary_artery_bypass_graft/page4.htm` (Accessed: 07 Oct 10).

[12] P.K. Hol, P. S. Lingaas, R. Lundblad, K. A. Rein, K. Vatne, H. J. Smith, S. Nitter-Hauge, and E. Fosse. Intraoperative angiography leads to graft revision in coronary artery bypass surgery. *Ann. Thor. Surg.*, 78:502–505, 2004.

[13] U. Jain, C. J. Laflamme, A. Aggarwal, J. G. Ramsay, M. E. Comunale, S. Goshal, L. Hgo, K. Ziola, M. Hollenberg, and D. T. Mangano. Electrocardiographic and hemodynamic changes and their association with myocardial infarction during coronary artery bypass surgery. *Anesthesiology*, 86:576–591, March 1997.

[14] R. Gianrossi, R. Detrano, D. Mulvihill, K. Lehmann, P. Dubach, A. Colombo, D. McArthur, and V. Froelicher. Electrocardiographic and hemodynamic changes and their association with myocardial infarction during coronary artery bypass surgery. *Circulation*, 80:87–98, 1989.

[15] G. Crescenzi, T. Bove, F. Pappalardo, A. M. Scandroglio, G. Landoni, G. Aletti, A. Zangrillo, and O. Alfieri. Clinical significance of a new Q wave after cardiac surgery. *Eur. J. Cardiothorac. Surg.*, 25:1001–1005, June 2004.

[16] M. J. London, G. Landesberg, M. Mosseri, Y. Wolf, Y. Vesselov, and C. Weissman. Perioperative myocardial ischemia and infarction: Identification by continuous 12-lead electrocardiogram with online st-segment monitoring. *Anesthesiology*, 96(2):264–270, 2002.

[17] T. Edvardsen, H. Skulstad, S. Aakhus, S. Urheim, and H. Ihlen. Regional myocardial systolic function during acute myocardial ischemia assessed by strain Doppler echocardiography. *J. Am. Coll. Cardiol.*, 37:726–730, 2001.

[18] M. E. Comunale, S. C. Body, C. Ley, C. Koch, G. Roach, J. P. Mathew, A. Herskowitz, and D. T. Mangano. The concordance of intraoperative left ventricular wall-motion abnormalities and electrocardiographic S-T segment changes: association with outcome after coronary revascularization. *Anesthesiology*, 88:945–954, April 1998.

[19] K. Skarvan, M. Filipovic, J. Wang, W. Brett, and M. Seeberger. Use of myocardial tissue Doppler imaging for intraoperative monitoring of left ventricular function. *Br. J. Anaesth.*, 91:473–480, 2003.

[20] JD. Kneeshaw. Transoesophageal echocardiography (TOE) in the operating room. *Br. J. Anaesth.*, 97:77–84, 2006.

[21] B. Hailer, I. Chaikovsky, S. Auth-Eisernitz, H. Scaafer, F. Stfinberg, and D. H. W. Gonemeyer. Magnetocardiography in coronary artery disease with a new system in an unshielded setting. *Clinical cardiology*, 26(10):465–471, 2003.

[22] M. Tysler, P. Kneppo, V. Rosik, S. Karas, E. Heblakova, and J. Muzik. Body surface potential mapping for noninvasive ischemia detection. In *14th Nordic-Baltic Conference on Biomedical Engineering and Medical Physics*, volume 20, pages 339–342, July 2008.

[23] F. Boudik, M. Stojan, Z. Anger, M. Aschermann, J. Vojacek, and P. Stovicek. Evaluation of body surface potential mapping changes after successful percutaneous transluminal coronary angioplasty. *Can. J. Cardiol.*, 12(8):745–749, Aug 1996.

[24] M.P. Grow, A. Singh, N. W. Fleming, N. Young, and M. Watnik. Cardiac output monitoring during off-pump coronary artery bypass grafting. *J. Cardiothorac. Vasc. Anesth.*, 18(1):43–46, Feb 2004.

[25] P.S. Halvorsen, L.A. Fleischer, A. Espinoza, O.J. Elle, H. Hoff, H. Skulstad, T. Edvardsen, and E. Fosse. Detection of myocardial ischaemia by epicardial accelerometers in the pig. *Br. J. Anaesth.*, 102(1):29–37, Jan 2008.

[26] L. Hoff, O.J. Elle, M.J. Grimnes, S. Halvorsen, H.J. Alker, and E. Fosse. Measurements of heart motion using accelerometers. *Procs. 26th IEEE EMNS, San Francisco*, pages 2049–2051, 2004.

[27] Institutional Animal Care and Use Committee. `http://www.iacuc.org/` (Accessed: 07 Oct 10).

Chapter 3

Review of Micromachined Accelerometers

3.1 Introduction

This chapter introduces a literature review of R&D and commercial three-axis accelerometers. A variety of different sensor solutions are introduced that implement different sensing techniques as different silicon micromachining techniques.

Acceleration, vibration, shock and tilt are manifestations of acceleration over different periods of time as can be visualised in Figure 3.1.

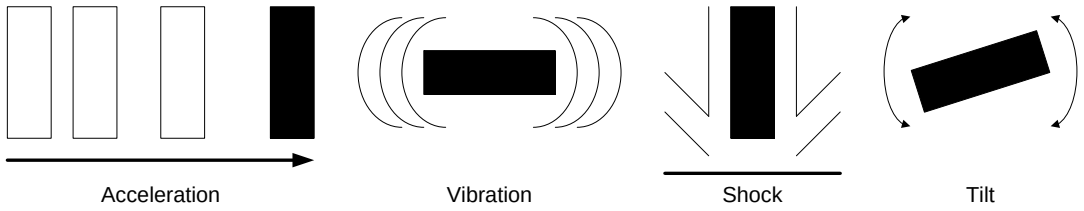

Figure 3.1: The four acceleration senses.

Acceleration including translational movement measures the change in velocity in a unit of time. Velocity, expressed in metres per second (m/s), includes both the rate of displacement and direction of movement. It follows that acceleration is measured in metres per second squared (m/s^2).

If we consider acceleration over various periods of time then vibration can be thought of as acceleration and deceleration that happens quickly and in a periodic manner. Similarly, shock is acceleration that occurs instantaneously but, unlike vibration, a shock is a non-periodic function that typically happens once.

When an object is moved to alter its tilt, or inclination, some change in position with respect to gravity is involved. This movement tends to happen rather slowly compared to vibration and shock. A MEMS accelerometer detects tilt by measuring the effect of the force of gravity on the different axes of the accelerometer. For the case of a three-axis accelerometer, three separate outputs measure acceleration along the x, y, and z axes of motion.

Because the four modes of motion sensing each involve a certain aspect of acceleration, they are measured by g force, the unit of force that gravity exerts on an object on the Earth ($1\ g = 9.8\ m/s^2$) .

3.2 Accelerometer theory

Many types of micromachined accelerometers have been developed and reported in the literature. The vast majority of these devices have in common a mechanical sensing element consisting of a proof mass attached by a mechanical suspension system to a reference frame. The accelerometer can thus be modelled by a second-order mass-damper-spring system as shown in Figure 3.2.

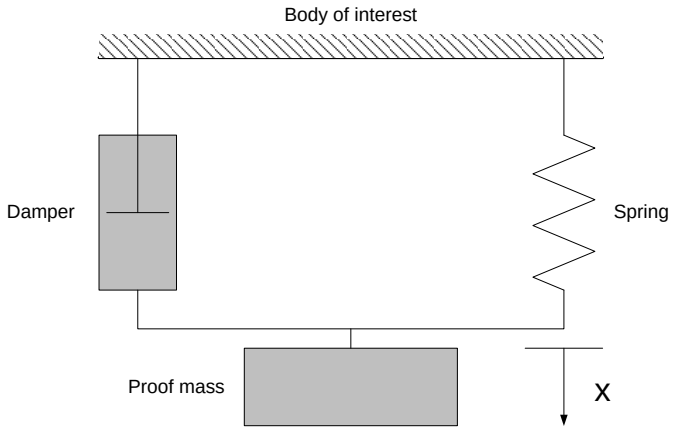

Figure 3.2: Lumped parameter model of an accelerometer consisting of a proof (or seismic) mass, a spring, and a damping element.

Any external inertial forces due to acceleration displace the support frame relative

to the proof mass according to Newton's second law. This in turn applies a force of $F{=}m \cdot a$ on the spring with m being the mass of the proof mass and a being the acceleration of the displacement. The spring is deflected until its elastic force equals the force produced by the acceleration. In the first order, the force acting on the spring is proportional to its deflection x, $F{=}k \cdot x$, with k being the mechanical spring constant. Therefore, in a static situation the deflection is proportional to the acceleration:

$$x = \frac{m}{k}a \tag{3.1}$$

Both the relative displacement and the suspension-beam stress can be used as measures the external acceleration.

The second order mechanical transfer function can be described as:

$$\frac{x(s)}{a(s)} = \frac{1}{s^2 + \frac{b}{m}s + \frac{k}{m}} \tag{3.2}$$

where b is the damping coefficient and s is the Laplace operator [1]. The natural resonant frequency (rad/s), ω_n, of this system is given by :

$$\omega_n = \sqrt{\frac{k}{m}} \tag{3.4}$$

[1]Sometimes it is preferred to write the transfer function in terms of the natural frequency and the quality factor Q:

$$\frac{x(s)}{a(s)} = \frac{1}{s^2 + \frac{\omega_n}{Q}s + \omega_n^2} \text{ with } Q = \frac{\omega_n m}{b} = \frac{\sqrt{mk}}{b} \tag{3.3}$$

Together, the mass and the spring determine the static mechanical sensitivity S $(m/(m/s^2))$:

$$S = \frac{m}{k} = \frac{x}{a} = \frac{1}{\omega_n^2} \tag{3.5}$$

As an accelerometer can typically be used at a frequency below its resonant frequency, an important design trade-off becomes apparent since sensitivity and resonant frequency increase and decrease with m/k, respectively. This trade-off can be partly overcome by including the sensing element in a closed loop, force-feedback control system.

The resonance frequency of the structure can be increased by increasing the spring constant and decreasing the proof mass, while the quality factor of the device can be increased by reducing damping and by increasing the proof mass and spring constant. Lastly, the static response of the device can be improved by reducing its resonant frequency.

The damping factor is crucial for the dynamic performance of an accelerometer. For maximum bandwidth the sensing element should be critically damped; it can be shown that for $b{=}2m\omega_n$ this is the case. In micromachined accelerometers the damping originates from the movement of the proof mass in a viscous medium. Depending on the mechanical design, however, the damping coefficient cannot be assumed to be constant but it increases with the deflection of the proof mass and with the frequency of movement of the proof mass - this phenomenon is called squeeze film damping [1].

A common factor for all micromachined accelerometers is that the displacement of the proof mass has to be measured by a position-measuring interface circuit and is then converted into an electrical signal. Many types of sensing mechanisms have

been reported such as capacitive, piezoresistive, piezoelectric, optical, and tunneling current, with the first three being the most commonly used. The characteristic and performance of any accelerometer is greatly influenced by the position measurement interface with the main requirements being low noise, high linearity, good dynamic response, and low power consumption. Ideally, the interface circuit should be represented by an ideal gain block, relating the displacement of the proof mass to an electrical signal [1–4].

3.3 Accelerometer terminology

Bandwidth

The bandwidth is the frequency range that the sensor operates in. Accelerometers generally have a frequency range from DC to the mechanical resonant frequency (-3 dB) defined by the sensor. This frequency range can be limited by adding an external filter on the output of the x, y and z axes. Some accelerometers have this filter internally built in.

Cross-axis sensitivity

The cross-axis sensitivity is the output on the sensing axis from accelerations on a perpendicular axis, expressed as a percentage of the sensitivity. Each axis has two cross-axis sensitivities:

- x: S_{XY}, S_{XZ}
- y: S_{YZ}, S_{YX}
- z: S_{XY}, S_{ZX}

Noise and noise density

Noise determines the minimum resolution of the sensor. The noise threshold can be lowered by lowering the bandwidth. The power spectral density is measured in $\mu g/\sqrt{Hz}$. When this value is multiplied by the square root of the measurement bandwidth, the result is the RMS acceleration noise of the sensor at nominal operating voltage and temperature. Accelerations below this value will not be resolvable.

Non-linearity

The transfer function of the sensor (input/output relationship) is not perfectly linear. The non-linearity is the maximum deviation of output voltage from a best fit straight line divided by the sensitivity of the device. This is expressed as a percentage of Full-Scale Output (FSO). The method for calculating the non-linearity is shown below:

$$\text{Non-Linearity} = \frac{\text{Maximum Deviation (g)}}{\text{Full Scale Output (g)}} \times 100\% \tag{3.6}$$

Offset and offset versus temperature

Offset refers to the DC output level of the accelerometer when no motion or gravity is acting on it, often called the 0 g-offset. It is the maximum change in the nominal zero-g output over the full operating temperature range.

Range

Is the maximum $\pm$ amplitude that the accelerometer can measure before distortion or clipping of the output signal occurs.

Ratiometricity and ratiometric error

The output offset voltage and sensitivity usually scale linearly with applied supply voltage. As the supply voltage increases, the sensitivity and offset increase. Ideally, the sensor is ratiometric which means that the output scales by the same ratio as V_{DD} changes. Ratiometric error is defined as the difference between the ratio that the 0 g offset or sensitivity has changed with the ratio that V_{DD} has changed.

For example, the offset ratiometric error at a nominal operating voltage of 3.3 V $\pm 5\%$ is defined as the maximum absolute value of:

$$\text{Error@}3.135V = \left(\frac{\text{Offset@}3.135V}{\text{Offset@}3.3V} - \frac{3.135V}{3.3V} \right) \times 100\% \tag{3.7}$$

$$\text{Error@}3.465V = \left(\frac{\text{Offset@}3.465V}{\text{Offset@}3.3V} - \frac{3.465V}{3.3V} \right) \times 100\% \tag{3.8}$$

Similarly for the sensitivity ratiometric error calculation:

$$\text{Error@}3.135V = \left(\frac{\text{Sensitivity@}3.135V}{\text{Sensitivity@}3.3V} - \frac{3.135V}{3.3V} \right) \times 100\% \tag{3.9}$$

$$\text{Error@}3.465V = \left(\frac{\text{Sensitivity@}3.465V}{\text{Sensitivity@}3.3V} - \frac{3.465V}{3.3V} \right) \times 100\% \tag{3.10}$$

Resolution

The resolution is the smallest detectable increment in acceleration and must be greater than the noise value of the sensor. The accelerometer bandwidth will determine the measurement resolution, but filtering can be used to lower the noise floor and improve the resolution further. The resolution can be improved by decreasing the bandwidth of the output low-pass filter. The resolution is calculated by the following equation:

$$Resolution = N \times \sqrt{BW_{LPF} \times 1.57} \tag{3.11}$$

where N is the power spectral density noise in $\mu g/\sqrt{Hz}$ and the equivalent noise bandwidth of a filter (BW_{LPF}) is the -3 dB bandwidth multiplied by a coefficient which is dependent on the order of the filter and is equal to 1.57 for a 1^{st} order filter.

Sensitivity

The sensitivity is the output voltage change per unit of input acceleration at nominal operating voltage and temperature, measured in mV/g (Voltage Output per g) [5].

3.4 Commercially available three-axis accelerometers

A small number of companies exist in the inertial MEMS sensor market. These companies offer sensor solutions that can lend themselves to certain applications. Inertial sensors are usually categorised by the following parameters: number of sensing axes, sensor output (i.e. analogue/digital), physical size, g range, sensitivity, noise, and power consumption. In this section, some three-axis acceleration sensors from some of the main competitors in the market are introduced. In particular, the

provision of low-g accelerometers from these companies i.e. accelerometers which measure accelerations less than 10 g are considered.

Some of the specifications of the sensors mentioned in this section are provided in Table 3.1.

3.4.1 Analog Devices

Analog Devices is the leading manufacturer of MEMS-based accelerometers and offers a large number of sensor solutions. The first device from Analog Devices came in the form of the single axis ADXL50 which was introduced in 1991 and went into volume production in 1993. It distinguished itself as the first commercially available device to employ surface micromachining. In addition to this, other firsts include:

- The first surface micromachined accelerometer to be manufactured in high volume.
- The first micromachined sensor with the motion sensor element, extensive signal conditioning circuitry and self-test circuitry on a single chip.
- The first micromachined sensor Integrated Circuit (IC) whose moving part moves in the plane of the chip.

Ultimately, these breakthroughs allowed the MEMS-based accelerometer to fall in line with the cost reductions in airbag electronics and thus open up a large market opportunity in the automotive industry.

The sensor is a polysilicon surface-micromachined structure built on top of a silicon wafer. Polysilicon springs suspend the structure over the surface of the wafer and provide a resistance against acceleration forces. The movement of the beam is controlled by the polysilicon springs holding the beam.

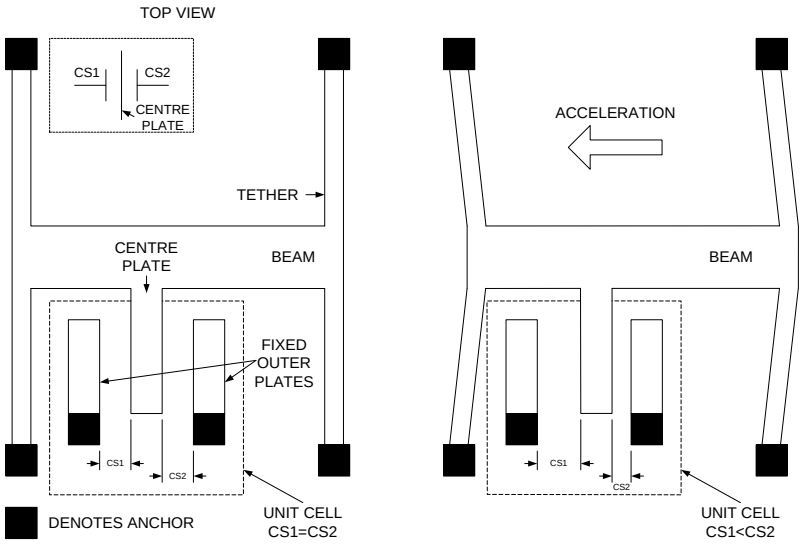

Figure 3.3: Working of an Analog Devices ADXL differential capacitive sensor [6].

The sensor element is a differential capacitor whose output is proportional to acceleration. The beam is made up of many interdigitated fingers whose operation is visualised in Figure 3.3 for one set of fingers.

During acceleration, the gap between the beam attached to the mass and the fixed beam on one side will increase by the same amount that the gap between the moving beam and the fixed one on the other side decreases. This change of distance provides a measure of acceleration. At steady state the nominal value of the capacitors are a few pF. When an acceleration is applied the maximum variation of the capacitive load is in the fF range. The beams form two back-to-back capacitors as shown in Figure 3.4. As the centre beam moves with acceleration, the distance between the beams changes and the value of each capacitor will change.

The silhouette plots in Figure 3.5(a) compare the structures used in the ADXL50 and the more recent ADXL150. Both sensors have numerous fingers along each side of the movable centre member which form the centre plates of a paralleled set of differential capacitors. Pairs of fixed fingers attached to the substrate interleave with the beam fingers to form the outer capacitor plates. The beam is supported by tethers, which serve as mechanical springs. The voltage on the moving plates is

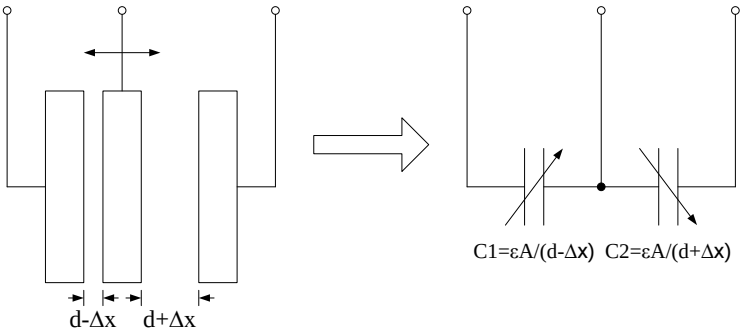

Figure 3.4: Simplified transducer physical model.

read via the electrically conductive tether anchors that support the beam.

The ADXL50's tethers extend straight out from the beam in an 'H' configuration. On the ADXL150, however, the tethers are folded, reducing the size of the sensor and halving the number of anchors, Figure 3.5(b).

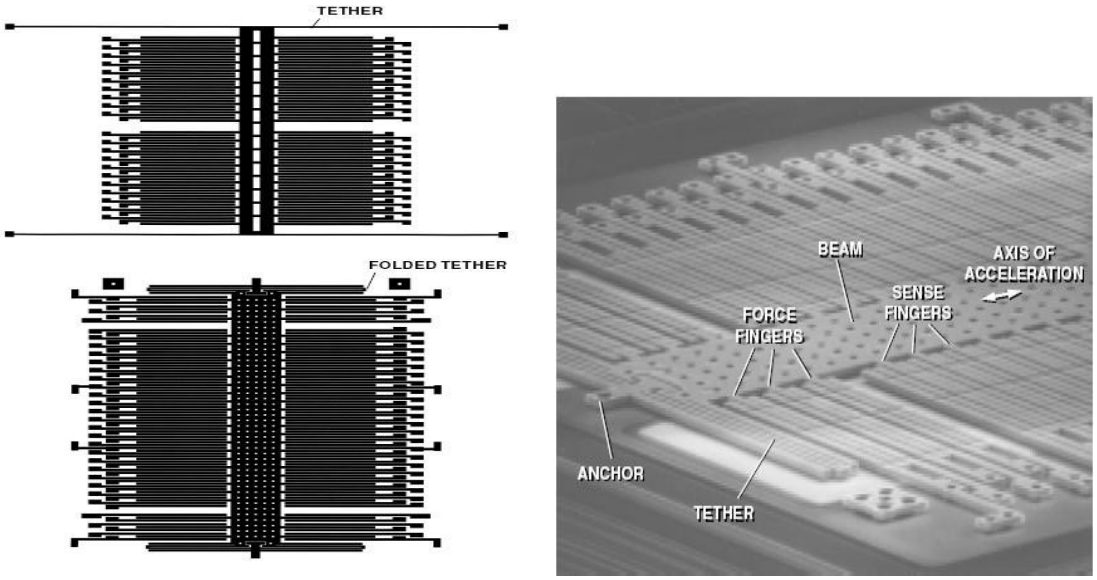

(a) (b)

Figure 3.5: (a) Silhouette plots of ADXL50 (upper) and ADXL150 (lower) with the axis of motion vertical. (b) Scanning Electron Microscope (SEM) view of one end of the ADXL150's sensor [7].

The fixed outer plates are driven with square waves that are 180° out of phase. When the movable fingers (and hence the beam) are centred between the fixed outer plates, both sides of the differential capacitor have equal capacitance and the AC voltage

on the beam is zero. Acceleration deflects the moving mass and unbalances the differential capacitor resulting in a sensor output whose amplitude is proportional to acceleration. Phase-sensitive demodulation techniques are then used to determine the magnitude and direction of the acceleration.

In addition to the sense fingers projecting from both sides of the beam, the ADXL150 has 12 force fingers (visible in Figure 3.5(b)) which are used for self-test actuation. The plates of a parallel-plate capacitor attract each other with an electrostatic force of:

$$F = \frac{\epsilon A V^2}{2d^2} \tag{3.12}$$

where V is the voltage across the capacitor. In normal operation, the fixed fingers on either side of the force fingers are at the same voltage potential as the beam and its fingers. With no voltage between the force fingers on the beam and the fixed fingers on the substrate, there is no electrostatic force. However, when a digital self-test input pin is activated, the fixed fingers on one side of the force section are driven to a non-zero DC voltage, applying a force to the sense fingers, deflecting the beam.

For each of the Analog Devices offerings and with capacitive sensing accelerometers in general, the MEMS structures are integrated with an Application Specific Integrated Circuit (ASIC) that evaluates the output of the acceleration-sensing element. This is done by stacking the MEMS structures on top of the ASIC or placing them alongside each other in the plastic mould.

The ASIC is fabricated using a standard Complimentary Metal-Oxide-Semiconductor (CMOS) process. It evaluates, corrects and amplifies the output signal of the MEMS acceleration-sensing element. It commonly consists of three voltage converters and

three signal conditioners, a channel multiplexer, a digital-to-analogue converter, memory and an internal RC oscillator.

The ADXL330 shown in Figure 3.6(a), was the first offering from Analog Devices that provided three-axis acceleration sensing. The MEMS sensing element integrated with its ASIC can be seen in Figure 3.6(a).

A major requirement for the production of the sensors is that the sensing element be protected from the plastic material injected during moulding. To achieve this the sensing element is often hermetically sealed by a bulk micromachined cap at wafer-level and this is usually performed with a glass frit. This process ensures that the sensing element will be free of any particles that may disturb it. With such a protection the transducer can then go through all the other process steps (dicing, packaging, etc.) without any damage. An example of this is shown in Figure 3.6(b).

The ADXL330 uses a 3-poly MEMS process with the 2.1 μm wide, poly-3 beam forming the minimum width feature in the MEMS portion of the die. The poly-1 layer is used as interconnect and the poly-3 layer forms the 4 μm thick proof mass which is supported by four springs, and incorporates the x and y sense capacitors. A poly-2 shield layer is present beneath the proof mass, which serves as the bottom plate of the z-axis sense capacitor.

Generally the sensors and specifically designed ASIC's are then assembled in small and thin Quad Flat No-leads (QFN) or Land Grid Array (LGA) packages.

The newest three-axis offering with analogue output from Analog Devices is the ADXL335 [8]. The device has a measurement range of ± 3 g minimum and uses a single structure for sensing the x, y, and z axes. The ADXL335 is $4 \times 4 \times 1.45$ mm^3 and is delivered in a plastic lead frame chip scale package (LFCSP_LQ).

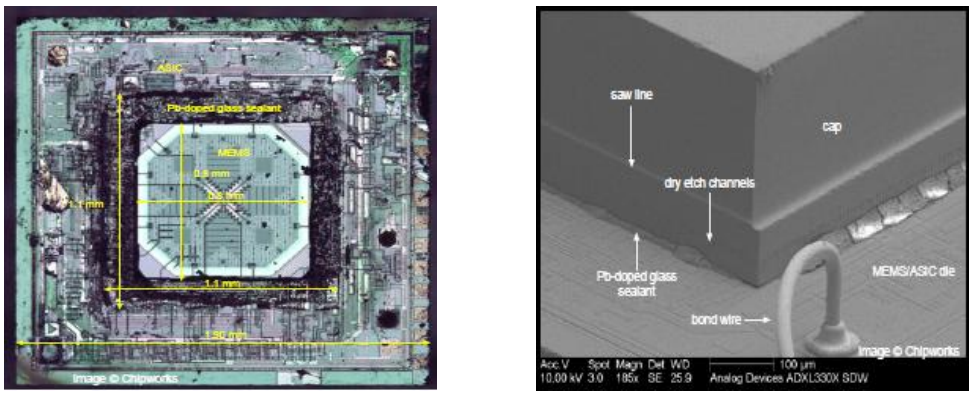

(a) (b)

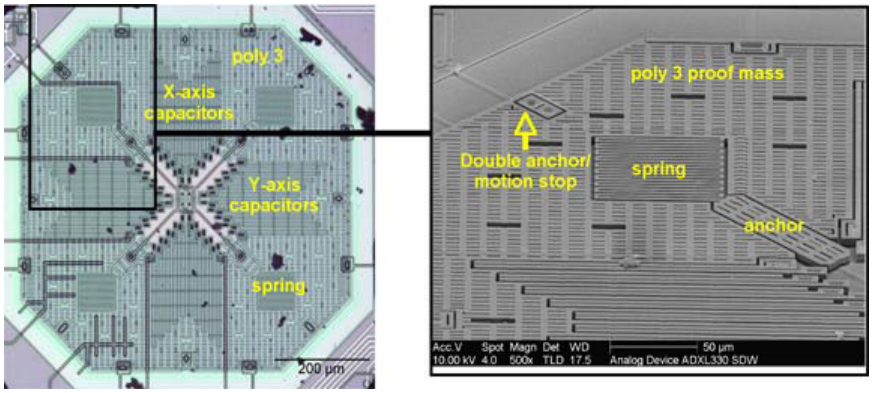

(c)

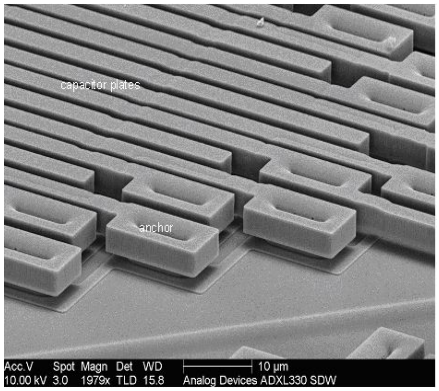

(d)

Figure 3.6: Images from the Analog Devices ADXL330 showing (a) MEMS structure with cap removed and surrounding ASIC, (b) ceramic cap over MEMS structure on top of ASIC, (c) SEM of capacitive fingers and anchors, (d) close-up of MEMS structure showing springs and the x- and y-capacitors [9].

In general with currently available analogue accelerometers and with this sensor, offerings include:

- Two operation modes: standby and normal mode.
- Ultra-low power consumption.
- Analog output signals: 3 parallel (x, y, z) plus 1 serial (multiplexed x, y, z).
- On-chip gain and offset compensation.
- Trigger-able self-test capability of MEMS sensor element and ASIC.

For a digital output offering, the ADXL346 is available and has selectable measurement ranges of ± 2 g, ± 4 g, ± 8 g, or ± 16 g. The ADXL346 is supplied in a $3 \times 3 \times 0.95$ mm^3 plastic LGA package [10].

A digital output accelerometer generally has the following typical features:

- User programmable g-range and bandwidth.
- Low-power consumption.
- SPI (3-wire/4-wire) and I^2C interface.
- User programmable interrupt engine.
- Ultra-low-power auto-wake-up mode.
- Self-test capability.

The interrupt feature offers the following motion detection scenarios:

- Any-motion (slope) detection.
- Tap sensing.

- Orientation change recognition.
- Low-g/high-g detection.
- Data-ready.
- Self-wake-up.

3.4.2 Bosch Sensortec

The production of the Bosch Sensortec sensing element is based on a standard semiconductor and MEMS process. The process cycle starts with the deposition of a thick epitaxial layer on a sacrificial oxide. The large thickness allows the design of working capacitances of up to 1 pF. The poly-layer is patterned by a Deep Reactive Ion Etch (DRIE) in an Inductively Coupled Plasma (ICP). A large aspect ratio and very high anisotropy are achieved by periodic passivation of the sidewalls in between etch intervals. Afterwards the sacrificial layer is removed. An SEM image of a Bosch sensor can be seen in Figure 3.7. In the image it is possible to see the polysilicon proof mass as well as some of the capacitive fingers implemented in the differential capacitive principle.

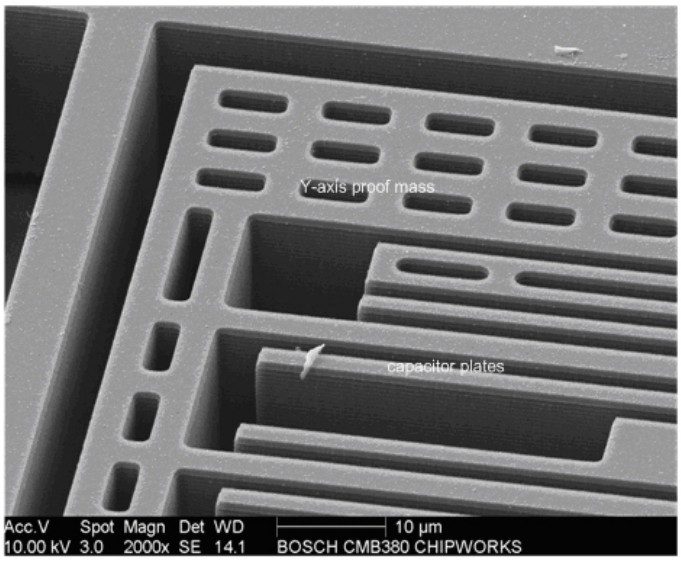

Figure 3.7: Bosch SMB380 three-axis accelerometer [9].

Like the Analog Devices sensors, these sensors rely on a differential capacitive principle to sense accelerations. The sensing element and ASIC is actually achieved using a two-chip arrangement as shown in Figure 3.8.

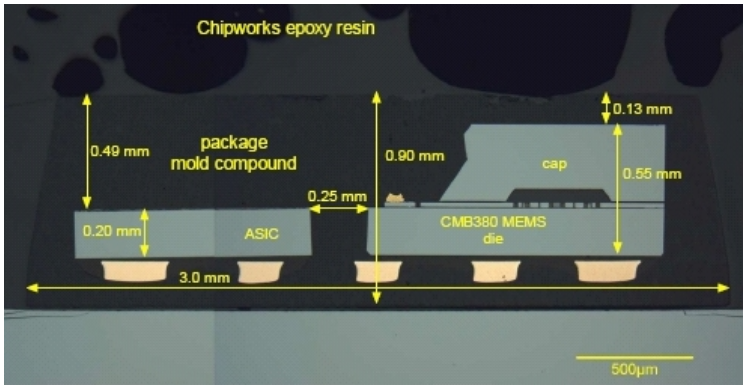

Figure 3.8: Bosch SMB380 three-axis accelerometer package cross-section [9].

The most recent device from Bosch with an analogue output is the BMA140 [11] which has a measurement range of ± 4 g minimum and is delivered in a $3{\times}3{\times}0.9$ mm^3 LGA package.

For a digital output, the BMA220 is considered [12]. The sensor has user selectable ranges of $\pm 16/8/4/2$ g and is available in a $2{\times}2{\times}0.98$ mm^3 LGA package.

3.4.3 Freescale

The Freescale accelerometer is a surface-micromachined IC accelerometer. The device consists of a polysilicon surface micromachined capacitive sensing cell and a signal conditioning ASIC contained in a single package, an example of which is shown in Figure 3.9. Freescale Semiconductor's latest offerings consist of a single-mass microstructure that measures acceleration in the x and y axes and flexes off the entire structure to measure acceleration in the z axis.

An analogue output three-axis sensor from Freescale is the MMA7361L [13]. The g-Select feature allows for the selection between two sensitivities. Depending on the

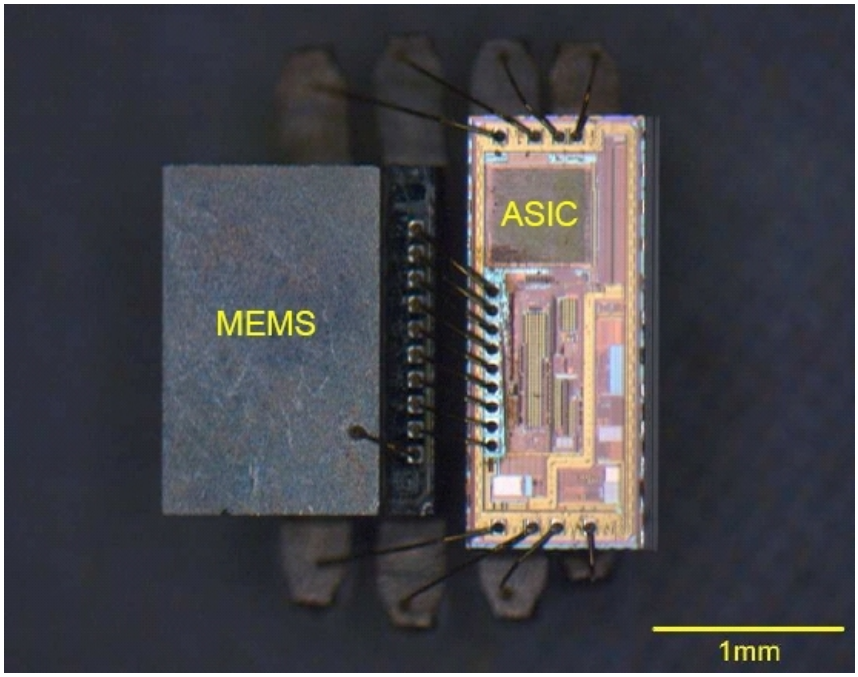

Figure 3.9: Decapsulated Freescale MMA7660FC accelerometer [14].

logic input placed on pin 10, the device internal gain will be changed allowing it to function with a 1.5 g or 6 g sensitivity. This feature is ideal when a product has applications requiring two different sensitivities for optimum performance. The sensitivity can be changed anytime during the operation of the product.

A digital output (I^2C) three-axis example from Freescale is the MMA7660FC which has a range of ± 1.5 g [15]. The device is housed in a $3 \times 3 \times 0.9$ mm^3 Dual Flat No-lead (DFN) package.

3.4.4 Kionix

In the Kionix accelerometers, acceleration sensing is based on the principle of a differential capacitance. Common mode cancellation is utilised to decrease errors from process variation, temperature, and environmental stress. The sensor element is fabricated from single-crystal silicon with a proprietary DRIE process as demonstrated in Figure 3.10(a). There are three sensors for sensing acceleration in the x, y and z axes as shown in Figure 3.10(b).

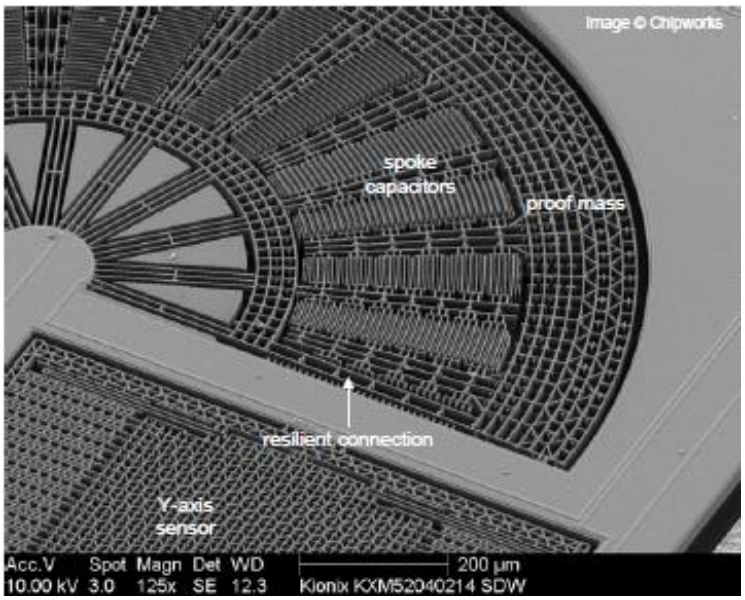

(a)

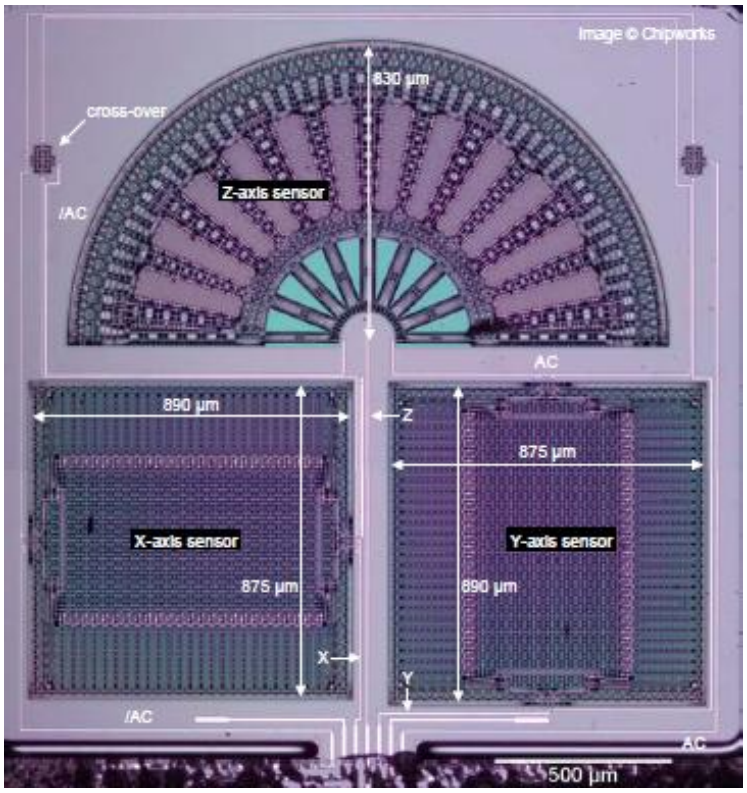

(b)

Figure 3.10: SEM images of a Kionix KXM52 accelerometer [9].

The sensor element and the ASIC are packaged in a DFN package. The sense element is hermetically sealed at wafer-level by bonding a second silicon lid wafer to the device using a glass frit. A separate ASIC device using a 2-metal, 2-poly 0.8

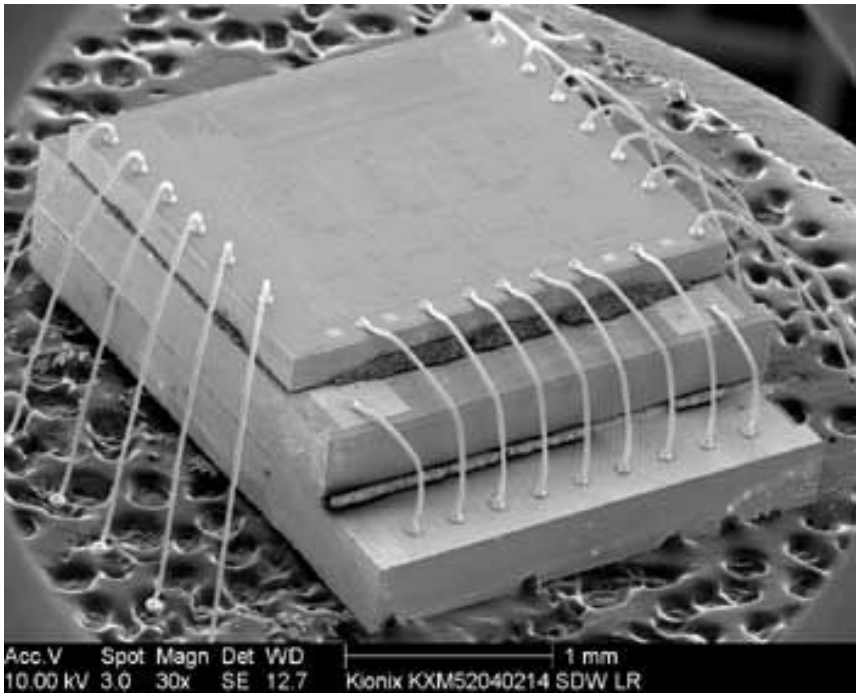

Figure 3.11: SEM image of a packaged Kionix KXM52 accelerometer [9].

μm CMOS process is stacked together with the sense element. This is demonstrated visually in Figure 3.11.

The KXSC7-2050 is a three-axis, analogue output, silicon micromachined accelerometer with a full-scale output range of ± 2 g. The accelerometer is delivered in an $3{\times}3{\times}0.9$ mm^3 LGA plastic package [16].

An example of a digital output (I^2C) three-axis accelerometer is the KXTF9-4100 [17]. The sensor offers ± 2 g, ± 4 g and ± 8 g ranges. Like its analogue counterpart, this sensor is delivered in an $3{\times}3{\times}0.9$ mm^3 LGA plastic package.

3.4.5 STMicroelectronics

With STMicroelectronics, a proprietary 2-poly process is used to create a surface micromachined accelerometer and the technology allows for suspended silicon structures which are attached to the substrate at a few locations. 15 μm thick polysilicon (poly-2) capacitor plates and beams are shown in Figure 3.12 and are fabricated using the classic Bosch process. This poly-2 layer is about five times thicker than that

used by Freescale and nearly four times than that used by Analog Devices in the ADXL330.

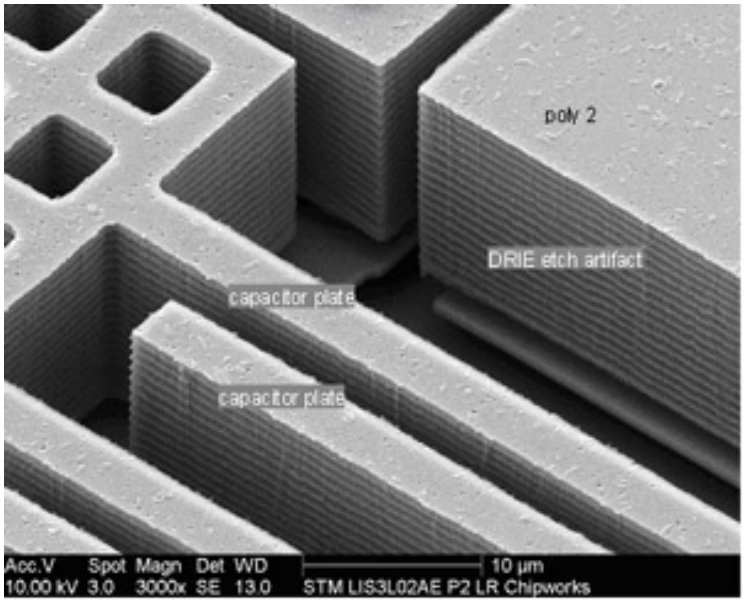

Figure 3.12: SEM image of a STMicroelectronics LIS3L02AE accelerometer with 15 μm thick polysilicon beams [9].

There is one proof mass for the x and y axes, and another proof mass for the z-axis motion as shown in Figure 3.13(a). The motion measured by the sensor is then interfaced and translated into an analogue or digital signal with an IC which is stacked together with the MEMS die as can be seen in Figure 3.13(b).

The most recent three-axis accelerometer with analogue output from ST is the LIS331AL [18]. The range of the sensor is ± 2 g and packaged in a $3{\times}3{\times}1$ mm^3 LGA plastic package.

The LIS331DL is a digital three-axis accelerometer that has user selectable full scales of ± 2 g and ± 8 g and is capable of measuring accelerations with an output data rate of 100 Hz or 400 Hz. The LIS331DL is housed in a $3{\times}3{\times}1$ mm^3 LGA plastic package [19].

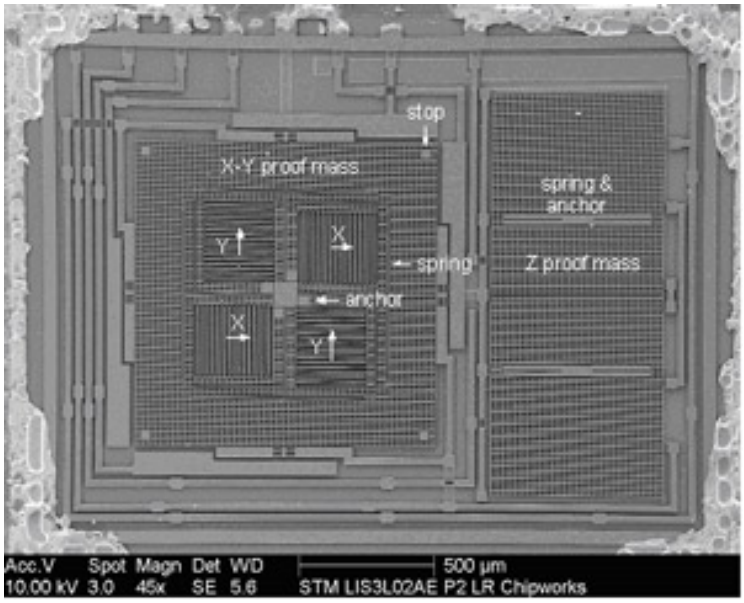

(a)

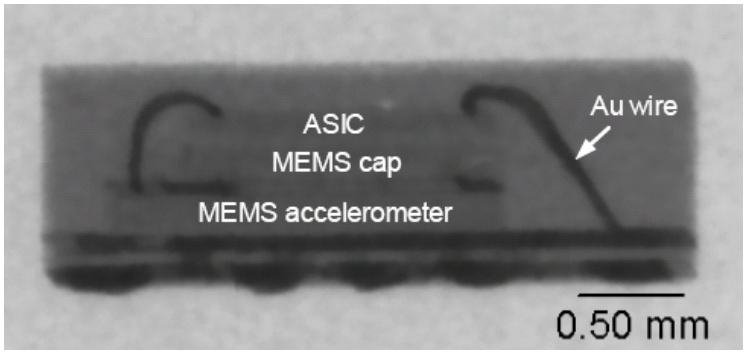

(b)

Figure 3.13: (a) SEM image of a STMicroelectronics LIS3L02AE accelerometer with its cap removed and showing the Poly 2 proof masses. (b) X-Ray of STMicroelectronics LIS331DL accelerometer packaging [9].

3.4.6 VTI Technologies

VTI's CMA3000 three-axis accelerometer targets motion measurement and control applications in portable consumer electronics. It is currently the industry's smallest sensor and has the lowest power consumption. Acceleration measurement with less than 10 μA current consumption at 40 Hz sample rate is possible.

The CMA3000 is fabricated using VTI's proprietary bulk 3-D MEMS technology.

The sensing element consists of three acceleration sensitive masses. The MEMS device is essentially a chip-scale sandwich of several layers, as shown in Figure 3.14, with the ASIC flip-chip bonded to the bottom side. The absence of a plastic mould package and utilisation of a stacked Chip Scale Package (CSP) allows for dramatic shrinking of the device. The addition of Through Silicon Via's (TSV's) through the MEMS cap die allows the ASIC to be flip-chip bumped to the top side of the cap die. Device sizes smaller than 2×2 mm^2 can be easily made. Whether the consumers will demand devices smaller than the current 3×3 mm^2 size being offered by the major suppliers will depend on the success of the VTI CMA3000 in the market place. This will also most likely determine whether these suppliers will adopt a CSP strategy.

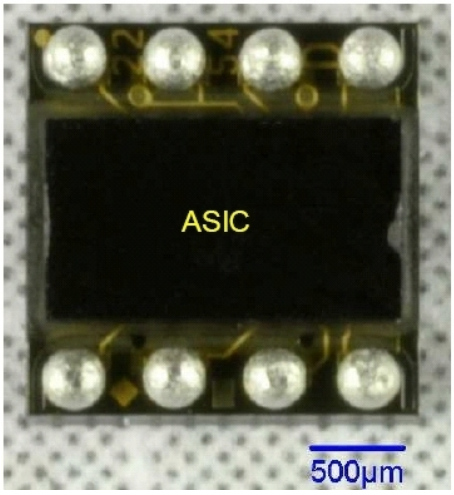

(a)

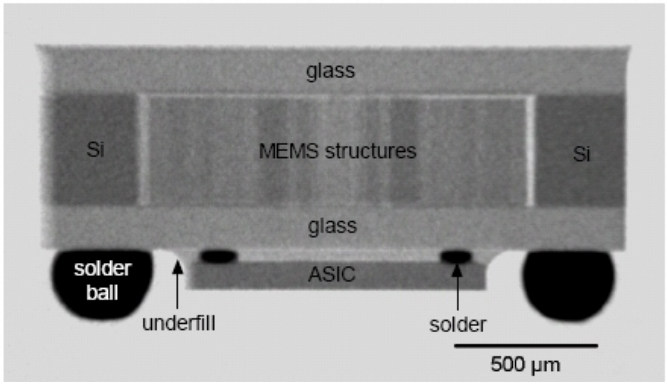

(b)

Figure 3.14: (a) Photograph of the underside of a VTI CMA300 accelerometer. (b) X-Ray of the packaging of a VTI CMA300 accelerometer [9].

The analogue sensor from the CMA3000 Series is the CMA3000-A01 which has three continuous time ratiometric analogue output signals to enable easy integration in systems where AD-converters are available [20]. It has user selectable ± 2 g and ± 8 g measurement ranges and has dimensions $2 \times 2 \times 0.95$ mm^3.

The CMA3000-D01 with digital SPI and I^2C interfaces is optimised for systems requiring ultra low power [21]. The device has user selectable measurement ranges (± 2 g and ± 8 g) as well as sample rate and frequency response and comes in the same size as the analogue equivalent.

3.4.7 MEMSIC

As has been demonstrated with the previous examples of commercially available accelerometers, the sensors are traditionally based on capacitive sensing technologies that measure the movement of a micro-mechanical mass structure. However, such technology suffers from inherent issues such as surface adhesion, known as stiction, hysteresis, mechanical ringing, ElectroMagnetic Interference (EMI), expensive custom fabrication processes, and other challenges associated with micro-mechanical moving structures. In order to resolve these issues, MEMSIC has developed a different technology based on thermal technology sensing. The sensor is a complete sensing system with on-chip mixed signal processing.

The principal of operation of MEMSIC devices is based on heat transfer by natural convection. The devices measure internal changes in heat transfer caused by acceleration, offering significant advantages over the use of a traditional solid proof-mass structure. Since the proof mass in the MEMSIC sensor design comprises gas molecules, movable mechanical structures are eliminated within the accelerometer. A MEMSIC accelerometer can therefore withstand a theoretical shock of over 50,000 g and the problems associated with stiction are eliminated.

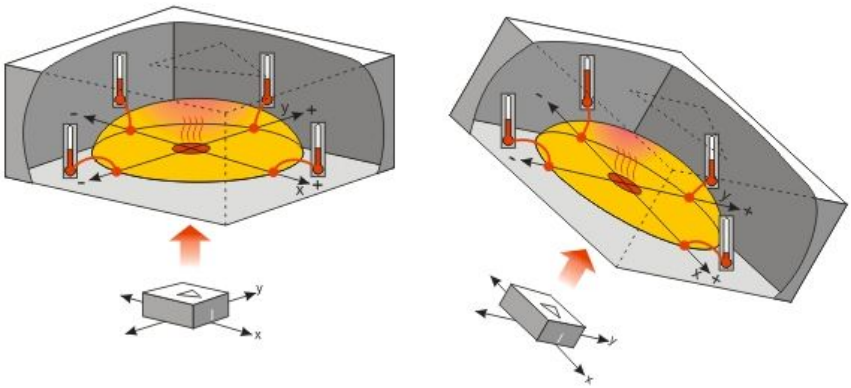

Figure 3.15: Principle of thermal sensing in a MEMSIC accelerometer [22].

The sensor has a chamber of gas and a heat source which is centered in the silicon chip and suspended above a cavity. Equally spaced aluminum/polysilicon thermopiles (groups of thermocouples) are located equidistantly on all four sides of the heat source.

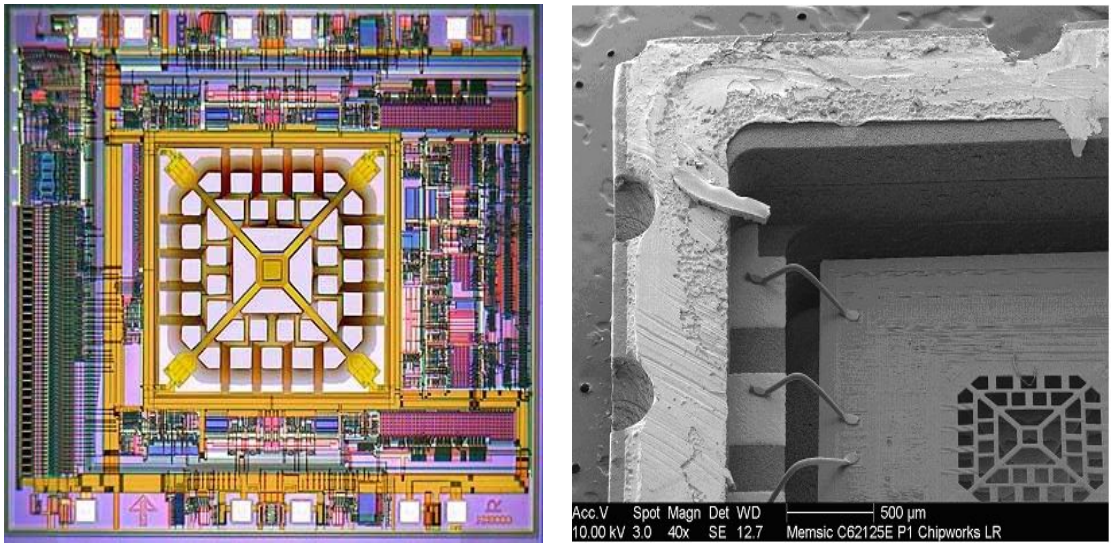

(a) (b)

Figure 3.16: (a) Photograph of MEMSIC accelerometer showing associated CMOS circuitry. (b) SEM image of a MEMSIC MXD6125Q thermal accelerometer [9].

As shown in Figure 3.15, when the accelerometer is level, the hot gas pocket rises to the top-centre of the chamber of the accelerometer, and all the temperature sensors measure the same temperature and produce the same output voltage. Depending on

the tilt of the accelerometer, due to free convection heat transfer, the temperature profile becomes asymmetrical and hot gas collects closer to one or two of the temperature sensors. The voltage output of the four thermopiles will then be different and the differential voltage at the thermopile outputs is directly proportional to the acceleration.

The analogue output MXR9500G/M sensor is an example of a sensor from MEMSIC that can sense in all three axes [23]. It is fabricated using a sub-micron CMOS process and can be seen in Figure 3.16. It is packaged in a surface mount Leadless Ceramic Carrier (LCC) 16-pin package that measures $7\times7\times1.8\ mm^3$.

3.5 Three-axis accelerometers developed in R&D laboratories

Many research micromachined accelerometers have been reported over the last three decades. An overview of some three-axis accelerometers is provided in this section according to their sensing mechanism.

3.5.1 Capacitive

In 2006, a research group from Japan published a paper on a five-axis motion sensor which was capable of detecting three-axis acceleration as well as two-axis angular rate acceleration using resonant electrostatic driving and a non-resonant capacitive detection [24]. The sensor structure is shown in Figure 3.17 and consists of three layers: a topside glass wafer (Glass-1), an Silicon-On-Insulator (SOI) wafer and a backside glass wafer (Glass-2). The inside of the sensor is vacuum sealed by anodic bonding with a getter in order to prevent a squeezed film damping effect. A silicon proof mass, located in the centre of the sensor chip, is suspended by four silicon beams which are formed in the active silicon layer (20 μm in thickness) of the SOI wafer. The proof mass can shift and tilt due to each axis force in the movable gaps formed in both sides of the mass. Each glass layer has five electrodes on its

	Analog Devices	Bosch Sensortec	Freescale	Kionix	MEMSIC	STMicroelectronics	VTI Technologies
Bandwidth (kHz)	1.6(x,y) 0.55(z)	1.5	0.4(x,y) 0.3(z)	4.0(x,y) 2.0(z)	0.17	2.0	120(x,z) 200(y)
Voltage Supply (V)	3.0	3.0	3.3	3.3	3.0	3.3	2.5
Range ($\pm$ g)	3.6	4.0	1.5,6.0	2.0	1.5	2.0	2.0,8.0
Sensitivity (mV/g)	300	300	800(1.5 g) 206(6.0 g)	660	500	479	417(2 g) 104(8 g)
Cross-Axis Sensitivity ($\pm$ %)	1.0	0.2	5.0	2.0	2.0	2.0	1.0
Non-Linearity ($\pm$ %)	0.3	0.5	1.0	2.0	0.5	0.5	1.5
Supply Current (μA) **Full Power: FP, Low Power: LP**	350	200(FP), 0.7(LP)	400(FP), 3(LP)	230(FP), 50(LP)	4.2	650(FP), 1.0(LP)	180(FP), <0.1(LP)
Noise Density ($\mu g/\sqrt{Hz}$)	150(x,y) 300 (z)	220	350	100	0.6(x,y) 0.9(z)	300	300

Table 3.1: Specifications of the presented commercially available three-axis accelerometers. N.B. All values are typical values.

surface that faces the silicon mass. The cross shape centre electrodes, T0 and B0, on the top and bottom glass layers respectively, are used for the electrostatic driving. The surrounding fixed electrodes, T1-T4 and B1-B4, and the proof mass each make capacitors for detection of five-axis motions. All fixed electrodes on both glass wafers are connected to the outer electrodes through the glass holes via Si pillars. The Non-Evaporated Getters (NEG) are inserted into the NEG pocket located in a corner for low-pressure sealing.

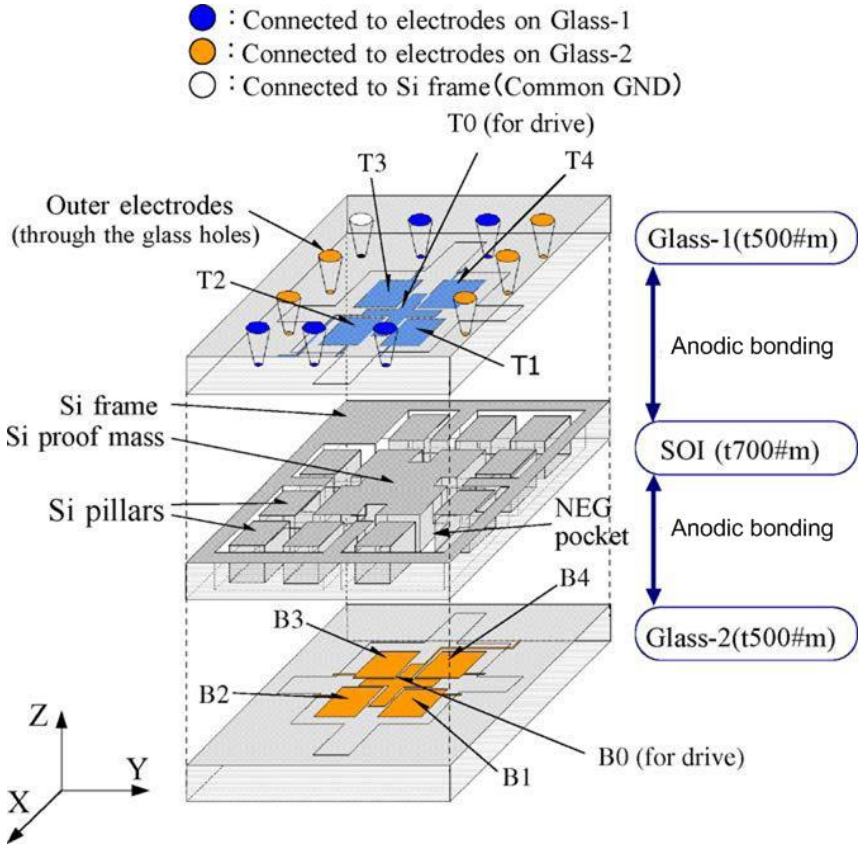

Figure 3.17: Schematic view of the sensor structure [24].

The displacements of the proof mass for the five-axis motions are shown in Figure 3.18. The proof mass, suspended by four silicon beams, is vibrated constantly in the z-axis by an electrostatic force as shown in Figure 3.18(a). When a z-axis acceleration (A_z) in the range of DC to several 10's of Hz is applied to the sensor, an inertial force of F_{A_z} shifts the mass along z-axis as shown in Figure 3.18(a). When x-axis acceleration (A_x) and y-axis acceleration (A_y) in the range of DC to several

10 Hz are applied to the sensor, inertial forces of F_{A_x} and F_{A_y} tilt the mass along the x- and y-axis, respectively as shown in Figure 3.18(b). When angular acceleration around the x-axis (Ω_x) and y-axis (Ω_y) are applied to the sensor, induced Coriolis forces make a tilting vibration around the x- and y-axis, respectively as shown in Figure 3.18(c).

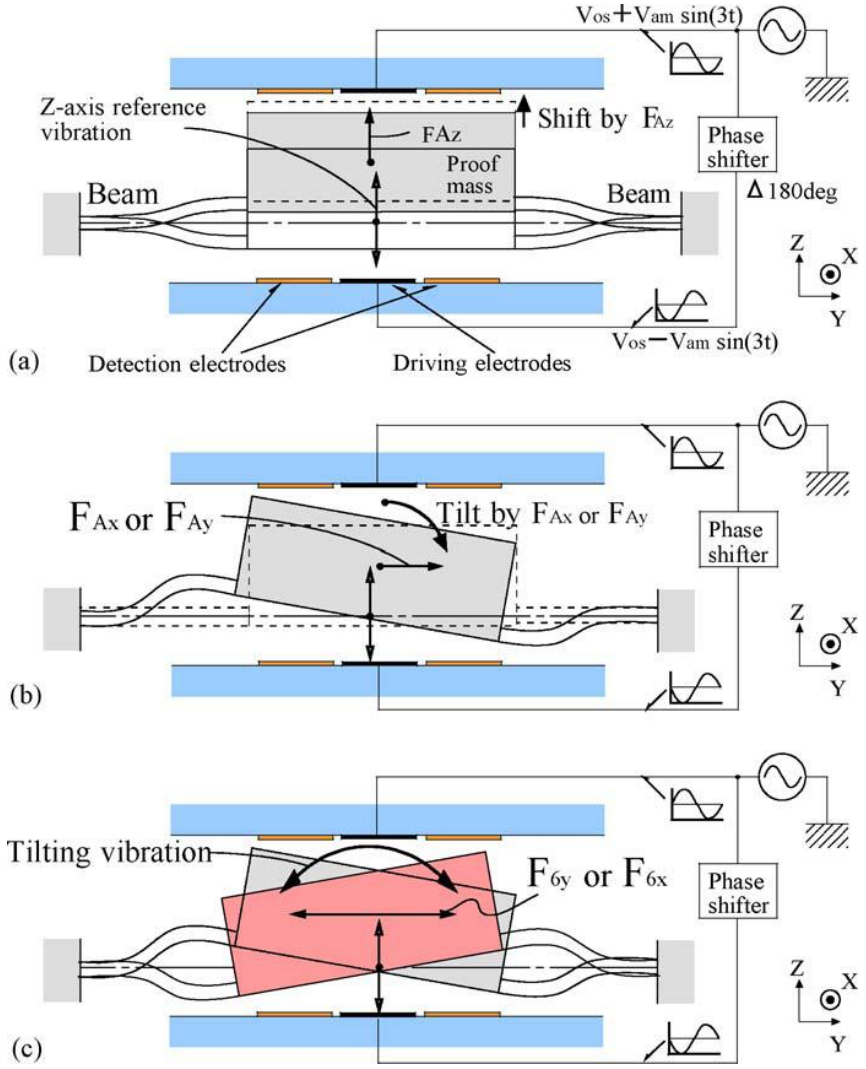

Figure 3.18: Movements of the proof mass by five-axis motions: (a) z-axis reference vibration and z-axis acceleration; (b) x- and y-axis acceleration; (c) angular rate around x- and y-axis [24].

The sensor was bulk micromachined on SOI wafers and measured 5.0×5.0×1.7 mm^3. The fabrication process sequence of the motion sensor is shown in Figure 3.19 and photographs of the fabricated sensor can be seen in Figure 3.20.

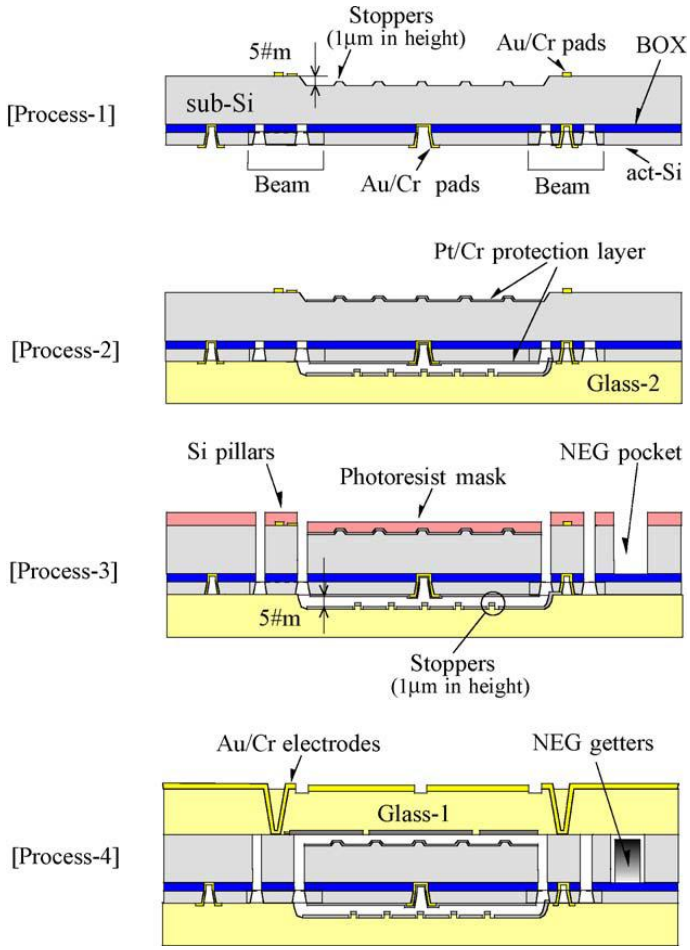

Figure 3.19: Fabrication process sequence of the motion sensor [24].

By applying an electrostatic reference vibration to the proof mass along the z-axis at a resonant frequency of 3.42 kHz, three-axis acceleration and two-axis angular rate acceleration can be detected capacitively using a non-resonant detection mode. Measured acceleration sensitivities along the x-, y- and z-axis are 1.9, 1.1 and 4.7 V/g, respectively. Angular rate sensitivities around the x- and y-axis are 6.7 and 12 $mV/(^\circ \cdot s)$, respectively. The non-linearity was characterised as being $<$3% full scale and the cross-axis sensitivity as $<$5%.

In 2007, a group from the University of Florida, USA, introduced a design that utilised a DRIE-based post-CMOS micromachining process to produce a capacitive sensing three-axis sensor [25]. CMOS-MEMS technology allows multifunction integration, scalability, small size, and potentially low cost. In particular, no CMOS

contamination problems exist and therefore access to all mainstream CMOS technologies is possible in principle. In the paper, several process issues that arise from using such a process are introduced and solutions are presented and discussed. These issues are namely sidewall contamination and severe silicon undercut caused by overheating of the suspended micro-structures during the DRIE process step.

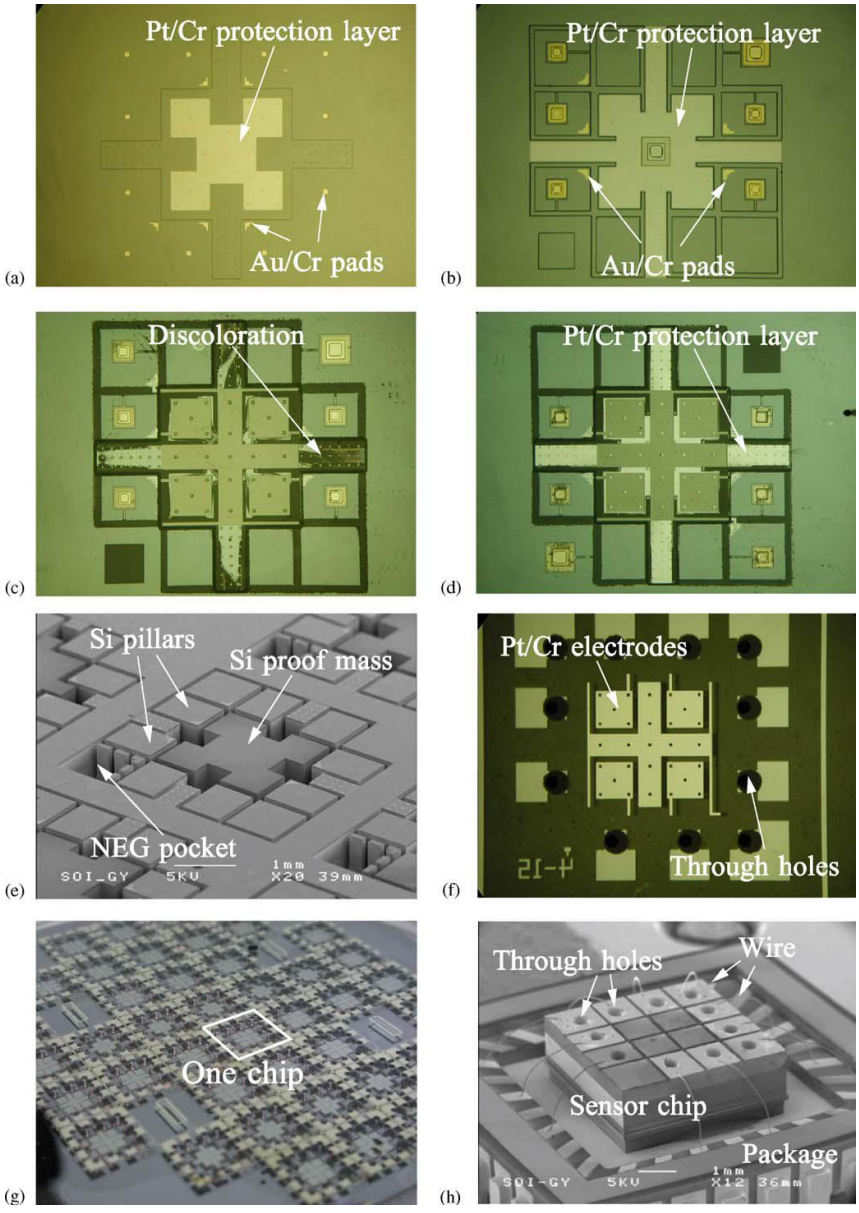

Figure 3.20: Photographs of fabricated sensor: (a) substrate-Si surface of an SOI wafer; (b) active-Si surface of an SOI wafer; (c) DRIE without Pt/Cr protection layer; (d) DRIE with Pt/Cr protection layer; (e) DRIE configuration; (f) fabricated glass-1 wafer; (g) vacuum sealed wafer; (h) developed motion sensor mounted on a package [24].

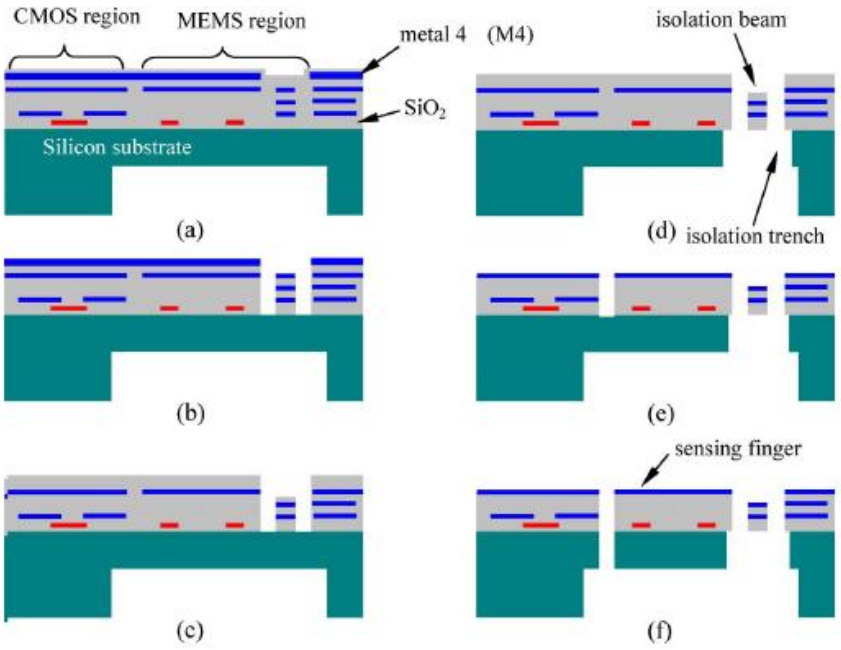

Figure 3.21: Process flow of the improved DRIE CMOS-MEMS process. (a) Backside Si etch. (b) Front-side anisotropic SiO_2 etch. (c) Top Al etch. (d) Deep Si etch and undercut to form isolation structures. (e) Anisotropic SiO_2 etch. (f) DRIE Si etch for device release [25].

Figure 3.21 shows the cross-sectional view of the process flow, where four metal interconnect layers are used. An SEM image of a fabricated three-axis accelerometer is shown in Figure 3.22(b), where a z-axis sensing element is embedded on the proof mass of the lateral-axis sensing element. The comb fingers anchored on the substrate are denoted as stator fingers, and those connected to the proof mass are denoted as rotor fingers.

In the process, bulk single crystal silicon (SCS) is used to fabricate the micro-structures. This was done to combat the curling of the composite metal-oxide micro-structures which is a limiting factor for the size of the structures. The thick SCS incorporated in the sensing comb fingers is utilised as a part of the sensing capacitor electrodes, yielding much larger sensing capacitance and, thus, higher Signal-to-Noise Ratio (SNR). The electrical isolation of the silicon is provided by thin-film isolation beams through isotropic silicon undercut etching. However, the silicon on

the sensing comb fingers is also laterally etched. This results in an increase of the gap between the sensing comb fingers, which in turn decreases the sensing capacitance and lowers the SNR.

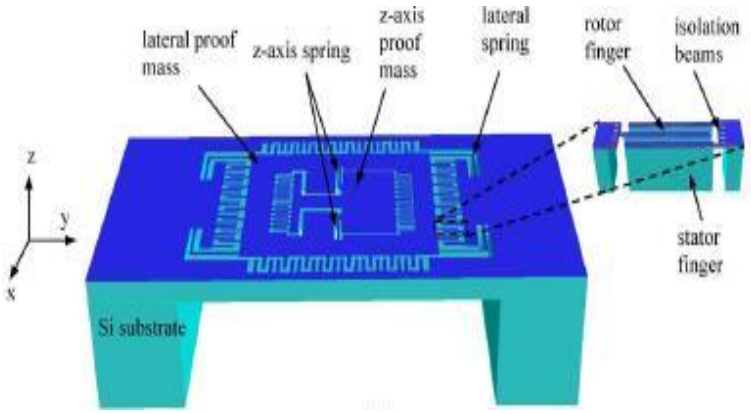

(a)

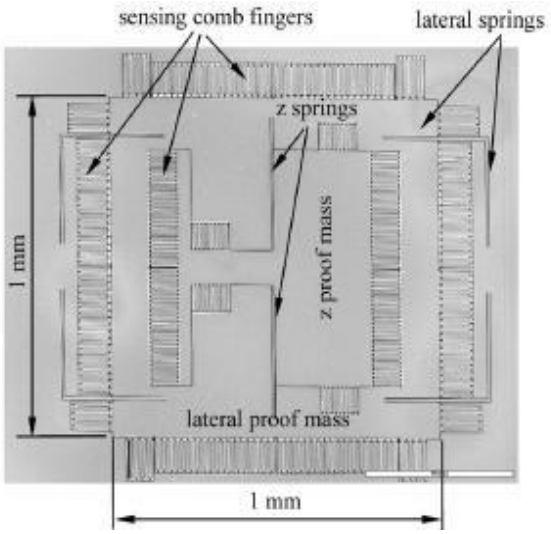

(b)

Figure 3.22: (a) Schematic and (b) SEM photograph of a fabricated three-axis accelerometer showing the micro-structures and device dimensions. The inset in (a) shows the mechanism of electrical isolation for sensing comb fingers [25].

To overcome this problem, a modified process was developed to decouple the silicon undercut of the isolation beams from the DRIE of the comb fingers. By using the top CMOS interconnect metal layer as an etch mask, electrical isolation structures can be fabricated separately, allowing fine process tuning in the comb-finger etch step. Thus, electrical isolation of the silicon can be realised without sacrificing the sensing

capacitance. It is demonstrated however, that this introduces some new problems, including contamination in the isolation trenches during the plasma etch steps, and the large undercut and even complete etch away of the SCS on the mechanical springs and comb fingers during the DRIE release process.

It was observed that these contaminants which were observed on the sidewalls of the aforementioned isolation trenches tend to accumulate in the bottom region of the trenches. This micro-masking effect leaves a connection line along the ends of the comb fingers next to the isolation trenches. Due to these contaminants, the etch-through DRIE takes much longer, which causes more undercut on comb fingers and also results in a very low yield.

Normally this severe effect takes place on the suspended MEMS structures during the silicon DRIE of the final device release step, or more precisely, during the over-etch period after the etch reaches the "ending point". After the DRIE etch-through, a rapid lateral undercut occurs. This is attributed to the rapid temperature rise on the suspended MEMS structures and changes the mechanical performance of the device dramatically. In the worst case, the SCS on the springs may be undercut completely, resulting in broken thin-film beams.

Another modified process is then proposed to combat the contamination and thermal problems. The basic idea of this modified process is to provide an additional thermal path for the suspended micro-structures during the over-etch period. In this modified process, photoresist is employed as shown in Figure 3.23 to provide the thermal path because photoresist can be easily removed at a later stage. Since this final photoresist removal can be done after dicing or even after wire bonding, this method also provides a way to protect fragile micro-structures during dicing, shipping, and wire bonding.

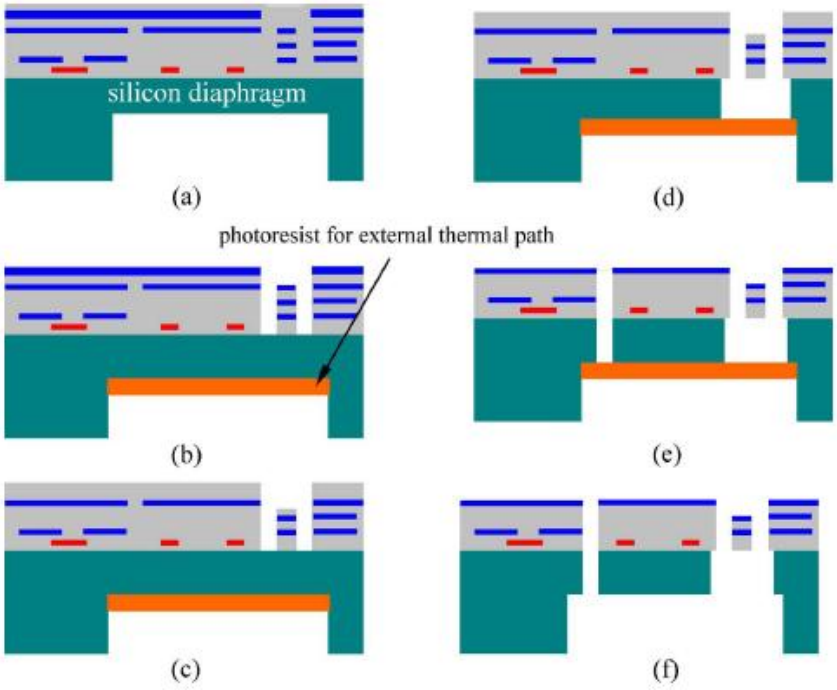

Figure 3.23: Modified accelerometer fabrication process with photoresist coating on backside. (a) Backside Si DRIE. (b) Backside photoresist coating followed by front-side anisotropic SiO2 etch. (c) Top Al etch. (d) Deep Si etch and undercut to form isolation structures. (e) Anisotropic SiO_2 etch and DRIE Si etch for comb fingers and mechanical springs. (f) Photoresist ashing for final release of the device [25].

The device, with a die size of 3×3 mm^2, is monolithically integrated with a low-power, low-noise, dual-chopper amplifier with an overall gain of 44 dB. The amplifier consumes 1 mW power in each axis with a voltage supply of 3.3 V. In the lateral axes, the accelerometer demonstrates a sensitivity of 560 mV/g and an overall noise floor of 12 $\mu g/\sqrt{Hz}$. For the z-axis, the sensitivity and noise floor are 320 mV/g and 110 $\mu g/\sqrt{Hz}$, respectively.

3.5.2 Piezoresistive

In 2003, a research group from Toyohashi University, Japan, presented a three-axis accelerometer for operation at high temperature which incorporated constant temperature control of the piezoresistors to reduce temperature drift [26].

The sensor is bulk micromachined using a TetraMethylAmmonium Hydroxide (TMAH) etchant and SOI wafers. The top and bottom views of the micromachined silicon structure are shown in Figure 3.24(a), and also the cross section from 'A' to 'B' is shown in Figure 3.24(b). Four folded beams are formed between the centre support and the surrounding mass to achieve high sensitivity for three-axis acceleration detection. Four p-type piezoresistors are positioned on each folded beam and are connected to form a Wheatstone bridge. The p-type micro-heaters are formed so that the piezoresistors are surrounded and these are formed in the SOI device layer together with the piezoresistors. The micro-heater areas are formed with low resistance to allow them to be supplied with sufficient electric power.

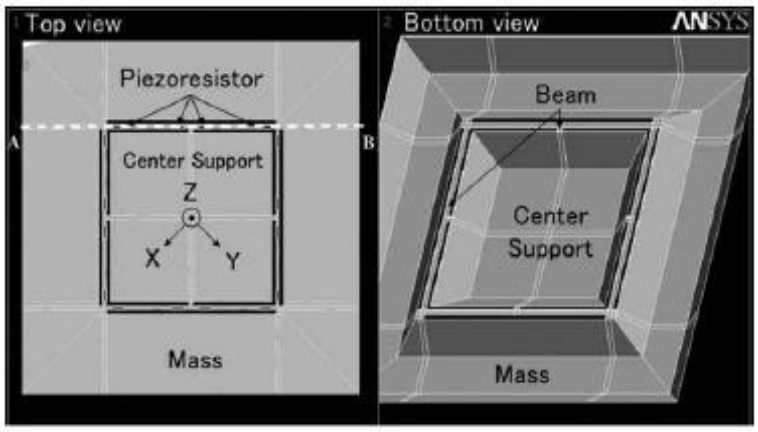

(a)

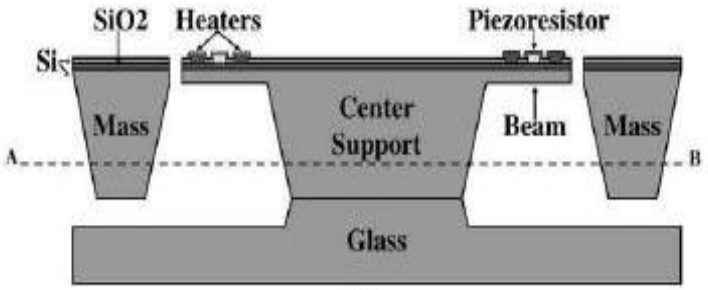

(b)

Figure 3.24: (a) Top and bottom views, and (b) cross section of the three-axis accelerometer [26].

Figure 3.25 shows the schematic diagram of a constant temperature control sys-

tem applied to the three-axis accelerometer in this study. The temperature sensor, piezoresistors, and micro-heaters are integrated onto the same chip. A reference voltage is set to the corresponding value of the output voltage of the temperature sensor at 300 $°C$. In the case that the feedback loop of the constant temperature control system is balanced, the differential amplifier does not supply power to the micro-heaters. On the other hand, if the output signal of the temperature sensor is lower than the reference voltage, the differential amplifier supplies power to the micro-heaters. If the output signal of the integrated temperature sensor is higher than the reference voltage, the differential amplifier stops supply of power to the micro-heaters.

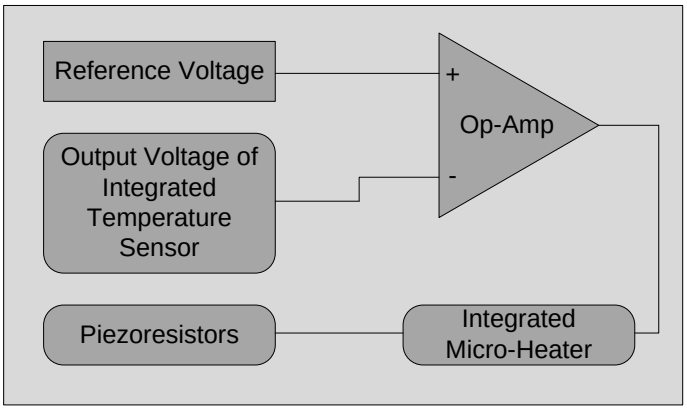

Figure 3.25: Schematic diagram of constant temperature control system: the temperature sensor, the piezoresistors and micro-heater are integrated in the three-axis accelerometer [26].

Figure 3.26 shows the results of FEM simulation when accelerations of 1 g in the x, y and z-axes are applied to the three-axis accelerometer. The x-axis acceleration can be detected by calculating each output voltage of the Wheatstone bridges (V_{o1-4}) with the following equation:

$$V_{out-x} = (V_{o2} + V_{o3}) - (V_{o1} + V_{o4}) \tag{3.13}$$

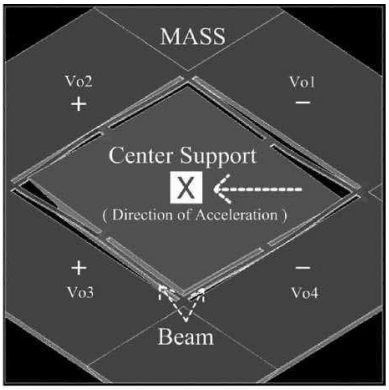

(a)

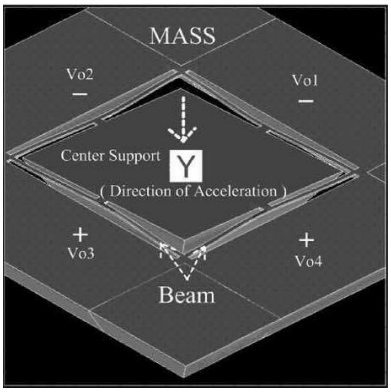

(b)

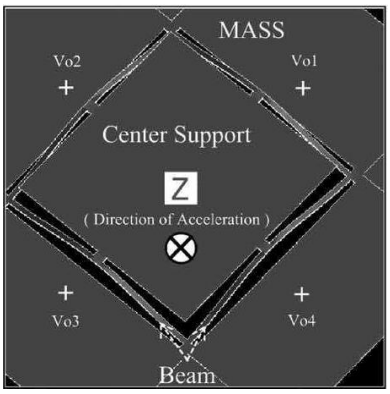

(c)

Figure 3.26: Shape of beam deformation for three-axis acceleration by FEM analysis (ANSYS): (a) direction of x-axis (1 g input), (b) direction of y-axis (1 g input), and (c) direction of z-axis (1 g input) [26].

The output for y and z-axis accelerations can be detected in the same manner as with the x-axis using the following equations:

$$V_{out-y} = (V_{o3} + V_{o4}) - (V_{o1} + V_{o2}) \tag{3.14}$$

$$V_{out-z} = V_{o1} + V_{o2} + V_{o3} + V_{o4} \tag{3.15}$$

The fabrication steps for the accelerometer can be seen in Figure 3.27 and are detailed here:

1. SOI wafer (2.2 μm thick active-silicon, 1.1 μm thick SiO_2, and 300 μm thick substrate silicon) is used as the starting material.

2. The whole of the active-silicon is implanted with boron to lower the value of the sheet resistance.

3. A masking layer is patterned and the active-silicon is etched by RIE to form an island of micro-heaters and piezoresistors.

4. Only the micro-heaters area is then implanted with boron to lower the value of the sheet resistance.

5. An etch groove (15 μm deep) is precisely formed by RIE to control the thickness of the beam structure in the following TMAH etch step. An aluminium layer is then deposited by sputtering and patterned by wet etching for wiring.

6. The aluminium layer is then coated by a fluorocarbon film. This material is used as a passivation layer for the aluminium for the bulk silicon etching process with 25 wt.% TMAH solution.

7. The masking layer of the wafer backside is patterned and the bulk silicon is etched in TMAH solution at 90 $^{\circ}C$ until the groove is penetrated through the

substrate. At this stage, the beam thickness is controlled to 15 μm. After the etching, the backside masking layer is removed by HF solution.

8. The passivation layers are then removed by O_2 plasma.

9. Anodic bonding glass is etched in HF solution to form 20 μm depth gaps to allow for mass movement.

10. The fabricated wafer and patterned glass are bonded with anodic bonding.

11. After anodic bonding, the beam structures are released using RIE and a photoresist mask.

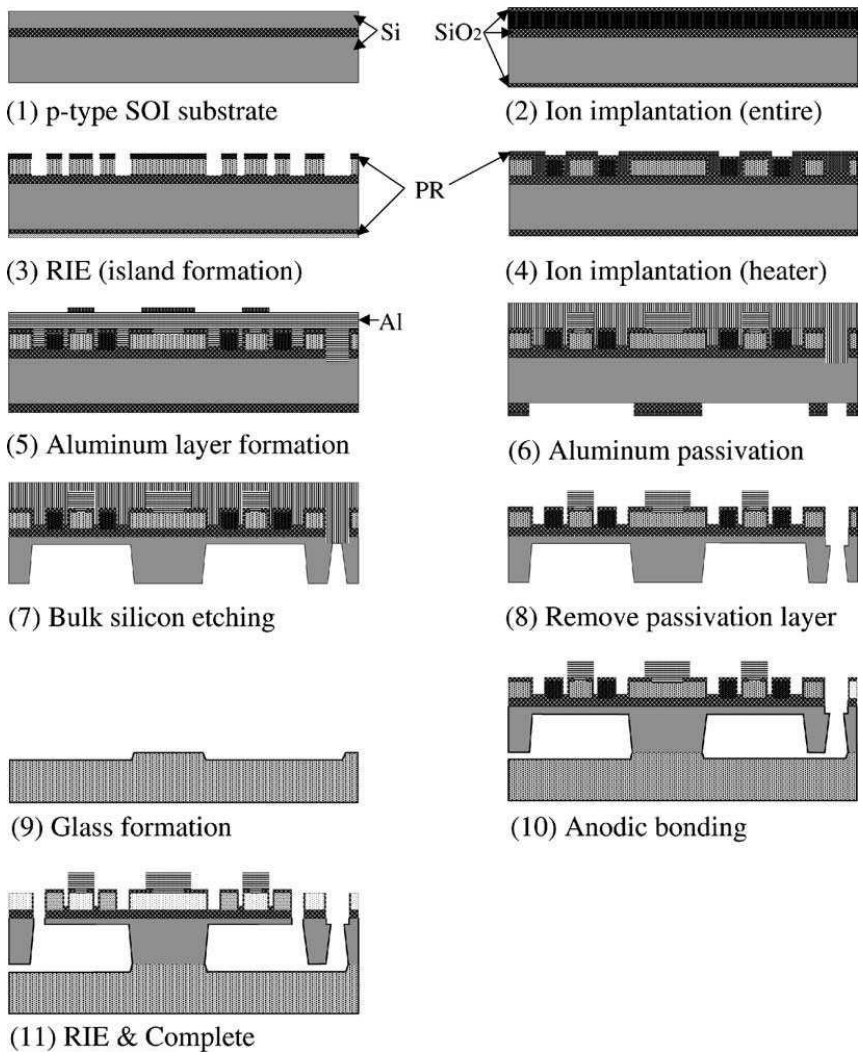

Figure 3.27: Outline of fabrication process of the three-axis accelerometer [26].

Figure 3.28 shows photographs of the fabricated accelerometer chip. The die size of the accelerometer is 6.5×6.5 mm^2. Figure 3.28(b) shows an SEM image highlighting some piezoresistors, the micro-heaters and the aluminum layer on one of the beams.

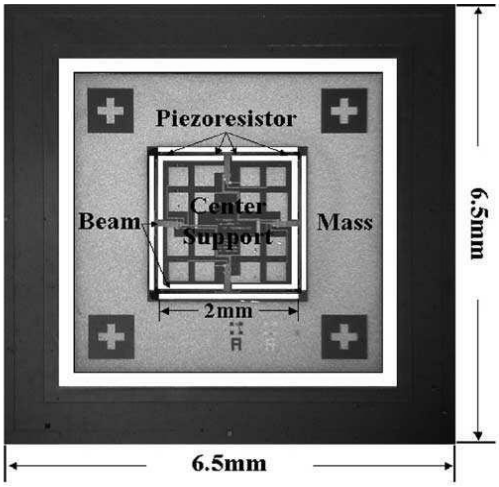

(a)

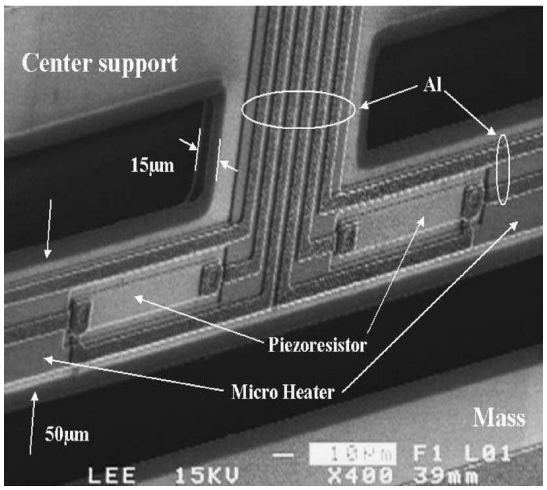

(b)

Figure 3.28: Photographs of the fabricated sensor: (a) overall chip; (b) SEM image of beam structure [26].

When the temperature control system is off, the temperature range is quite large and varies from 27 to 300 $°C$. The Temperature Coefficient of Sensitivity (TCS) is 1051 $ppm/°C$ due to the sensitivity reduction of the piezoresistors at high temperatures. The measured sensitivity for z-axis is about 8.1 mV/g at room temperature, and 5.8 mV/g at 300 $°C$.

When implementing the temperature control system to make the device temperature 300 $^{\circ}C$, the measured sensitivity for the z-axis becomes about 6.3 $mV/V \cdot g$ at room temperature. If the atmospheric temperature of the accelerometer becomes 300 $^{\circ}C$, the sensitivity for z-axis becomes 5.8 $mV/V \cdot g$, which is 92% of the room temperature sensitivity. The TCS of the accelerometer is reduced to 298 $ppm/^{\circ}C$ in this case.

In 2005, a research team from Ritsumeikan University, Japan, presented a sensor that was capable of sensing three components of linear acceleration and three components of angular acceleration i.e. six Degrees Of Freedom (DOF) [27]. The structure consists of a central volume of mass with extruding volumes of mass at each corner. The structure is suspended with a cross-beam that is attached to each side of the central volume of mass. The seismic mass is then bonded to another identical seismic mass symmetrically on the beam axes plane. The overall active device area is 3×3×0.9 mm^3.

The working principle of the sensor can be explained as follows: when the sensor senses acceleration, the beam structure has four kinds of important vibration modes that form four deflection modes. Schematic drawings in Figure 3.29 of deformed shapes of the beam structure are used to describe the working principle of the accelerometer. The first type shown in Figure 3.29(a) is caused by the z-component of the linear acceleration (A_z). A_z causes the seismic mass to move vertically up and down. The second type shown in Figure 3.29(b) is caused by the x- or y-components of linear acceleration (A_x, A_y). The third type shown in Figure 3.29(c) is caused by the angular acceleration around the z-axis (E_z). In this case, the mass is rotated around the z-axis. Finally, the fourth type shown in Figure 3.29(d) is caused by the angular acceleration around the x- or y-axis (E_x, E_y). These deflections of the beams as a result of the applied acceleration component on the sensor generate strain on the cross-beam structure. Finally, stress variations on the beam(s) surfaces are produced linearly as a consequence of the strain.

In total, six Wheatstone bridges are required to sense the generated strain. These are formed by interconnecting 20 p-type piezoresistors that are diffused into the surface of the beam structure.

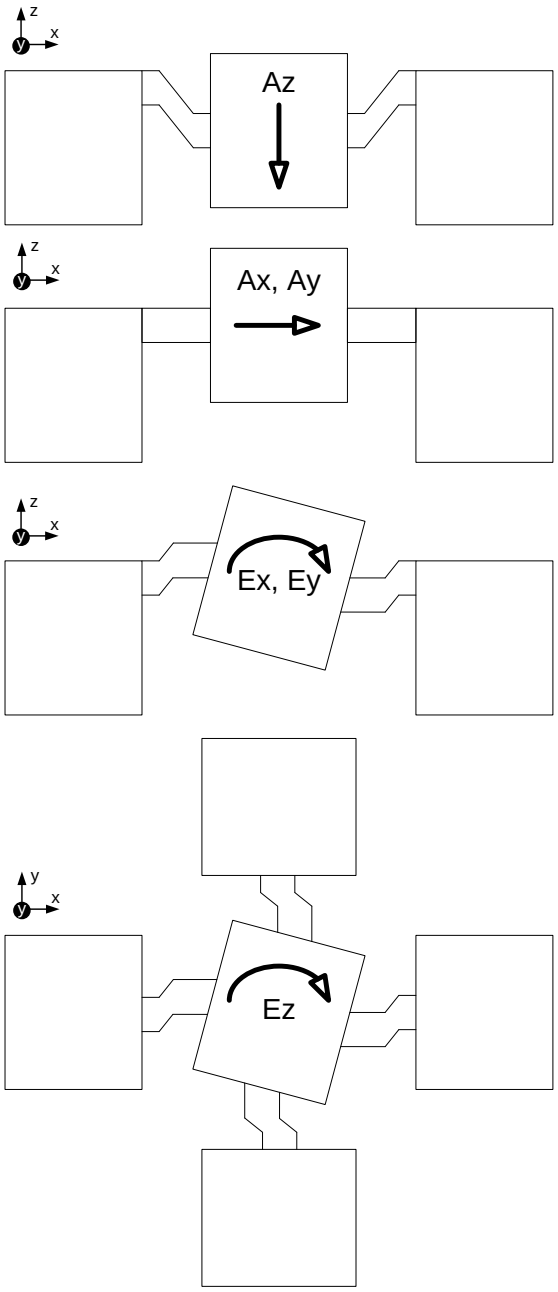

Figure 3.29: (a) Displacement view of the structure for applied linear acceleration A_z. (b) Displacement view of the structure for applied linear acceleration A_x (or A_y). (c) Displacement view of the structure for applied angular acceleration E_x (or E_y). (d) Displacement view of the structure for applied angular acceleration E_z [27].

The detailed sequence for the fabrication process flow of the accelerometer is shown in Figure 3.30.

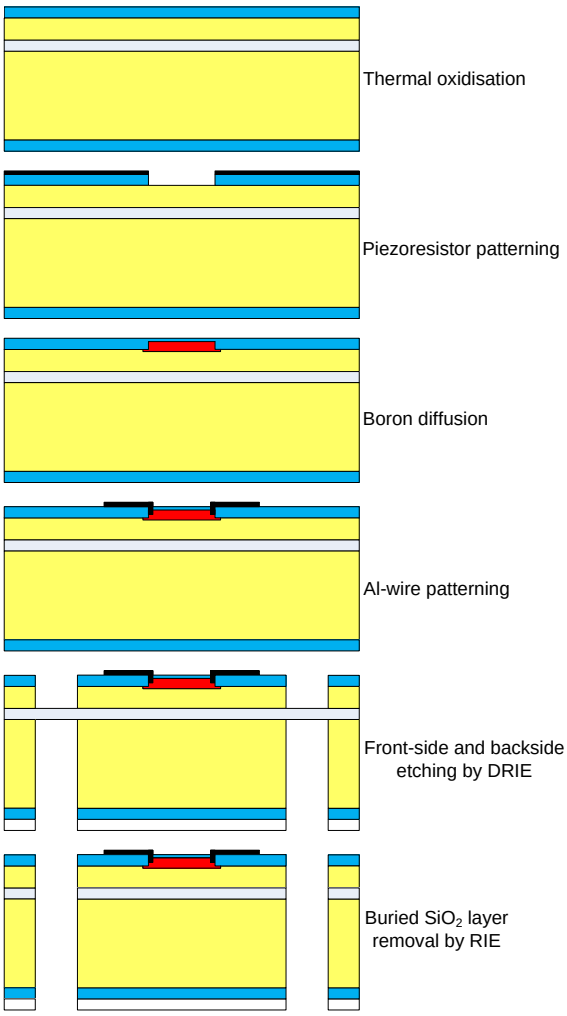

Figure 3.30: Fabrication process flow of the accelerometer [27].

The accelerometer is designed with a total of six masks, including one for over-range protection and thin film air damping control on the backside of the silicon wafer. A double-side-polished, n-type (100) oriented SOI wafer was used. The thicknesses of the device layer, substrate layer and buried silicon dioxide layer are 10 μm, 450 μm and 1 μm, respectively. First, SiO_2 layers are grown on both sides of the SOI wafer by a thermal oxidation process. Next, photolithography is conducted on the front side of the wafer to pattern the piezoresistors. The piezoresistors are formed by a boron diffusion process followed by a drive-in process step. After contact holes are opened by wet etching in a buffered HF solution, a metallisation process is used

to interconnect the piezoresistors and to form the bonding pads. The cross-beam is patterned on the top side of the wafer and a DRIE process is conducted on this side until the buried silicon dioxide layer of the SOI has been reached. A DRIE process is then conducted from the backside to form the geometry of the beams and the seismic mass of the sensor.

A three-axis movable alignment device was designed and bonded to an identical seismic mass. A thermosetting silicone resin was used to bond the symmetrical seismic mass on the sensor and sensor die. Figure 3.31(a) shows the fabricated accelerometer without an upper seismic mass and Figure 3.31(b) shows the accelerometer with a bonded seismic mass.

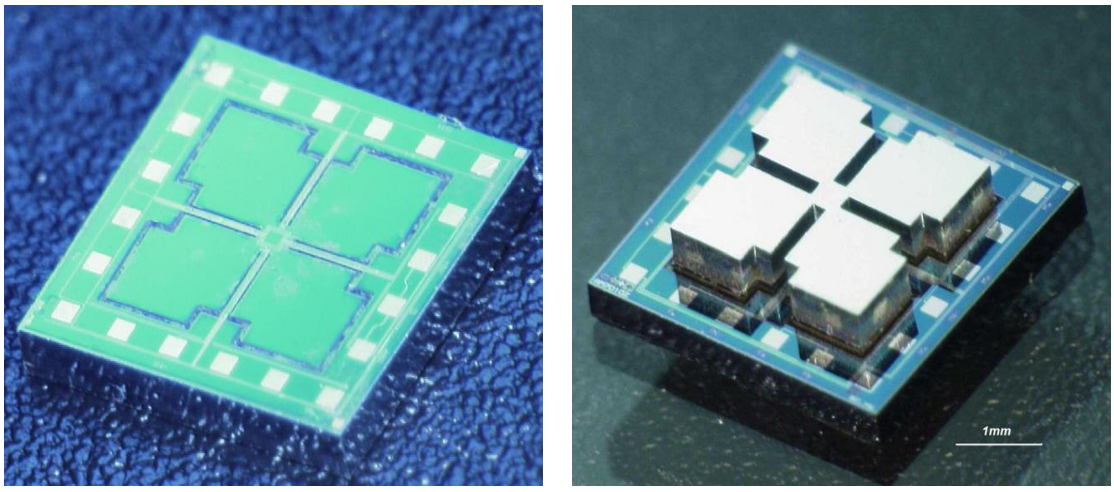

(a) (b)

Figure 3.31: Microphotograph of fabricated accelerometer (a) without an upper seismic mass, and (b) with an upper seismic mass [27].

The average sensitivities for linear accelerations, A_x, A_y, A_z on the x-, y- and z-axes were 0.122 $mV\ (Vg)^{-1}$, 0.103 $mV\ (Vg)^{-1}$ and 1.776 $mV\ (Vg)^{-1}$, respectively, and angular accelerations, E_x, E_y, E_z around the x-, y- and z-axes were 2.554 $mV\ (Vrads^{-2})^{-1}$, 1.974 $mV\ (Vrads^{-2})^{-1}$ and 0.124 $mV\ (Vrads^{-2})^{-1}$, respectively.

The maximum measured cross-axis sensitivity was 4%. The maximum non-linearities (NL) of each of the components were NL_{Ax} = 1.04%FS, NL_{Ay} = 1.02%FS, N_{Az} =

0.58%FS, NL_{Ex} = 1.21%FS, NL_{Ey} = 1.18%FS and NL_{Ez} = 1.32%FS.

3.5.3 Piezoelectric

In 2001, a research group from the Royal Institute of Technology in Sweden reported the first micromachined three-axis single-mass accelerometer with integrated piezoelectric thin film detectors [28]. The accelerometer consists of a seismic mass, supported by four thin beams that each have two thin film lead zirconate titanate (PZT)-elements on the top side consisting of a platinum bottom electrode, the PZT and a platinum top electrode. The charge sensitivity achievable with the design was found to be 22 pC/g in the vertical direction and 8 pC/g in the parallel direction. The active device area (supporting beams and mass) was 7.2×7.2 mm^2.

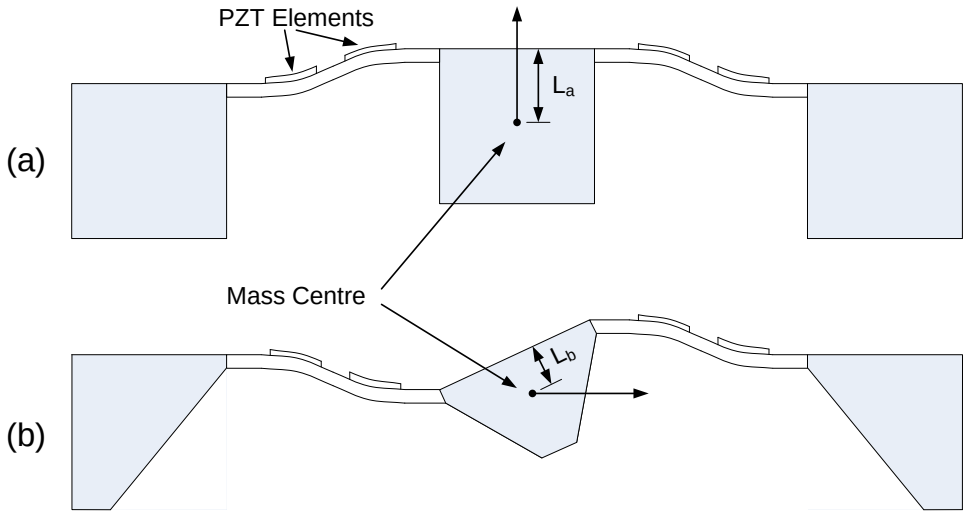

Figure 3.32: Schematic view of the mass deflection of a (a) DRIE mass for perpendicular acceleration, and a b) KOH etched mass for parallel acceleration. Note the lower centre of mass for the DRIE etched device, i.e. the distance L_a from the centre of the mass to the accelerometer surface is larger than the distance L_b for the KOH etched mass, resulting in higher deflection for parallel accelerations due to a higher momentum, thus resulting in higher sensitivity to these accelerations [28].

The principle of operation for the accelerometer is shown in Figure 3.32. For trans-

verse acceleration the suspension beams bend symmetrically as demonstrated in Figure 3.32a. This causes a symmetrical stress distribution in the four beams. For parallel acceleration two suspension beams bend asymmetrically (Figure 3.32(b)) and two suspension beams twist around their longitudinal-axis (not shown). As the polarisation of the charge developed in the eight PZT-elements depends on whether concave or convex deformation occurs, these two different motions can be distinguished. The twisting of a suspension beam around its longitudinal-axis does not generate a signal.

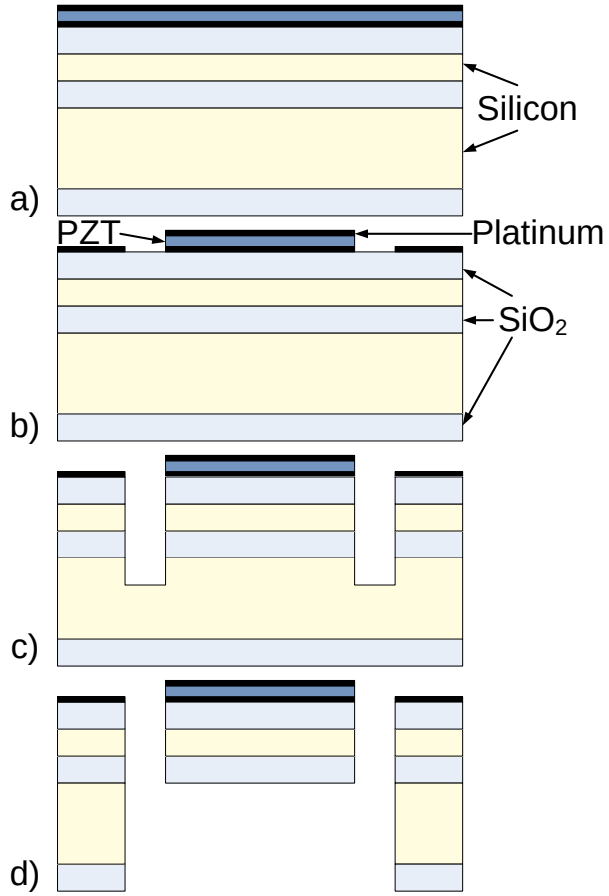

Figure 3.33: Fabrication process of the three-axis accelerometer: a) depositing all layers, silicon dioxide, platinum bottom electrode, PZT, platinum top electrode and gold bond pads; b) patterning of top electrode, PZT and bottom electrode; c) silicon DRIE and silicon dioxide RIE dry etching of the front using the bottom electrode as a mask; d) DRIE of the back [28].

The accelerometers were fabricated using DRIE of SOI wafers. The thin silicon

dioxide layer of the SOI acts as an etch stop on the bottom side of the suspension beams to accurately define the thickness of the suspension beams. Other advantages of using DRIE instead of KOH etching are that the position of the centre-of-mass is further away from the top surface resulting in a higher sensitivity to x- and y-accelerations and no special encapsulation is required to protect the PZT from the etchant. To illustrate the fabrication process, a schematic cross-sectional view of one suspension beam is shown in Figure 3.33. A fabricated structure can be seen in Figure 3.34.

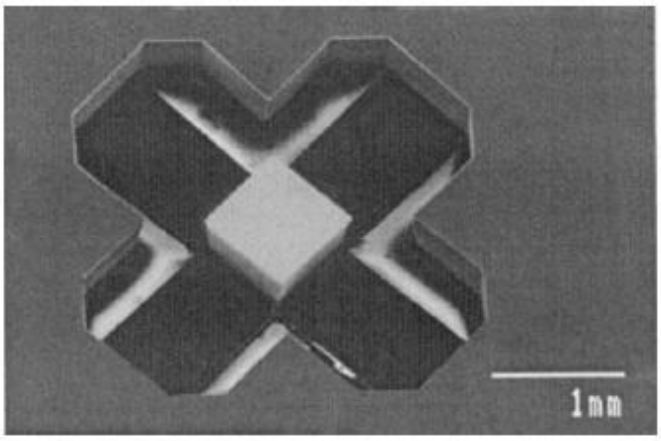

Figure 3.34: View of the backside of the three-axis accelerometer [28].

In 2008, a research group from the University of Southern California, USA, presented a three-axis piezoelectric-bimorph accelerometer built on parylene beams and ZnO films [29]. The structure is a highly symmetric quad-beam bimorph structure with a single proof mass.

The team argued that all of the previously reported micromachined piezoelectric accelerometers used single crystal silicon, polysilicon, or Si_xN_y as the material of choice for the supporting beams. The limiting characteristics of these materials are high stiffness and residual stress which limits the performance of the accelerometers. The use of parylene is shown to improve the sensitivities due to the very low Young's modulus ($\sim 3.2\,GPa$) and non-brittle characteristics of the material. When parylene film is used as a support beam for piezoelectric accelerometers, it is difficult to place

the neutral plane outside the piezoelectric layer with a unimorph structure because of the extremely low stiffness of parylene. Thus, the team used a bimorph structure with two ZnO piezoelectric films of opposite C-axis orientations to make the neutral plane location outside of the ZnO films and to maximize the sensitivities of the accelerometers.

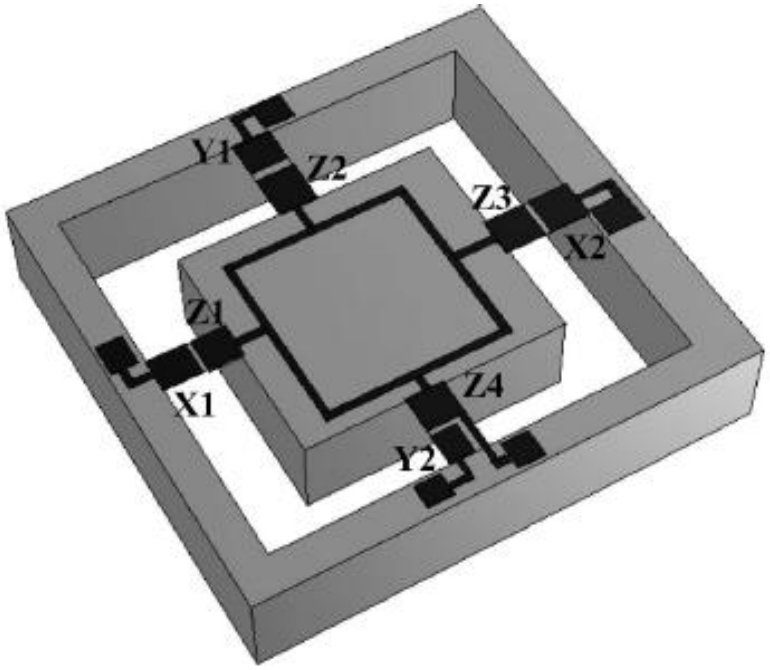

Figure 3.35: Schematic view of the three-axis piezoelectric-bimorph accelerometer [29].

Figure 3.35 shows the schematic of the three-axis accelerometer with a single seismic mass suspended by four symmetric parylene/Al/Si_xN_y/ZnO/Si_xN_y/Al/Si_xN_y/ ZnO/Si_xN_y/Al bimorph beams. The electrodes on the top side of the four beams are segmented into Z_1, Z_2, Z_3, Z_4 (for z-axis sensing), X_1, X_2 (for x-axis sensing), and Y_1, Y_2 (for y-axis sensing). The operating principle of the three-axis accelerometer is shown in Figure 3.36. When the seismic mass is accelerated vertically (along the z-axis), it produces tensile stress in the top half of the bimorph in X_1, X_2, Y_1, and Y_2 and compressive stress in Z_1-Z_4. Furthermore, there exists a finite voltage (V_z) between the parallel-connected Z_1-Z_4 and the electrode on the other face of the diaphragm because the top and bottom halves of the bimorph have opposite stress distribution. However, the voltage (V_x) between X_1 and X_2 (and also V_y

between Y_1 and Y_2) is almost zero because the net stress between the two electrodes is zero. When the seismic mass is accelerated laterally (e.g. the x-direction), it rotates around the y-axis and produces tensile stress in X_1 and Z_3 and compressive stress in Z_1 and X_2. It also produces shear stress in Y_1, Y_2, Z_2, and Z_4, which can be neglected. Thus, acceleration along the x-direction produces a finite differential signal V_x but almost zero V_y and V_z because of zero net stress between Y_1 and Y_2 and of Z_1 and Z_3 canceling each other, respectively. The same principles apply when the seismic mass is accelerated laterally in the y-direction.

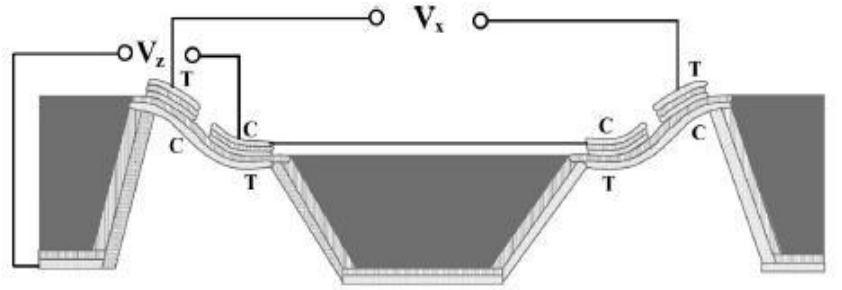

(a)

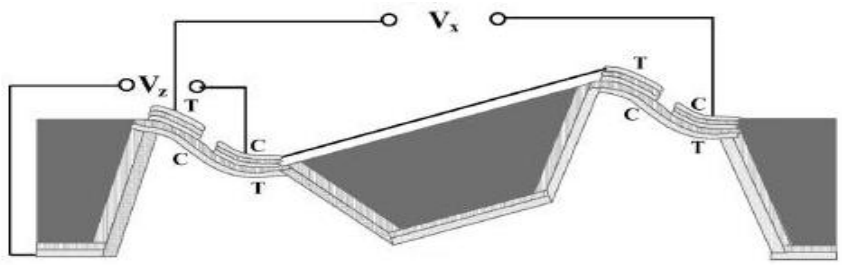

(b)

Figure 3.36: Operating principle of the three-axis piezoelectric-bimorph accelerometer: (a) with vertical acceleration applied (z-axis), and (b) with lateral acceleration applied (x- or y-axis) [29].

The fabrication steps are shown in Figure 3.37. The silicon is bulk micromachined to form a 0.8-μm-thick Si_xN_y diaphragm and a proof-mass silicon island (by KOH etching with convex corner compensation) in the middle of the Si_xN_y diaphragm. Figure 3.38 shows the front-side and backside views of a completed three-axis piezoelectric-bimorph accelerometer.

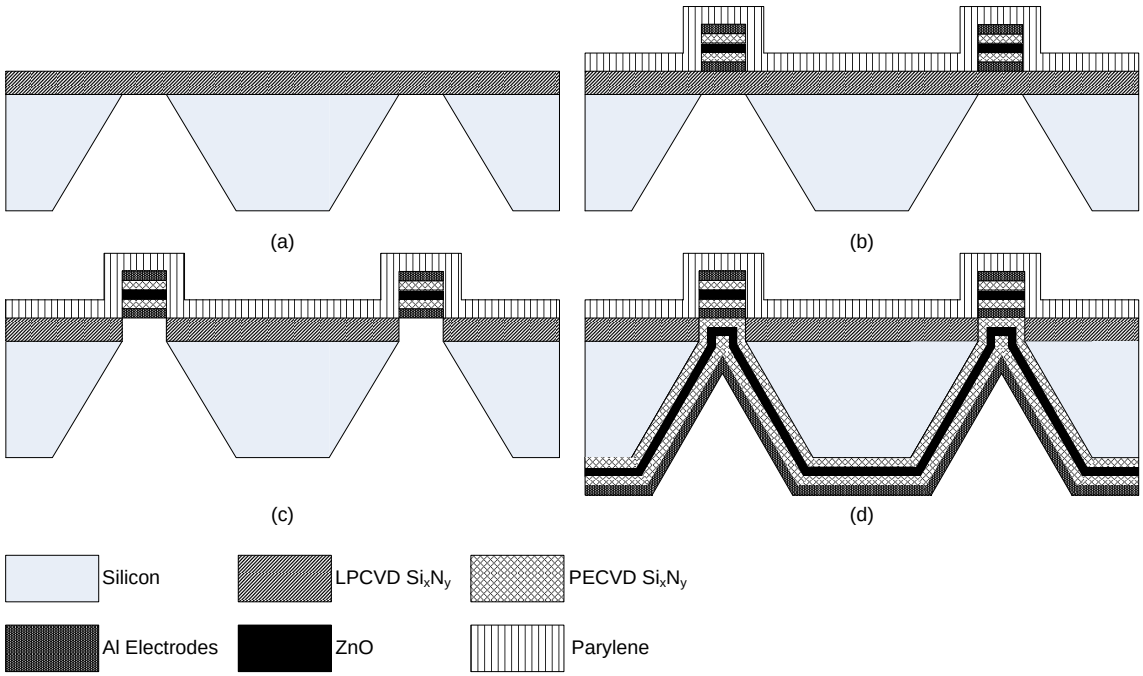

Figure 3.37: Fabrication process of the three-axis piezoelectric-bimorph accelerometer: (a) bulk-micromachined Si; (b) deposit and pattern 0.4-μm Al, 0.1-μm Plasma-Enhanced Chemical Vapour Deposition (PECVD) Si_xN_y, 0.3-μm ZnO, 0.1-μm PECVD Si_xN_y, 0.4-μm Al, and 2.1-μm parylene on the wafer front side; (c) etch Si_3N_4 from the wafer backside; (d) deposit 0.1-μm PECVD Si_xN_y, 0.3-μm ZnO, 0.1-μm PECVD Si_xN_y, and 0.4-μm Al on the wafer backside [29].

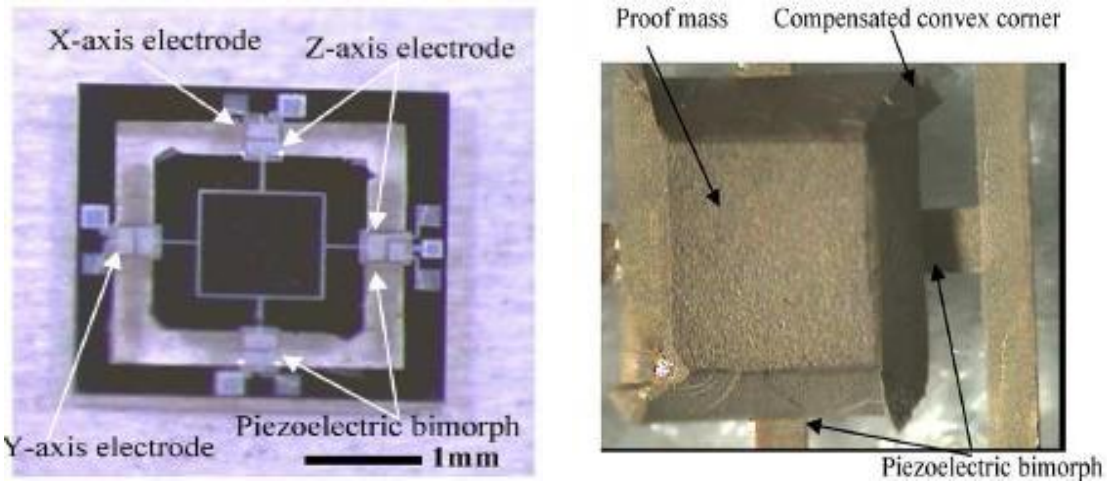

(a) (b)

Figure 3.38: Photographs of a completed triaxis piezoelectric-bimorph accelerometer from the (a) front side, and the (b) backside [29].

The unamplified sensitivities of the x-, y-, and z-axis electrodes in response to the accelerations in x-, y-, and z-axes are 0.93, 1.13, and 0.88 mV/g, respectively. The minimum detectable signal of the sensor was measured to be 0.04 g over a bandwidth ranging from sub-hertz to 100 Hz. The cross-axial sensitivity among the x-, y-, and z-axis electrodes is found to be less than 15%.

3.6 MEMS accelerometer industries

The MEMS market was worth $6 billion dollars in 2006 with accelerometers representing 11% of the share of the market. It has been forecast that the automotive sector will still represent more than 55% of the MEMS accelerometer market in 2011 and that growth will mainly come from high end applications (i.e. industrial, aeronautic and defence) [30]. The market enablers of MEMS such as size, batch manufacturing, power consumption and reliability will help lower the cost, improve the performance and open up new market oppportunities to further extend their reach beyond the the traditional automotive and industrial markets. It is predicted that by 2013, accelerometers will become the top-selling MEMS application [31]. The main areas in growth and development of accelerometers are discussed in the subsequent sections.

3.6.1 Automotive

Originally the large volume of demand for accelerometers was due to the application of high-g sensors for airbags in the automotive industry. Other applications include rollover detection (integrated roll rate sensor combined with low-g sensor in y- and z-directions), tyre pressure monitoring sensors which use battery powered devices that have power down and wake up functions made possible using accelerometers, electronic parking brake, vibration monitoring, navigation, security systems and active suspension.

One of the key growth drivers is the Electronic Stability Control (ESC) systems segment. These systems use three sensors - a gyroscope, an accelerometer, and a steering angle sensor - to detect any discrepancy between the driver's intention and the vehicle's actual motion. In case of a variation, the system intervenes to control the vehicle. Europe currently leads the global stability control systems market as these systems become standard in new vehicles in countries such as Germany, Sweden and France. Other countries are expected to follow suit as car manufacturers, responding to both customer demand and competition, include ESC systems as a standard feature on most vehicles [32].

Future accelerometers for automotive applications will be low-g sensors that are networked together. All sensors of the vehicle will be linked together and are used to provide motion data to several safety systems. Development areas include compensated compasses, headlight positioning, occupant detection and anti-theft. This growth will be more explosive with the European Commission having announced intentions to make both electronic stability control systems and tyre pressure monitoring mandatory by 2012 [30, 31].

3.6.2 Aeronautic, space and defence

Compared to the automotive and consumer industries, MEMS are scarcely used in defence applications today. The majority of military and aerospace applications are still too unique for them to be satisfied by the associated advantages of very low cost production of MEMS. The truly high-volume application, which would be analogous to the airbag accelerometer in the automotive industry, has yet to arrive. This is due in part to the extreme environments that the sensors are subjected to such as temperature, radiation, radio frequency interference and electromagnetic fields.

However, there are potential opportunities in areas such as aerodynamics, mobility, stealth, sensing, power generation and management, and smart structures and

materials. Unmanned aerial vehicles require flight control functions to provide navigation, guidance and stabilisation controls during image acquisition. This flight control is provided by the mean of an inertial measurement unit that correct flight commands using three-axis angular rate and acceleration sensing. This can also be applied to autonomous ground vehicles.

To date, the most established application of MEMS in defence is in inertial measurement units for weapons, guidance, navigation, and stabilisation which can be used to correct trajectory and increase target accuracy. In 2005, inertial sensors, of which accelerometers and gyroscopes are predominant, used for weapon guidance accounted for half of the MEMS defence market [33].

One major development area in aerospace is in Attitude and Heading Reference Systems (AHRS) in which three-axis sensors provide heading, attitude and yaw information for aircraft. AHRS are designed to replace the traditional mechanical gyroscopic flight instruments and provide superior reliability and accuracy. AHRS consist of MEMS gyroscopes, accelerometers and magnetometers on all three axes [30, 34].

In space, inertial sensors can be used in the development of micro- and nano-satellites to help in reducing mass and volume as well as providing platform stabilisation.

3.6.3 Consumer

Even though MEMS motion sensing has been around for a couple of decades in the automotive industry, it has taken the motion-sensing user interfaces of products like the Nintendo Wii and the Apple iPhone to increase the awareness of what inertial sensors are capable of in this area and how they can take consumer products to a new level. This has been possible, in part, due to these sensors becoming smaller, cheaper and requiring less power. Moreover, in contrast to the automotive industry, consumer applications feature relaxed specifications including higher failure rates.

Therefore accuracy and reliability can be sacrificed to an extent to enable even lower unit prices [31, 35].

Accelerometers in mobile phones are used to provide image stability, shock detection, menu navigation, text scroll, gaming control, silent mode activation and motion dialing, among others. Less than 3% of mobile phones had accelerometers in 2007; this was close to 10% in 2008. The combination of micromachined accelerometers and the appropriate application software eliminates the need for conventional switches or button and thumb wheels for the scrolling, zooming, and panning of Web pages, e-books, and spreadsheets [31, 32, 36].

Another application is the possibility to detect when a notebook or laptop is dropped. MEMS accelerometers are used to protect the hard disk by detecting the fall and signaling the hard drive to park its read head safely. When a free-fall is detected and a shock is expected, the write current is turned off so that the data on the other tracks is not corrupted. After this occurs the data can be rewritten to the desired track. To this end, companies such as IBM, Toshiba, and Apple have incorporated accelerometers into their higher-end notebook computer models and this is becoming a trend for most models. The trend toward larger-capacity hard disk drives incorporated into smaller products is forcing industry participants to consider accelerometers as a means of avoiding data loss. This is also used in MP3 players [32].

Camcorders and still cameras also use accelerometers. These can be applied to image stabilisation for anti-blur capturing. The camera holds off snapping the CCD "shutter" when the camera is moving. Some digital cameras also contain accelerometers to determine the orientation of the photo being taken and some also for rotating the current picture when viewing.

Portable and vehicle navigation systems use Global Positioning System (GPS) receivers to determine position and provide route guidance. With any GPS system, the signal reception is not always 100% reliable e.g. in urban areas where GPS

signals are blocked due to underground tunnels, bridges, and skyscrapers, making accurate navigation difficult. In this context, micromachined motion sensors can assist and substitute for the GPS. If there is signal loss, a dead reckoning system continues tracking movements when satellite signals are not visible or where they are not sufficiently accurate. Furthermore, to implement dead reckoning, it is necessary to know the distance and direction travelled. Therefore, a motion measurement unit, including an accelerometer, a gyroscope, and often a magnetometer, is required.

Pedometers are another application area and are used to measure burnt calories as well as the speed and distance travelled by an individual on foot. For this application, an accelerometer detects the motion of a walking person. The wireless pedometer can be worn on or in a shoe and can communicate with another personal device such as a stopwatch to display the measurements, providing athletes with a complete training tool. Pedometers also represent an important building block for personal navigation devices and have begun to be integrated in MP3 players and media phones [36].

3.6.4 Industrial

Applications of MEMS inertial sensors in industrial applications include the control of robotics and the monitoring of vibration and shock. Vibration and shock can be monitored for fatigue, health and safety and quality monitoring such as in machinery (including the operation of), transportation and buildings. MEMS sensors can also be placed in tight and harsh environments to provide measurements inside engines to maintain performance and reliability.

Very precise, low-g accelerometers can also be used as seismic sensors for oil exploration. A better achievable SNR makes for more accurate detection of oil fields. A reduction in the number and size of components makes this quicker to implement which also results in cost saving. Earthquake detection is also possible with these

sensors. [30]

3.6.5 Medical

There is a tremendous amount of development taking place in the medical sector. This is the last great frontier for MEMS and its full impact is yet to be felt. In comparison to other sectors such as automotive, the growth rate of adopting MEMS based technologies in healthcare and medicine has been slow. This is because most devices are still in research and the development stage and time required to market these devices are significant. In the medical field, accelerometers must be very small and consume low power.

One of the most common implementations of accelerometers in this field is the integration with heart pacemakers. The accelerometer is used to detect small changes in the users movement and activity level. This information is then used to deliver the appropriate level of electrical stimuli to the patient's heart and thereby improve the users comfortableness and quality of life.

In addition, accelerometers can also be used to monitor the motion or detect the position/activity level of patients for remote monitoring and raise an alarm when a lack of activity or a fall has been detected.

Another application is in the measurement of blood pressure which is influenced by the arm height and position. MEMS accelerometers enable an exclusive wrist-height guiding function to improve measurement accuracy. The accelerometer senses the angle and height of the users elbow and starts measurements only after the wrist is set at the right position. If the elbow moves during the measurements and the wrist shifts out of the proper position, the measurements are automatically stopped [30].

3.7 Summary and conclusions

In this chapter, the fundamental theory of accelerometers as well as some of the associated terminology have been introduced to explain the performance characteristics of the accelerometers presented.

Seven MEMS companies have been considered here that offer three-axis accelerometers and represent a very large proportion of the market. All but one of the commercial sensors presented employ capacitive sensing. The performance of the capacitive sensing accelerometers is indisputable but the technology suffers from inherent issues such as stiction and expensive fabrication processes that must be custom developed. Iterative process development is something that can be afforded by the manufacturers which results in a well defined and well understood fabrication process with a high degree of control and reproducibility. In addition, many of these companies draw on many years of CMOS experience and this can be integrated with the MEMS sensing structures to offer on-chip features such as signal conditioning and self-test. A large area of development and challenge for these manufacturers is in their quest to further miniaturise these sensors especially in packaging. Many of these sensors stack the MEMS sensing structure together with the hermetic cap and the IC and there has been demonstration of using stacked CSP [37, 38].

All manufacturers offer sensors that have analogue or digital outputs. This offers more flexibility in terms of system integration and allows the option of doing away with the need for analogue-to-digital converters. The sensors offer features such as activity and inactivity sensing, tap sensing, free-fall detection, and orientation detection allowing these sensors to operate at extremely low power as well as making them more versatile and multi-functional for different applications.

Note that this review of commercially available sensors was performed after the initial decision was made to design our own sensor in-house. At that time, very small sensors were not available. Today, commercially available three-axis sensing

accelerometers are available as small as $3\times3\times0.95\ mm^3$ which certainly lend themselves to many different applications where size is a limiting factor.

There are more examples of capacitive sensing three-axis accelerometers that are published in scientific journals. These sensors generally do not offer the same high standard of performance and certainly do not achieve the same levels of yield and reproducibility as their commercially available counterparts. This is due largely to limited access to well-defined and reproducible fabrication processes and financial restrictions for design iterations.

References

[1] M. Kraft S. P. Beeby, G. Ensel and N. White. *MEMS Mechanical Sensors*. Artech House Publishing, 2004.

[2] J.C. Lotters. *A Highly Symmetrical Capacitive Triaxial Accelerometer*. PhD thesis, Universiteit Twente, 1997.

[3] N. Yazdi, F. Ayazi, and K. Najafi. Micromachined inertial sensors. *Proceedings of the IEEE*, 86(8):1640–1659, Aug 1998.

[4] MultiMEMS website. `http://www.multimems.com/` (Accessed: 07 Oct 10).

[5] Freescale Semiconductor. Accelerometer terminology guide, May 2007. `www.freescale.com/` (Accessed: 07 Oct 10).

[6] James Doscher. Accelerometer design and applications. `http://www.meche.net/MAE%20334/Lab%205/Lab%205%20Report/sensor%20comparisons.pdf` (Accessed: 07 Oct 10).

[7] Analog Devices Inc. Single- and dual-axis micromachined accelerometers, 1996. `http://www.analog.com/library/analogDialogue/cd/vol30n4.pdf#page=3` (Accessed: 07 Oct 10).

[8] Analog Devices Inc. ADXL335 data sheet, January 2010. `http://www.analog.com/static/imported-files/data_sheets/ADXL335.pdf` (Accessed: 07 Oct 10).

[9] Chipworks Website. `http://www.chipworks.com/` (Accessed: 07 Oct 10).

[10] Analog Devices Inc. ADXL346 data sheet, October 2009. `http://www.analog.com/static/imported-files/data_sheets/ADXL346.pdf` (Accessed: 07 Oct 10).

[11] Bosch Sensortec GmbH. Bosch Sensortec BMA140 data sheet, April 2008. http://www.bosch-sensortec.com/content/language1/downloads/BMA140_DataSheet_Rev1.1_04APR2008.pdf (Accessed: 07 Oct 10).

[12] Bosch Sensortec GmbH. Bosch Sensortec BMA220 flyer. http://www.bosch-sensortec.com/content/language1/downloads/Flyer_BMA220_12_2009_LY02.pdf (Accessed: 07 Oct 10).

[13] Freescale Semiconductor Inc. Freescale Semiconductor MMA7361L data sheet, April 2008. http://www.freescale.com/files/sensors/doc/data_sheet/MMA7361L.pdf?pspll=1 (Accessed: 07 Oct 10).

[14] Chipworks Inc. The evolution of three-axis MEMS inertial sensor packaging - size does matter!, September 2009. http://www.i-micronews.com/news/Evolution-Three-Axis-MEMS-Inertial-SensorPackaging--Size,3515.html (Accessed: 07 Oct 10).

[15] Freescale Semiconductor Inc. Freescale Semiconductor MMA7660FC data sheet, November 2009. http://www.freescale.com/files/sensors/doc/data_sheet/MMA7660FC.pdf?pspll=1 (Accessed: 07 Oct 10).

[16] Kionix Inc. Kionix KXSC7-2050 data sheet, January 2008. http://www.kionix.com/Product-Specs/KXSC7-2050%20Specifications%20Rev%201.pdf (Accessed: 07 Oct 10).

[17] Kionix Inc. Kionix KXTF9-4100 data sheet, December 2009. http://www.kionix.com/Product-Specs/KXTF9-4100%20Specifications%20Rev%201.pdf (Accessed: 07 Oct 10).

[18] STMicroelectronics. ST LIS331AL data sheet, September 2007. http://www.st.com/stonline/products/literature/ds/13947.pdf (Accessed: 07 Oct 10).

[19] STMicroelectronics. ST LIS331DL data sheet, April 2008. http://www.st.com/stonline/products/literature/ds/13951.pdf (Accessed: 07 Oct 10).

[20] VTI Technologies. VTI CMA3000-A01 data sheet. http://www.vti.fi/midcom-serveattachmentguid-0634c7d8cdf911de8350ddb23e5085558555/cma3000_a01_datasheet_8278700a.01.pdf (Accessed: 07 Oct 10).

[21] VTI Technologies. VTI CMA3000-D01 data sheet. http://www.vti.fi/midcom-serveattachmentguid-ef9ca374cdf811de8893630e7553f222f222/cma3000_d01_datasheet_8277800a.01.pdf (Accessed: 07 Oct 10).

[22] Parallax Inc. Getting started with an accelerometer. http://forums.parallax.com/forums/default.aspx?f=6&m=55816.

[23] MEMSIC Inc. MEMSIC MXR9500G/M data sheet, February 2007. http://www.memsic.com/data/products/MXR9500G&M/MXR9500G&M.pdf (Accessed: 07 Oct 10).

[24] Y. Watanabe, T. Mitsui, T. Mineta, Y. Matsu, and K. Okada. SOI micromachined 5-axis motion sensor using resonant electrostatic drive and non-resonant capacitive detection mode. *Sensors and Actuators A-Physical*, 130:116–123.

[25] H. W. Qu and H. K. Xie. Process development for CMOS-MEMS sensors with robust electrically isolated bulk silicon microstructures. *Journal of Microelectromechanical Systems*, 16(5):1152–1161.

[26] K. I. Lee, H. Takao, K. Sawada, and M. Ishida. Low temperature dependence three-axis accelerometer for high temperature environments with temperature control of SOI piezoresistors. *Sensors and Actuators A-Physical*, 104(1):53–60.

[27] R. Amarasinghe, D. V. Dao, T. Toriyama, and S. Sugiyama. Design and fabrication of a miniaturized six-degree-of-freedom piezoresistive accelerometer. *Journal of Micromechanics and Microengineering*, 15(9):1745–1753.

[28] K. Kunz, P. Enoksson, and G. Stemme. Highly sensitive triaxial silicon accelerometer with integrated PZT thin film detectors. *Sensors and Actuators A-Physical*, 92(1-3):156–160.

[29] Q. Zou, W. Tan, E. S. Kim, and G. E. Loeb. Single- and triaxis piezoelectric-bimorph accelerometers. *Journal of Microelectromechanical Systems*, 17(1):45–57.

[30] High performance inertial mems markets. Technical report, Yole Development, September 2007.

[31] Jeremie Bouchaud and Richard Dixon. MEMS market brief. Technical report, iSuppli, January 2009.

[32] Prashanth Venkatesh. MEMS in automotive and consumer electronics, November 2007. `http://www.sensorsmag.com/` (Accessed: 07 Oct 10).

[33] MEMS market for defense and aerospace to hit $265 million by 2009, February 2006. `http://mae.pennet.com/` (Accessed: 07 Oct 10).

[34] Accelerometer for AHRS application. Technical report, Colibrys.

[35] Harvey Weinberg and Rob O'Reilly. The five motion senses: MEMS inertial sensing to transform applications, January 2010. `http://www.sensorsmag.com/` (Accessed: 07 Oct 10).

[36] Benedetto Vigna. Riding the wave of consumerization. `http://www.smalltimes.com/` (Accessed: 07 Oct 10).

[37] The Evolution of Three-Axis MEMS Inertial Sensor Packaging - Size Does Matter! `http://www.i-micronews.com/news/Evolution-Three-Axis-MEMS-Inertial-SensorPackaging--Size,3515.html` (Accessed: 07 Oct 10).

[38] Ahra Lee, SangChul Lee, Sungsik Lee, Chang Han Je, Sunghae Jung, Myoung-Lae Lee, Gunn Hwang, Byoung-Gon Yu, and Chang Auck Choi. Chip scale packaging with surface mountable solder ball terminals for microsensors. In *Nano/Micro Engineered and Molecular Systems, 2009. NEMS 2009. 4th IEEE International Conference on*, pages 612 –615, 5-8 2009.

Chapter 4

Design of a Micromachined Three-Axis Accelerometer

4.1 Introduction

At the beginning of the design phase, it was necessary to find a means to consider how and where the authors' sensor designs would be fabricated. It was not possible, with the MISEC cleanroom facilities, to fabricate these in-house so it was then necessary to look at outside foundry processes. The obvious solution came in the form of the MultiMEMS Multi Project Wafer (MPW) process offered by SensoNor Technologies AS with whom Vestfold University have close relations [1]. This process offers a stable bulk micromachined process with piezoresistive sensing. This technology has been used for the fabrication of commercial inertial sensors for the past two decades. As part of this process, a set of design rules are to be followed to qualify the designs for placement on the wafer layout [2]. These design rules restrain the design, referred to as the "MultiMEMS" design forthwith, and the steps necessary in fabricating these designs.

A DRIE process step was however required in addition to the established process. In the MultiMEMS process, the seismic masses are defined by the n-type diffusion together with a wet anisotropic etch and a pn-junction etch-stop. This results in masses that are only 23 μm thick and the profile of the diffusion results in angled sidewalls. As a result, the masses lack sensitivity to in-plane accelerations due to the small value of the vertical centre of gravity of the mass. The process used for this approach is offered by the Scottish Microelectronic Centre (SMC) and the associated

designs will be referred to as the "SMC" designs henceforth [3]. The basic building block of the sensor designs is common for both processes and the necessary design considerations to make these designs suitable for fabrication are discussed here.

4.2 Sensor structure

The most basic and common building block for piezoresistive acceleration sensors is the cantilever beam with a seismic mass attached at its end. Here, the acceleration-induced mass deflection is detected using piezoresistors located on the thin supporting beams. Various single and dual beam structures are implemented in the two design phases presented in this thesis.

For the MultiMEMS process, the thin beams are defined by a grown 3 μm thick epitaxial layer. The seismic masses are defined by an implanted 23 μm thick n-well. In the SMC process, the standard silicon wafers that are used in the MultiMEMS process are replaced by SOI wafers. In doing this, the silicon device layer is used to define the beams which are chosen to be 4 μm thick. The 380 μm silicon handle layer is then used to define the masses. The fabrication process for the MultiMEMS and SMC designs can be seen in Chapter 6.

4.3 Mechanical analytical calculations

One of the fundamental rules for qualifying the designs was that the structure must not exceed a maximum stress value for a given acceleration. In the case of the MultiMEMS design phase, this rule corresponds to a maximum of 500 MPa for 2000 g of acceleration in any direction. For the SMC designs this rule becomes 500 MPa for 500 g of acceleration in any direction and thus offers the possibility of a more acceleration-sensitive design solution. The basic building blocks of the MultiMEMS and SMC designs are the same. The following mechanical calculations

can be applied for both processes. Any differences between the two designs will be highlighted.

With reference to Figure 4.1, during bending the surface of the cantilever beam on the convex side lengthens, and the surface on the concave side shortens. At a first-order approximation, the stress distribution increases linearly from the tip of the cantilever beam to the base where the beam is fixed, and varies linearly across the beam thickness. In the case of a prismatic beam there is a point of zero stress halfway through the thickness of the beam where there is a transition from a tensile stress to a compressive one as shown in Figure 4.2. The plane of these points along the length of the cantilever is called the neutral axis.

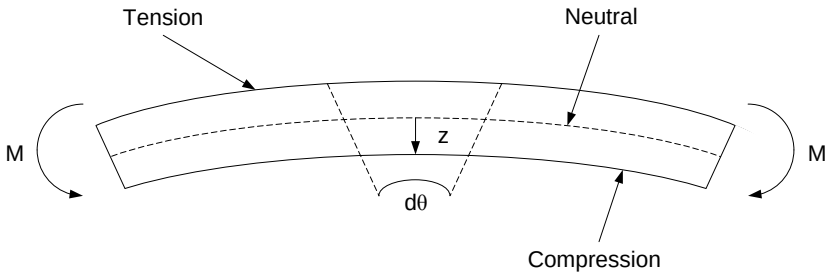

Figure 4.1: Pure bending of a transversely loaded beam.

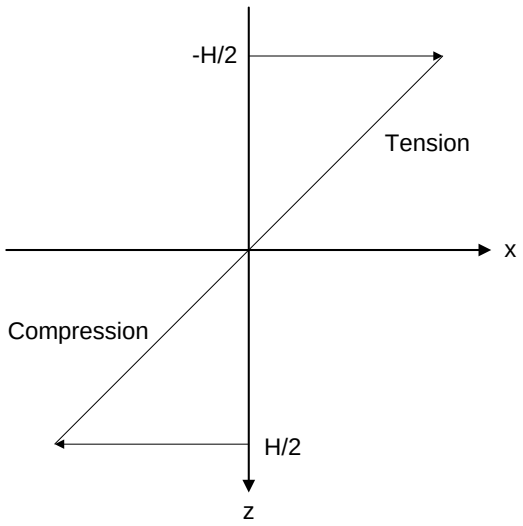

Figure 4.2: Stress variation through the height of a beam.

The maximum stress in the beam occurs at the section of greatest bending moment, M. To understand how the internal stress works, let us assume that the beam only bends at one point along its length. The magnitude of the bending moment at this point is given by:

$$M = F\,(L - y) \tag{4.1}$$

where L is the length of the beam, y is the position along the beam from the base, and F is the force. The greatest bending moment and thus the greatest stress occurs at y=0 i.e. the base of the beam.

The fundamental equation to evaluate the stress (σ) experienced in a cantilever when under transversal loading is:

$$\sigma = \left(\frac{M}{I}\right) z_c \tag{4.2}$$

where the variable z_c denotes the distance from the neutral axis to the surface of the beam, which is simply half the height ($H_b/2$) for a beam with a rectangular cross-section, and I is the rectangular moment of inertia with respect to the neutral axis. This relation is only valid for small deformations. For virtually all MEMS devices, the angles encountered are very small - a few degrees. Therefore, this small-angle approximation is justified. For a rectangular cross section of height H_b and width W_b the moment of inertia is:

$$I = \frac{W_b H_b^3}{12} \tag{4.3}$$

Stress due to in-plane accelerations, σ_{IP}, of a cantilever beam with a mass at the end can be formulated as:

$$\sigma_{IP} = \left(\frac{M_{IP}}{I}\right) z_c \tag{4.4}$$

The total bending moment, M_{IP} is given by:

$$M_{IP} = \left(\frac{F}{2}\right) r0 = \left(\frac{m_{mass}a}{2}\right) r0 \tag{4.5}$$

where m_{mass} is the mass of the seismic mass as calculated from Equation 4.21, a is the acceleration that the device is subjected to and $r0$ is the distance from the neutral axis of the cantilever beam to the vertical centre of gravity of the mass as given in Equation 4.24 for the MultiMEMS design or is simply $(H_m{+}H_b)/2$ for the SMC design. The reason that F is halved is to represent a dual-beam structure which is implemented in the design and introduced in Section 4.5.

The value of the in-plane stress is therefore:

$$\sigma_{IP} = \left(\frac{\left(\left(m_{mass}a\right)/2\right) r0}{\left(\frac{W_b H_b^3}{12}\right)}\right) \left(\frac{H_b}{2}\right) \tag{4.6}$$

For stress due to out-of-plane accelerations:

$$\sigma_{OP} = \left(\frac{M_{OP}}{I}\right) z_c \tag{4.7}$$

Here, the value of the bending moment is given by:

$$M_{OP} = M_1 + M_2 \tag{4.8}$$

where M_1 is given by:

$$M_1 = \left(\frac{F}{2}\right)\left(\frac{L_m}{2}\right) \tag{4.9}$$

and M_2 is:

$$M_2 = \left(\frac{F}{2}\right)(L_b - y) \tag{4.10}$$

The calculations for I and for z_c still apply. The out-of-plane stress is therefore [4, 5]:

$$\sigma_{OP} = \left(\frac{\left((F/2)\left(\left(\frac{L_m}{2}\right) + (L_b - y)\right)\right)}{\left(\frac{W_b H_b^3}{12}\right)}\right)\frac{H_b}{2} \tag{4.11}$$

Geometric properties of the seismic masses

MultiMEMS design

To complete the calculations of the maximum stress in the system it is necessary to know the geometrical properties of the beams and the masses that are implemented in the designs.

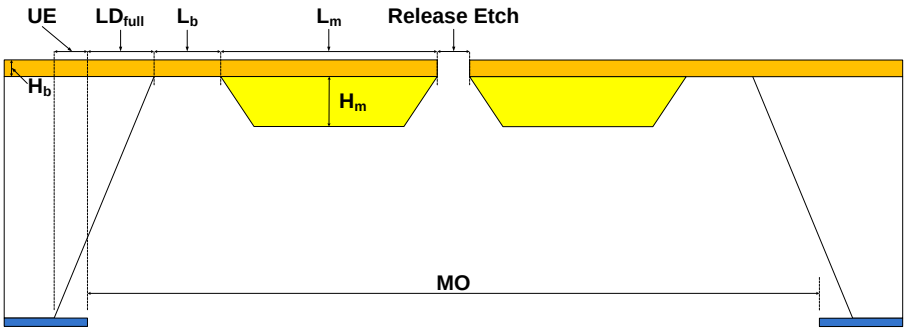

(a)

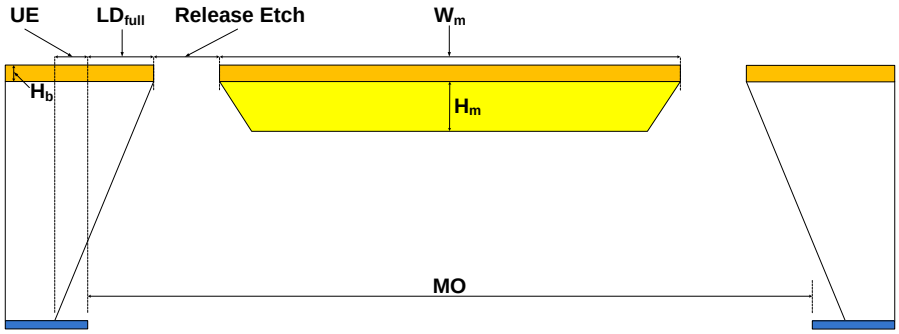

(b)

Figure 4.3: MultiMEMS cross-section of (a) the length of a pair of beam and mass structures (a-a in Figure 4.7(a)), and (b) width of a single mass (b-b in Figure 4.7(a)). N.B. MO is the mask opening required for a pair of structures, UE is the under etch of the oxide mask, and LD_{full} is the lateral displacement of the backside etch.

The mass in the MultiMEMS design is formed using n-well implantation followed by wet etching. This process step results in sidewalls with a vertical angle of α_{nwell} = 38°, as shown in Figures 4.3 and 4.4.

For each step dz, the width of the mass W_m, will decrease with dx, effectively reducing the volume of a mass of dz thickness. dx can be defined as a function of α and dz:

$$dx = \frac{dz}{\tan(\alpha)} \tag{4.12}$$

and

$$W_m(z) = W_m - \frac{2z}{\tan(\alpha)} \tag{4.13}$$

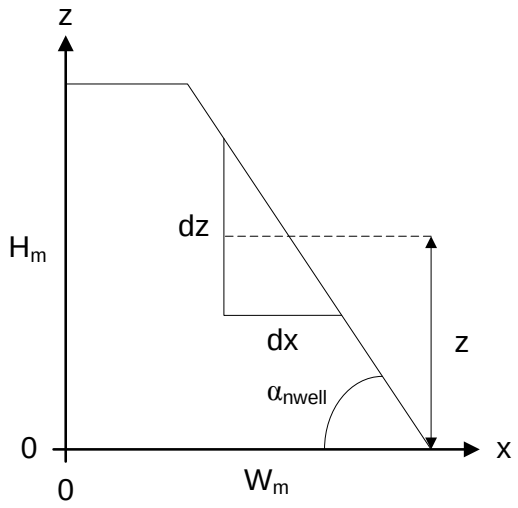

Figure 4.4: Cross-section of the MultiMEMS n-well mass.

Then, assuming the same shrinkage in the y-direction, the length of the mass, L_m, will decrease with dy for each step dz such that:

$$dy = \frac{dz}{\tan(\alpha)} \tag{4.14}$$

and

$$L_m(z) = L_m - \frac{2z}{\tan(\alpha)} \tag{4.15}$$

Because both dy and dx are defined by the n-well doping profile, $dx = dy$. Therefore the area of the mass is:

$$A(z) = W_m(z) L_m(z) \tag{4.16}$$

The volume of the mass is given by:

$$Volume = \int_0^{H_m} A(z)\, dz \tag{4.17}$$

The value of the mass is then:

$$m_{nwell} = Volume\rho \tag{4.18}$$

where ρ is the density of silicon and has a value of 2330 kg/m^3. Therefore,

$$m_{nwell} = \int_0^{H_m} A(z)\, \rho dz \tag{4.19}$$

This then equates to:

$$m_{nwell} = \frac{H_m}{3}\left(\frac{4H_m^2 - 3H_m L_m \tan(\alpha_{nwell}) - 3W_m H_m \tan(\alpha_{nwell}) + 3W_m L_m \tan^2(\alpha_{nwell})}{\tan^2(\alpha_{nwell})}\right)\rho \tag{4.20}$$

When taking into account the thin epitaxial layer that is grown on the top of the seismic masses, the total mass of the seismic masses becomes:

$$m_{mass} = m_{nwell} + m_{epi} \tag{4.21}$$

where

$$m_{epi} = (W_m L_m H_b)\,\rho \tag{4.22}$$

The location of the vertical centre of mass for a seismic mass of lumped elements can be defined as:

$$z_{cm} = \frac{m_1 z_1 + m_2 z_2 + ...}{m_1 + m_2 + ...} = \frac{\sum_i m_i z_i}{\sum_i m_i} \tag{4.23}$$

i.e. the centre of mass is a mass-weighted average position of the lumped masses that form the seismic mass.

$r0$ is the distance from the neutral axis of the beam to the centre of mass of the seismic mass as shown in Figure 4.5:

$$r0 = \frac{H_b}{2} + z_{cm} \tag{4.24}$$

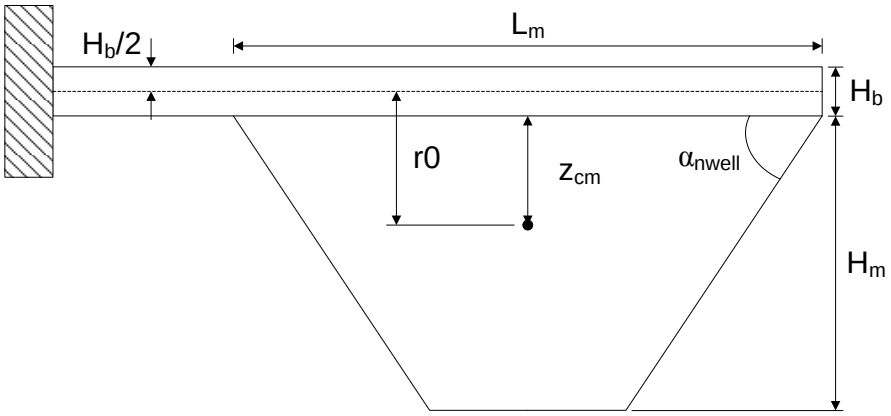

Figure 4.5: Cross-section of the MultiMEMS mass and beam structure.

The centre of gravity is located at z (refer to Figure 4.4). Therefore the centre of mass of the seismic mass is given by:

$$z_{cm} = \frac{\int_0^{H_m} A(z)\,\rho z dz}{\int_0^{H_m} A(z)\,\rho z} \tag{4.25}$$

With the origin taken at the bottom of the epi-layer as shown in Figure 4.5, this equates to:

$$z_{cm} = \frac{H_b}{2}\left(\frac{6H_m^2 - 4H_m L_m \tan(\alpha_{nwell}) - 4W_m H_m \tan(\alpha_{nwell}) + 3W_m L_m \tan^2(\alpha_{nwell})}{4H_m^2 - 3H_m L_m \tan(\alpha_{nwell}) - 3W_m H_m \tan(\alpha_{nwell}) + 3W_m L_m \tan^2(\alpha_{nwell})}\right) \tag{4.26}$$

SMC design

Because the SMC designs have approximately vertical sidewalls the following amendments have to be made to the equations above:

- For the SMC designs, the silicon handle layer of the SOI wafers is used to form the seismic masses. Therefore Equation 4.20 is replaced by m_{handle}=$(W_m L_m H_m)\,\rho$ for rectangular masses. Some of the designs have masses defined as triangles

and further simple changes are made to accommodate this.

- The centre of gravity of the mass (z_{cm}) simply becomes $(H_b + H_m)/2$. This expression replaces Equation 4.26 and can also be applied to Equation 4.24.

Note that the epitaxial layer in the MultiMEMS process and the silicon device layer in the SMC process can be used interchangeably in the above equations because they are both rectangular layers with uniform thickness that are located above the corresponding seismic masses.

4.4 Wheatstone bridge theory

A resistive bridge circuit called a Wheatstone bridge is used to measure the acceleration-induced resistance changes. A basic Wheatstone bridge circuit contains four resistances, a constant voltage input, and a voltage gauge as shown in Figure 4.6. Commonly, the piezoresistors are arranged such that adjacent resistors within the bridge show a change of resistivity which is opposite in sign, as this increases the sensitivity. This is usually done by using the fact that the piezoresistive coefficients for longitudinal and transverse stresses are equal and opposite.

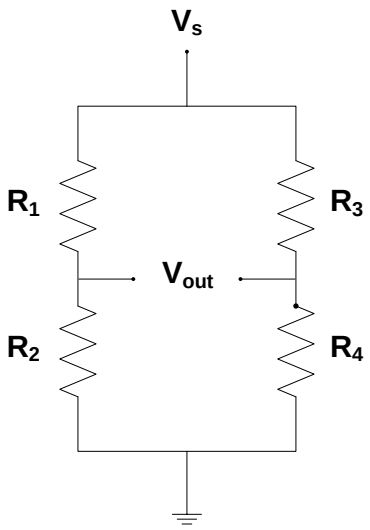

Figure 4.6: Wheatstone bridge.

The output of the Wheatstone bridge, using a voltage bias, is given by:

$$V_{out} = \frac{R_1 \cdot R_4 - R_2 \cdot R_3}{(R_1 + R_2)(R_3 + R_4)} V_s \tag{4.27}$$

If the four resistors are equal (R_1=R_2=R_3=R_4=R), the output is zero. In the ideal case, when a stress is applied to the sensor the four resistors will change in the following way:

$$\begin{aligned} R_1 &= R + \Delta R = R(1 + \delta) \\ R_2 &= R - \Delta R = R(1 - \delta) \\ R_3 &= R - \Delta R = R(1 - \delta) \\ R_4 &= R + \Delta R = R(1 + \delta) \end{aligned} \tag{4.28}$$

which, when using Equation 4.27 gives:

$$V_{out} = \delta V_s = V_s \frac{\Delta R}{R} \tag{4.29}$$

Therefore the output is proportional to the relative resistor variation.

4.5 MultiMEMS sensor design

To sense acceleration in all three axes, the arrangement of masses as shown in Figure 4.7 was adopted. The basic building block of the sensor is a seismic mass supported by two cantilever beams. Four identical blocks were used and grouped into two pairs which essentially represent two dual-axis accelerometers. The masses of each pair

face each other whilst the two pairs were rotated at 90° to each other as shown in Figure 4.7. Each pair of masses are designed to detect accelerations perpendicular to the sensor plane (z-axis) and accelerations in the sensor plane (x-axis and y-axis depending on the pair) as demonstrated pictorially in Figure 4.8.

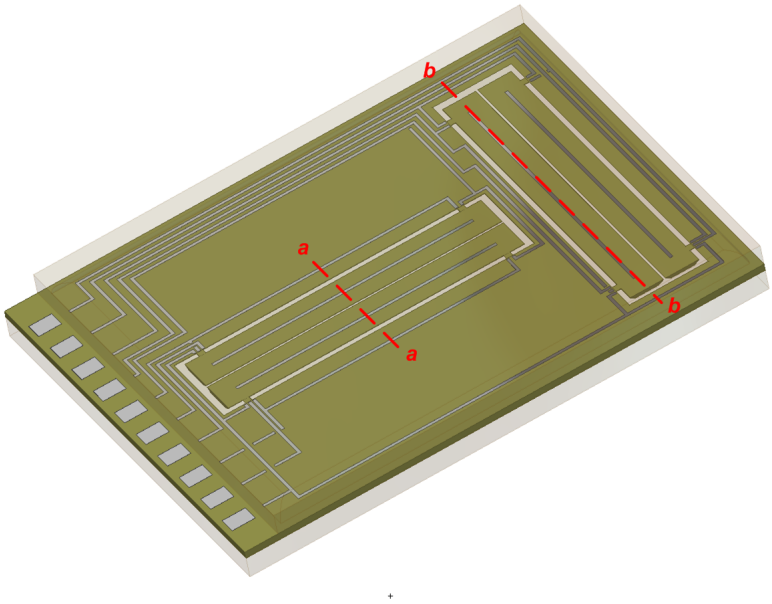

(a)

(b)

Figure 4.7: MultiMEMS design (a) top view, and (b) bottom view.

For this process the 20 μm thick implanted n-well is best suited to form the seismic masses which would be supported by the 3 μm thick epitaxial layer. With the

process, four template sizes were available to the designer (width×length, with the length having the bond pad area on one side): 3×3 mm^2, 3×6 mm^2, 6×3 mm^2, and 6×6 mm^2. The aim of the design of the structures was to make them as sensitive as possible to acceleration i.e. work towards the maximum stress value of 500 MPa at 2000 g [2].

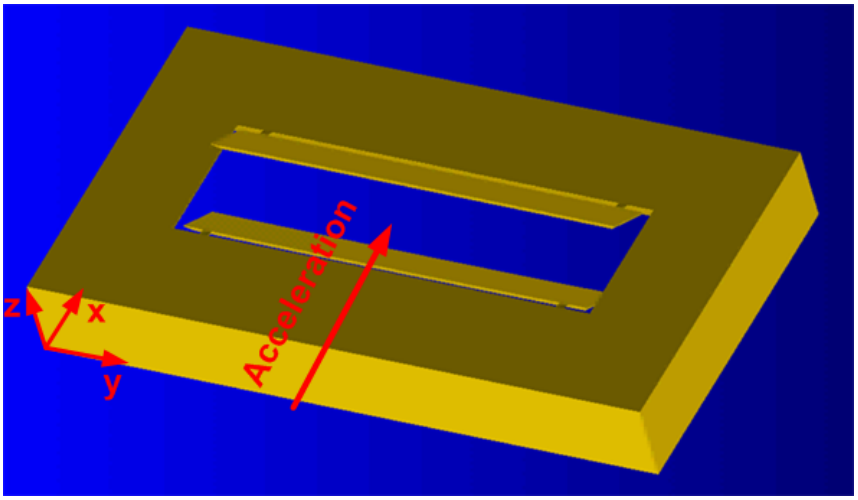

(a)

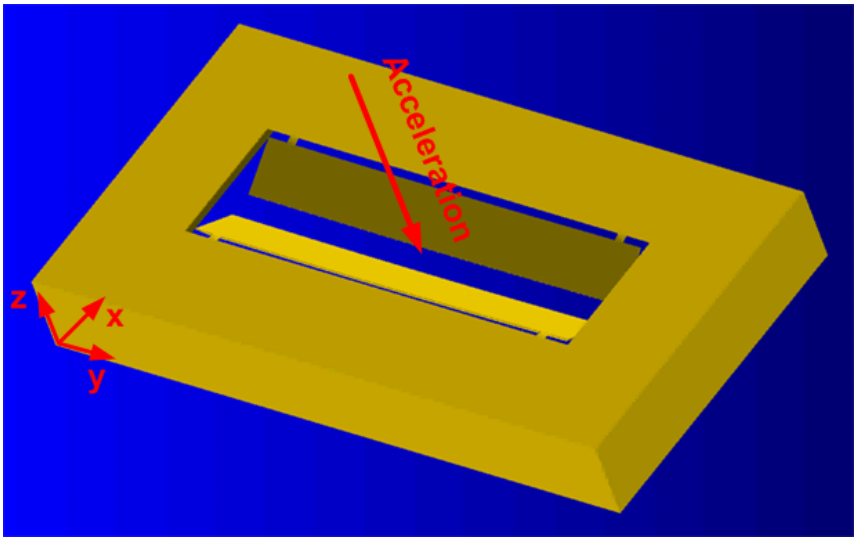

(b)

Figure 4.8: Deflected masses of MultiMEMS design for (a) in-plane acceleration (x-axis), and (b) out-of-plane acceleration (z-axis).

In the initial design, the width and length of the beams, W_b and L_b respectively, were made to be as narrow and as short as possible whilst still meeting the design

rules with regards to the placement of the necessary piezoresistors and associated electrical connections on the beams. The width of the masses, W_m, were then made as wide as possible whilst ensuring that they fitted on the template and allowed room for electrical connections to go around the sensing structures from the sensing piezoresistors to the outside bond pads. The space required for this was dictated by the associated layer design rules as well as intra- and inter-design rules associated with the bonding areas and released structures. Making the masses as wide as possible and having the length of the beams short made the structures less susceptible to in-plane accelerations other than the ones that they were designed to sense. All these factors dictated the length of the mass when applied to calculations to tune the structure to the maximum allowable stress for 2000 g. In doing this, it quickly became apparent from the equations outlined in Section 4.3 that the four structures, when designed to be as sensitive to acceleration whilst still in accordance with the design rules, could not be fitted on a 3×3 mm^2 template so it was decided to go with the longer template, 3×6 mm^2, which was better suited to the final application of the sensor.

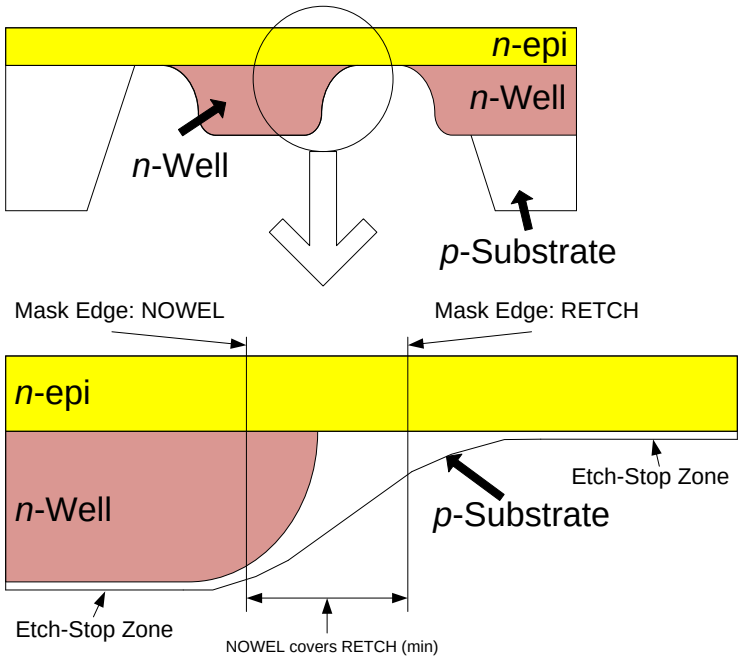

Figure 4.9: Etching profile after etch-stopping on a structure with a two-level junction.

An important consideration was the correct placement of the top side release etch in relation to the boundary of the n-well mass at the bottom of the epi-layer. When bulk etching is performed on a structure with a two-level pn-junction etch-stop, a transition region between these two thicknesses is present. The transition region profile is shown in Figure 4.9. It is then necessary to have the opening of the n-well mask 34 μm inside the mask for the release etch (a in Figure 4.10). Further, it was necessary to have two notches in the n-well mask at the interface between the end of the beams and the seismic mass (b in Figure 4.10). This was to ensure that the transition region would not interfere with the thin beams and therefore make them less sensitive to accelerations.

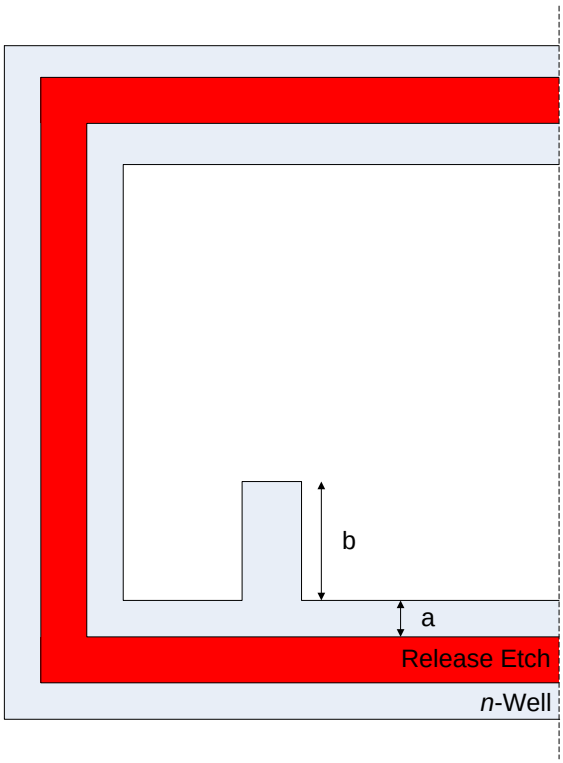

Figure 4.10: Inter-layer relationship between the n-well and front side release etch masks.

Once the outline of a pair of beam-masses structures was known, it was then possible to consider the mask for the TMAH backside etch. The boundary around the outside edge of the release etch is highlighted in Figure 4.11. This is the area where the backside etch is designed to stop when it reaches the bottom of the epi-layer. To do this, the dimensions for the opening of the mask on the backside of the wafer has to

be calculated according to the etchant characteristics and the depth of the etch. The etch is anisotropic along the (111) planes which slowly etch resulting in an inclination at 54.74° with respect to the (100) wafer-planes. However, the measured effective angle of the sidewalls after the standard electrochemical etch stop is 53.5° due to the lateral under-etch of the backside oxide mask, UE, which equates to 55±10 μm. For an etch depth of 400 μm i.e. the silicon wafer thickness, the associated lateral displacement, LD_{full}, defined as the distance between the edge of the mask opening on the bottom of the wafer to the edge that meets the bottom of the epi-layer, is 240 μm as shown in Figure 4.3. The backside etch mask therefore had to be 240 μm larger on each side of the outline of the top-side release etch as shown in Figure 4.11.

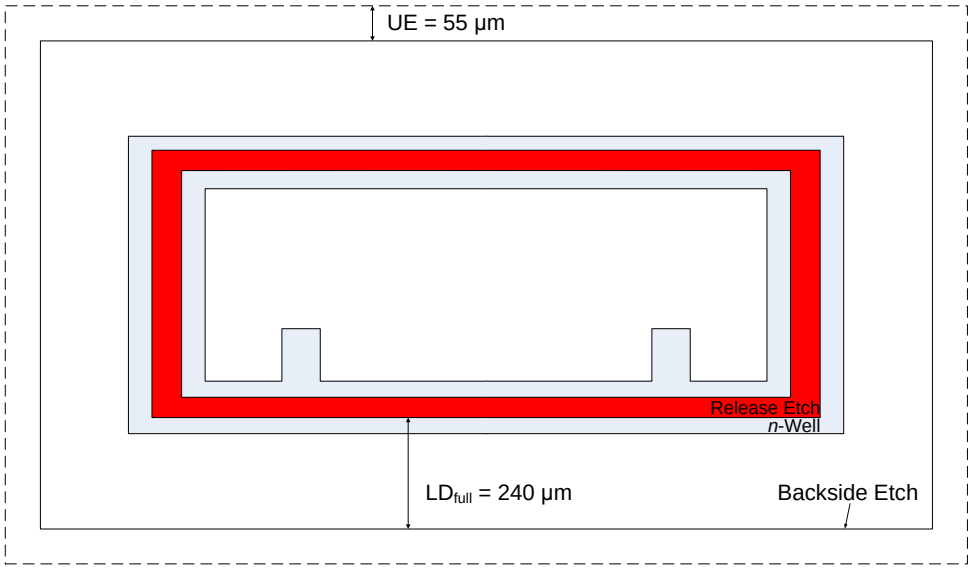

Figure 4.11: Inter-layer relationship between front side release etch and backside etch.

Boron p-type implanted conductors and aluminium metal conductors were used to electrically interconnect the piezoresistors and the bond pads. Only the implanted conductors were used on the thin cantilever beams where only the epi-layer is present. The minimum line design rule for this layer can then be used to enable the beam to be as narrow as possible i.e. 4 μm instead of the minimum 26 μm when used in conjunction with the contact hole and metal conductor layers. This introduced a redundancy where if anything happened to one of the conductive path layers then

the other would be present to complete the connection. This was employed where the larger width for the conductive track was less critical i.e. from the base of the beam and out to the bond pad area.

The metal tracks and surface conductors cease at the point where the conductive tracks reach the packaging interface as the packaging used requires a perfectly planar surface to bond to. Instead, buried conductors, located approximately 0.6 μm below the surface of the silicon, were used to provide the connection from the inside to the outside of the package.

The resulting final dimensions of the mass-beam structure can be seen in Table 4.1.

Dimension	**Abbreviation**	**Value (μm)**
Width of the beams	W_b	44
Length of the beams	L_b	34
Thickness of the beams	H_b	3
Length of the mass	L_m	230
Width of the mass	W_m	2050
Thickness of the mass	H_m	23

Table 4.1: Structural dimensions of the MultiMEMS design. Refer to Figure 4.3.

Using the values in Table 4.1, the obtained values of stresses for 2000 g of in-plane and out-of-plane accelerations (σ_{IP} and σ_{OP}, respectively) according to the analytical equations in Section 4.3 are 29 MPa and 481 MPa respectively. The respective Matlab files for this calculation can be found in Appendix A. As can be seen with these values, the structures experience a much lower value of stress for in-plane acceleration compared to the equivalent out-of-plane acceleration and therefore have a lower sensitivity to in-plane accelerations. As discussed previously, the sensitivity to in-plane accelerations is indeed due to the value of $r0$, the centre of gravity of the n-well mass, which has a relatively low value of 10.72 μm using Equation 4.24.

For out-of-plane accelerations, the first-order approximation of the stress profile follows the length of the beam as shown in Figure 4.12. The stress reduces linearly from a maximum value situated at the base of the beam. For in-plane accelerations the stress has a constant value along the length of the beam.

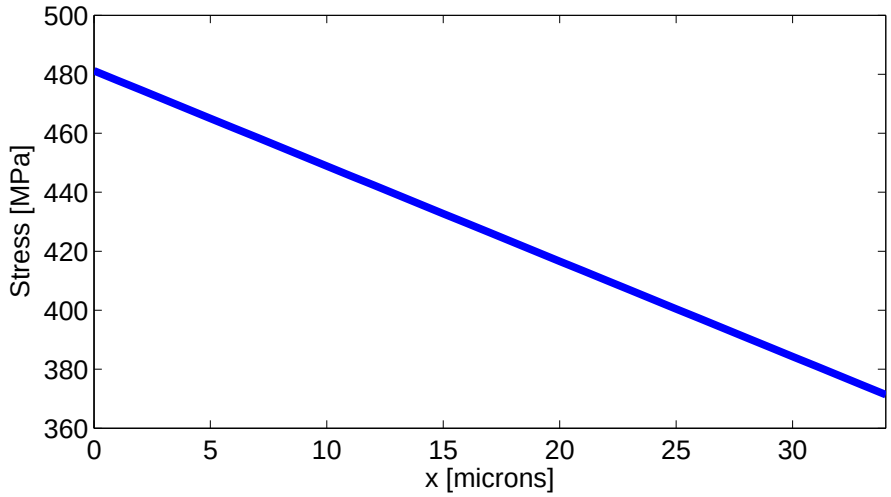

Figure 4.12: MultiMEMS design stress profile plot using Matlab file for out-of-plane acceleration.

These calculations are confirmed using FEA as explained in Chapter 5.

In total, four Wheatstone bridges comprising sixteen piezoresistors were implanted in regions of high stress on the beams. The length of the piezoresistors was 20 μm and the width used was 4 μm. The effective length of the sensing piezoresistors is in fact 8 μm due to a design rule that requires that the surface resistor overlaps the surface conductor connection by 6 μm.

When subject to a mechanical stress, the piezoresistors change electrical resistance due to the piezoresistive effect [6–8]. This delivers a constant voltage directly related to the position of the mass and changes when a motion offsets the mass. The magnitude of the resistivity change with stress depends on the doping level of the silicon, the crystal orientation and the temperature. Longitudinal and transversal piezoresistors are connected in such a way that the Wheatstone bridges can identify

and quantify the direction and magnitude of the acceleration. The piezoresistive coefficients for the surface piezoresistors are 5.7±0.6 and -5.3±0.6 ($10^{-10}Pa^{-1}$) for the longitudinal piezoresistive coefficient, π_L, and the transversal piezoresistive coefficient, π_T, respectively. This means that the resistance value increases for the longitudinal piezoresistors and decreases for the transversal shows how the piezoresistors are placed and connected.

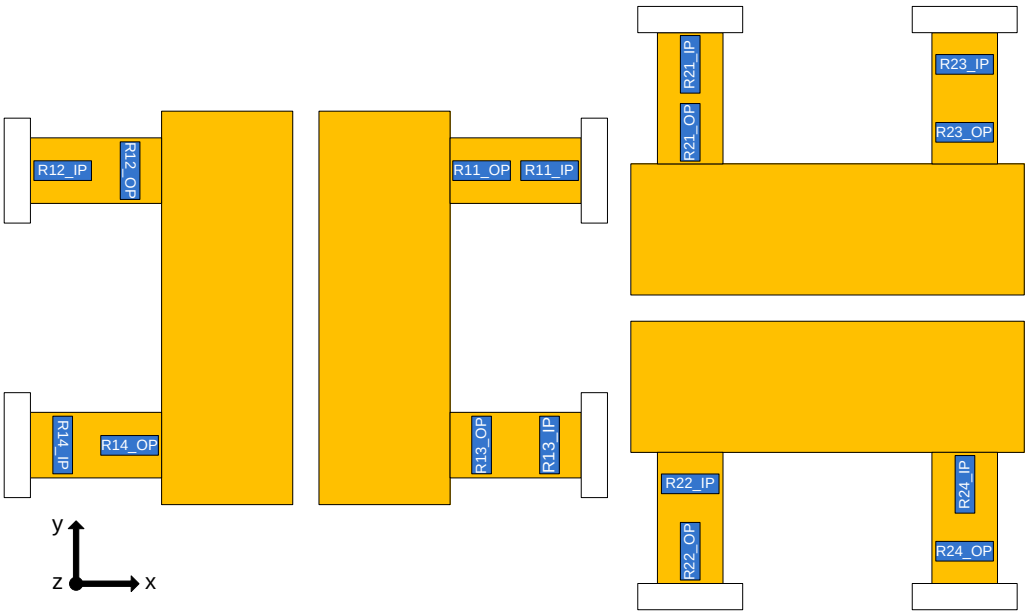

(a)

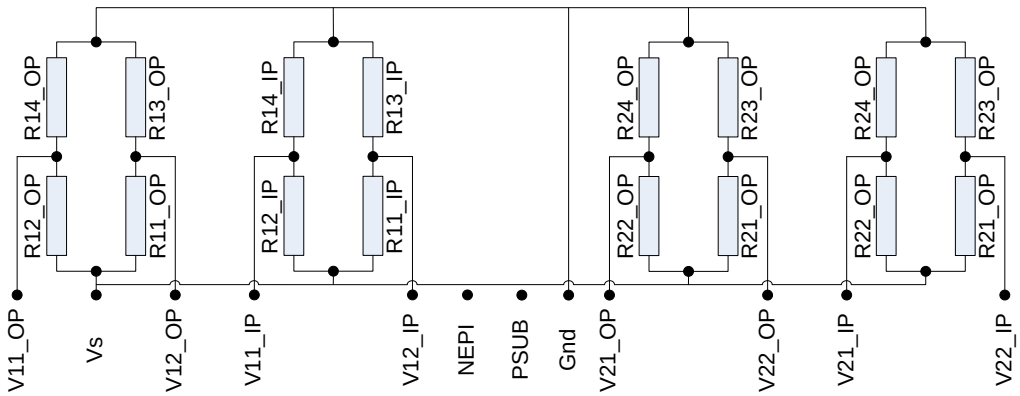

(b)

Figure 4.13: MultiMEMS design (a) piezoresistor placement, and (b) connection.

For each pair of masses the piezoresistors at the base of each beam are connected to form a Wheatstone bridge to sense in-plane accelerations. This is then repeated for

the other piezoresistors on each beam to sense out-of-plane accelerations.

In Figure 4.8 it is possible to see the behaviour of the masses when subjected to in-plane and out-of-plane accelerations. The effect that these mass deflections have on the individual piezoresistors is summarised in Table 4.2 for one pair of masses (refer to Figure 4.13).

	$R11_{IP}$	$R12_{IP}$	$R13_{IP}$	$R14_{IP}$	$R11_{OP}$	$R12_{OP}$	$R13_{OP}$	$R14_{OP}$
***x*-Axis Accel.**	-	+	+	-	-	-	+	+
***z*-Axis Accel.**	+	+	-	-	+	-	-	+

Table 4.2: MultiMEMS design resistance changes. Note that + represents an increase in resistance and - represents a decrease in resistance.

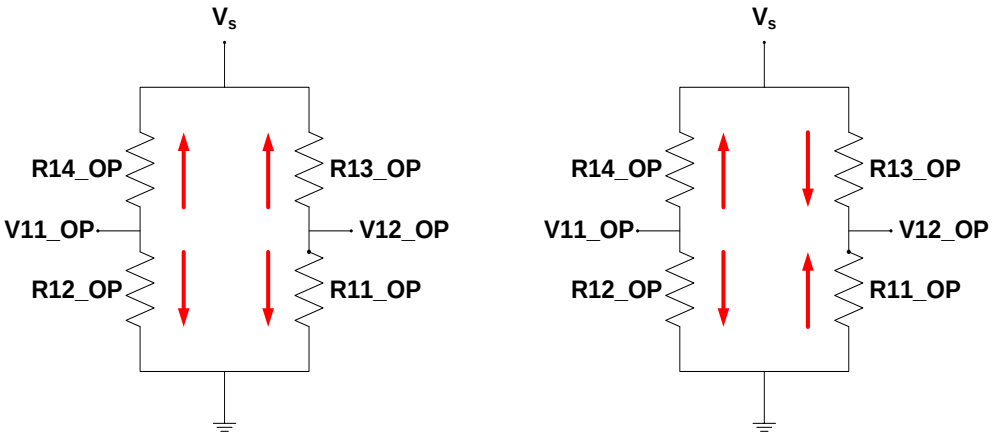

(a) (b)

Figure 4.14: Out-of-plane Wheatstone bridge behaviour for (a) in-plane acceleration, and (b) out-of-plane acceleration.

The theory presented in Section 4.4 is then applied to the setup in Figure 4.13(b). When considering the out-of-plane Wheatstone bridge on the left-hand side pair of masses in Figure 4.13(a), the behaviour of the individual piezoresistors can be seen in Figure 4.14.

When the out-of-plane Wheatstone bridge is subjected to in-plane accelerations the following changes in resistance, shown in Figure 4.14(a), are:

$$\begin{aligned} R11\_OP &= R - \Delta R = R\,(1-\delta) \\ R12\_OP &= R - \Delta R = R\,(1-\delta) \\ R13\_OP &= R + \Delta R = R\,(1+\delta) \\ R14\_OP &= R + \Delta R = R\,(1+\delta) \end{aligned}$$

so that:

$$V_{out} = 0$$

For out-of-plane accelerations, the following changes in resistance, shown in Figure 4.14(b), are:

$$\begin{aligned} R11\_OP &= R + \Delta R = R\,(1+\delta) \\ R12\_OP &= R - \Delta R = R\,(1-\delta) \\ R13\_OP &= R - \Delta R = R\,(1-\delta) \\ R14\_OP &= R + \Delta R = R\,(1+\delta) \end{aligned}$$

such that:

$$V_{out} = \delta V_s$$

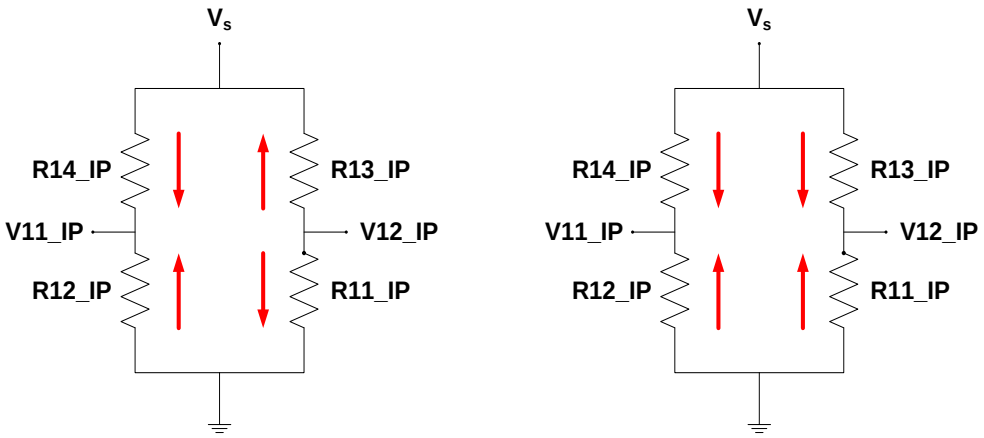

(a) (b)

Figure 4.15: In-plane Wheatstone bridge behaviour for (a) in-plane acceleration, and (b) out-of-plane acceleration.

For in-plane accelerations, shown in Figure 4.15(a), the following changes in resistance are found:

$$\begin{aligned} R11\_OP &= R - \Delta R = R\,(1-\delta) \\ R12\_OP &= R + \Delta R = R\,(1+\delta) \\ R13\_OP &= R + \Delta R = R\,(1+\delta) \\ R14\_OP &= R - \Delta R = R\,(1-\delta) \end{aligned}$$

which gives:

$$V_{out} = \delta V_s$$

For out-of-plane acceleration, shown in Figure 4.15(b), the resistance changes for the in-plane Wheatstone bridge are:

$$
\begin{aligned}
R11\_OP &= R + \Delta R = R\,(1+\delta) \\
R12\_OP &= R + \Delta R = R\,(1+\delta) \\
R13\_OP &= R - \Delta R = R\,(1-\delta) \\
R14\_OP &= R - \Delta R = R\,(1-\delta)
\end{aligned}
$$

which gives:

$$V_{out} = 0$$

This behaviour is mirrored for the other pair of masses except that the structures are sensitive to in-plane accelerations in the y-axis rather than the x-axis.

In addition to the design just discussed, another design was submitted as part of the MultiMEMS design evaluation. The purpose of this design was to increase the sensitivity of the beam-mass structures to in-plane accelerations. Beyond the diaphragm thickness of the epi-layer (3 μm) and the n-well (23 μm), the only other available thickness was the full wafer thickness of 400 μm. Using this thickness to form the seismic masses increased the centre of gravity to 138.06 μm as compared to 9.54 μm for the n-well.

For this to be possible it was necessary to incorporate corner compensation methods as a result of the faster rate of etching experienced at convex corners when using the TMAH etchant [9]. When etching rectangular convex corners, deformation of the edges occurs due to undercutting. Unlike concave corners, convex corners are not stable because higher order planes are exposed and etch rapidly, leading to rounding and eventually complete elimination of the convex corner. Corner compensation techniques have been developed to eliminate this effect and these typically involve adding masking features to the corners. The most common compensation masks are

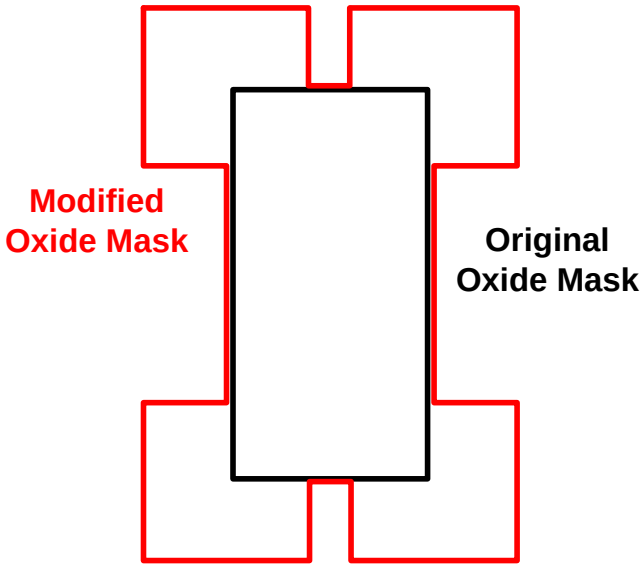

Figure 4.16: Modified oxide mask for full wafer thickness mass.

normally square and an example of this can be seen with reference to Figure 4.16.

To aid in the design of such compensation structures, a software program called Simode was used [10]. Unfortunately the outcome of the etching process did not match the simulations and the prototypes were unsuccessful due in part to the etchant used. A modified etchant recipe that had been developed by SensoNor was used for the etching process step. The age of the etchant was later called into question and it was hypothesised therefore that the characteristics of the etch did not match what was simulated for the process entered into the Simode program. In addition to this, the same etchant was used for both batches of wafers and therefore the performance of the etchant may have been compromised due to contaminants from the previous batch, ultimately resulting in the etchant characteristics being changed further. The final outcome was a batch of wafers under-etched as shown in Figure 4.17. Another batch was over-etched which is shown in Figure 4.18. As a result of this, this design was not pursued further.

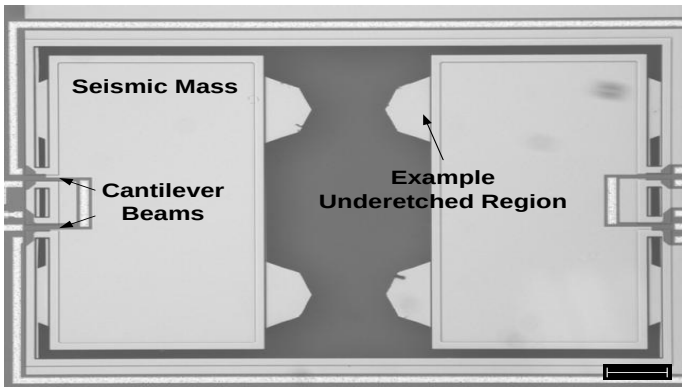

(a)

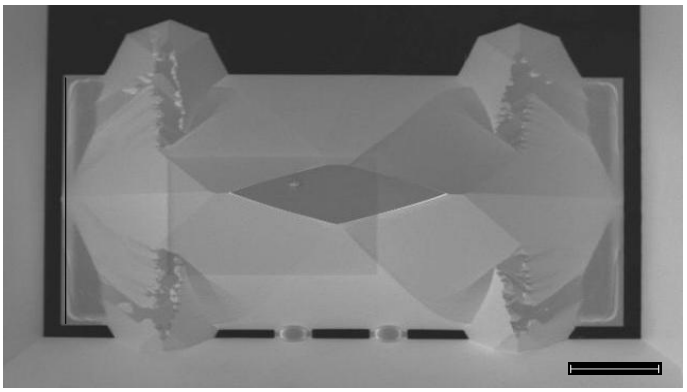

(b)

Figure 4.17: SEM images of the MultiMEMS design with underetched full wafer thickness masses as viewed from (a) above, and (b) below. Scale bars = 200 μm.

To provide a hermetic package, the fabricated chips were anodically bonded at wafer level. This results in a glass-silicon-glass stack with a thickness of 1.5 mm. On one side of the length of the chip, bond pads are exposed for future wirebonding to the outside world by removing the top glass cap in this area. A cavity in the bottom of the top glass was necessary to allow room for upwards vertical deflection of the acceleration-sensitive structures and this was achieved using an isotropic etch. This was not required in the bottom glass cap because the masses are only 23 μm thick and the bulk of the silicon onto which the glass caps are bonded is 400 μm thick.

(a)

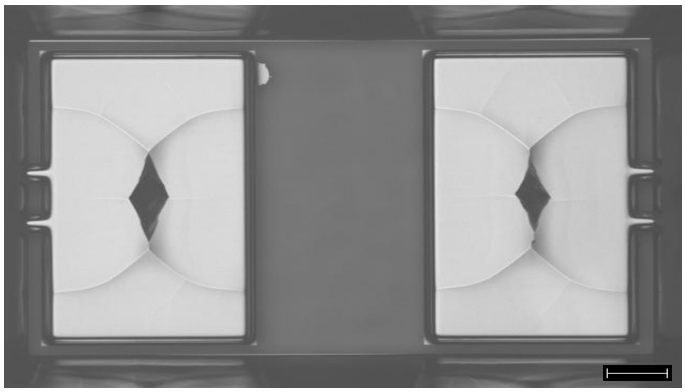

(b)

Figure 4.18: SEM images of the MultiMEMS design with overetched full wafer thickness masses as viewed from (a) above, and (b) below. Scale bars = 200 μm.

4.6 SMC sensor design

Following on from the MultiMEMS design, further designs were submitted with a view to improving the performance of the sensors to in-plane acceleration. As discussed previously, to do this, it was necessary to increase the value of the centre of gravity ($r0$) of the seismic masses. The simplest way of achieving this was to submit designs to a foundry process that had DRIE capability for the manufacture of seismic masses with near vertical sidewalls. This ultimately meant that the value of $r0$ increased to approximately half the thickness of the employed seismic mass i.e. $H_m/2$. In numerical terms this value become 192 μm compared to the value of 10.72 μm for the MultiMEMS design. In addition to this increase of sensitivity

to in-plane accelerations, seismic masses with a greater mass can be accommodated with a comparable footprint. This meant that a mass of $127{\times}10^3$ ng was achievable compared to $22{\times}10^3$ ng for the MultiMEMS design seismic masses.

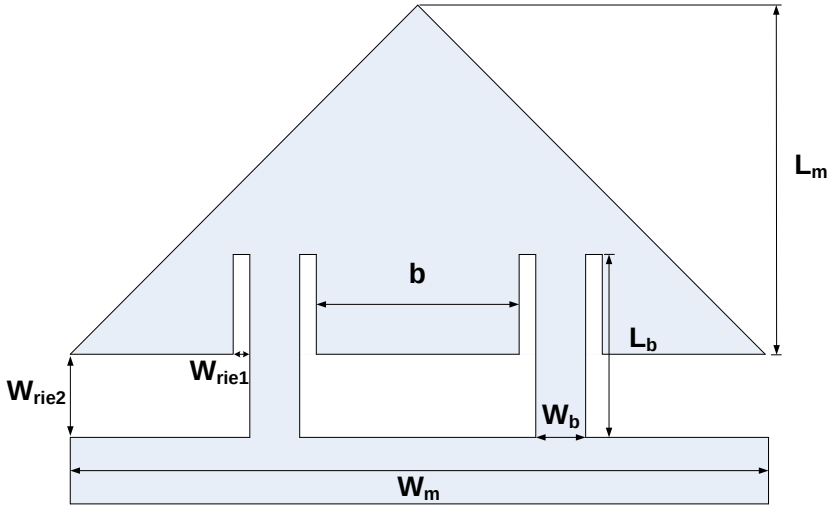

(a)

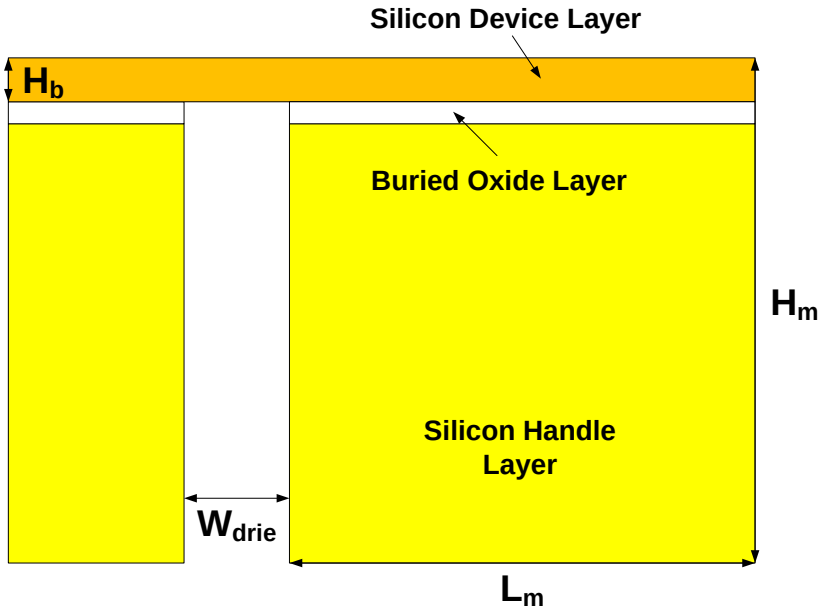

(b)

Figure 4.19: SMC Design 1 (a) top view, and (b) side view.

It was decided to use the foundry process offered by the Scottish Microelectronic Centre (SMC) in Edinburgh, Scotland. In total, four different designs were submitted for fabrication. Like the MultiMEMS design, each design consisted of four,

acceleration-sensitive, free-standing structures that are bulk micromachined. These structures have a thick seismic mass supported by either a single or two thin cantilever beams. Acceleration sensing was again achieved using piezoresistors implanted in the stress-sensitive cantilever beams. For the purposes of this thesis, the focus will be on one design and this will be referred to as "SMC Design 1" henceforth. A schematic view of this design can be seen in Figure 4.19.

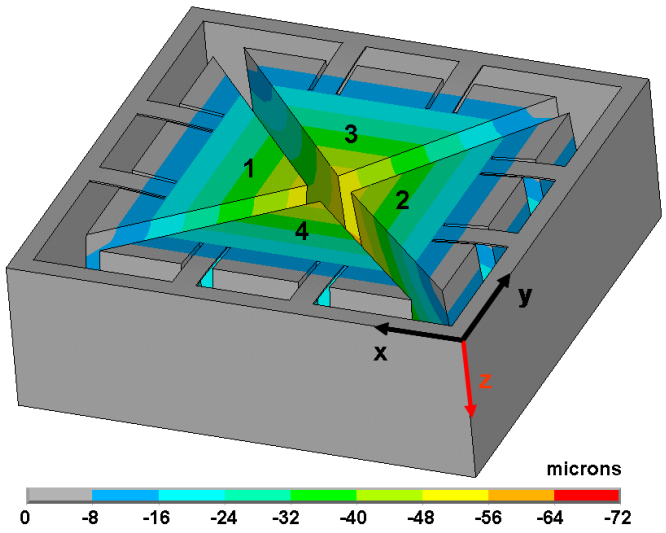

(a)

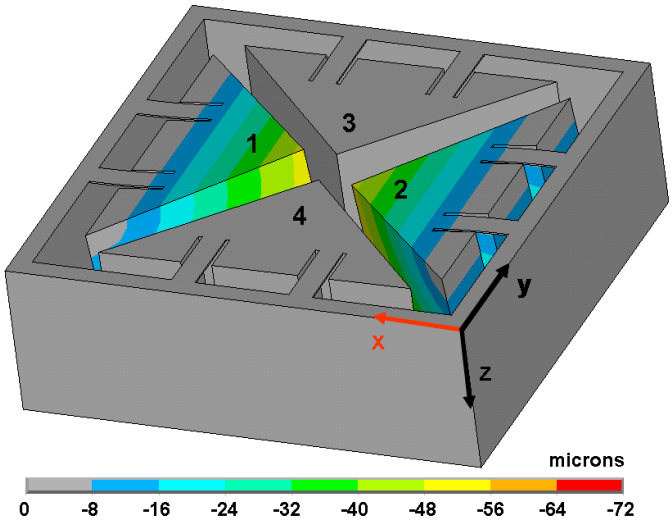

(b)

Figure 4.20: Simulation of the vertical displacement of the seismic masses of SMC Design 1 when subjected to (a) out-of-plane, and (b) in-plane accelerations.

As in the MultiMEMS design, the four beam-mass structures can essentially be

thought of as two dual-axis accelerometers positioned at 90° to one another. One pair of masses measures in-plane accelerations in one axis (the x-axis) and the other in-plane accelerations in the other axis (the y-axis) with both pairs capable of measuring out-of-plane accelerations (the z-axis). This behaviour can be seen in Figure 4.20 for design 1. For negative out-of-plane acceleration (z-axis) in Figure 4.20(a), all masses are displaced uniformly downwards. In Figure 4.20(b), masses 1 and 2 are displaced upwards and downwards respectively for positive in-plane acceleration (x-axis). In the same figure, masses 3 and 4 are not displaced and there is therefore negligible stress in the respective beams causing no change of voltage in that particular Wheatstone bridge. When considering in-plane acceleration in the positive y-axis, the behaviour of masses 1 and 2 is mirrored in masses 3 and 4, respectively.

Unlike the MultiMEMS design, the structures were machined from SOI wafers. As such, the thicknesses of the masses and beams was fixed by the choice of which SOI wafers to use for fabrication. The cantilever beams are defined by the silicon device layer which, for this process run, was 4 μm thick and the masses were defined by the 380 μm thick silicon handle layer. To etch these layers, an ICP etch was used. One of the benefits of using this process step in conjunction with SOI wafers is that the Buried OXide (BOX) layer of the SOI wafers can be used as an etch-stop from the front and backsides of the wafer. This removes the need for either additional process steps to provide an etch-stop mechanism or the uncertainties associated with a timed etch stop. The following process step was to ensure that the width of the opening in the mask for etching was the same all of the way round the masses and in the recesses for the beams to enable the best chance of a constant etch rate.

With the thicknesses of the cantilever beams (H_b) and seismic masses (H_m) fixed, the beam width (W_b) was made as narrow as possible according to design rules associated with the placement of the piezoresistors and the necessary electrical interconnect. The length of the beams (L_b) was also fixed so that it was possible to achieve matched mechanical sensitivity to in-plane and out-of-plane accelerations.

To make this theoretically achievable, the distance between the centre of the out-of-plane sensing piezoresistors and the lateral centre of gravity of the masses (y_{cg}) was required to be equal to the vertical centre of gravity for the mass ($y_{cg} = r0 = H_m/2 = 192\ \mu m$). For this to be possible and to reduce the overall footprint of the masses, the masses were wrapped around the supporting beams to bring y_{cg} closer to the base of the beams as shown in Figure 4.19(a).

The remaining critical dimensions of the sensor structures i.e. the width and length of the masses were then decided upon in conjunction with a process limited maximum stress of 500 MPa for 500 g of acceleration in any direction. The final dimensions for SMC Design 1 can be seen in Table 4.3. Note that this approach was repeated for each of the other designs and the dimensions of these can be seen in Appendix B.

Dimension	**Abbreviation**	**Value** (μm)
Length of the mass	L_m	400
Width of the mass	W_m	800
RIE around the masses	W_{rie2}	80
DRIE around the masses	W_{drie}	80
RIE along the length of the beams	W_{rie1}	10
Length of the beams	L_b	192
Width of the beams	W_b	60

Table 4.3: Structural dimensions for SMC Design 1. Refer to Figure 4.19.

The same approach was used for the electrical interconnect as with the MultiMEMS design. The only deviation was where the electrical interconnect crossed the bonding area for the top cap to reach the bond pad area. As discussed with the MultiMEMS design, buried conductors were employed to provide the planar surface necessary for the anodic bonding. Anodic bonding was not employed for this design approach so

the metal conductors continued out to the bond pad area.

Using the values in Table 4.3, the obtained values of stress for 500 g of in-plane and out-of-plane accelerations according to the analytical equations in Section 4.3 were 372 MPa and 436 MPa, respectively. The out-of-plane stress value is the maximum at the base of the beam i.e. $x = 0$. The centre of the out-of-plane sensing piezoresistor is actually located 30 μm along the beam from the base and the stress value here is calculated to be 377 MPa which is in close agreement with the in-plane stress value. The stress profile along the length of one of the beams for 500 g of out-of-plane acceleration can be seen in Figure 4.21. The respective Matlab files can be found in Appendix A.

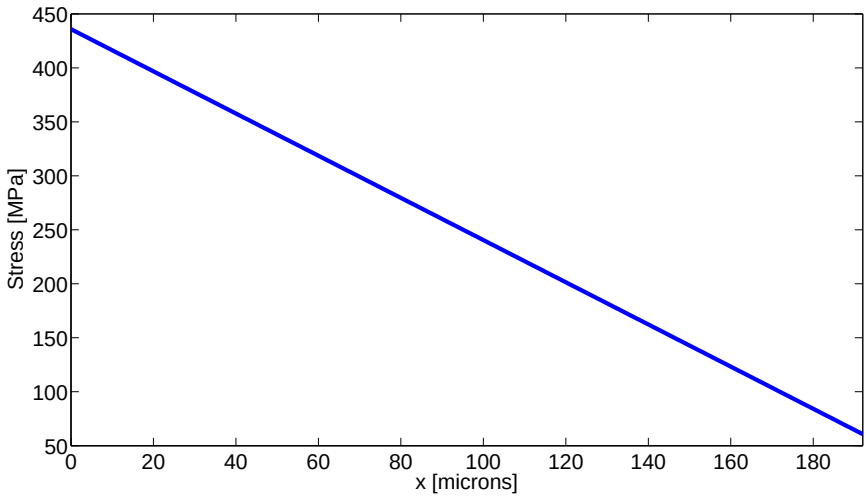

Figure 4.21: SMC Design 1 stress profile plot using Matlab file for out-of-plane acceleration.

These calculations are confirmed using FEA as explained in Chapter 5.

One point of interest from the other three designs that were submitted to SMC was that, in one of the designs ("SMC Design 2"), the rectangular beams that had normally been employed were replaced by tapered beams as shown in Figure 4.22. As discussed earlier with regards to the stress profile along the length of rectangular cantilever beams when subjected to out-of-plane acceleration, the stress reduces

linearly along the length of the beam with a maximum at the base of the beam. This is in contrast with the near constant stress profile along the length of the beam for in-plane acceleration. This linear behaviour of the stress makes the placement of the piezoresistors on the beams critical. To overcome this critical positioning of the piezoresistor, the width of the beam is narrowed from the base of the beam to negate the linear decrease in stress and the piezoresistor used to sense out-of-plane accelerations is positioned in this tapered region. The width of the beam is then increased again to join with a rectangular region. The width of this rectangular region is chosen so that when subjected to in-plane acceleration the resulting constant stress has a value equal to that in the tapered region for the same amount of out-of-plane acceleration. This is where the in-plane sensing piezoresistor is placed. The dimensions for the beam were decided upon using FEA described in Chapter 5.

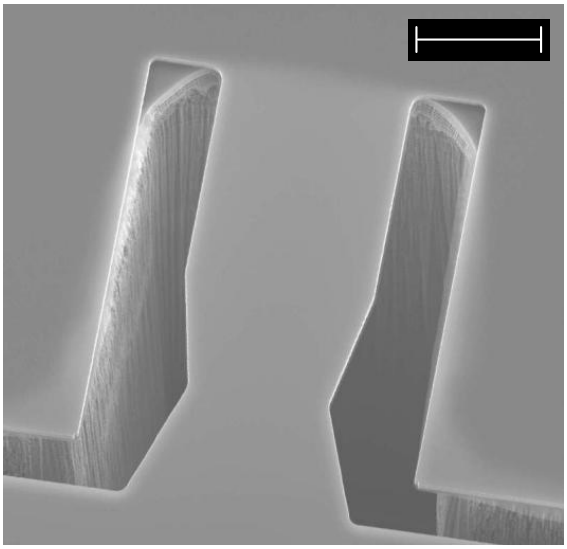

Figure 4.22: SEM top view of fabricated SMC Design 2 showing tapered beam. Scale bar = 50 μm.

In the MultiMEMS process, the chips were anodically bonded at wafer-level which lends itself to a dicing process step. Because packaging was not going to take place at wafer-level for this design, it was necessary to decide upon a technique to singulate the chips from the wafer for packaging at chip-level. Without capping, the fragile structures would be left exposed to contamination and damaging vibrations. The

solution was to use the backside and front side etching steps to define two tabs on one of the edges of the chip that were left to support each chip once the processing had been completed. The tabs were the thickness of the silicon device layer i.e. 4 μm and measured 20 μm in width and 80 μm in length. The dimensions were decided upon using a previous process run. Once the chips were ready to be packaged, individual chips were removed carefully from the wafer using a small amount of downward pressure on a safe part of the chip.

For packaging, the designs were packaged using glass caps bonded to the silicon using the adhesive BenzoCycloButene (BCB) as discussed in further detail in Section 6.3.4. This resulted in a glass-silicon-glass stack with a thickness of approximately 1.4 mm as shown in Figure 4.23. On the bottom, a glass cap that matches the size of the silicon chip is bonded whilst on the top side a smaller cap is bonded that does not cover the bondpad area. The thickness of the adhesive is enough to allow the masses to deflect sufficiently. It was decided to have a minimum bonding width of 300 μm and that the inner outline of this bonding area be no less than 300 μm from the outline of the released sensing structures. At the chip edge where the metal tracks were routed out to the bond pad area, the BCB ring is still complete so the adhesive bonds around and on top of the metal tracks have a thickness of approximately 1.5 μm.

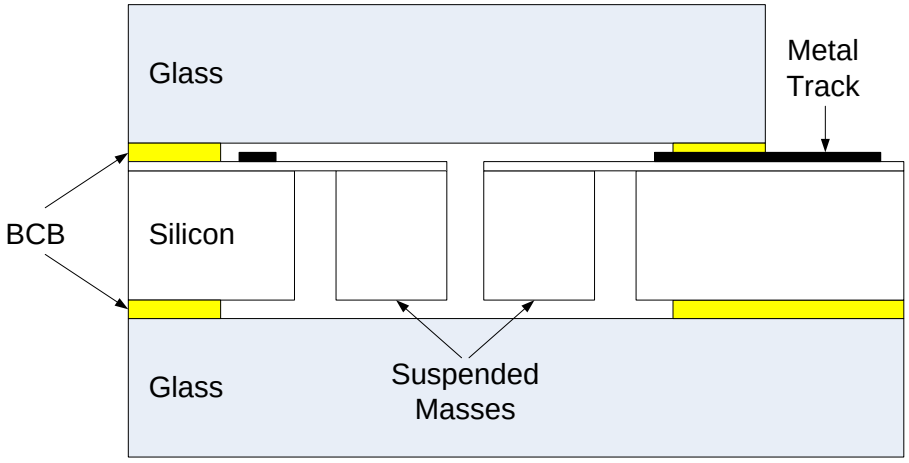

Figure 4.23: Cross-section of packaged SMC design.

In the bond pad area, two sets of bond pads were laid out. The larger set consisted of bond pads that measure 100 μm in width and were spaced 50 μm apart and were used for the purposes of wirebonding and characterisation. The other set measured 50 μm in width and were spaced 21 μm apart and were there to bond to a micro-ribbon cable for the sensors intended application as a heart sensor.

The resulting chip sizes are 3.5 mm in length, 2.5 mm in width and 1.4 mm in height. All of the designs were made to have the same chip size even though some designs could actually have been smaller. In terms of the width, the chips are too large compared to the specifications given in Chapter 2. However, it was agreed within the project team that these initial specifications were mainly just indicative of the size we should be trying to achieve.

4.7 Summary and conclusions

In this chapter, designs that were produced for fabrication using the MultiMEMS foundry process and the process at the Scottish Microelectronic Centre have been presented. Both designs use seismic masses supported by thin cantilever beams and piezoresistive sensing to convert accelerations into electrical output signals. The piezoresistors are placed onto the stress-sensitive beams and are interconnected into different Wheatstone bridges to measure and discriminate different accelerations in the three directions.

The primary difference between the designs is that the MultiMEMS design has 23 μm thick seismic masses resulting from a phosphorous diffusion step whilst the SMC process uses SOI wafers and a DRIE process step so that the 380 μm thick silicon handle layer of the wafers is used to define the masses. The resulting masses also have near vertical sidewalls. This helps to improve the overall sensitivity of the device and in particular sensitivity to in-plane accelerations.

It was attempted to partially overcome this drawback of the MultiMEMS process

by using the full wafer thickness to represent the masses but this introduced further design and fabrication problems and ultimately was not a success.

Additional features that were included in the SMC designs are: theoretical matching of mechanical sensitivity to in-plane and out-of-plane accelerations, tapered beams to compensate for the linear decrease of stress along the length of rectangular beams when subjected to out-of-plane accelerations, and packaging tabs used to remove the need for dicing and make the designs suitable for chip-level packaging.

References

[1] MultiMEMS website. `http://www.multimems.com/` (Accessed: 07 Oct 10).

[2] MultiMEMS. *MultiMEMS Design Handbook*. Third edition, 2003.

[3] The Scottish Microelectronics Centre website. `www.scotmicrocentre.co.uk` (Accessed: 07 Oct 10).

[4] Stephen D. Senturia. *Microsystem Design*. Springer-Verlag, first edition, 2000.

[5] W.C. Young. *Roark's Formulas for Stress and Strain*. McGraw-Hill Professional, seventh edition, 2001.

[6] C. Smith. Piezoresistance effect in germanium and silicon. *Phys. Rev.*, 94(1):42–49, Apr 1954.

[7] Y. Kanda. A graphical representation of the piezoresistance coefficient in silicon. *IEEE Trans. Electron Devices*, 29(1):64–70, Jan 1982.

[8] T. Toriyama and S. Sugiyama. Analysis of piezoresistance in p-type silicon for mechanical sensors. *J. Microelectromech. S.*, 11(5):598–604, 2002.

[9] K. Lian. Development and characterisation of anisotropic silicon etching for MEMS using TMAH. Master's thesis, Edinburgh University, 1999.

[10] Amtec Application Center for Microtechnologies Chemnitz GmbH. Simulation of orientation dependent etching (Simode) flyer. `http://www.amtec-chemnitz.de/fileadmin/user_upload/Simode2003.1.pdf` (Accessed: 07 Oct 10).

Chapter 5

ANSYS Simulation of a Micromachined Three-Axis Accelerometer

5.1 Introduction

The primary objective of FEA is to examine how a structure responds to certain loading conditions. Using FEA with computer software allows a designer to verify the model of a system through simulation rather than experimentation. This has obvious benefits in that money and time is saved by avoiding unnecessary failures of submitted designs through a deeper understanding of the behaviour of the device. This can also be applied to design optimisation and thus help in producing more reliable, better quality components.

The software package used during this design phase was from ANSYS, Inc. [1]. The software is a general purpose Finite Element Modelling (FEM) package for numerically solving a wide variety of mechanical problems. These problems include: static/dynamic structural analysis (both linear and non-linear), heat transfer and fluid problems, as well as acoustic and electromagnetic problems.

In general, a finite element solution may be broken into the following three stages:

1. Preprocessing. In this stage the problem is defined and follows the major steps outlined below:
   (a) Definition of the keypoints/lines/areas/volumes.
   (b) Definition of the element types and material/geometric properties.

(c) Definition of the mesh lines/areas/volumes as required.

2. Solution. Here the solvers are defined and applied.

3. Postprocessing. The results from the previous stage can be processed to present the following results in different ways:

   (a) Lists of nodal displacements.

   (b) Element forces and moments.

   (c) Deflection plots.

   (d) Stress contour diagrams.

This technique approximates the differential equations governing a continuous system with a set of algebraic equations related to a finite number of variables. To do this, the device to be modelled is divided up into small discrete regions known as finite elements. These elements are defined by nodes and interpolation functions. Governing equations are written for each element and these elements are assembled into a global matrix. Loads and constraints are applied and the solution is then determined. A major decision to be made is how small the elements must be before the solution can be trusted. There is no real firm answer to this and it is often necessary to conduct convergence tests. The finer the mesh is, the more accurate the results are but the more calculational time and computational memory is then required.

With ANSYS, several processors are available. A processor is defined in ANSYS as a set of functions that perform a specific analysis task. For example, the model is built in the general preprocessor (PREP7); in the solution processor (SOLUTION) the loads are applied and the solution obtained. In the general postprocessor (POST1), the results of a solution are evaluated. An additional postprocessor, POST26, enables the time evolution of results at specific points in the model.

In the ANSYS family of products, seven types of structural analyses are available:

1. Static analysis is used to determine linear and non-linear displacements, stresses, etc. under static loading conditions. Non-linearities can include plasticity, stress stiffening, large deflection, large strain, hyperelasticity, contact surfaces and creep.

2. Modal Analysis is used to calculate the natural frequencies and mode shapes of a structure. Different mode extraction methods are available. A modal analysis can also serve as a starting point for another, more detailed, dynamic analysis, such as a transient dynamic analysis, a harmonic response analysis, or a spectrum analysis.

3. Harmonic analysis is used to determine the response of a structure to harmonically time-varying loads. Any sustained cyclic load will produce a sustained cyclic response (a harmonic response) in a structural system. This enables verification of whether or not a design will successfully overcome resonance, fatigue and other harmful effects of forced vibrations.

4. Transient dynamic analysis is used to determine the response of a structure to arbitrarily time-varying loads. All non-linearities mentioned under the static analysis section can be simulated.

5. Spectrum analysis is an extension of the modal analysis which is used to calculate stresses and strains due to a response spectrum or a Power Spectral Density (PSD) input (random vibrations).

6. Buckling analysis is used to calculate the buckling loads and determine the buckling mode shape. Both linear buckling and non-linear buckling analyses are possible.

7. Explicit dynamic analysis is used to calculate fast solutions for large deformation dynamics and complex contact problems.

5.2 Building an ANSYS model

ANSYS can be used with its Graphical User Interface (GUI) or by using the ANSYS Parametric Design Language (APDL). The latter involves typing the commands for your simulation directly into a text file. This approach was implemented in this work and will be introduced here.

The steps necessary to build, analyse, and review results from the MultiMEMS design are introduced in the following sections. This approach is also suitable for and is very similar to the SMC design except that the dimensions have to be changed in accordance with the device dimensions and mass profile. The complete code listing for the MultiMEMS design as well as the SMC Design 1 can be seen in Appendix C.

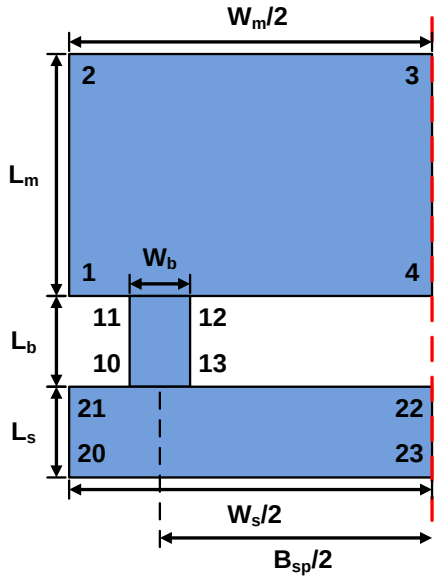

Figure 5.1: Keypoint placement and positioning for half of the MultiMEMS structure.

Geometry

Firstly, the PREP7 preprocessor is used to define the model geometry. At this stage the program does not assume a system of units for the analysis. Except in magnetic

field analyses, any system of units can be used so long as they are consistent for all the data entered. The dimensions for the MultiMEMS design can be seen in Table 5.1.

To build the model from the bottom up, the starting point is to define the lowest-order solid model entities which are the keypoints. From here it is then possible to define lines, areas, and volumes connecting these keypoints. Keypoints are the vertices, lines are the edges, areas are the faces, and volumes are the interior of the object.

Nomenclature	**Abbreviation**	**Value** (μm)
Length of the mass	L_m	230
Width of the mass	W_m	2050
Length of the beam	L_b	34
Width of the beam	W_b	44
Thickness of the epi layer	H_{epi}	3
Thickness of the beam	H_b	Equal to H_{epi}
Thickness of the nwell	H_{nwell}	20
Distance between the near edges of two beams	B_{sp}	1762
Length of the mass support	L_s	50
Width of the mass support	W_s	Equal to W_m
Thickness of the mass support	H_s	50
Lateral displacement of the mass	LD_{nwell}	25.6

Table 5.1: Naming convention and associated values for the ANSYS MultiMEMS structure.

From the dimensions in Table 5.1, the keypoints are defined that represent one half of the structure in 2-D. The keypoint 'syntax' is **K** and the use of this is demonstrated in the following piece of script. Within this command the x, y and z coordinates of

the keypoint are defined. The following code is suitable to define the keypoints of Figure 5.1 with the origin at keypoint number 22:

```
!***Half Mass (LHS)
K,1,-Wm/2,Lb,0
K,2,-Wm/2,Lb+Lm,0
K,3,0,Lb+Lm,0
K,4,0,Lb,0
!***Single Beam (LHS)
K,10,-Bsp/2-Wb,0,0
K,11,-Bsp/2-Wb,Lb,0
K,12,-Bsp/2,Lb,0
K,13,-Bsp/2,0,0
!***Half Support (LHS)
K,20,-Wm/2,-Ls,0
K,21,-Wm/2,0,0
K,22,0,0,0
K,23,0,-Ls,0
```

Having defined the keypoints, the areas then have to be defined using the **A** command.

```
!***Half Mass (LHS)
A,  1,2,3,4
!***Single Beam (LHS)
A,  10,11,12,13
!***Half Support (LHS)
A,  20,21,22,23
ARSYM, X, ALL, 0, 0, 0
AADD,1,4
AADD,3,6
```

Then, to have a complete geometry the **ARSYM** command is used to mirror the previously declared areas.

Volumes

To complete the geometry, the areas have to be extruded to make volumes using the **VEXT** command. The resulting volume can be seen in Figure 5.2.

```
!***Extrude Epi Layer of Mass
VEXT, 7,,,,,-Hb
!***Extrude Epi Layer of Beams
VEXT, 2,5,3,,,-Hb
!***Extrude Support
VEXT, 1,,,,,-Hs
!***Extrude n-Well Mass Below Epi Layer
VEXT, 3, 0, , -Ldnwell, Ldnwell, -Hnwell
VEXT, 3, 0, , -Ldnwell, -Ldnwell, -Hnwell
VEXT, 3, 0, , Ldnwell, -Ldnwell, -Hnwell
VEXT, 3, 0, , -Ldnwell, Ldnwell, -Hnwell
VINV, 5, 6, 7,8
AADD, 27,28
AADD, 24,25
AADD, 10,11
AADD, 6,8
AADD, 57,59,60
AADD, 34,62
VADD,1,9
VGLUE,ALL
```

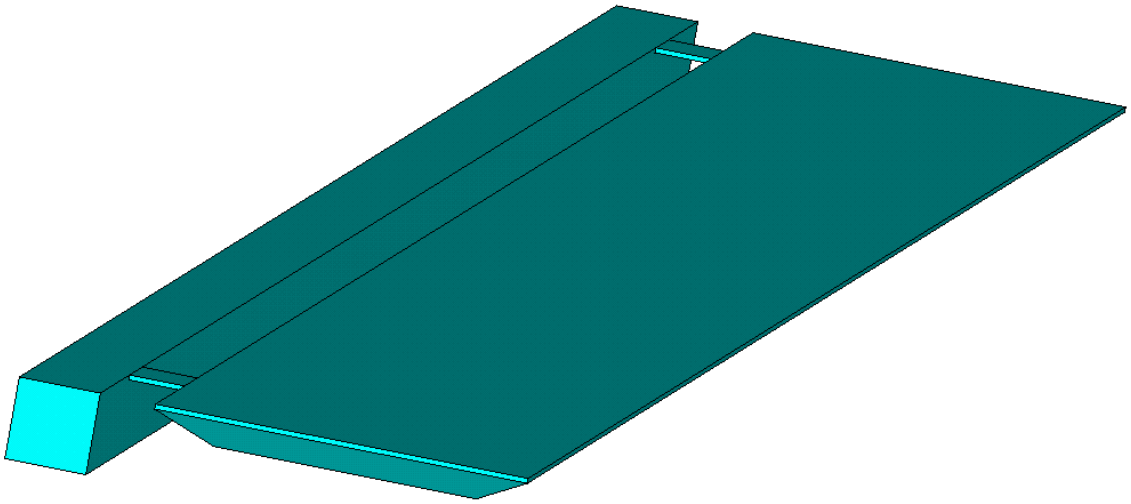

Figure 5.2: Resulting volume created for the MultiMEMS structure.

Here, it is possible to issue the **VSEL** command to select the mass volume and then issue the **VSUM** command to calculate and print the geometry of the selected volume which can then be compared with the analytical calculations using Equations 4.20 and 4.21. Before doing this it is necessary to issue the **VATT** command so that element attributes can be applied to selected, unmeshed volumes.

```
VATT,1
/OUTPUT,massdata,txt
VSUM,FINE
```

The final step for the generation of the geometry is to join all of the volumes using the **VGLUE** command. When the loads are applied to the structure, this command ensures that the volumes behave like a complete structure that is constrained properly.

Material properties

Having defined the geometry, the material properties are assigned to this volume for subsequent analyses. Care has to be taken to ensure that the units used here

coincide with those chosen for the geometric dimensions.

```
ET,1,SOLID92
VATT,1,,1,0
MP,DENS,1,2.33E-15
MP,EX,1,169E9*1E-6
MP,PRXY,1,0.3
```

To begin with, a local element type from the element library is chosen. This is done by issuing the **ET** command. The ANSYS element library contains more than 150 different element types. The element type determines, among other things:

- The set degree-of-freedom which in turn implies the discipline - structural, thermal, magnetic, electric, etc.
- Whether the element lies in 2-D or 3-D space.

The element type that is used for this model is SOLID92. This element type is a 3-D 10-Node Tetrahedral Structural Solid which has a quadratic displacement behavior and is well suited to model irregular meshes.

Next, the necessary material properties are assigned to the element. Depending on the application, material properties can be linear or non-linear. As with the element types, each set of material properties has a material reference number. The table of material reference numbers versus material property sets is called the material table. Within one analysis, multiple material property sets can co-exist which correspond to multiple materials used in the model. ANSYS identifies each set with a unique reference number.

The material properties are defined using the **MP** command. The following properties are defined by changing the **Lab** field of this command:

- *DENS* to define the mass density.
- *EX* to define the elastic moduli.
- *PRXY* to define major Poisson's ratio.

Meshing

For this structure, the volume of the mass is first selected and the **SMRTSIZE** command is issued to specify the meshing parameters for an automatic element sizing. The volumes that make up the rest of the structure, i.e. the support and the cantilever beams, are then selected and different parameters are then applied to these.

```
VSEL,S,LOC,Y,Lb,Lb+Lm
SMRTSIZE,10
VMESH,ALL
VSEL,NONE
ALLSEL,ALL
VSEL,S,LOC,Y,-Ls,Lb
SMRTSIZE,5
VMESH,ALL
VSEL,NONE
ALLSEL,ALL
ASEL,S,LOC,X,-Bsp/2-Wb/2,-Bsp/2+Wb/2
ASEL,A,LOC,X,Bsp/2-Wb/2,Bsp/2+Wb/2
AREFINE,ALL,,,1
ALLSEL,ALL
```

The mesh on the cantilever beams is then locally refined by issuing the **AREFINE** command and by selecting all of the areas associated with the beams. The parameters for each of these steps are decided upon using common sense, prior knowledge,

and a balance of computing time versus simulation accuracy. The resulting meshed volume can be seen in Figure 5.3.

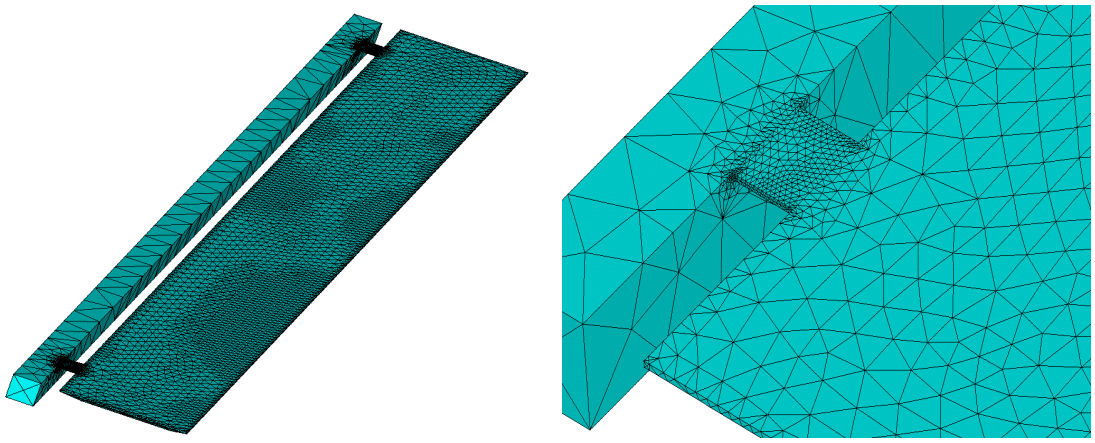

(a) (b)

Figure 5.3: (a) Resulting meshed volume for the entire structure, and (b) close-up of a meshed beam for the MultiMEMS Design.

Applying loads

The PREP7 preprocessor is also used to apply the loads. The term loads encompasses boundary conditions such as constraints, supports, or boundary field specifications as well as other externally and internally applied loads.

Before applying loads, the geometry needs to be constrained on the support. This is done by using the **DA** command.

```
ASEL, NONE
ASEL, ALL
ASEL, S, LOC, Y, -Ls,
DA,ALL,ALL,0
```

In our case, an out-of-plane acceleration of 2000 g is to be applied since the design rules state that our device should not exceed 500 MPa under 2000 g of acceleration in any direction. For this design, the most sensitive direction to acceleration is

the out-of-plane direction hence the structure is analysed for accelerations in this direction. To apply accelerations to the structure, the value of g is defined with the appropriate units and the fields for the value of accelerations in the x, y, and z axes are also defined. The linear acceleration is then applied by issuing the **ACEL** command.

```
G=9.80665E6
AX=0*G
AY=0*G
AZ=2000*G
ACEL,AX,AY,AZ
```

Obtaining a solution

The SOLUTION processor is used to define the analysis type, analysis options and to initiate the finite element solution. The analysis type, **ANTYPE**, is chosen based on the loading conditions and the response to calculate. Static, modal, and harmonic analyses are performed in this design phase. The second field is *0* for a static analysis, *2* for a modal analysis, and *3* for a harmonic analysis.

```
/SOLU
ANTYPE,0
SOLVE
FINISH
SAVE
```

When performing a modal analysis, the **MODOPT** command is used to specify the modal analysis options. The second field, **LANB**, states that the Block Lanczos method is to be used and that the first four significant modes are considered by making the third field equal to *4*. This method is used as it is the recommended

method for large symmetric eigenvalue problems whilst having shorter run times with equivalent accuracy compared to other available methods.

```
/SOLU
ANTYPE,2
MODOPT,LANB,4
SOLVE
FINISH
SAVE
```

Lastly, a harmonic analysis is performed. With knowledge gained from the modal analysis it is possible to define a frequency range using the **HARFRQ** command and lastly the number of sub steps to be taken for the analysis using the **NSUBST** command. The **SOLVE** command is then issued to obtain the solution.

```
/SOLU
ANTYPE,3
HARFRQ,7000,7250
NSUBST,1000
SOLVE
FINISH
SAVE
```

Reviewing the results

Once the solution has been obtained the ANSYS postprocessors are implemented to review the results. As soon as the desired results data are stored in the database, it is possible to review them through graphics displays and tabular listings using these postprocessors.

The /**POST1** command is issued to enter the database results postprocessor. From here it is possible to plot the displaced structure by issuing the **PLDISP** command.

The **PLNSOL** command is used to display the results as continuous contours. The structural displacement can be viewed in this manner by entering *U* in the second field of this command whilst the stress can be viewed by entering *S*.

At this point it is possible to produce graphics and animated sequences which can be saved to a file for later consideration.

In addition, it is possible to define paths to enable data such as stress along the length of a cantilever beam to be plotted using the command sequence shown below.

```
/POST1
PATH,beamlength,2,,Lb
PPATH,1,,-Bsp/2-Wb/2,0
PPATH,2,,-Bsp/2-Wb/2,Lb
PDEF,stressy,S,Y
PLPATH,stressy
```

The resulting data and images are presented in the following sections for the MultiMEMS Design and for SMC Design 1. In addition the stress profile along the tapered beams of SMC Design 2 is presented to demonstrate the suitability of the approach of this type of beam for the creation of constant stress along the beam.

5.3 MultiMEMS sensor simulation

5.3.1 MultiMEMS Design static results

Displacement results

The displacement of the structure when submitted to 2000 *g* of out-of-plane acceleration can be seen in Figure 5.4. This displacement profile is of importance in packaging as the cavity of the package must be deep enough to avoid any contact

between the mass and the inner surface of the cavity. In the MultiMEMS process the depth for the optional cavities above and below the suspended structures was 250 μm. Therefore we can see that even when subjected to shocks of 2000 g of acceleration there will be no contact between the masses and the packaging caps. Consideration of displacement at resonance frequency was not carried out due to the fact that the intending operation of the sensor is less than 40 Hz and first resonance for this design is shown later to be 7 kHz.

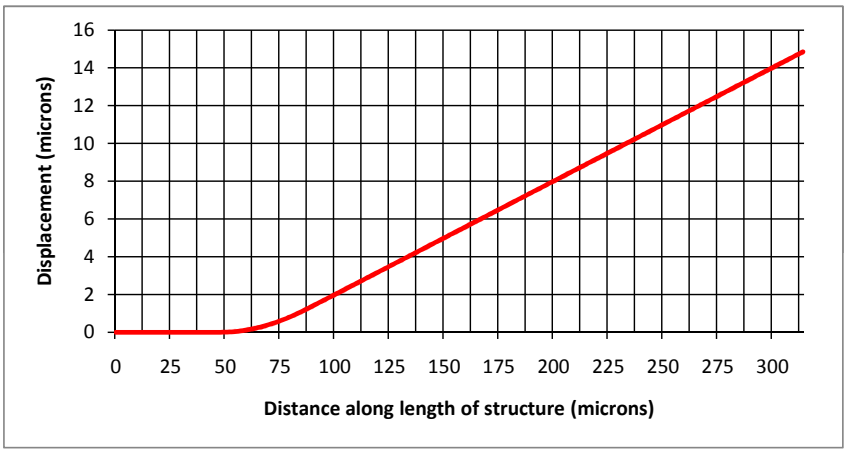

Figure 5.4: Displacement profile following the top surface and along the length of one of the structures of MultiMEMS Design for 2000 g of out-of-plane acceleration.

Stress analysis results

The results from the static analysis can be plotted as continuous contours using the **PLNSOL,S,Y** command. The resulting plot when the structure is subjected to 2000 g can be seen in Figure 5.5 for out-of-plane and in-plane accelerations.

Next, the start point and end point of a 2-D line is defined using the **PPATH** command. The line, which is referred to as a path, follows the centre of one of the beams and along its top surface. The values of stress following the length of the beam are then interpolated along this path using the **PDEF** command and the result is then plotted for out-of-plane and in-plane accelerations using the **PLPATH** command. The results from this are shown in Figures 5.6(a) and 5.6(b), respectively.

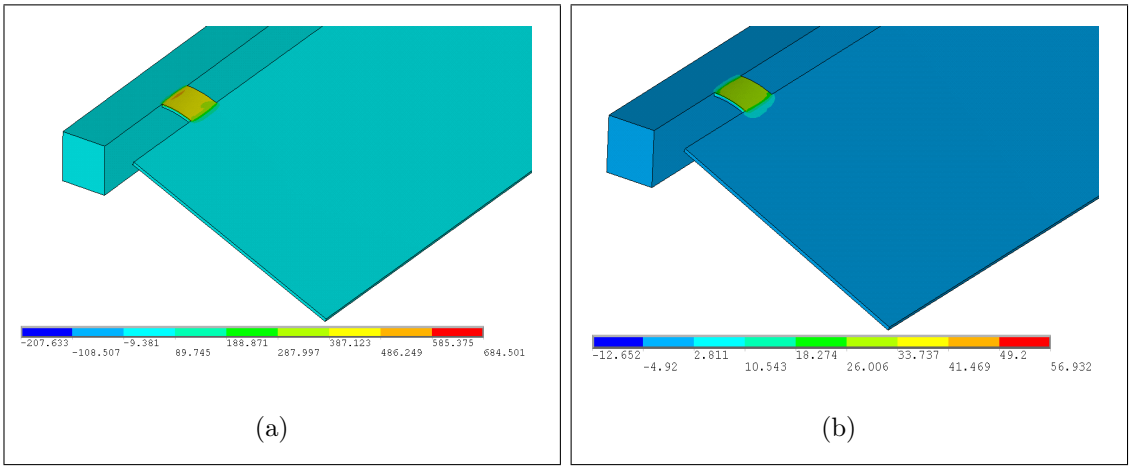

Figure 5.5: Resulting stress contour plot for the MultiMEMS Design as a result of 2000 g of (a) out-of-plane acceleration, and (b) in-plane acceleration.

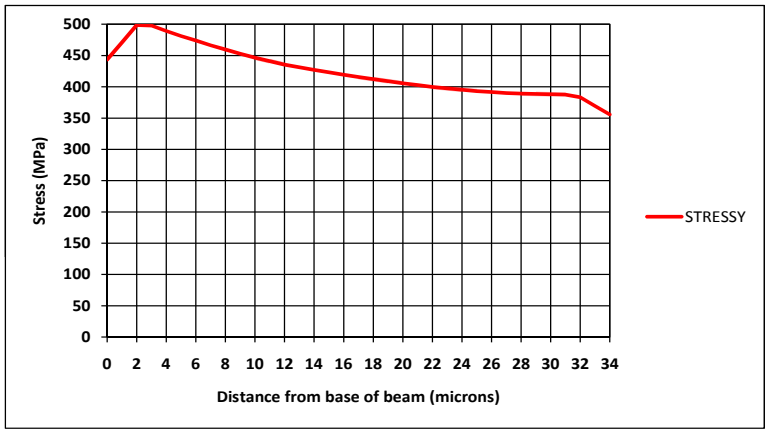

(a)

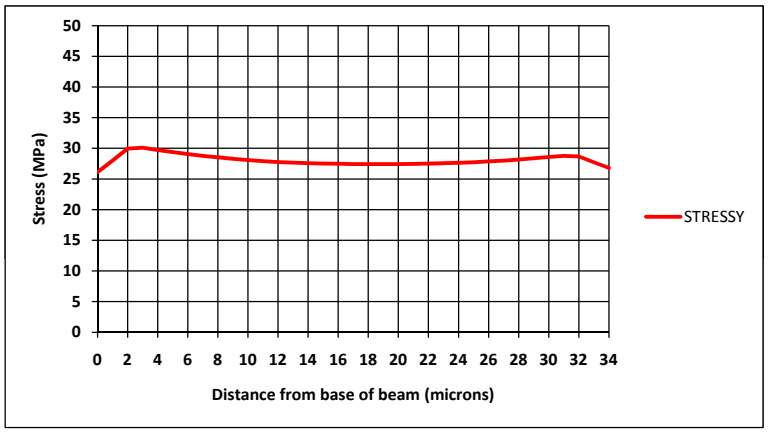

(b)

Figure 5.6: Resulting stress profile following the length of one of the beams for the MultiMEMS Design as a result of 2000 g of (a) out-of-plane acceleration, and (b) in-plane acceleration.

These results together with the analytical results obtained in Chapter 4 are plotted together in Figure 5.7, which allows us to see the deviation between the two plots particularly near the base of the beam. This discrepancy is due to the first-order approximation of the analytical approach. A linear data fit of the FEA results shows that the previous two plots are in close accordance with one another. A goodness of fit is used to summarise the discrepancy between the observed values from ANSYS and the values from the analytical approach [2]. The goodness of fit values are calculated to be 0.999 for Figure 5.7(a) and 0.996 for Figure 5.7(b).

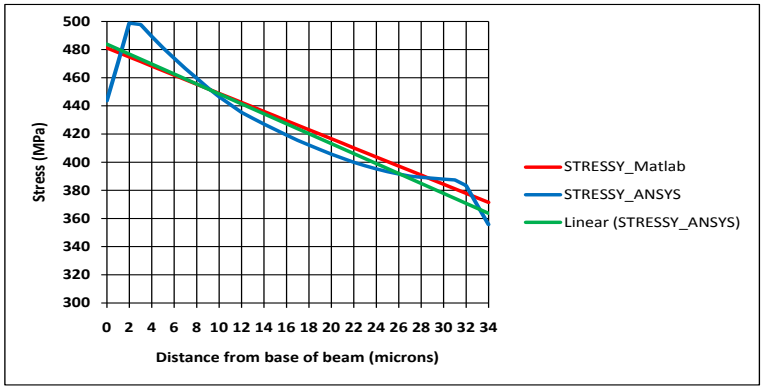

(a)

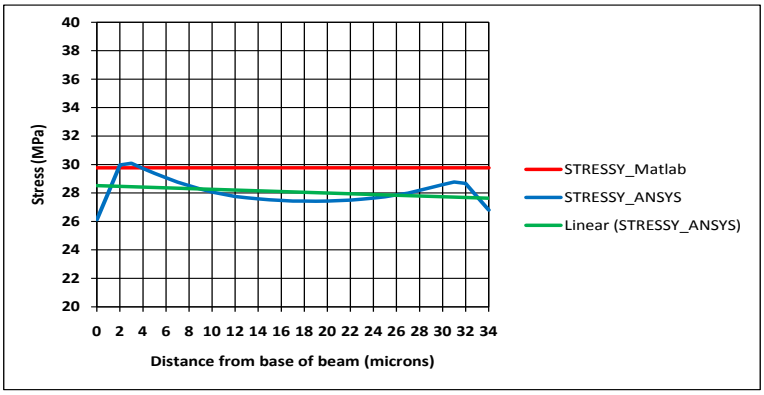

(b)

Figure 5.7: Comparison of the resulting stress profile following the length of one of the beams for the analytical results and the simulated results for the MultiMEMS Design as a result of 2000 g of (a) out-of-plane acceleration, and (b) in-plane acceleration.

Stress values obtained using ANSYS simulations and analytical calculations are compared in Table 5.2. The stress value at the centre of the sensing piezoresistor

located 30 μm from the base of the beam is also quoted. The stress values show a good agreement.

Measurand	**FEA value** (MPa)	**FEA linear fit value** (MPa)	**Analytical value** (MPa)
Out-of-plane stress	481	500	499
Out-of-plane stress at piezoresistor	397	391	392
In-plane stress	29	29	30

Table 5.2: Stress values obtained from simulated and analytical approaches for the MultiMEMS Design.

5.3.2 MultiMEMS Design modal results

Images obtained by the FEA for the first four modes are shown in Figure 5.8. The corresponding resonant frequencies are summarised in Table 5.3.

Mode	**Frequency** (kHz)
1st **Mode**	7.073
2nd **Mode**	44.882
3rd **Mode**	78.674
4th **Mode**	155.05

Table 5.3: Summary of modal frequency values obtained from ANSYS software simulations for the first four modes of the MultiMEMS Design.

The following equation is used to calculate the value of the first resonance frequency [3]:

$$\omega_n = \sqrt{\frac{EI\left(6f^2+6f+2\right)}{mL_b^3\left(8f^4+14f^3+\frac{21}{2}f^2+4f+\frac{2}{3}\right)}} \tag{5.1}$$

where E is Young's modulus, I is the moment of inertia of the cross-section of the beam given in Equation 4.3, m is the mass of the seismic mass and is given in Equation 4.21, L_b is the length of the cantilever beam and f is given by:

$$f = \frac{L_m}{2L_b} \tag{5.2}$$

where L_m is the length of the seismic mass. This equation produces a value of 7.095 kHz which is in close agreement with the value quoted for the 1^{st} mode in Table 5.3.

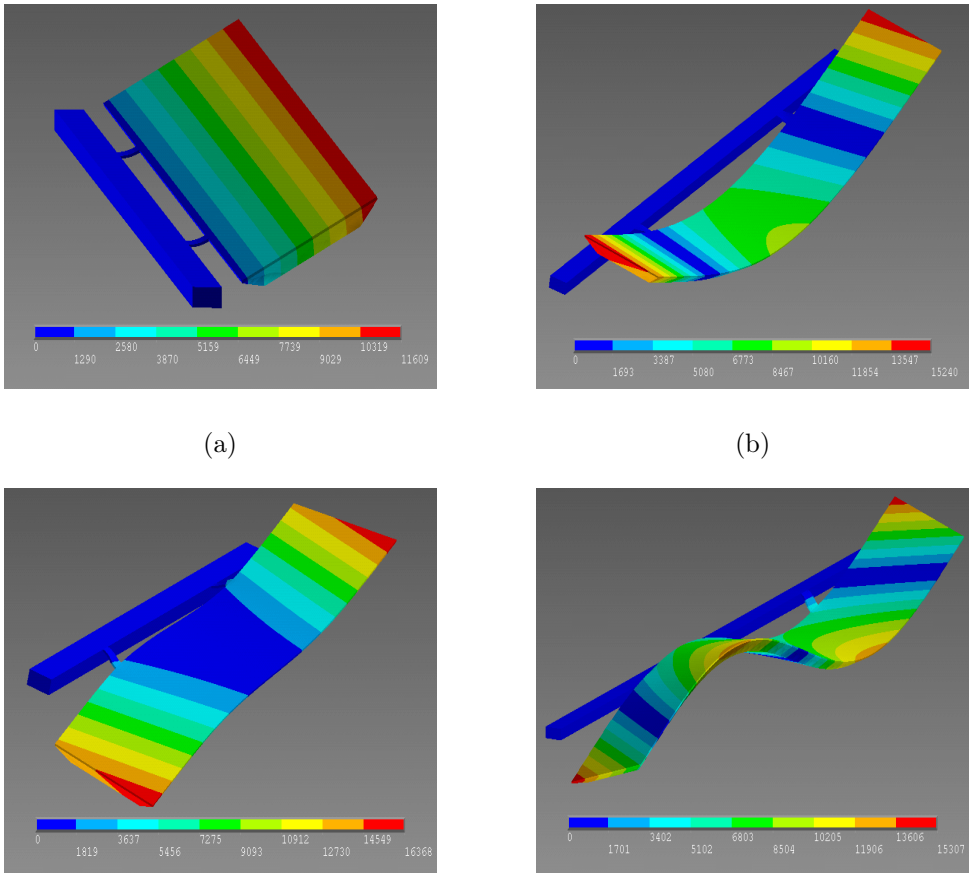

(a) (b)

(c) (d)

Figure 5.8: Resonant mode shapes for the MultiMEMS Design from ANSYS simulations: (a) 1^{st} mode at 7.073 kHz; (b) 2^{nd} mode at 44.882 kHz; (c) 3^{rd} mode at 78.674 kHz; (d) 4^{th} mode at 155.05 kHz.

5.3.3 MultiMEMS Design harmonic results

The resulting plot of the 1^{st} mode of the MultiMEMS Design structure using harmonic analysis can be seen in Figure 5.9.

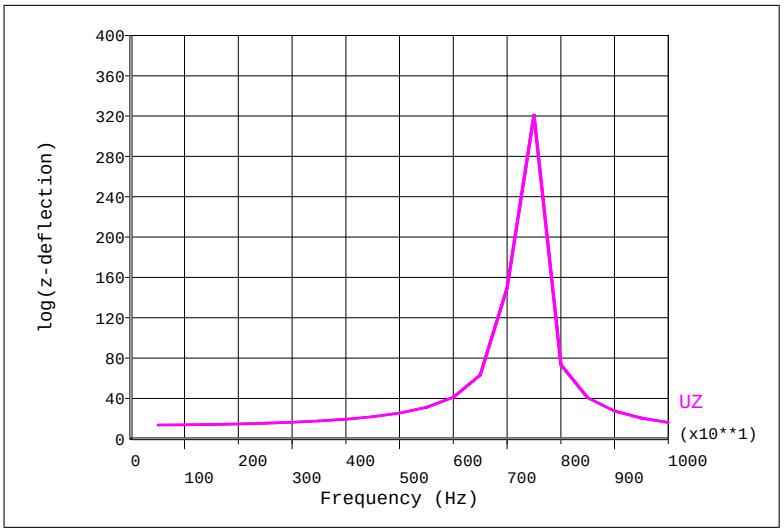

Figure 5.9: Harmonic result for the 1^{st} mode of the MultiMEMS Design.

The calculation of structure response, usually displacement, at several frequencies allows one to investigate identified "peak" responses on the resulting graph and review stresses at these peak frequencies. More detailed results can be obtained from this type of analysis by increasing the number of frequencies but this is very computationally intensive.

5.4 SMC sensor simulation

5.4.1 SMC Design 1 static results

Displacement results

The packaging caps used with these designs have no cavities. The result of this is that the gap that is allowed for the displacement of the suspended structures is restricted to the thickness of the adhesive for the packaging which is approximately 18 μm. The

displacement along the bottom of one of the masses is then simulated with increasing values of acceleration and it is found that this gap equates to approximately 150 g of out-of-plane acceleration as shown in Figure 5.10. From the simulations it is deemed that this gap is sufficient for normal operation of the devices.

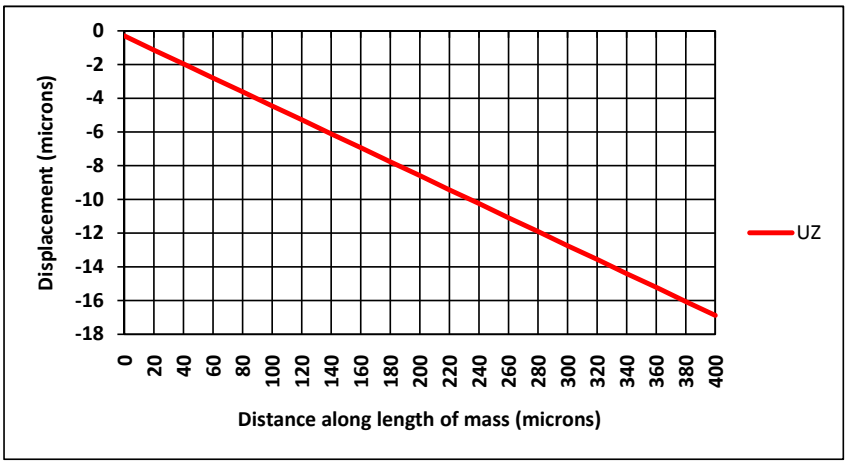

Figure 5.10: Displacement profile along the length of the bottom of one of the masses of SMC Design 1 for 150 g of out-of-plane acceleration.

Stress analysis results

For the purposes of processing and handling unpackaged devices, it is necessary to analyse the stress experienced by the structure when subjected to 500 g of out-of-plane and in-plane accelerations. The results from this can be seen in Figure 5.11.

Next, a path is defined that follows the length of one of the beams. A labeled path item is then interpolated along the path and the result is plotted onto a graph. The displacement of the structure can be seen for 500 g of out-of-plane and in-plane accelerations in Figures 5.12(a) and 5.12(b), respectively.

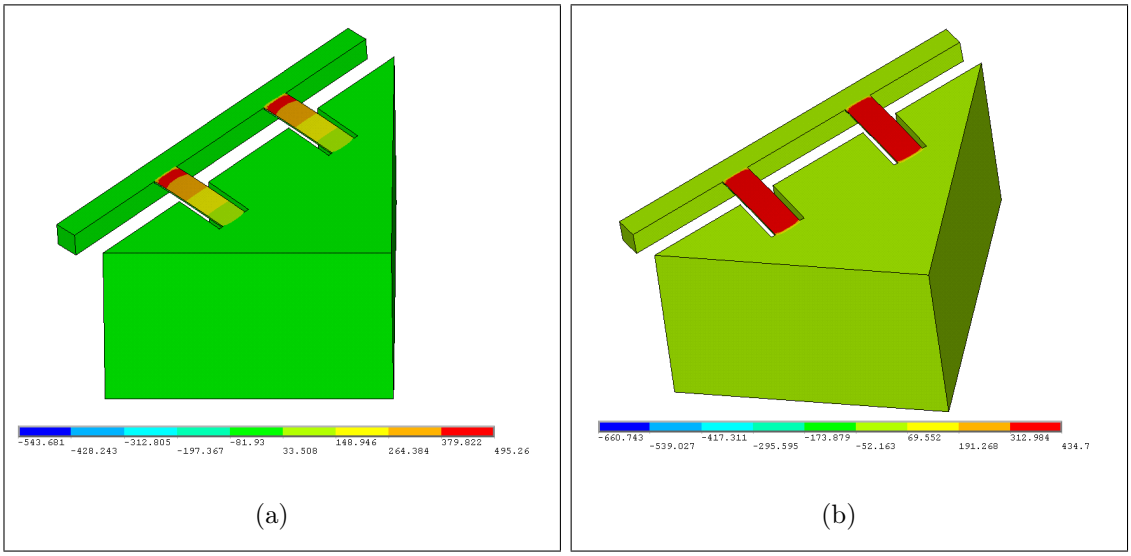

(a) (b)

Figure 5.11: Resulting stress contour plot for SMC design 1 as a result of 500 g of (a) out-of-plane acceleration, and (b) in-plane acceleration.

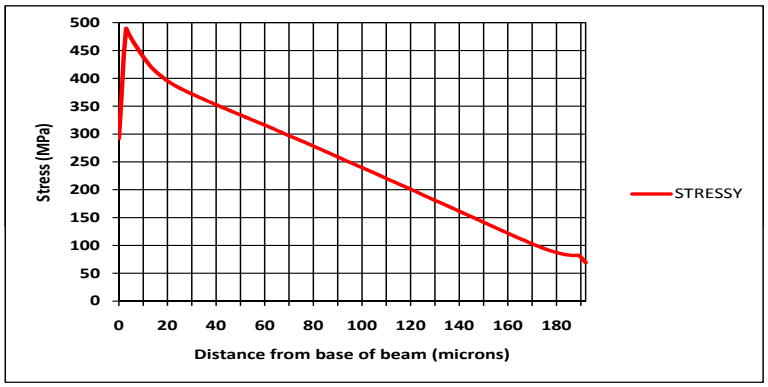

(a)

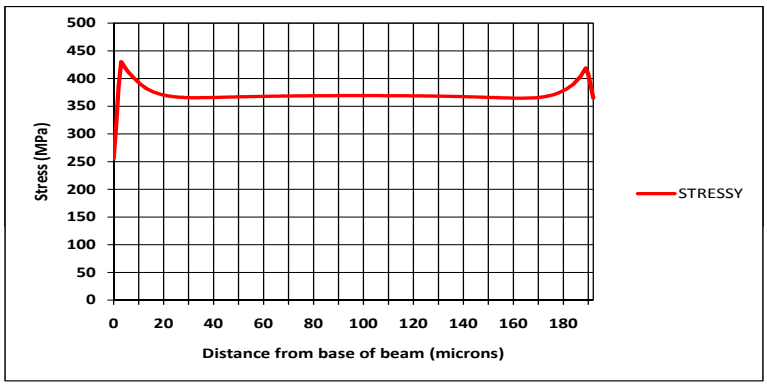

(b)

Figure 5.12: Resulting stress profile following the length of one of the beams for SMC Design 1 as a result of 500 g of (a) out-of-plane acceleration, and (b) in-plane acceleration.

These results, together with the analytical results obtained in Chapter 4, are plotted together in Figure 5.13. As with the results of the MultiMEMS design simulations, the same type of deviation between the plots was found, particularly near the base of the beam and can be explained as before. A first-order approximation and a linear data fit of the FEA results show that the plots are in good agreement with one another. The goodness of fit values are calculated to be 0.983 for Figure 5.13(a) and 0.999 for Figure 5.13(b) [2].

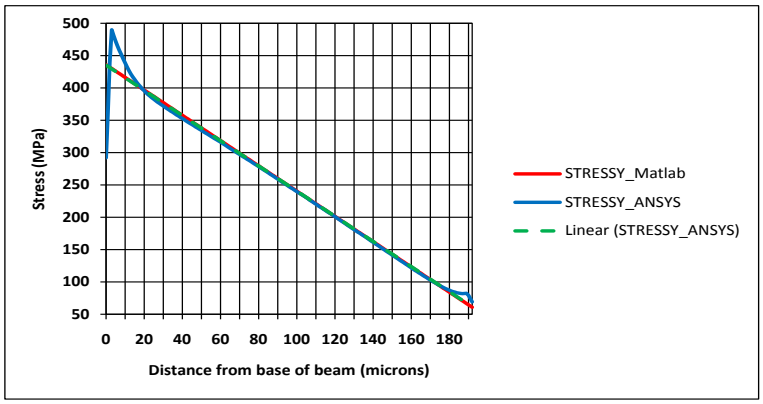

(a)

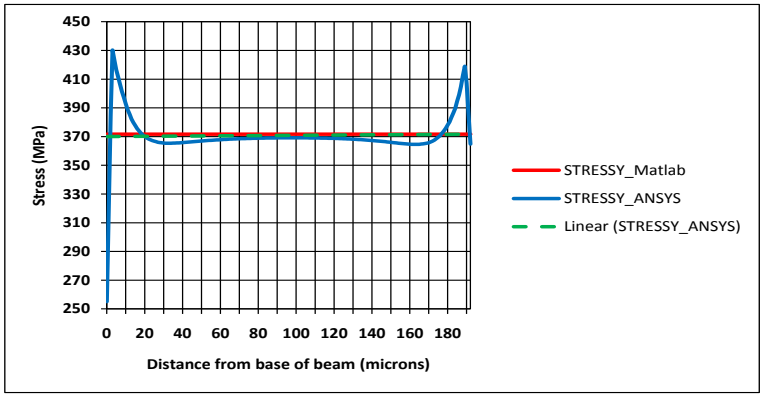

(b)

Figure 5.13: Comparison of the resulting stress profile following the length of one of the beams for the analytical results and the simulated results for SMC Design 1 as a result of 500 g of (a) out-of-plane acceleration, and (b) in-plane acceleration.

The stress values obtained using ANSYS simulations and analytical calculations are compared in Table 5.4. The stress value at the sensing piezoresistor located 30 μm

from the base of the beam is also quoted. Good agreement between the values is shown.

Measurand	**FEA value** (MPa)	**FEA linear fit value** (MPa)	**Analytical value** (MPa)
Out-of-plane stress	490	436	436
Out-of-plane stress at piezoresistor	378	378	377
In-plane stress	423	372	372

Table 5.4: Stress values obtained from simulated and analytical approaches for SMC Design 1.

5.4.2 SMC Design 2 static results

Following on from SMC Design 1 that employed rectangular beams, it was discussed in Section 4.6 the benefits of employing tapered beams in a further design, namely SMC Design 2. With this profile of beam compared to its rectangular counterpart, it is possible to combat the associated linear decrease of stress as a result of out-of-plane acceleration, starting from the base of the beam and continuing along its length. This is achieved by narrowing the width of the beam from the base and provides a region for the piezoresistor used to sense out-of-plane accelerations to be positioned with a constant stress along its length, thus making its placement less critical. The width of the beam is then increased again to join with a rectangular region. The width of this rectangular region is chosen so that when subjected to in-plane acceleration the resulting constant stress has a value equal to that in the tapered region for the same amount of out-of-plane acceleration. This is where the in-plane sensing piezoresistor is placed.

Stress analysis results

Figure 5.14 shows contour plots comparing the beam stress profiles of the rectangular beam employed in SMC Design 1 and the tapered beam employed in SMC Design 2.

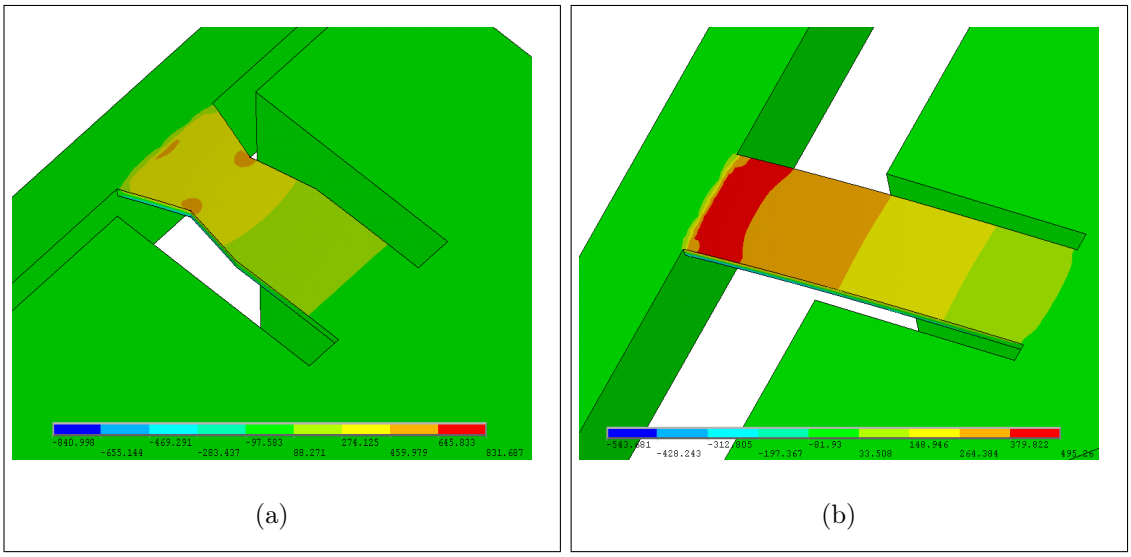

Figure 5.14: Contour plot of the resulting beam stress as a Result of 500 g of out-of-plane acceleration for (a) SMC Design 2, and (b) SMC Design 1.

With the tapered beam profile it is possible to place the out-of-plane acceleration sensing piezoresistor in the region of the beam near the base. The resulting stress profile is shown in Figure 5.15(a) for out-of-plane acceleration. A near constant stress is distributed across the piezoresistor. The in-plane acceleration sensing piezoresistor is placed on the rectangular section after the taper of the beam. The resulting stress profile is shown in Figure 5.15(b). Matching the values of stress for in-plane and out-of-plane accelerations is possible by adjusting either the width or the taper of the beam. Sensitivity to out-of-plane and in-plane accelerations is therefore possible. The dimensions of the device for this design and the other SMC designs can be seen in Appendix B.

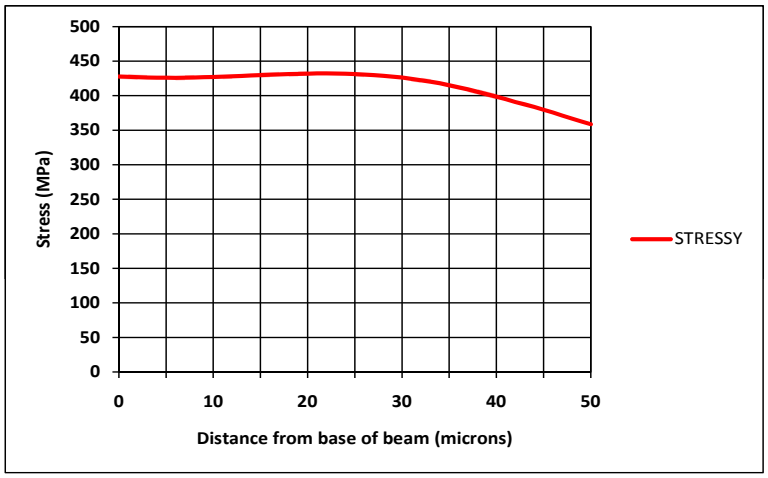

(a)

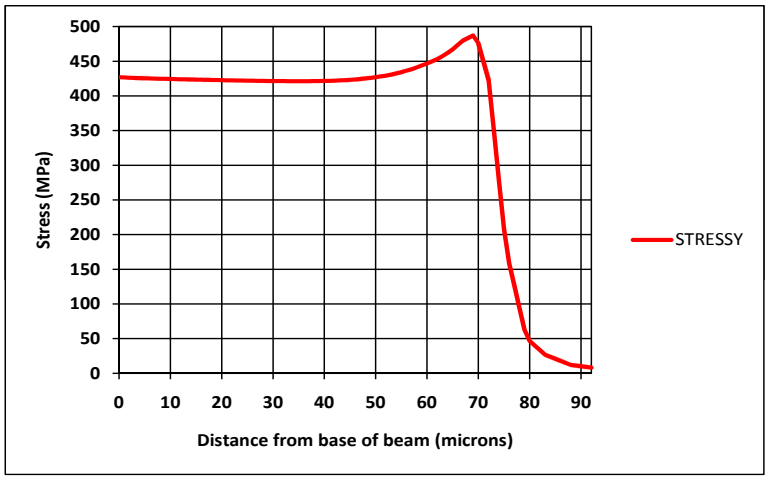

(b)

Figure 5.15: Resulting stress profile following the length of the (a) first tapered section, and (b) rectangular section of a beam from SMC Design 2 as a result of 500 g of out-of-plane acceleration and in-plane acceleration respectively.

5.4.3 SMC Design 1 modal results

The images for the first four modes can be seen in Figure 5.16 and the corresponding resonant frequencies are summarised in Table 5.5.

Mode	Frequency (kHz)
1^{st} Mode	1.239
2^{nd} Mode	3.709
3^{rd} Mode	6.965
4^{th} Mode	101.67

Table 5.5: Summary of modal frequency values obtained from ANSYS software simulations for the first four modes of SMC Design 1.

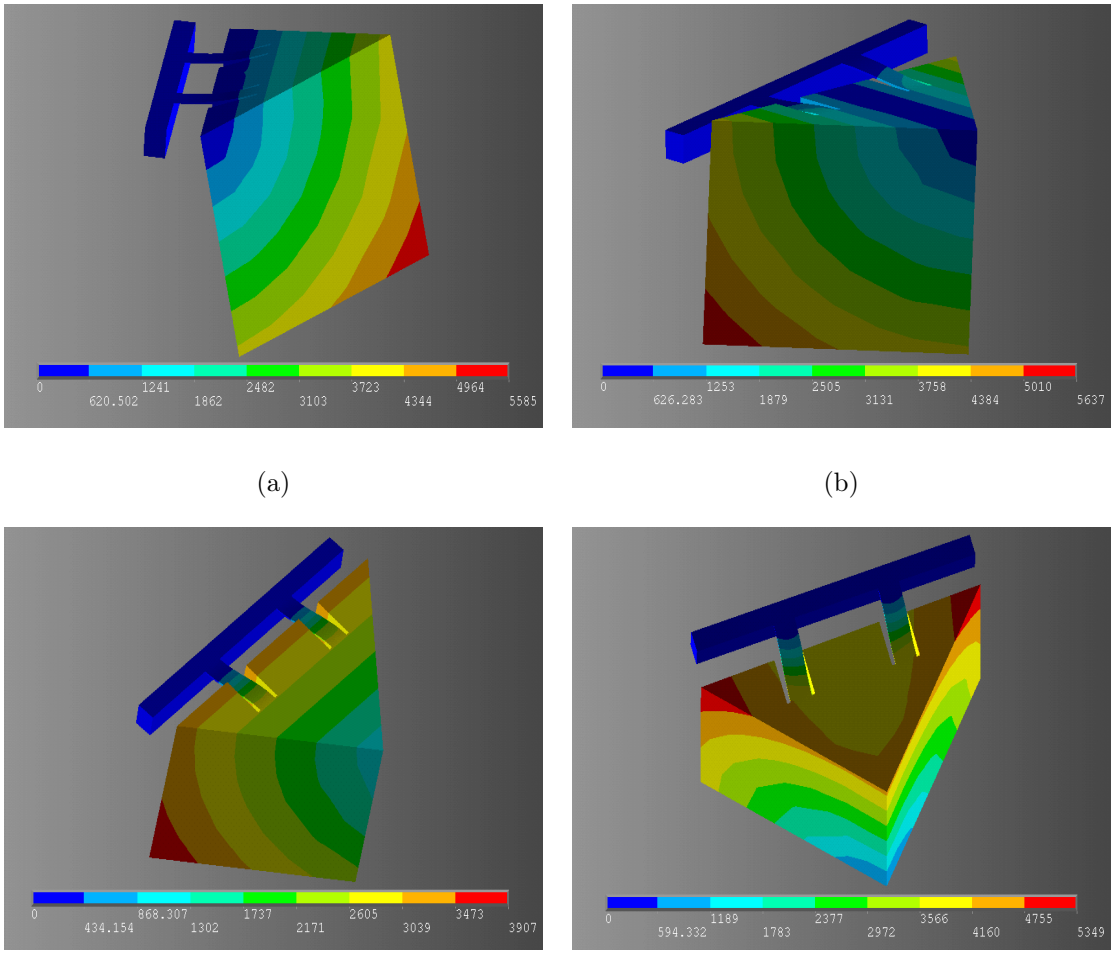

(a) (b)

(c) (d)

Figure 5.16: Resonant mode shapes for SMC Design 1 from ANSYS simulations: (a) 1^{st} mode at 1.239 kHz; (b) 2^{nd} mode at 3.709 kHz; (c) 3^{rd} mode at 6.965 kHz; (d) 4^{th} mode at 101.67 kHz.

5.5 Summary and conclusions

This chapter has presented results obtained using the Finite Element Analysis software ANSYS. This design process simulates the behaviour and performance of the sensing structures without the need for fabrication. This modelling stage saves cost and time in the sensor design and offers a better understanding of the behaviour of the structures for performance optimisation and better yield.

Many of the results that are extracted from the FEA simulations have been compared to analytical results presented in Chapter 4. Good agreement exists between the modelled and analytical results, confirming thereby the usefulness of the fundamental analytical equations in providing quickly a basic understanding of the performance of such structures. Access to FEA software was not possible for the first set of designs that were submitted for fabrication at MultiMEMS which resulted in complete dependence on the analytical models.

ANSYS can also be used for modelling of further device behaviour such as damping and a piezoresistive analysis for example. The modelling of damping was not considered to be critical for the MultiMEMS designs but this could be readdressed as good design practise. Access to the necessary version of ANSYS to perform piezoresistive analysis was not gained until later in the project but this could also be considered for future work and good design practise.

Other software programs were available in the analysis of MEMS devices such as the offering from CoventorWare [4]. The decision to use ANSYS in this project was simply to do with access to the software.

References

[1] ANSYS website. http://www.ansys.com/ (Accessed: 07 Oct 10).

[2] Curvefit website. http://www.curvefit.com/goodness_of_fit.htm (Accessed: 07 Oct 10).

[3] L.M. Roylance and J.B. Angell. A batch-fabricated silicon accelerometer. *Electron Devices, IEEE Transactions on*, 26(12):1911 – 1917, Dec 1979.

[4] CoventorWare website. http://www.coventor.com/coventorware.html (Accessed: 07 Oct 10).

Chapter 6

Fabrication of a Micromachined Three-Axis Accelerometer

6.1 Introduction

This chapter focuses on the fabrication of the different generations of sensors. The fabrication took place at three different foundries with various degrees of success, emphasising the difficulty in manufacturing a sensor of such small dimensions.

1. The original designs were fabricated as part of the MultiMEMS MPW which is based on a well established process from SensoNor Technologies AS (Norway). This process includes anisotropic silicon etching, phosphorous implantation and drive-in to define the seismic masses, and boron implantation for the definition of the surface piezoresistors. These sensors were then packaged using anodic bonding to form glass-silicon-glass structures.

2. Efforts then went towards gaining access to a foundry that could provide a thicker seismic mass through the use of DRIE and SOI wafers. This was possible at Sintef MiNaLab (Norway) [1]. The process run concentrated on characterising the etch steps to define the beam-mass structures.

3. Following this, a full process using DRIE on SOI wafers was carried out at the Scottish Microelectronic Centre (SMC, UK). This process included the necessary piezoresistors and conductors to make the structures electrically active. The fabricated sensors were then packaged in house using an adhesive bonding technique to form glass-silicon-glass structures ready for characterisation.

These approaches are covered in the following sections except for the fabrication steps at Sintef as the process development is similar to the one carried out at SMC.

6.2 MultiMEMS sensor fabrication

6.2.1 Introduction

This first run of fabrication was done using the MultiMEMS MPW [2]. The process is based on SensoNor's well established key technologies such as [3]:

- Sensitive surface piezoresistors and metal tracks from the sensors to the bond pads.
- Phosphorous implant and diffusion for n-wells to provide a diaphragm thickness and areas for boron implanted conductive tracks.
- Epitaxial layer for monocrystalline thin beams with a well controlled thickness.
- Precise control of mass thickness using ECES.
- Release etch of moving structures by RIE.
- Patented buried conductor crossing of anodic bonding areas.
- Hermetic cavities sealed by anodic bonding. The triple-stack glass-silicon-glass combination allows full protection of the silicon sensing element and reduces sensitivity to packaging stress. The top and bottom glass caps are offered with a cavity depth of 250 μm.

6.2.2 MultiMEMS fabrication process

The material specifications for the substrates used with this process are outlined in Table 6.1.

Silicon Substrate	
Type/Dopant	p (Boron)
Orientation	(100) $\pm$ 0.5°
Resistivity	3 $\pm$ 20% ($Ohm \cdot cm$)
Diameter	100 (mm)
Thickness	400 $\pm$ 10 (μm)
Total thickness variation (TTV)	less than 3 (μm)
Finish	Double-side polished
Epitaxial Layer	
Type/Dopant	n (Arsenic)
Thickness	2.2 $\pm$ 5% (μm)
Resistivity	0.11 $\pm$ 7% ($Ohm.cm$)
Glass	
Type	Pyrex, Corning 7740
Thickness	525 $\pm$ 30 (μm)
Diameter	100 (mm)

Table 6.1: MultiMEMS Silicon Wafer Specifications.

The process used for the design fabrication consists of twelve mask layers and these are now introduced. Note that the dimensions in the following figures are not to scale [4, 5].

Implantation of the *n*-well

A thermal oxide is grown on the top surface of the wafer which is subsequently patterned to provide a mask to define the n-well. The n-type (phosphorous) implant dose and diffusion time determine the well depth and thus the diaphragm thickness after wet etching. The oxide is then removed once this process has been completed.

The implantation for the MultiMEMS design can be seen in Figure 6.1 and is used to define the seismic masses in this design. Where the n-well is not implanted, the backside etch stops on the bottom of the epitaxial layer rather than the bottom of the n-well to define areas of thin diaphragm thickness.

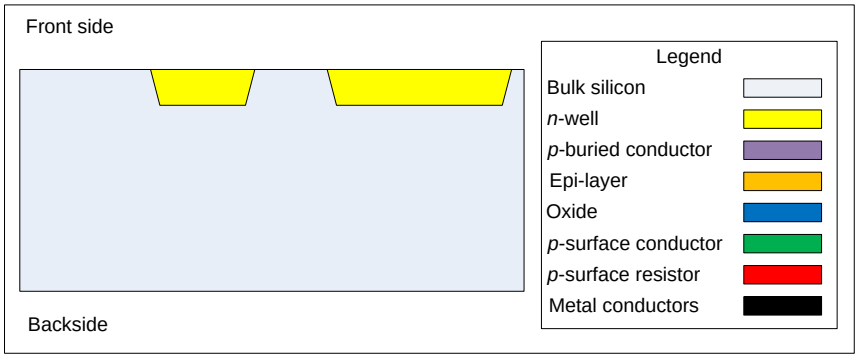

Figure 6.1: Implantation of the MultiMEMS n-well.

Implantation of the buried conductors

Thermal growth of silicon oxide is performed on the front side of the wafer. A p-type (boron) implantation is then performed through the oxide layer with a resist mask. This is then followed by a thermal diffusion to drive the implants deeper and the oxide is then removed as shown in Figure 6.2.

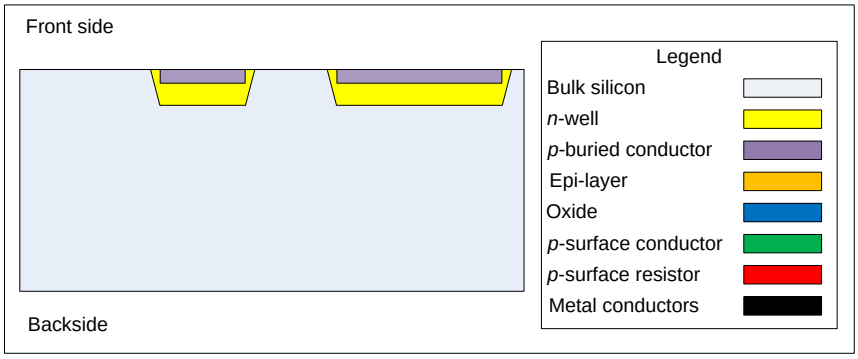

Figure 6.2: Implantation of the MultiMEMS p-type buried conductors

The buried conductors are particularly useful at the interface for the bonding of the glass caps to the silicon die. The presence of metal conductors and oxide is not

allowed in areas where the anodic bonding is to take place. The reason for this is due to the fact that the more planar the surface the glass caps are bonded to the better the bond strength and hermeticity that is achievable. In addition to this, the presence of oxide impedes the migration of the sodium ions in the glass which at the elevated temperature are displaced from the bonding surface of the glass by the applied electrical field. The depletion of sodium ions near the surface of the glass makes the surface highly reactive with the silicon surface of the other substrate forming a solid chemical bond. With the removal of the passivation in these areas it is then not suitable to place surface conductors in these regions and therefore the buried conductors are used instead as demonstrated in Figure 6.3. In addition, this layer can also be used together with the metal conductor layer to provide a crossing where it is necessary to overlap the conductive paths. The thick oxide is used as insulation between the two conductive layers for this to work.

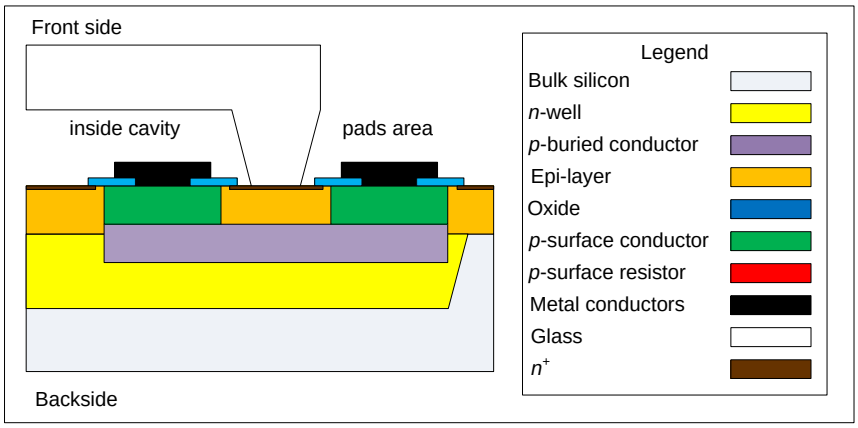

Figure 6.3: Cross-sectional view through the buried feed-through.

Growth of the epitaxial layer

An n-type (arsenic) epitaxial layer is grown on the top surface of the wafer as shown in Figure 6.4. This layer represents the thinnest diaphragm thickness possible with this process in conjunction with the etch-stop mechanism.

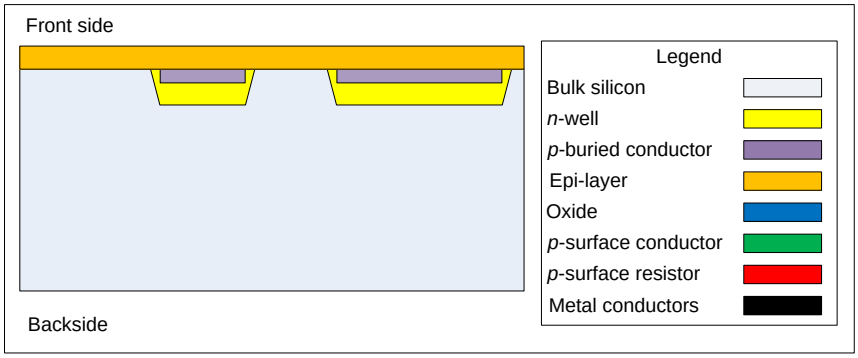

Figure 6.4: Growth of the MultiMEMS n-type epitaxial layer.

Growth of thick oxide

A thick SiO_2 is grown on both sides of the wafer. The front side oxide is patterned and then a thin passivation oxide is grown on the front side as shown in Figure 6.5. The passivation oxide is required in combination with the surface conductors and resistors in order to avoid leakage currents along the silicon surface. The thickness of the thick oxide is 400 nm whilst the thin oxide is 100 nm thick. The thick oxide is used as isolation between the buried conductors and crossing metal conductor lines as well as acting as a masking material for the backside bulk silicon etching. During the oxidation steps, the buried conductors diffuse into the n-epi and n-well layers.

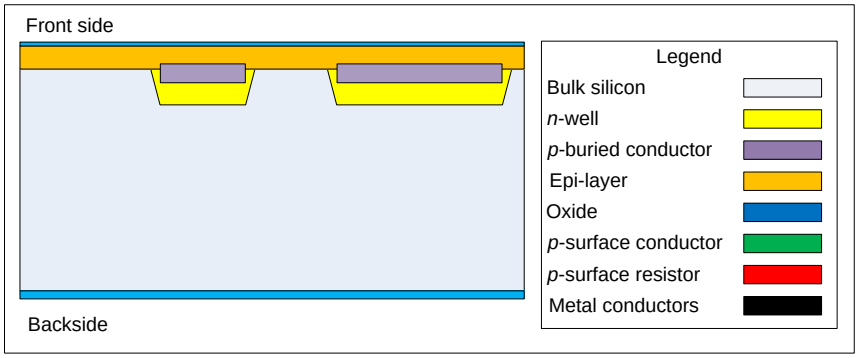

Figure 6.5: Growth of the MultiMEMS thick and thin oxides.

Implantation of the surface conductors

The implantation of p-type (boron) is carried out through a resist mask. An insulating oxide is deposited followed by thermal diffusion. This layer is used to make contact with buried conductors as well as making it possible to place conductive paths on the thin diaphragms due to its shallower depth. The depth of the surface conductors are approximately 0.9 μm with around 9 μm for the buried conductors. The epitaxial layer is approximately 3 μm. This step is shown in Figure 6.6.

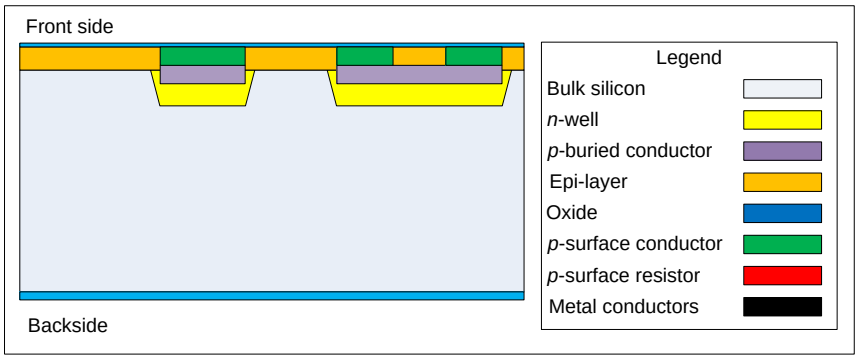

Figure 6.6: Implantation of the MultiMEMS p-type surface conductors.

Implantation of the surface resistors

Another p-type (boron) implant through a resist mask is carried out followed by the deposition of an insulating oxide. This defines sensitive piezoresistors that can be placed on the thin diaphragms as shown in Figure 6.7.

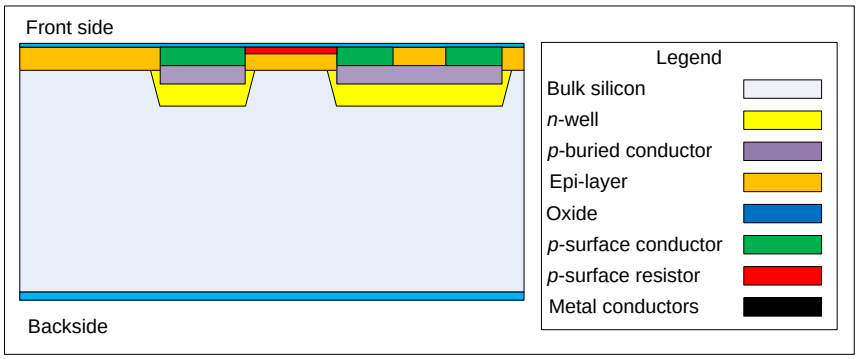

Figure 6.7: Implantation of the MultiMEMS p-type surface resistors.

Definition of the contact holes

Contact holes are etched into the insulating oxide using a buffered HF and a resist mask as shown in Figure 6.8. The layer is used to establish an electrical connection between the surface/buried conductor layers and the metal layer.

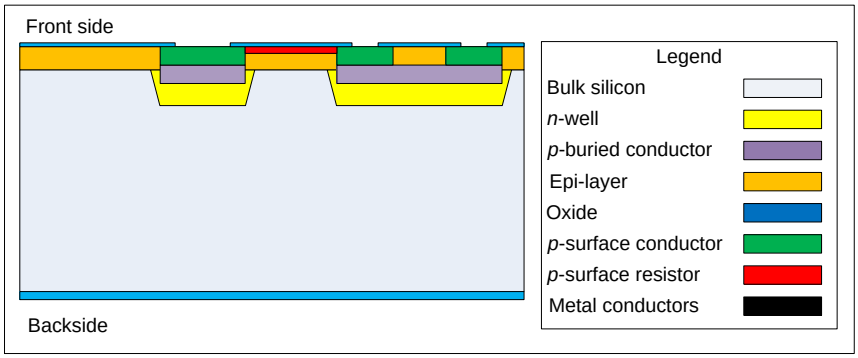

Figure 6.8: Etch step for the MultiMEMS contact holes.

Deposition of the metal conductors

High-purity Al is sputtered onto the front side of the wafer. This is then patterned by wet etching to form metal conductor tracks followed by an annealing step. This layer defines the pattern of the aluminium for the bond pads as well as connection to these pads as shown in Figure 6.9.

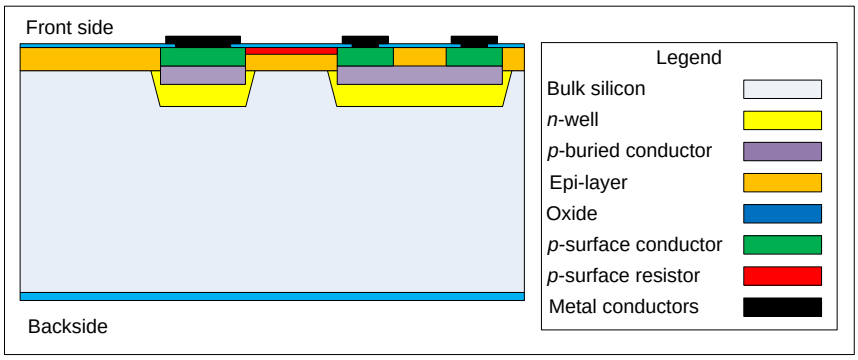

Figure 6.9: Deposition of the MultiMEMS metal conductors.

Etching from the backside

The thick oxide on the backside of the wafer is patterned. Anisotropic etching of the p-type Si is performed in TMAH etchant and uses an electrochemical etch stop on the pn-junction. [6–8]. This results in diaphragm thicknesses of either 3.0 μm (n-type epi-layer) or 23 μm (n-well). This step is shown in Figure 6.10.

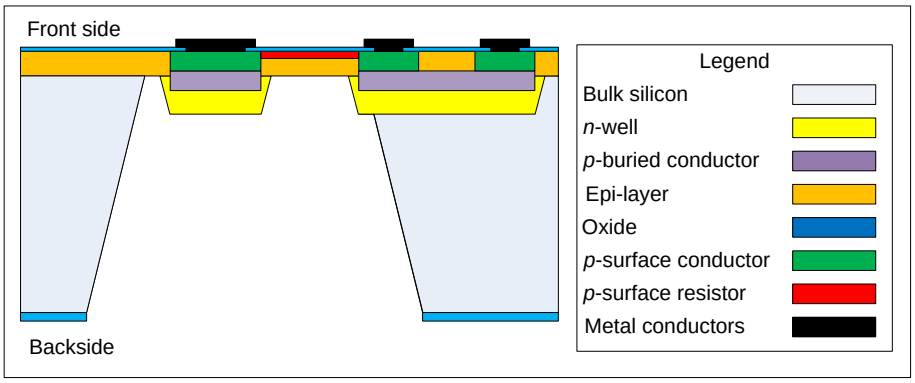

Figure 6.10: MultiMEMS backside etch process.

The etching in TMAH, as in all the alkaline etchants, will proceed as long as the electric potential of the silicon does not exceed the passivation potential. This characteristic opens up the possibility of controlling the etching by employing an ECES. By employing reverse biased pn-junctions, as in the arrangement illustrated in Figure 6.11, it is possible to etch unmasked p-type material, but not the passivated n-type layers. Thus the etching depth can be effectively controlled by establishing the pn-junctions at the desired locations [8–10].

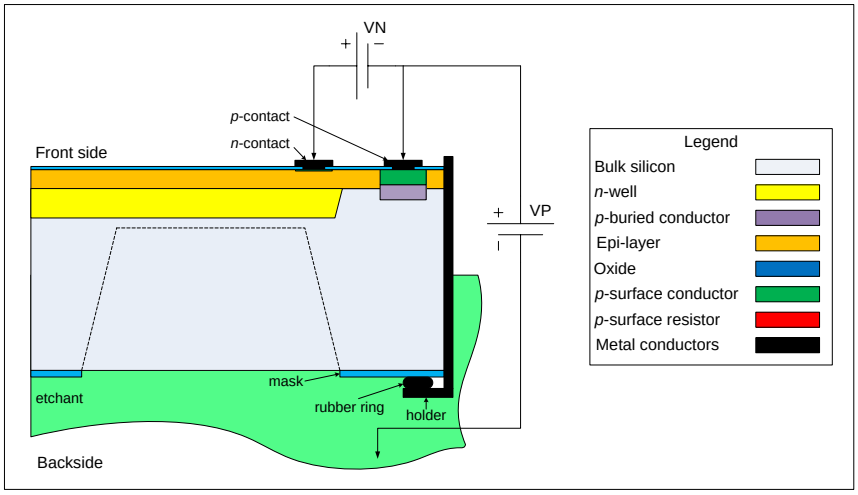

Figure 6.11: The set-up for the wet, anisotropic etching of bulk silicon with electrochemical etch stop.

No bonding area

A wet etching process using buffered HF is employed to etch the insulating oxide and expose bare Si where the anodic bonding will take place. Photoresist is used as a masking layer on the front side and the oxide on the backside is simultaneously removed as shown in Figure 6.12.

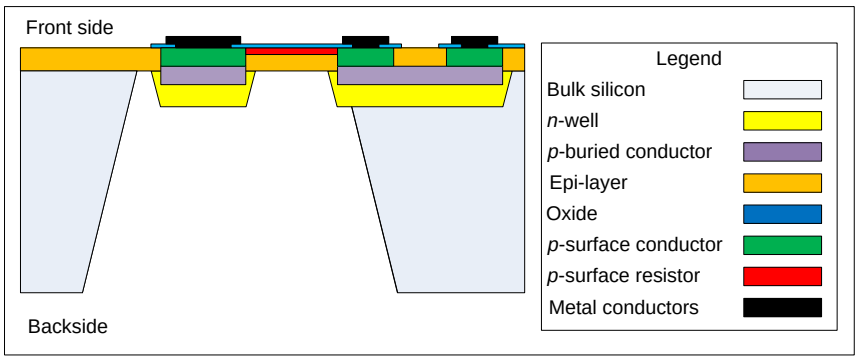

Figure 6.12: MultiMEMS thin oxide etch step to expose bare silicon and define interface areas for packaging.

Front side release etch

This process step releases the structures using RIE through the thin diaphragm (epi-layer) and uses a resist mask. The process step has a maximum etch through depth of approximately 6 μm. The release etch can be seen in Figure 6.13.

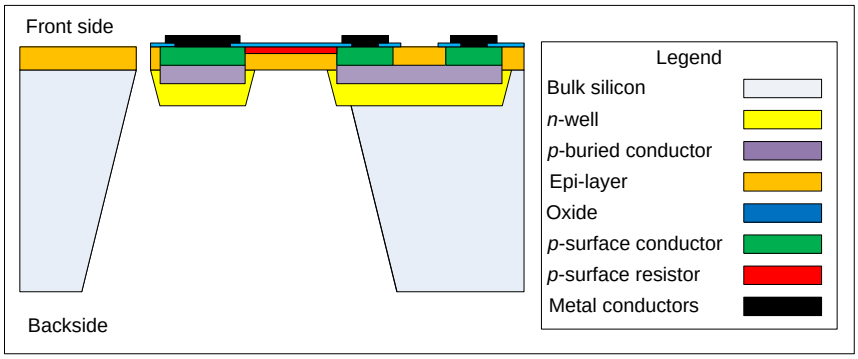

Figure 6.13: MultiMEMS front side release etch step.

6.2.3 MultiMEMS packaging

In this process, etching of the top and bottom caps of the glass lid is available using an isotropic etch. An etched cavity in the top cap was only necessary for the design because the seismic masses were only 23 μm thick whilst the wafer thickness was 400 μm. The bottom cap of the glass lid was never going to impede the motion of the masses as shown in Figure 6.14. The glass wafers are etched prior to wafer-level bonding.

The actual method using for bonding the glass caps to the silicon wafer is anodic bonding and is performed at wafer-level. The anodic bonding technique is a simple field assisted thermal sealing which results in a high strength, reliable and hermetic seal. A simplified sketch of the triple-stack anodic bonding principle is shown in Figure 6.15. The bonding temperature lies typically between 250 and 400 $°C$ and bonding voltage typically between 700 and 1500 V.

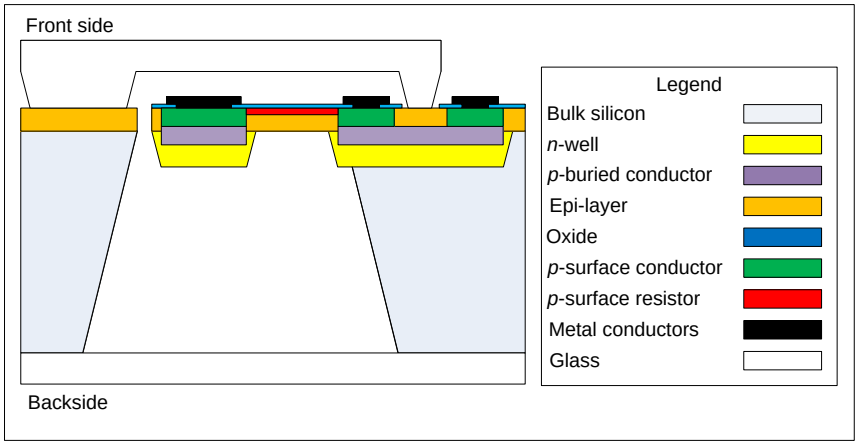

Figure 6.14: Packaging of the MultiMEMS Design.

Triple-stack anodic bonding gives the possibility to control the atmosphere around the mechanical sensing element and to protect its structure from the environment. In the MultiMEMS MPW process, the silicon and glass wafers are sealed in vacuum.

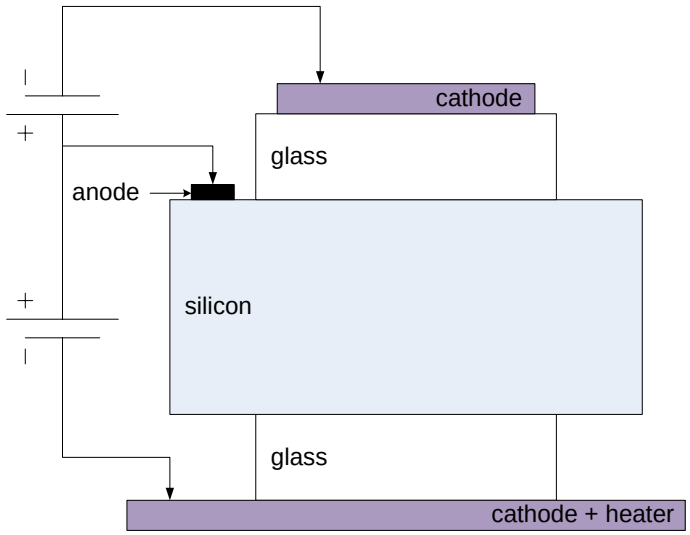

Figure 6.15: Triple-stack anodic bonding between silicon and glass wafers.

Because the bonding process is performed at wafer-level, it is then necessary to remove the areas of top glass that cover the wirebond pads in order to enable access. The removal of these glass strips is done in three steps, as illustrated in Figure 6.16 and explained further below:

- The cavities are wet etched in the top glass in places that will eventually house the wirebond pads. This is done simultaneously with the device-related cavity or through-hole etching.
- The top glass and the silicon wafers are then bonded.
- The glass strips located above the wirebond pads are sawn off in two parallel and subsequent passes.

The packaged wafers are then diced to produce individual die. Some of these dies are then glued to ceramic substrates with metallisation, wirebonded and the wires glob-topped for protection as shown in Figure 6.17.

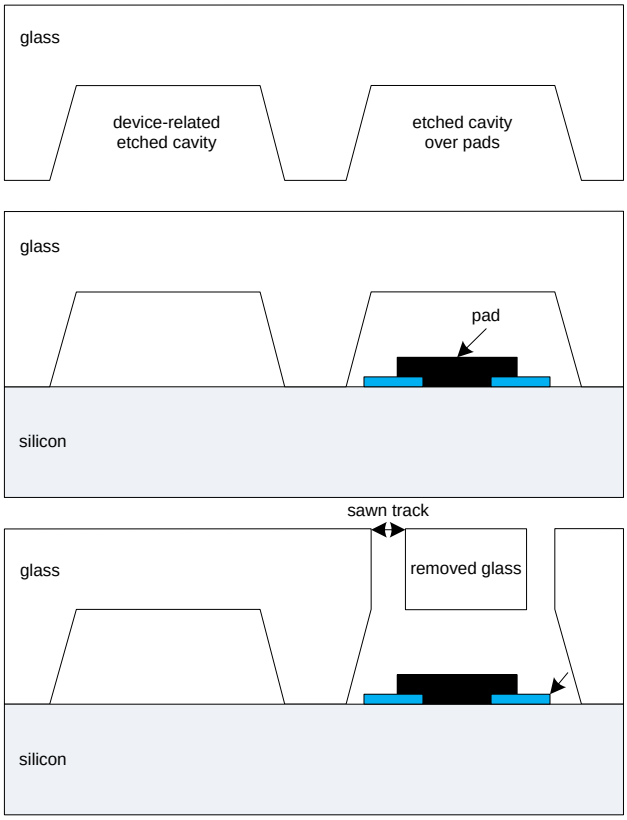

Figure 6.16: The removal of the glass strips above the wire-bond pads. Top: cavity etching; middle: anodic bonding; bottom: bridge sawing.

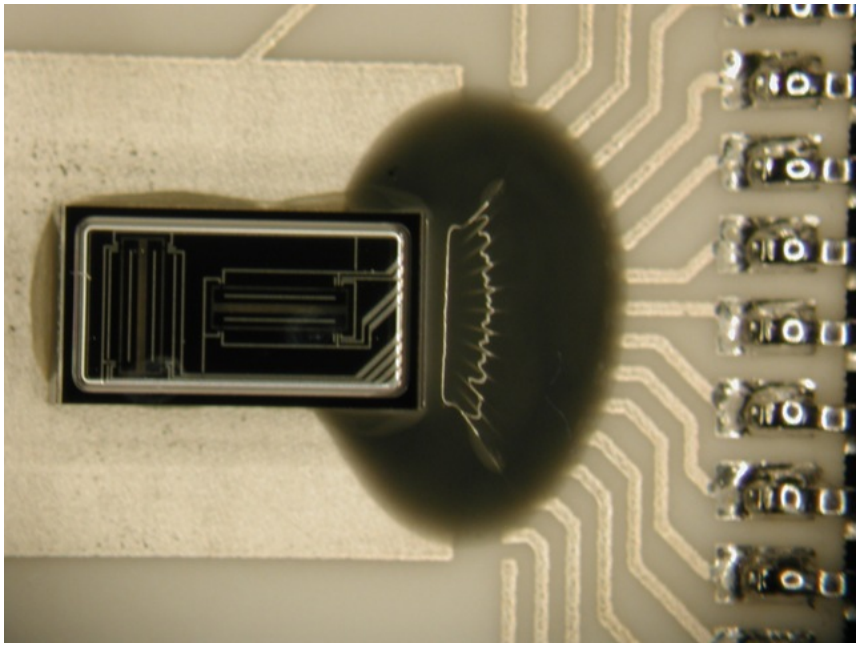

Figure 6.17: MultiMEMS Design on ceramic substrate.

6.2.4 Results from the MultiMEMS fabrication

Results and yield from this process run were very good since the process is very stable, well characterised, and offered with in-depth design rules. Through a simple visual inspection it was ascertained that the structures on each of the chips were fully intact and also fully released as shown in in Figure 6.18 for a specific example.

Figure 6.19 shows a closer inspection of one of the cantilever beams from the Multi-MEMS Design. It is possible to see that the notches that were included in the mask for the n-well masses as discussed in Section 4.5 were a success because the n-well does not encroach onto the thin cantilever beams which would affect the mechanical behaviour and stress profile of the beams.

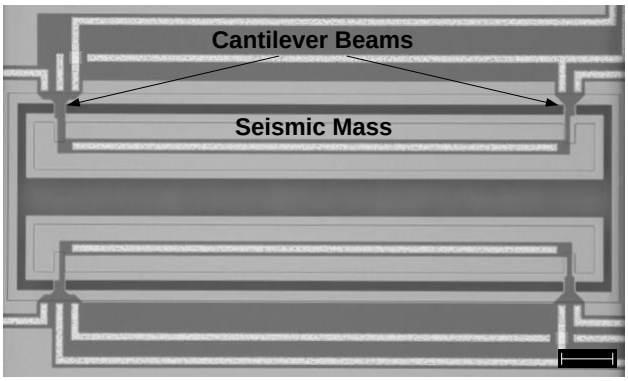

(a)

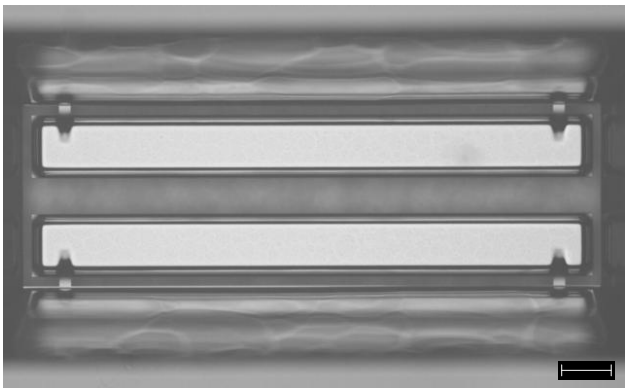

(b)

Figure 6.18: SEM images of a fabricated MultiMEMS Design showing one pair of the masses from the (a) front side, and (b) the backside. Scale bars = 200 μm. Images captured from FEA of the displacement of these masses when subjected to acceleration can be seen in Figure 4.8.

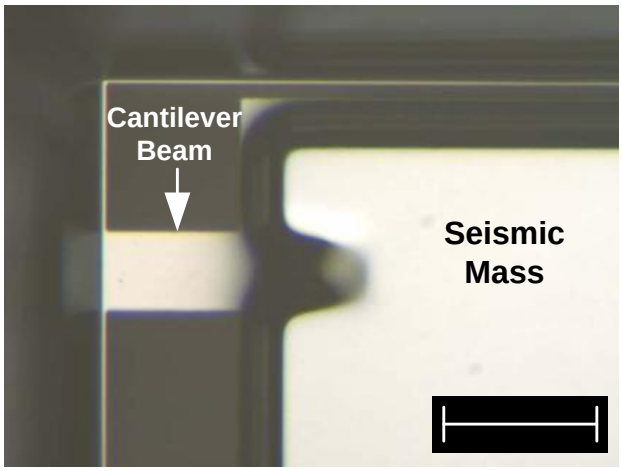

Figure 6.19: Close-up of one of the MultiMEMS Design beams. Scale bar = 50 μm.

The packaging and dicing were also successful. A batch of accelerometers as per the design and layout were therefore available for characterisation.

6.3 SMC sensor fabrication

6.3.1 Introduction

As discussed in Chapter 4, the only major difference between this process and the MultiMEMS process is with the etching process. Here a DRIE process step was used instead of an anisotropic wet etchant resulting in seismic masses with near vertical sidewalls through the full wafer thickness.

Device Layer	
Type/Dopant	n (Phosphorous)
Orientation	<100>
Thickness (μm)	4 ± 0.5
Resistivity ($Ohm.cm$)	1 - 10
Finish	Polished
Buried Oxide (BOX) Layer	
Thickness (μm)	0.5 ± 5 %
Handle Layer	
Type/Dopant	n (Phosphorous)
Orientation	<100>
Thickness (μm)	380 ± 5
Resistivity ($Ohm.cm$)	1 - 10
Finish	Polished

Table 6.2: SMC SOI Wafer Specifications.

Rather than relying on a timed etch it was decided to use SOI wafers. The advantage of using SOI wafers is that the BOX layer can be used as an etch-stop from the

front side and the backside due to etch selectivity. The silicon device and handle layers are used to define the thin cantilever beams and the thick seismic masses, respectively. These can be ordered in thicknesses that suit the design and the chosen wafer specifications are outlined in Table 6.2.

Interconnect of the stress sensitive p-doped (boron) piezoresistors is made firstly using implanted p-doped (boron) conductors. A metal conductor step provides an interconnect redundancy away from the beams and is routed out to the bond pad area which is located outwith the area of the top cap packaging. A connection between the implanted conductors and the surface metal conductors is made possible by firstly etching the thin oxide on the top surface of the wafer. The presence of these metal tracks across the bonding area is not detrimental to the packaging as outlined later in Section 6.3.4. To define the outline and release of the acceleration sensitive structures, 4 μm of silicon is etched from the front side with the BOX layer acting as an etch-stop. The masses are defined DRIE from the backside of the wafer. This process etches the 380 μm thick silicon handle layer and once again the BOX layer is used as an etch-stop. Finally, to fully release the structures a RIE step is used to etch the BOX layer.

6.3.2 SMC fabrication process

The process used for this fabrication consists of seven mask layers and these are now introduced. The specifications of each of these layers were chosen to match those of the MultiMEMS process and the necessary processing details were decided upon by the process engineers at SMC.

Growth of the thick oxide

An oxide of thickness 7500 Å is deposited on both sides of the wafer using PECVD. This oxide is then patterned on the front side of the wafer using a resist mask and

RIE. Oxide is left in areas where the bonding of the top and bottom packaging caps is to take place. The oxide is also removed to leave channels for future placement of metal conductors onto the bond pad area.

A thin insulating oxide of thickness 1000 Å is then grown on the front side of the wafer. These steps can be seen in Figure 6.20.

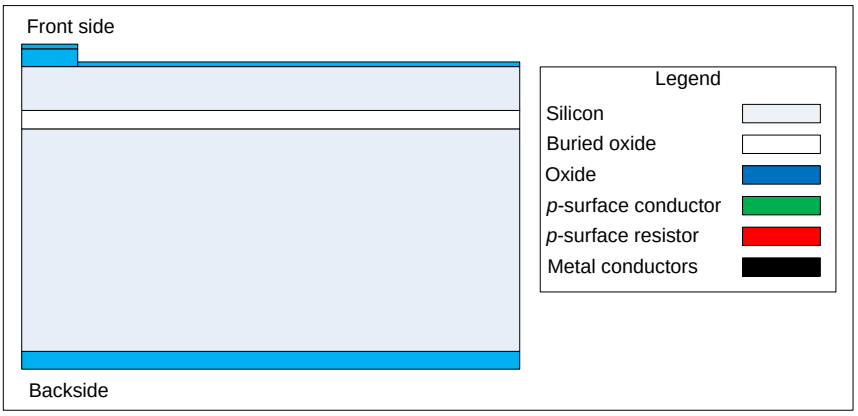

Figure 6.20: Growth of the SMC thick and thin oxides.

Implantation of the surface conductors

Resist spun on the front side of the wafer was patterned for the placement of the implanted conductors. This was then followed by a p-doped (boron) implantation step through the insulating oxide as shown in Figure 6.21. This layer is used for the conductive tracks on the areas of thin silicon. The freedom of not needing metal conductors in this area allows for beams to be made as narrow as possible. Elsewhere on the chip, the surface conductors are used as a redundancy for the conductive paths out to the bond pad area.

The buried conductors that were used in the MultiMEMS fabrication are not required here due to the different packaging technique being used for this process as discussed in Section 6.3.4.

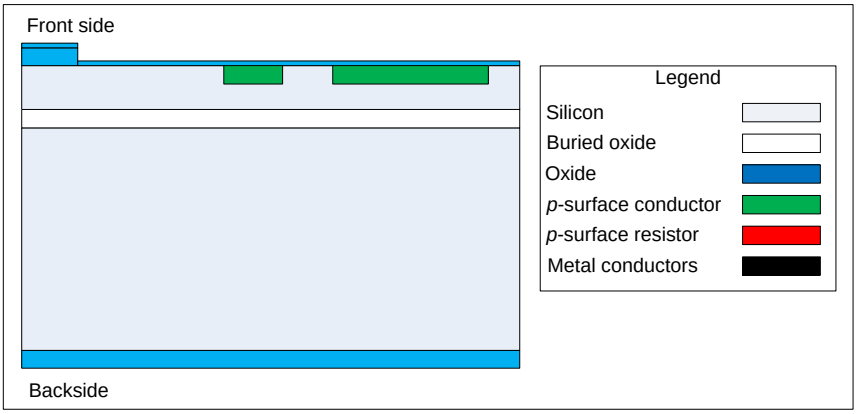

Figure 6.21: Implantation of the SMC p-type surface conductors.

Implantation of the surface resistors

Photolithography of resist is carried out on the front side of the wafer to define the areas where the sensing resistors are to be implanted. This is followed by a p-doped (boron) implantation step through the thin insulating oxide as shown in Figure 6.22.

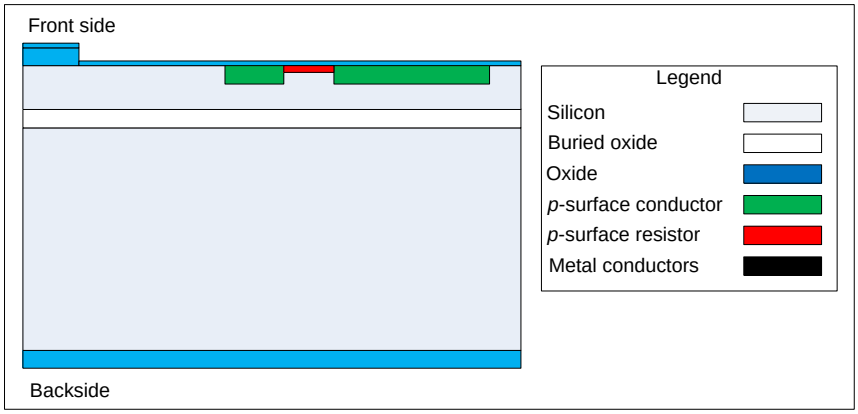

Figure 6.22: Implantation of the SMC p-type surface resistors.

Definition of the contact holes

Contact holes are etched into the front side insulating oxide using a resist mask and RIE as seen in Figure 6.23. This step enables additional electrical connection between the surface conductors and the metal layers.

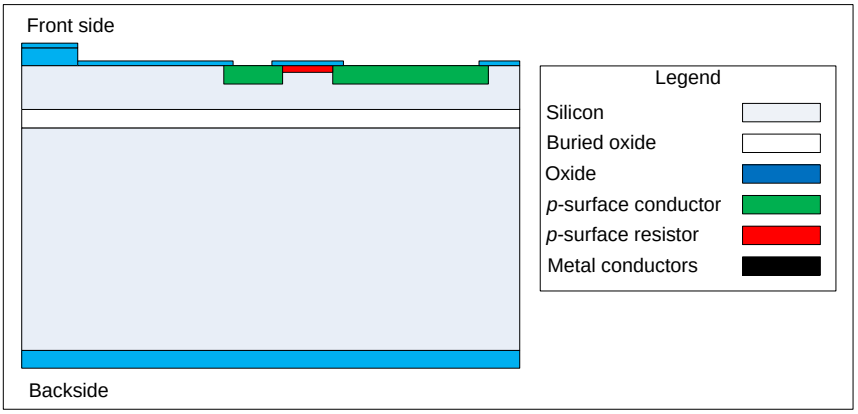

Figure 6.23: Etch step for the SMC contact holes.

Deposition of the metal conductors

1.5 μm thick aluminium is sputtered onto the front side of the wafer. A resist is then patterned using the metal conductor mask, followed by a wet etch to define the metal conductor tracks and bond pads as shown in Figure 6.24.

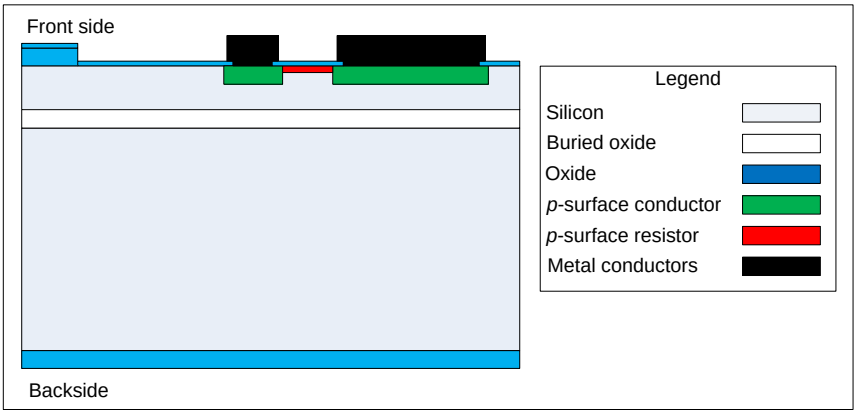

Figure 6.24: Deposition of the SMC metal conductors.

Etching from the front side

Photolithography of resist using a front side etch mask is followed by an RIE step to etch the thin oxide to the bare silicon. The 4 μm thick silicon device layer is then etched using an ICP etch until the BOX layer acting as an etch-stop due to etch

selectivity, is reached. This process step is completed by a resist strip as shown in Figure 6.25.

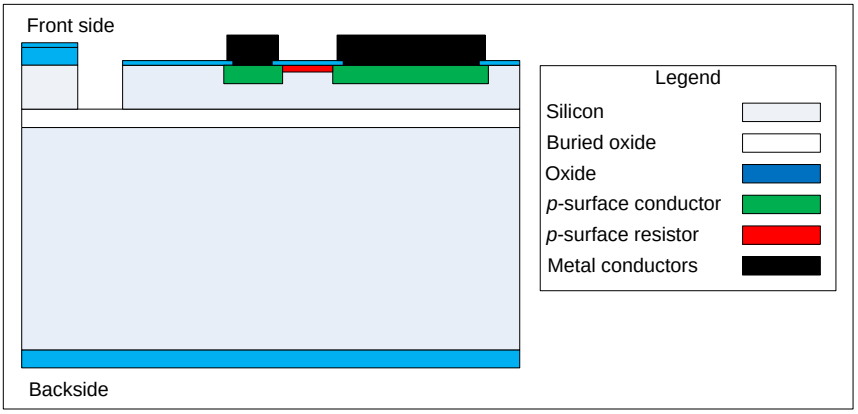

Figure 6.25: SMC front side release etch.

Etching from the backside

Photolithography of a thick resist was carried out using the backside etch mask. This was followed by a RIE step to etch the oxide on the backside of the wafer. Then the 380 μm thick silicon handle layer was etched using an ICP DRIE using the BOX layer as an etch-stop. The devices were then fully released using a RIE step to etch the BOX layer. This process step is completed by a resist strip and is shown in Figure 6.26.

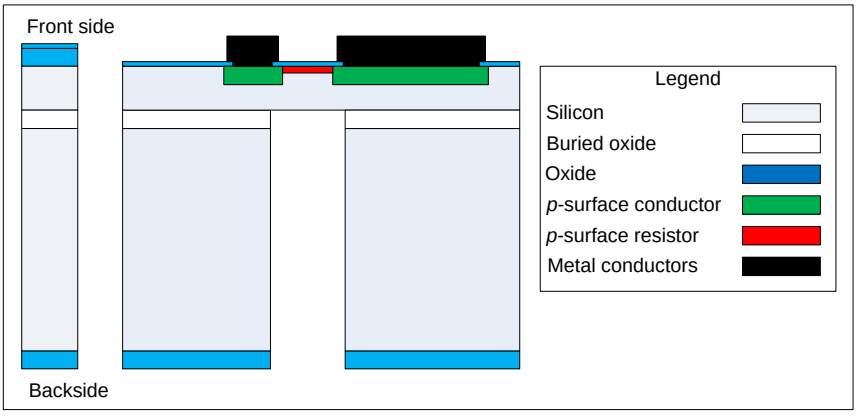

Figure 6.26: SMC backside etch process.

6.3.3 *Results from the SMC fabrication*

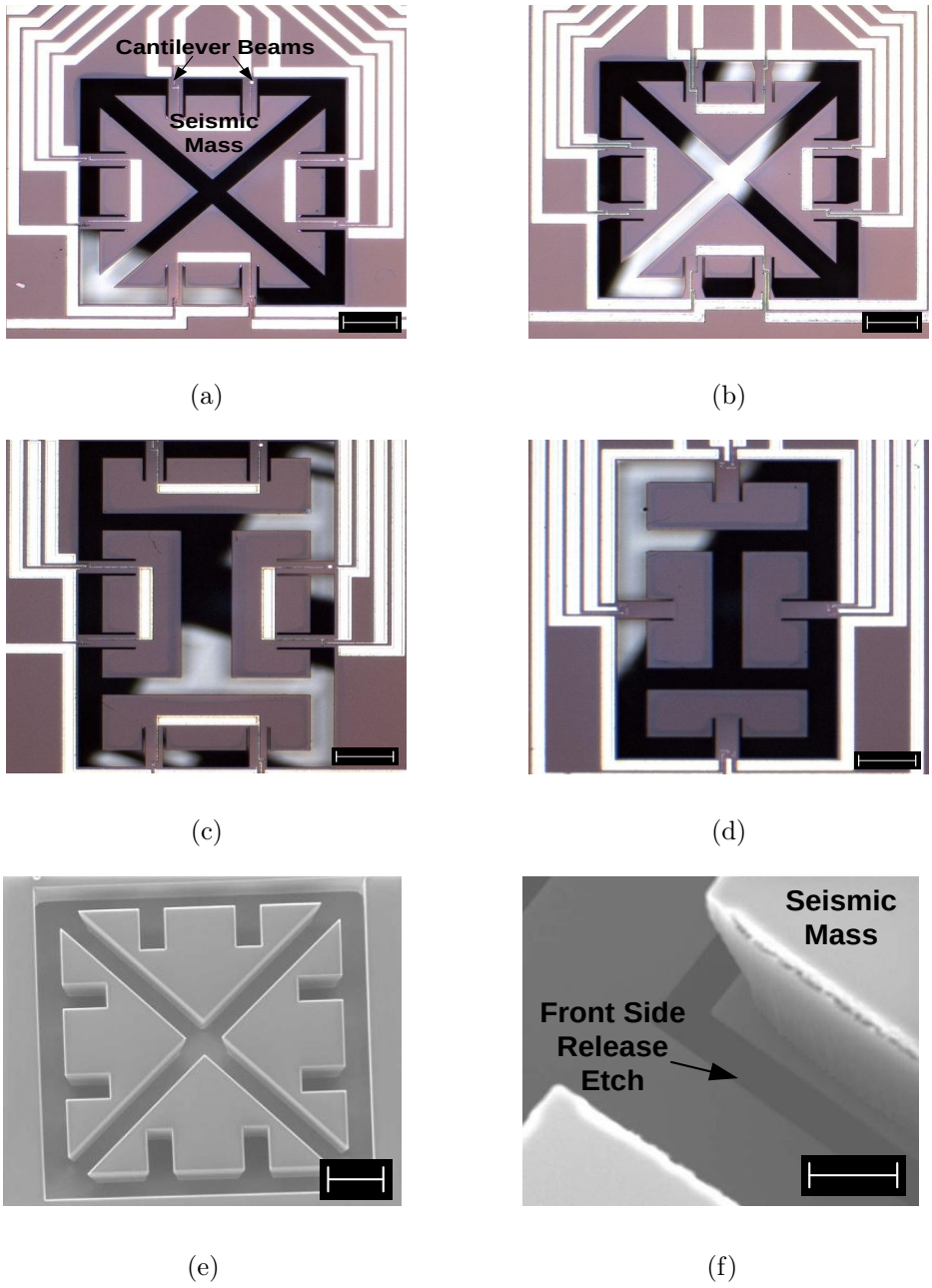

Figure 6.27: Images highlighting successful etching of SMC Designs: (a) front side of completed SMC Design 1 (Scale bar = 200 μm). Images captured from FEA of the displacement of these masses when subjected to acceleration can be seen in Figure 4.20; (b) front side of completed SMC Design 2 (Scale bar = 200 μm); (c) front side of completed SMC Design 3 (Scale bar = 200 μm); (d) front side of completed SMC Design 4 (Scale bar = 200 μm); (e) backside of SMC Design 1 prior to full release (Scale bar = 200 μm); (f) backside of completed SMC Design 1 (Scale bar = 20 μm).

Over the area of a wafer, it was demonstrated that it was possible to produce fully released structures exhibiting near vertical sidewalls. Examples of each of the four designs that were submitted for processing are shown in Figures 6.27(a) to 6.27(d).

From Figure 6.27(e) it can be seen that the resulting seismic masses have near vertical sidewalls and the underside of the oxide layer where the etch has stopped is clean. Figure 6.27(f) shows an edge of one of the masses from Design 1 which shows the full release of the seismic mass.

However, these results were only obtained for a small percentage of the sensors laid out on the wafer. Less successfully released structures can be seen in Figure 6.28. Figure 6.28(a) shows the front side of the die where masses have been pulled downwards. This deflection might be caused as a result of residual stresses in the under-etched buried oxide layer. The deformation has ultimately resulted in some parts of the wafer in the fracture of two cantilever beams as shown in Figure 6.28(b), or one beam as in Figures 6.28(c) and 6.28(d). From the images it is clear to see that the fracture of the silicon beam follows the contours of the unreleased buried oxide layer.

In addition to the poor control of the etch results across the wafer, a mistake was made by a process engineer at SMC that resulted in the mask used for the implanted conductors being erroneously reused for the deposition of the metal conductors. As a result the electrical functionality of the sensor may have been compromised due to metal conductors being too close to each other. This mistake also resulted in metal conductors being unintentionally deposited on the thin cantilever beams. This additional layer makes the mechanical behaviour of the structures less predictable due to possible issues such as residual stress or additional mass.

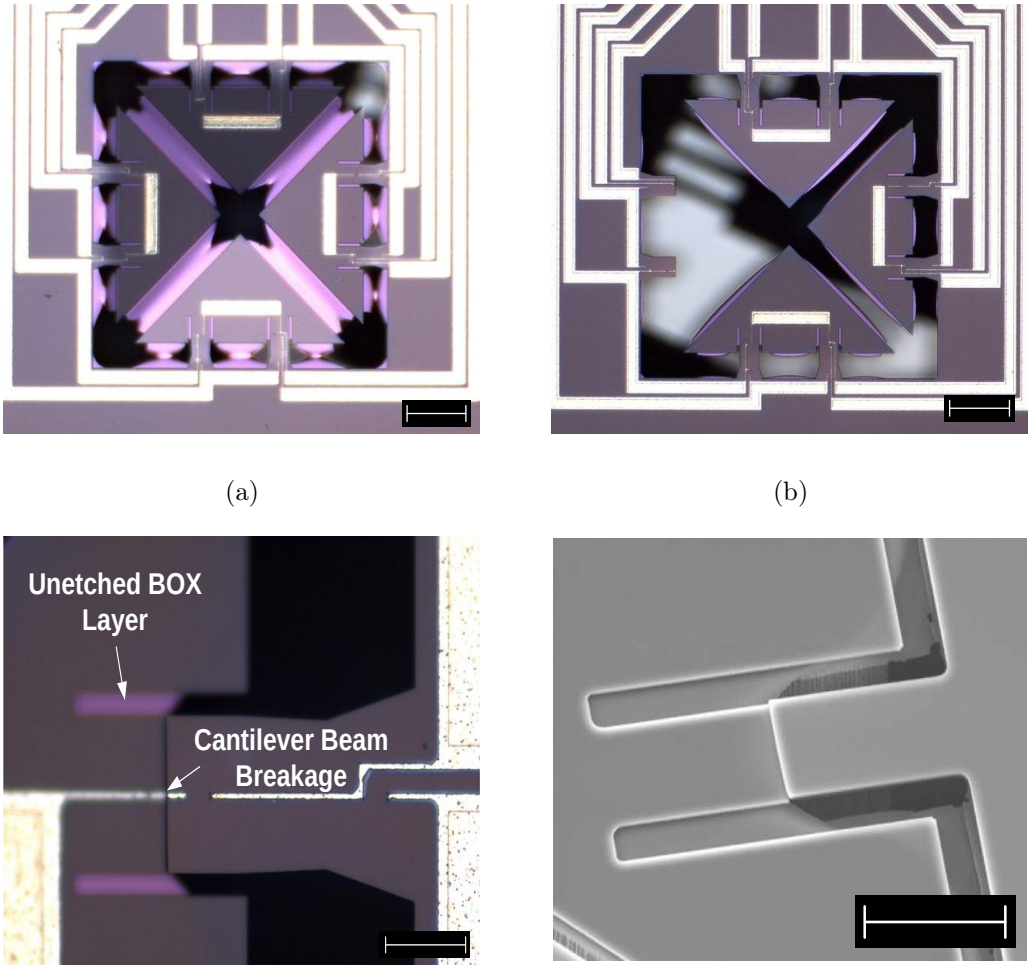

Figure 6.28: Front side images highlighting etching problems with the SMC process: (a) incomplete release of structures exhibiting deformation due to stress (Scale bar = 200 μm); (b) partial release but at a later stage of etching destroying the beams holding one of the masses (Scale bar = 200 μm); (c) (Scale bar = 50 μm) and (d) beam breakages following the contour of the non-etched buried oxide layer (Scale bar = 100 μm).

6.3.4 SMC packaging

Unlike with the MultiMEMS design in which the packaging is part of a single fabrication process, the packaging of the SMC sensor designs was performed in-house and separate from the fabrication process at SMC. Therefore this section is considered after the consideration of the fabrication results unlike with the MultiMEMS design. The SMC sensor designs were packaged at chip-level rather than wafer-level,

due to limited access to the necessary facilities. Once the fabrication of the wafers were completed, each chip on the wafer was only held in-place by two tabs of the same thickness as the silicon handle layer. The tabs were manufactured using the backside DRIE etch, an example of which can be seen in Figure 6.29. To release the chips from the wafer, a small downward pressure is applied to each individual chip to snap them free. This fabrication step acted as a replacement to a dicing process step but does not fully release the chips which would risk damage to the unprotected released structures. A dicing saw process was not a viable solution as it would damage the fragile free standing structures due to the sawing vibrations, or spoil them due to the fluids used.

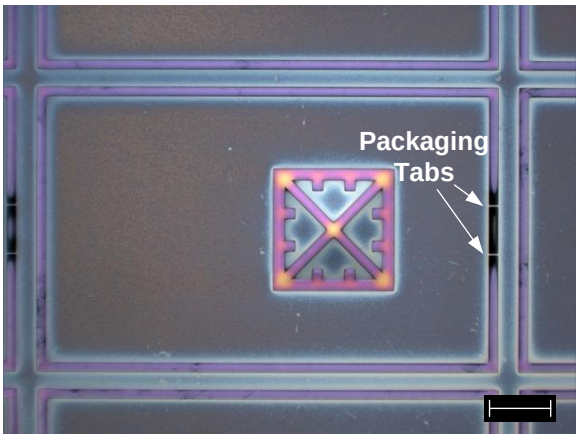

(a)

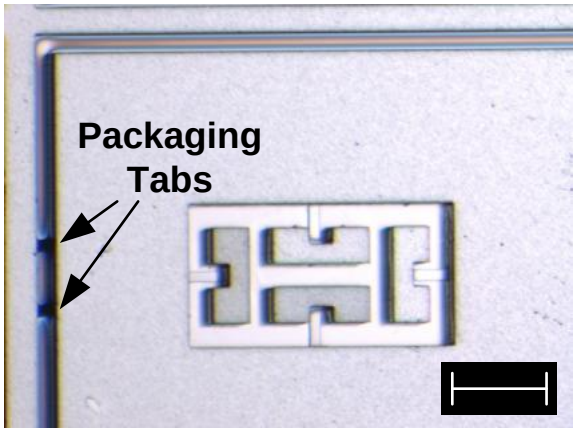

(b)

Figure 6.29: Location of the packaging tabs from the backside of (a) SMC Design 1, and (b) SMC Design 4. Scale bars = 500 μm.

The actual packaging process involved the bonding of the top and bottom glass caps to the silicon die. As a replacement for the wafer-level anodic bonding used for the MultiMEMS Design, a polymer bonding technique was performed at chip-level using BCB [11, 12].

A major benefit of this packaging approach is that it has the possibility to bond directly onto non-planar surfaces. This opens up the opportunity of bonding directly across the metal tracks that go out to the wirebond pads. This approach also removes the need for buried conductors as in the MultiMEMS process.

For the BCB deposition, a 4 *inch* glass wafer of 500 μm thickness was spin-coated with BCB. The BCB was then exposed to UV light through a photomask to define the sealing ring structure. After exposure the film was baked again at $85°C$ for 90 *seconds* to ensure a consistent developing time. During development, the unexposed BCB was dissolved by a developer solvent and the UV exposed areas in the BCB film were left on the glass wafer. The resultant polymer structures were then baked at $85°C$ for 60 *seconds*. Finally, the glass wafer was diced into square chips by sawing. The resulting thickness of the BCB was approximately 18.5 μm which was confirmed using interferometry and shown in Figure 6.30(a). As no cavities were fabricated into the glass wafers, the thickness of the BCB defines the gap between the top and bottom surfaces of the masses and the caps, respectively. To measure the thickness of the BCB post-bonding, a glass cap was removed from one of the sensors and the image produced using interferometry in Figure 6.30(b) was used to determine that the thickness was 18 μm. From FEA, this gap is equivalent to the deformation of the sensing structures when an acceleration of approximately 150 g is applied.

The individual glass caps were then carefully removed from the dicing tape. The top and bottom caps could be identified by the fact that the top glass cap was smaller and did not cover the wire bond area. The bottom cap had the same dimensions as the silicon die.

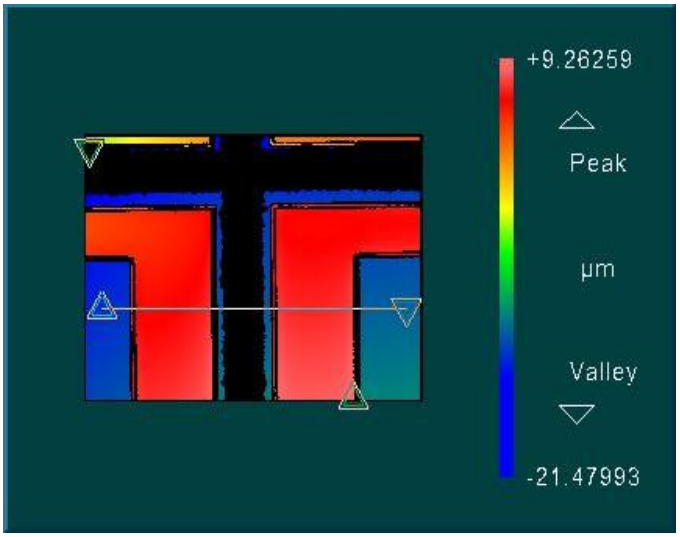

(a)

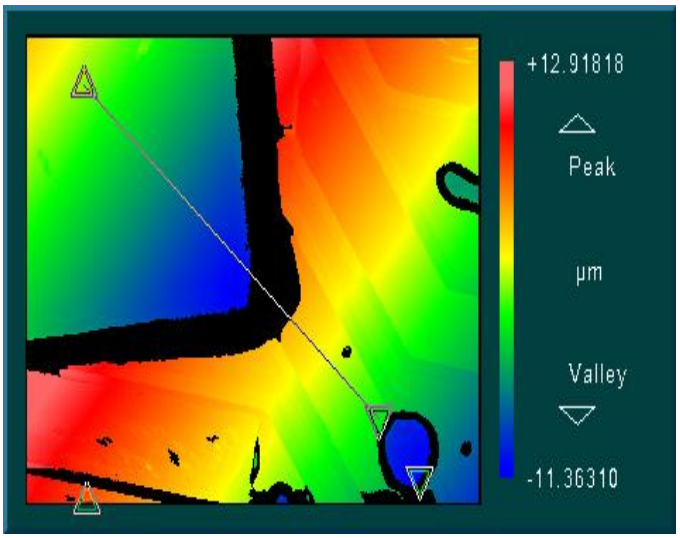

(b)

Figure 6.30: Interferometer scans of BCB thickness (a) before bonding, and (b) after bonding.

The bottom glass cap, silicon die, and top glass cap were then stacked together by hand under a microscope ensuring that the sides of the glass caps with BCB on mated with the silicon die. A brass weight attached to a 3 *inch* glass wafer was placed on top of the top glass cap to provide the force necessary for the bond. The glass wafer provided a surface that could be mated with the top glass cap and would evenly distribute the weight of the brass weight. In the centre of the brass weight, a viewing window was machined out to provide a means of positioning the weight on top of the stack using the microscope. To increase the accuracy of the alignment,

crosshairs were scribed into the glass wafer.

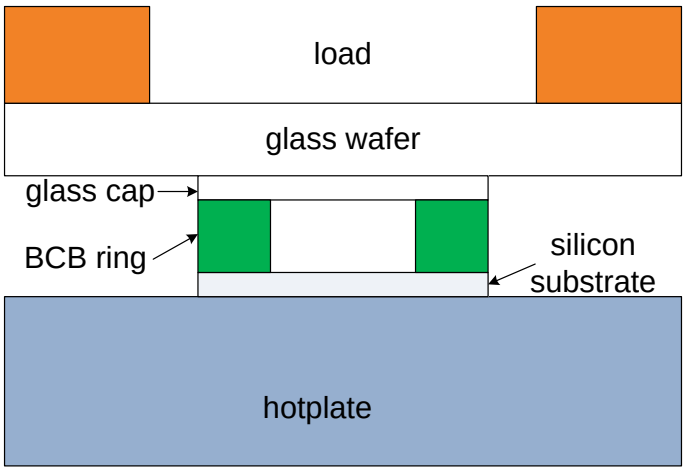

Figure 6.31: Schematic of hotplate BCB bonding setup. The bonding of the top cap is shown only.

The bonding was performed on top of a hotplate as shown in Figure 6.31. This relatively low temperature process requires a maximum temperature of 250°C to be effective. A temperature ramping process consists of a pre-bonding step and a final bonding step. For the pre-bonding step the hotplate is ramped up to 150°C and is held at that temperature for 5 *minutes*. The temperature is then ramped up to 250°C for the final bonding process for 15 *minutes*. The hotplate is then left to cool down and the bonding process is complete as shown in Figure 6.32.

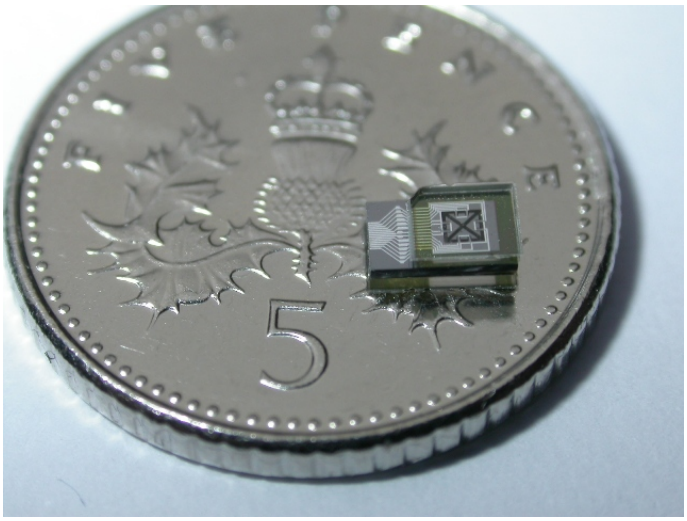

Figure 6.32: Packaged SMC Design on top of a five pence piece.

Different approaches were also investigated to allow further movement of the masses, if required. One method was to employ top and bottom glass spacers with through-cavities resulting in a glass-glass-silicon-glass-glass stacked structure. The cavities were made possible using powder blasting. The fine particles etched through the thickness of the glass spacers. A blue tape positioned by hand provided a crude mask along the periphery of the glass. Results from this can be seen in Figure 6.33.

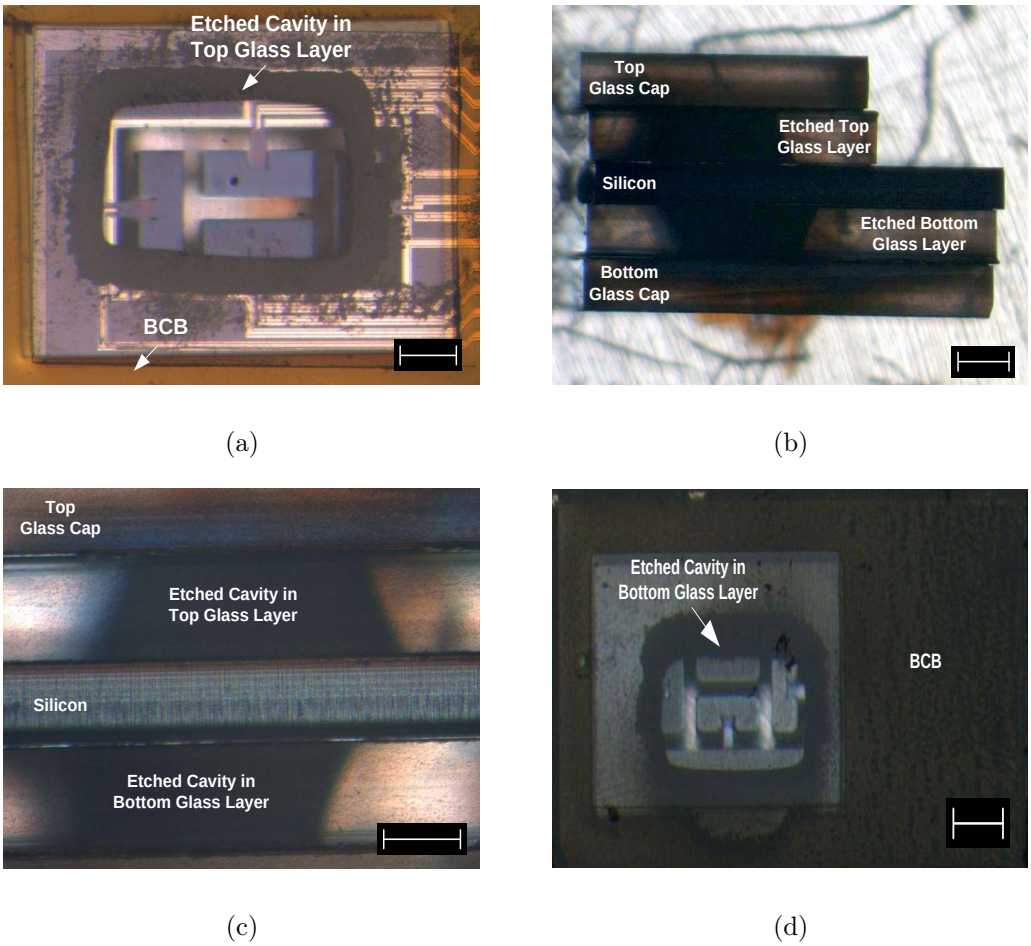

Figure 6.33: BCB bonding with powder blasted glass spacer layers. (a) Top-view showing powder-blasted cavity in top-glass spacer (Scale bar = 250 μm). (b) Side view showing five layers of package (Scale bar = 500 μm). (c) Side view of powder blasted glass cavities (Scale bar = 500 μm). (d) Bottom-view showing powder-blasted cavity in bottom-glass spacer (Scale bar = 500 μm).

The glass wafers that were used for producing the caps and the spacers measured 500 μm in thickness. These could of course be thinner and were used here due to

availability. Better control of the powder blasting may have been attained using a dry film resist instead of the tape and this would have allowed for more accurate definition of the area to be powder blasted [13, 14].

In the layout, two sets of bond pads were used for electrical connection off the chip as shown in Figure 6.34(a). The larger set on the left measure 100 μm in width and were spaced 50 μm apart and these were included to be used for the purpose of wirebonding and characterisation. The other set to the right measured 50 μm in width and were spaced 21 μm apart. This set was included for the purpose of bonding to a micro-ribbon cable and intended for the sensor final application as a heart sensor. This is discussed further in Section 6.4.

The chips chosen for characterisation were glued and wirebonded into side-brazed Dual In-line Packages (DIP's) as shown in Figures 6.34(b) and 6.35.

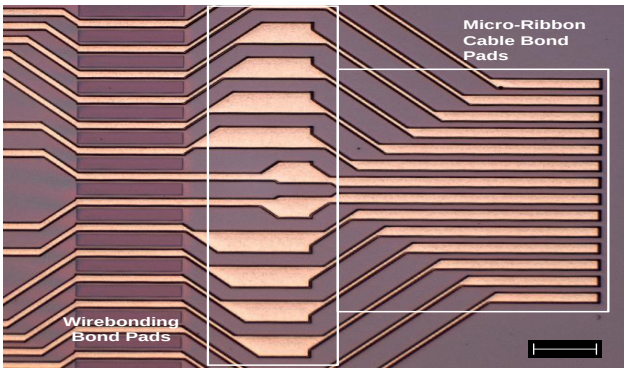

(a)

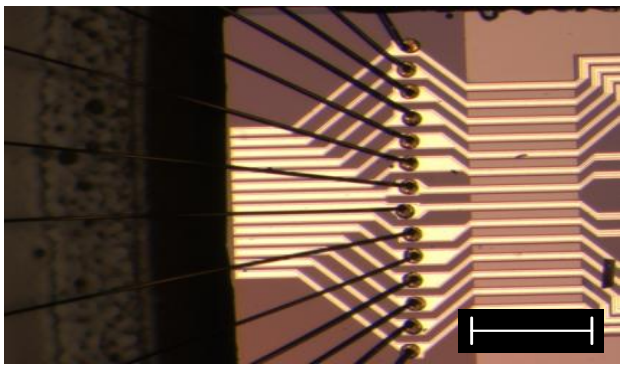

(b)

Figure 6.34: (a) Two sets of bond pads of the SMC Design (Scale bar = 250 μm). (b) Wirebonded SMC Design (Scale bar = 500 μm).

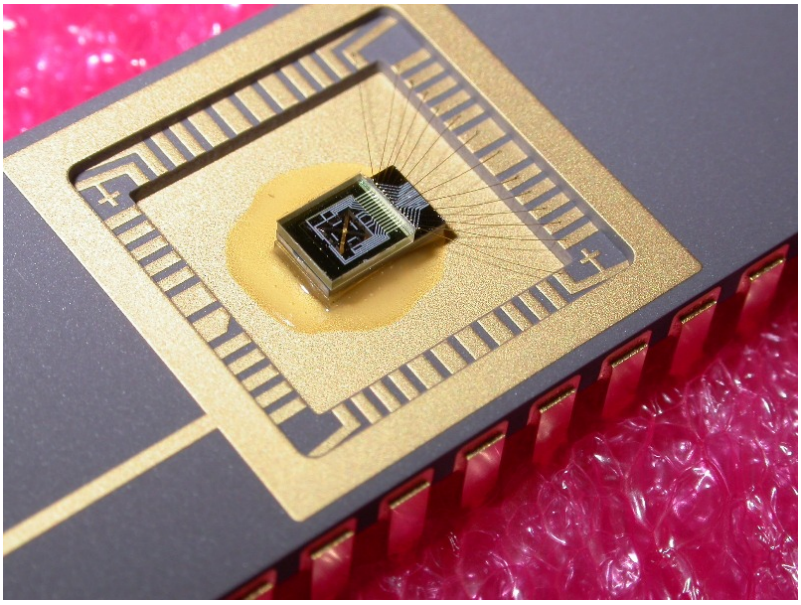

Figure 6.35: SMC sensor glued and wirebonded into chip carrier.

6.4 Second generation packaging

As discussed previously the SMC designs include two sets of bond pads with the smaller bond pads measuring 50 μm in width and spaced 21 μm apart. The reason for this arrangement was to avoid the need for the sensor to be glued to a carrier substrate and for the bond pads to be wirebonded to this substrate. Instead, the connections from the cable to sensor would be directly bonded on the sensor and therefore helps reducing greatly the overall size of sensor. The narrowness of the footprint of these bond pads also means that the overall width of the sensor would not be dictated by the pad dimensions.

This interconnect must exhibit good mechanical strength such that it can withstand being pulled free of the stitches holding it to the heart of the patient and then out of the patient's chest.

Two further approaches were studied by the team: wedge bonding and Non-Conductive Adhesive (NCA) flip-chip interconnection. Both techniques demonstrated encouraging results and some initial results that have been published are shown in Figure

6.36 [15]. A downside of the wedge bonding approach is that it involves bonding each of the wires of the ribbon cable individually. A limiting factor of the bonding with NCA technique is that it requires critical alignment of the cable and the substrate.

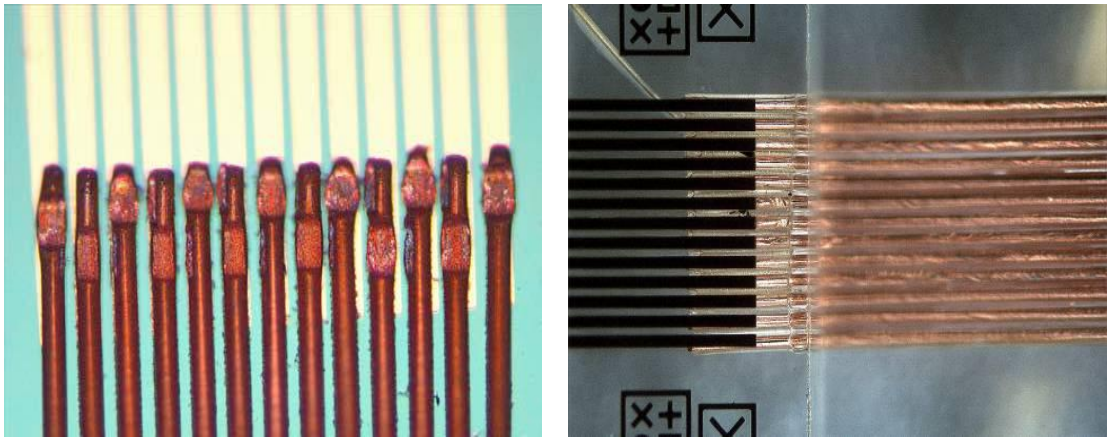

(a) (b)

Figure 6.36: Images of a (a) wedge bonded ribbon cable, and (b) NCA bonded cable [15].

As the sensors are meant to operate *in vivo*, the final step to make the sensors suitable for clinical studies is to make them biocompatible.

The material to be used for the final packaging step had to be approved for at least 29 *days* of implantation, be electrically insulating and prevent body fluid from penetrating. It was decided that silicone would be the material of choice because it is a well established material for use in invasive devices and it is suitable for prototyping and moulding.

To minimise the injury to the heart and the surrounding body tissues, an encapsulation with a round shape was preferred. Combined with a smooth surface, this shape also ensures easy and proper cleaning. A reliable fixation to the heart was important to minimise the self-motion of the sensor, which could interfere with the sensor signals and cause misinterpretations of the data. The sensor is to be fixed to the heart surface by sutures. The encapsulation was therefore designed with suture holes at each corner as shown in Figure 6.37.

To mould the silicone around the sensor, a two-part negative mould was milled out of aluminium and squeezed together, by use of a clamp, and placed in a heating chamber. The assembly was pre-cured at $145°C$ for 2 $hours$. The sensor was removed from the mould and post cured for 7 $days$ at $145°C$. In order to obtain good sealing between the silicone and the cable, a primer was applied to the cable, substrate and components and allowed to dry for 15 $mins$ at $100°C$ prior to moulding.

The assembly of the sensor was carried out in a non-sterile environment. It was thus necessary to clean the sensor and part of the cable with 100% isopropanol to remove surface contamination prior to moulding. The sterilisation procedure selected was low-temperature hydrogen peroxide gas plasma method. This method has a short cycle time (less than 1 $hour$), low process temperature and humidity and is also compatible with a wide range of materials, among them being silicone [16].

Figure 6.37: Schematic of the silicone moulded sensor.

6.5 Summary and conclusions

Two fabrication processes were presented in this chapter. The first process was using the MultiMEMS MPW foundry service based on the established process from

SensoNor Technologies AS whilst the second process was provided by SMC.

The MultiMEMS process used standard silicon wafers together with an anisotropic chemical etch and an ECES approach. This approach allowed for the n-type epitaxial layer grown on the front side of the wafer to represent the thin beams whilst implanted n-wells defined the seismic masses. The SMC process used SOI wafers together with a DRIE whilst using the BOX layer as an etch-stop mechanism due to etch selectivity. The thin beams and the seismic masses were defined using the silicon device and silicon handle layers of the wafer respectively. The seismic masses had the full wafer thickness rather than the depth of the n-wells and had near vertical sidewall profiles.

Both processes used implanted piezoresistors as a means of measuring acceleration. Interconnection of these piezoresistors as well as connection to the wirebond pads was achieved using implanted conductors as well as deposited metal conductors. The MultiMEMS process had an additional implanted conductor process step to offer conductors that are diffused deeper into the silicon to guarantee a planar surface in the packaging bonding areas.

The MultiMEMS MPW process was a good introductory process for the fabrication of the accelerometers. The process is based on the SensoNor foundry process and as such is very stable having been built on over 40 years of knowledge in piezoresistive fabrication. Having followed strict design guidelines, a high yield was achieved with the MultiMEMS fabricated designs. An approach to achieve full wafer thickness masses was however not a success. This SMC process followed the same process as the MultiMEMS with the exception of a backside etch that was not a standard offering.

To avoid the uncertainties of trying to achieve full wafer thickness masses using a wet anisotropic etch together with compensation structures to protect the convex corners of the seismic masses, a process that used DRIE was used to define the seismic

masses. The outcome from the SMC process was that it was difficult to achieve a good yield. The primary reason for this was due to wafer thickness variation which resulted in some structures not being fully released. The partially released structures suffered from the introduction of stress intensity factors leading to fracturing of the beams, and to over-etching which narrowed the width and thicknesses of the beams leading ultimately to breakages.

In addition a mask was reused by accident in the processing and this resulted in the metal conductors having the same layout as the implanted conductors. The spacing between the metal tracks was then compromised and made the electrical behaviour of the sensors uncertain. It also resulted in metal being present on the beams which potentially could lead to a change in the mechanical behaviour of the beams.

The MultiMEMS designs were packaged at wafer-level using anodic bonding of glass wafers with cavities etched into them. These were then diced to free the individual chips and resulted in a high yield. The SMC designs were packaged at chip-level due to lack of resources. This was performed using a low-temperature polymer based bonding method using BCB to form a glass-silicon-glass stack. A benefit of this process was that bonding could take place directly on top of the metal conductors routed out to the bond pad area, thus simplifying the overall packaging process.

Biocompatible packaging to make the sensor suitable for *in vivo* applications was also presented as well as the use of micro-ribbon cable to reduce the necessary cable termination area and thus the overall size of the sensor solution.

References

[1] Sintef MiNaLab website. `http://www.sintef.no/Home/Information-and-Communication-Technology-ICT/Microsystems-and-Nanotechnology/Home-Microsystems-and-Nanotechnology/` (Accessed: 07 Oct 10).

[2] MultiMEMS website. `http://www.multimems.com/` (Accessed: 07 Oct 10).

[3] SensoNor Technologies Website. http://www.sensonor.com. (Accessed: 07 Oct 10).

[4] H. Jakobsen and D. Lapadatu. Building of silicon sensors by micromachining of bulk silicon and anodic bonding. *Phys. Scr.*, 79:32–41, 1999.

[5] MultiMEMS. *MultiMEMS Design Handbook*. Third edition, 2003.

[6] K. Lian. Development and characterisation of anisotropic silicon etching for MEMS using TMAH. Master's thesis, Edinburgh University, 1999.

[7] O. Tabata, R. Asahi, H. Funabashi, K. Shimaoka, and S. Sugiyama. Anisotropic etching of silicon in TMAH solutions. *Sensors and Actuators A: Physical*, 34(1):51–57, July 1992.

[8] Maluf N.I. Kovacs, G.T.A and K.E. Petersen. Bulk micromachining of silicon. *Proc. of the IEEE*, 8(86):1536–1551, August 1998.

[9] B. Kloeck, S.D. Collins, N.F. de Rooij, and R.L. Smith. Study of electrochemical etch-stop for high-precision thickness control of silicon membranes. *IEEE Transactions on Electron Devices*, 36(1):663–669, Apr. 1989.

[10] E.D. Palik, J.W. Faust Jr., H.F. Gray, and R.F. Greene. Study of the etch-stop mechanism in silicon. *J. Electrochem. Soc.*, 129(9):2051–2059, 1982.

[11] C.H. Wang, J. Zeng, K. Zhao, and H.L. Chan. Chip scale studies of BCB based polymer bonding for MEMS packaging. In *Electronic Components and Technology Conference, 2008. ECTC 2008. 58th*, pages 1869 –1873, 27-30 2008.

[12] F. Niklaus, P. Enoksson, E. Kalvesten, and G. Stemme. Low-temperature full wafer adhesive bonding. *J. Micromech. Microeng.*, 11(2):100–107, 2001.

[13] Ki-Il. Kim, Jung-Mu. Kim, Jong-Man. Kim, Gun-Chul. Hwang, Chang-Wook. Baek, and Yong-Kweon Kim. Packaging for RF MEMS devices using LTCC substrate and BCB adhesive layer. *J. Micromech. Microeng.*, 16(1):150–156, 2006.

[14] A. Baram and M. Naftali. Dry etching of deep cavities in pyrex for MEMS applications using standard lithography. *J. Micromech. Microeng.*, 16(11):2287–2291, 2006.

[15] K. Imenes, K. Aasmundtveit, G. Bjornsen, P. Moreno, and J.R.V. de Aldana. Micro ribbon cable bonding for an implantable device. In *Electronics System-Integration Technology Conference, 2008. ESTC 2008. 2nd*, pages 265 –270, 1-4 2008.

[16] K. Imenes, K. Aasmundtveit, E.M. Husa, J.O. Hogetveit, S. Halvorsen, O.J. Elle, P. Mirtaheri, E. Fosse, and L. Hoff. Assembly and packaging of a three-axis micro accelerometer used for detection of heart infarction. *Biomedical Microdevices*, 9(6):951–957, December 2007.

Chapter 7

Characterisation of a Micromachined Three-Axis Accelerometer

7.1 Introduction

The characterisation of the sensors is split into two parts which are both presented in this chapter. The first approach looks at the dynamic mechanical characterisation of the sensors whilst the second part looks at the dynamic electrical characterisation of the sensors. The necessary preparations and setup for each of these approaches are introduced in Section's 7.2 and 7.3, respectively, as well as the obtained results and discussion.

7.2 Dynamic Mechanical Characterisation

This part of the chapter looks at characterising the dynamic mechanical behaviour of the different versions of sensors. A Polytec MicroSystem Analyser (MSA) was used to measure the velocity and acceleration response of the mechanically driven devices [1]. This equipment is capable of measuring in-plane and out-of-plane displacements using stroboscopic and vibrometry techniques, respectively. To achieve this, die were fixed to miniaturised PieZoElectric (PZE) actuators to create the input stimuli. The results obtained are compared to the results obtained from the FEA results in Chapter 5.

7.2.1 Measurement setup

The equipment used for the measurements is a Polytec MSA-400 accessible at the National Physical Laboratories (NPL). Images of the setup can be seen in Figure 7.1 [2]. A summary of the capabilities and benefits of using this equipment is as follows:

- Doppler vibrometry and stroboscopic video. The rapid movements of the sensor are frozen with short stroboscopic bursts of light and the images are recorded with a synchronised video camera. The video stroboscopic microscopy technique measures the in-plane deformations. The Doppler technique measures out-of-plane deformations.
- Non-contact and zero mass-loading method avoiding thereby damage to the free-standing sensitive structures.
- Short setup and measurement time enable many measurements to be taken quickly.
- The system quickly identifies and allows a visualisation of all of out-of-plane and in-plane resonances.
- It is possible to integrate the setup it with most probe stations.

The MSA optical unit is made up of a compact sensor head, an optimised integration of vibrometer scanning optics, video stroboscope and microscope optics, and the fibre-optic laser interferometer for vibrometer measurements. It is possible for the scanning interferometer to make differential measurements using two laser beams. By measuring the relative movement between two sample points, undesired whole body or common-mode movements are eliminated. The high-resolution video display on the sensor head is used to visualise both the object under investigation and the measurement process. Thus, the reference beam can be positioned at a suitable

point and the measurement grid can be defined and oriented with respect to the object under investigation.

Electromechanical shaking of the sensors is needed to measure their vibrational modes. Two PZE actuator based shaking platforms were built and tested, for in- and out-of-plane activation [3]. These actuators were screwed to an adjustable XY stage that was fixed inside the environmental chamber as shown in Figure 7.1(b). The necessary electrical connections to the adjustable stage and the actuator were made possible using ports in the chamber in compliance with vacuum testing.

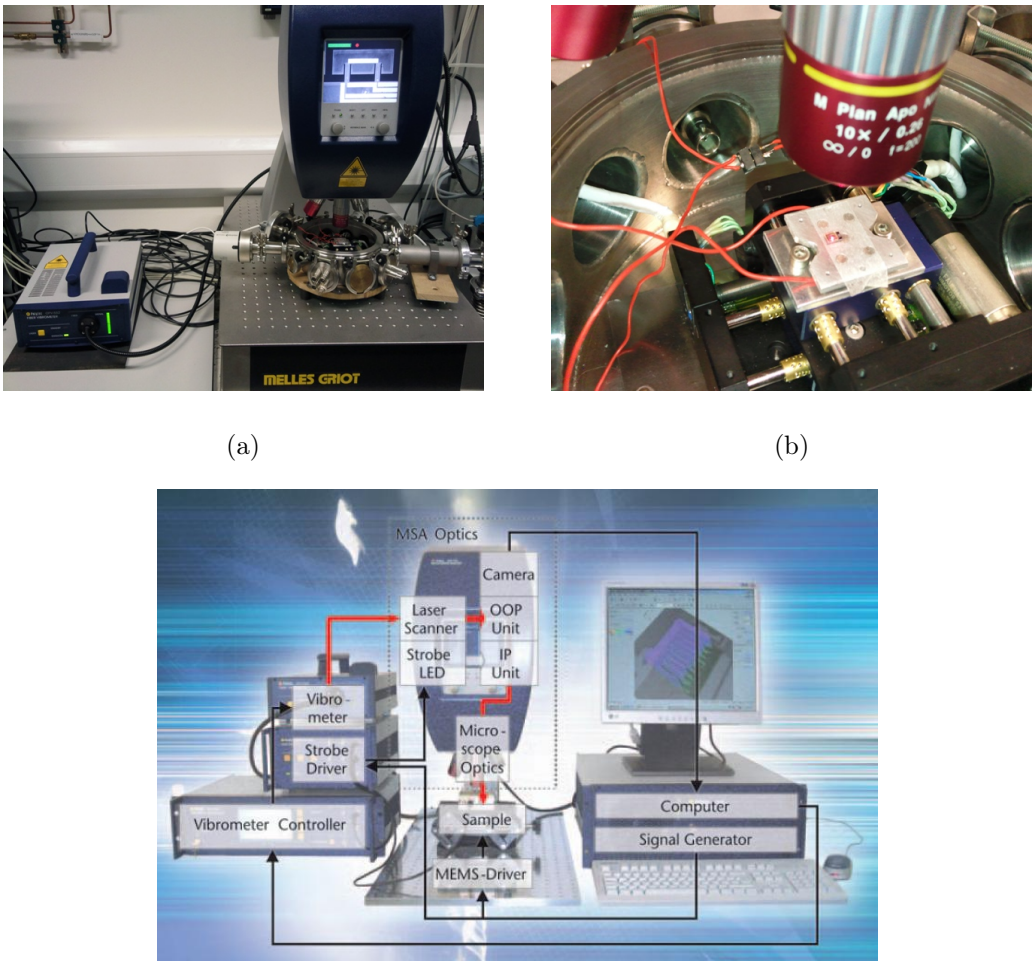

(a) (b)

(c)

Figure 7.1: (a) Optics with video display, vibrometer, and environmental chamber of the Polytec MSA. (b) Close-up of sensor fixed to a PZE actuator and placed on stages inside the chamber. (c) Complete setup of the MSA [4].

The next stage of the setup was to fix the sensors to the PZE actuators to ensure that the whole chip did not move when excited. It was also desirable to remove the sensor under test from the actuator without damaging it. Only the mechanical behaviour of the chips was going to be characterised with this approach and as such it was decided to avoid the possibility of introducing many extra resonant modes when using a Dual In-line Package (DIP) socket mount. As a result of this it was decided just to mount the actual sensors directly on the actuators.

Temporary bonding approaches such as double-sided adhesive, vacuum grease and acoustic couplant were investigated and were found to provide suitable out-of-plane mechanical transfer for the small silicon die. However, in shear mode it was discovered that the acoustic couplant was not suitable and, as a result, double-sided adhesive from 3M was used throughout the measurements.

7.2.2 Dynamic Mechanical Results

In the follow sections, the results obtained from the MSA are presented and compared to the results obtained from the FEA previously presented in Chapter 5. The MultiMEMS Design as well as SMC Design 1 are considered. Note that the results were recorded with the top cover of the vacuum chamber left open i.e. not in a vacuum environment.

An area of interest on the sensor was brought into view and focused using the 10X objective typically. A scanning grid with an appropriate density was then defined across the beams and masses of the captured structures. It was possible to have up to 512×512 measurement points and the decision on the value implemented was in accordance with how much of the location of the grid was of interest. A suitable frequency range together with frequency increments was then selected for the acquisition settings. At this point it was useful to draw on experience from the FEA results in that it was possible to identify the existence of a mode in a frequency

range of say $\pm 500\ Hz$ of the FEA result. This would originally be done using larger frequency increments and then decreased to the order of $1/64\ Hz$. The decisions on the grid density, frequency range and frequency increments directly affect the processor requirements and time for processing. As such a balance had to be found in achieving reliable results and not wasting unnecessary computation time. Suitable voltage input and acceleration values were also chosen here for the generator used to power the actuator. The maximum value possible here is $10\ V$ but a value of around $2\ V$ was typically used with this value decided upon by experiment.

It is possible to view these results in video format but, in this thesis, image files have been used which could also be viewed with 3-D rotation as well as zooming, if the thesis were to be provided in an electronic format.

MultiMEMS sensor design

For the MultiMEMS Design a single pair of masses was focused upon and the first four modes of each mass were studied. Results are shown in Figures 7.2 to 7.5. In these figures, images captured from the Polytec equipment are displayed together with images from FEA of corresponding modal shapes. The purpose of this is to demonstrate that the corresponding results show that the modal shapes match albeit with some phase difference. It was only necessary to concentrate on out-of-plane measurements because it is known from the knowledge gained from the FEA simulations that neither of these modes contain significant in-plane deformations.

A summary of all these results is given in Table 7.1 which show close agreement between simulation and measurement. Any discrepancies are noted to be well within tolerances of manufacturing. From the figures it is possible to see that the modal shapes obtained with this approach match the simulated results albeit with some phase difference in some cases.

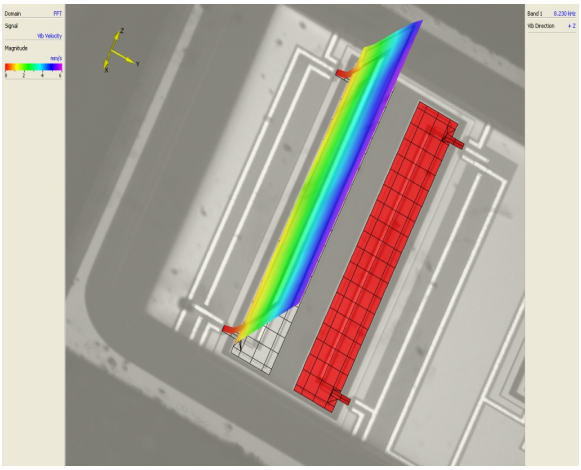

(a)

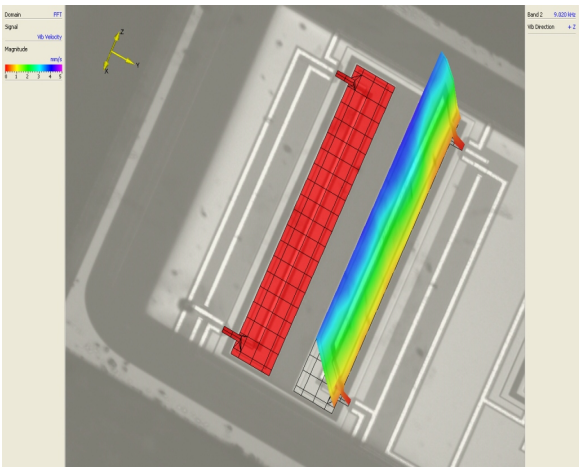

(b)

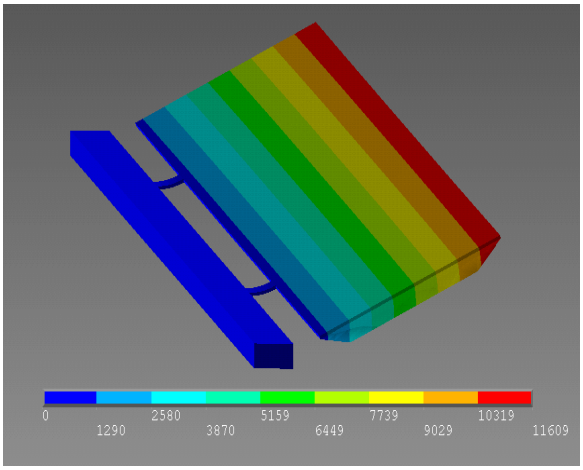

(c)

Figure 7.2: Shapes of the (a) measured 1^{st} mode for one mass at 8.23 kHz, (b) measured 1^{st} mode for the other mass at 9.02 kHz and (c) ANSYS simulated 1^{st} mode at 7.07 kHz for the MultiMEMS Design.

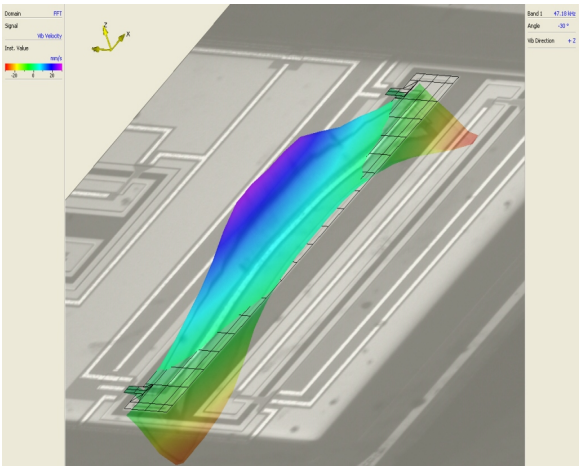

(a)

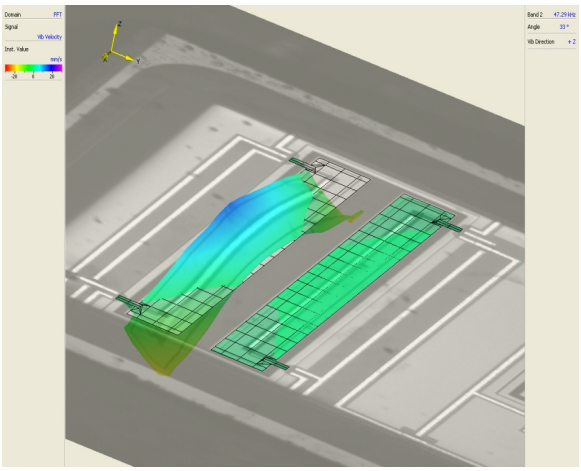

(b)

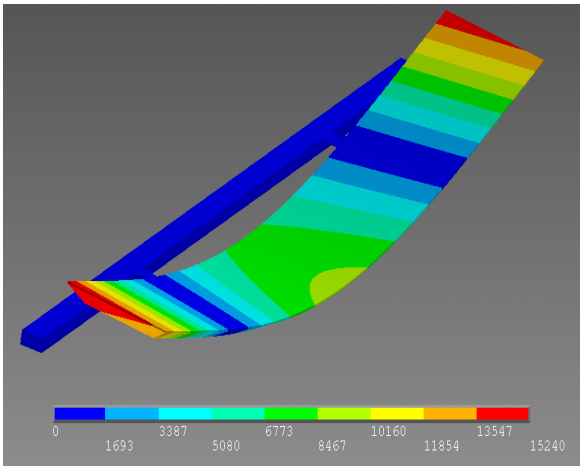

(c)

Figure 7.3: Shapes of the (a) measured 2^{nd} mode for one mass At 47.18 kHz, (b) measured 2^{nd} mode for the other mass at 47.29 kHz and (c) ANSYS simulated 2^{nd} mode at 44.88 kHz for the MultiMEMS Design.

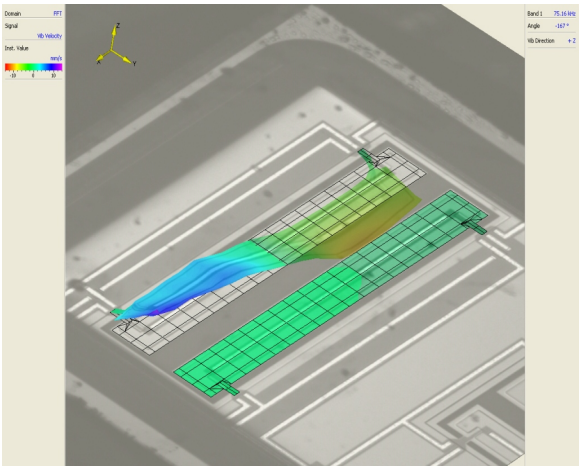

(a)

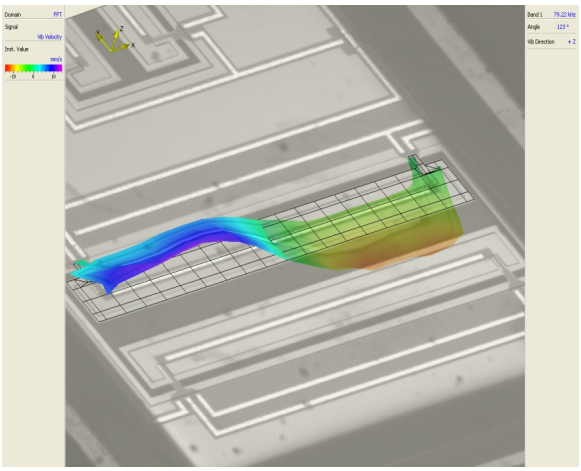

(b)

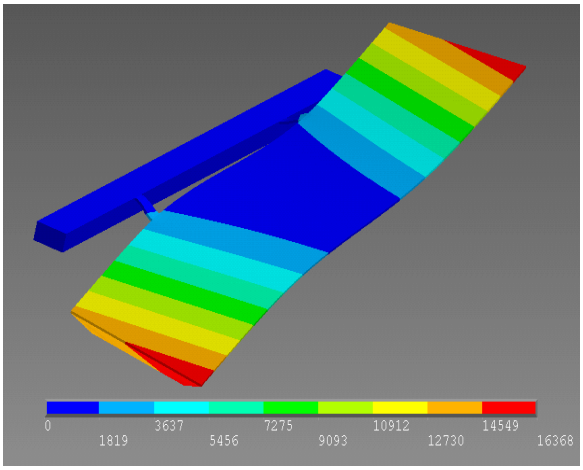

(c)

Figure 7.4: Shapes of the (a) measured 3^{rd} mode for one mass at 75.16 kHz, (b) measured 3^{rd} mode at 79.22 kHz for the other mass and (c) ANSYS simulated 3^{rd} mode at 78.67 kHz for the MultiMEMS Design.

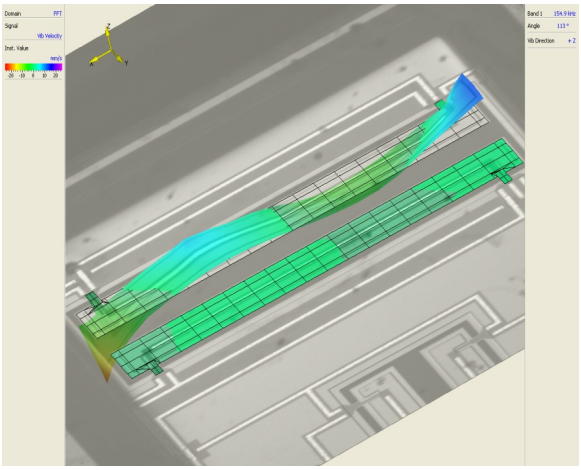

(a)

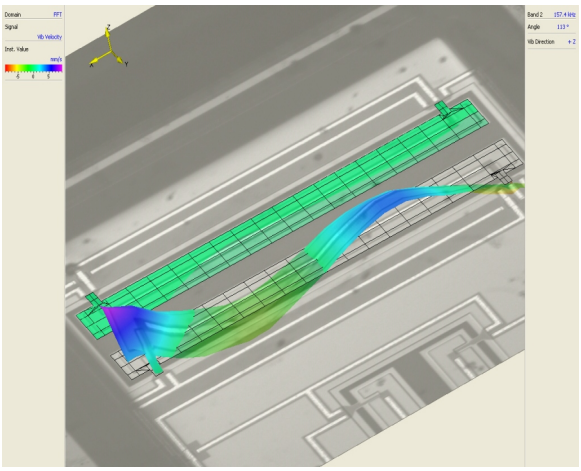

(b)

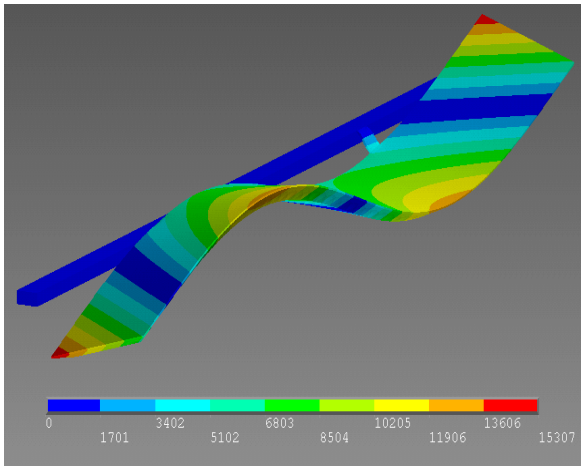

(c)

Figure 7.5: Shapes of the (a) measured 4^{th} mode at 154.90 kHz for one mass, (b) measured 4^{th} mode at 157.40 kHz for the other mass and (c) ANSYS simulated 4^{th} mode at 155.05 kHz for the MultiMEMS Design.

Mode	ANSYS Freq. (kHz)	Polytec Freq. 1 (kHz)	Polytec Freq. 2 (kHz)
1st Mode	7.073	8.230	9.020
2nd Mode	44.882	47.18	47.29
3rd Mode	78.674	75.16	79.22
4th Mode	155.05	154.9	157.4

Table 7.1: Comparison of the modal frequency values of the MultiMEMS Design obtained from the Polytec Micro-System Analyser and ANSYS simulations. "Polytec Freq. 1" and "Polytec Freq. 2" represent the values for the different masses of the pair.

SMC sensor design

Only the results from SMC Design 1 are presented here in this sub-section.

A single mass was focused upon and the first four modes of the mass were then studied. The results are shown in Figures 7.6 to 7.9. Again, as with the MultiMEMS Design, it was only necessary to concentrate on out-of-plane measurements.

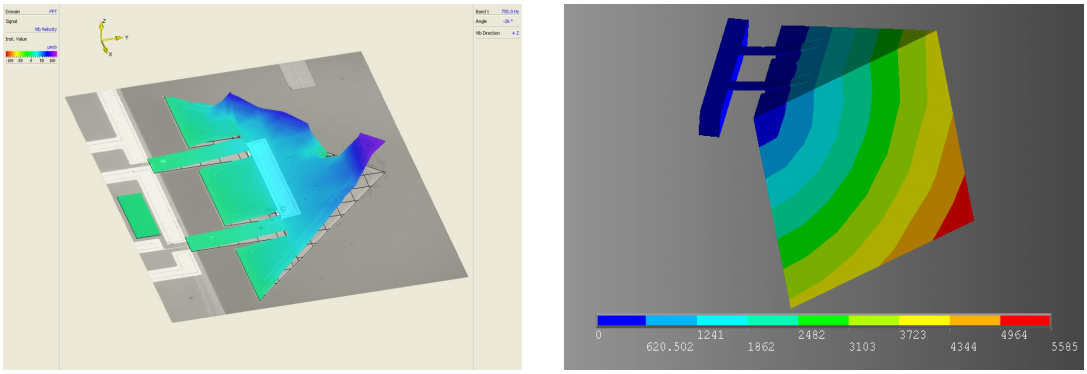

(a) (b)

Figure 7.6: 1st mode shapes from (a) the measurement at 0.75 kHz, and (b) the ANSYS simulated result at 1.29 kHz for SMC Design 1.

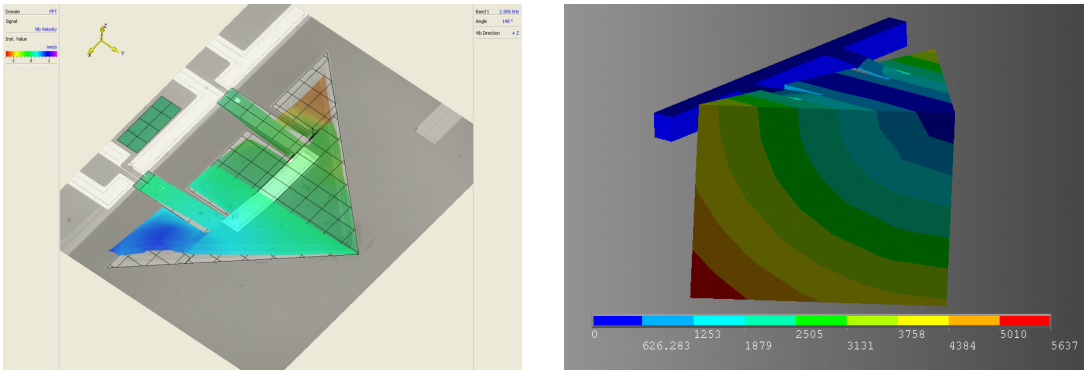

(a) (b)

Figure 7.7: 2^{nd} mode shapes from (a) the measurement at 2.00 kHz, and (b) the ANSYS simulated result at 3.71 kHz for SMC Design 1.

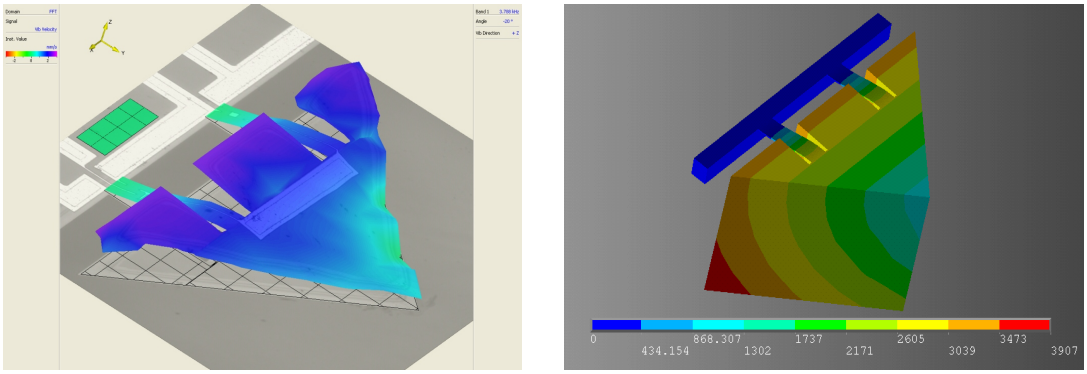

(a) (b)

Figure 7.8: 3^{rd} mode shapes from (a) the measurement at 3.78 kHz, and (b) the ANSYS simulated result at 6.70 kHz for SMC Design 1.

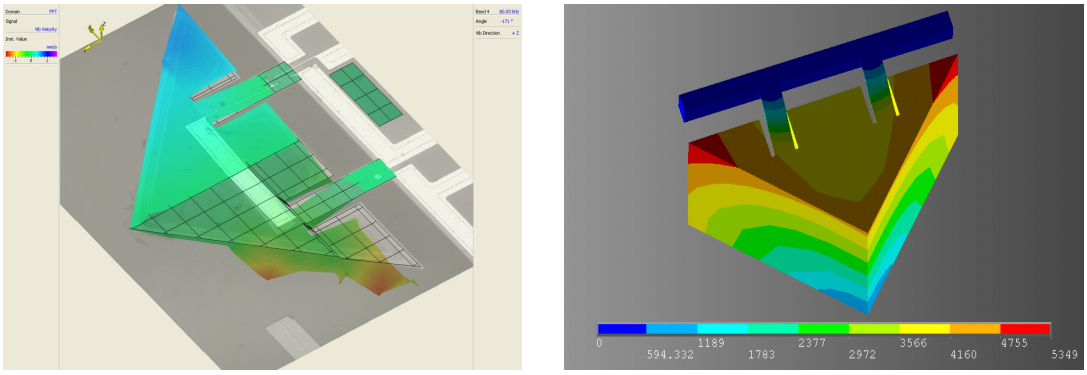

(a) (b)

Figure 7.9: 4^{th} mode shapes from (a) the measurement at 80.80 kHz, and (b) the ANSYS simulated result at 101.67 kHz for SMC Design 1.

A summary of all of these results is given in Table 7.2. The results do not match each other well. Figures 7.6 to 7.8 show that the modal shapes are the same as the simulated ones but this is not the case for Figure 7.9. The approach used to simulate these modal shapes is verified by the close results obtained from the MultiMEMS Design. As discussed previously, problems were encountered with the fabrication process and in particular the etching. The manufactured free-standing structures are not those designed, which makes characterisation of their dynamic behaviour difficult to model and leads to large discrepancies in the comparison of simulated and measured results.

Mode	**ANSYS Frequency** (kHz)	**Polytec Frequency** (kHz)
$\mathbf{1}^{st}$ **Mode**	1.293	0.750
$\mathbf{2}^{nd}$ **Mode**	3.709	2.000
$\mathbf{3}^{rd}$ **Mode**	6.695	3.780
$\mathbf{4}^{th}$ **Mode**	101.671	80.800

Table 7.2: Comparison of the frequency values obtained from the Polytec MSA and the ANSYS simulated results for the 1^{st} four modes.

Results obtained using a Polytec Micro System Analyser have been presented in this chapter for the MultiMEMS Design and SMC Design 1. This characterisation tool incorporates vibrometry as well as stroboscopic techniques to measure out-of-plane and in-plane deformations, respectively. The sensor chips were fixed to PZE actuators to mechanically excite the free-standing structures. Double-sided adhesive tape was found to be the best option to fix the sensors in this instance. The actuator with the mounted sensor was then fixed to a movable stage and placed under the optical setup of the analyser.

The measured results from the MultiMEMS Design match up well with the FEA simulated results. Any variations can be attributed to fabrication variations where the structures have slight dimensional variations compared to the designed values.

For the SMC devices, large deviations between simulated and measured frequencies were obtained due to fabrication problems as described in Chapter 6. In one case the mode shape was even not the same.

It would be possible to break a mass from a die. The mass could then be placed in a SEM and the cross-section of the mass could be measured to give a better idea of the structure of the seismic mass following fabrication. These results together with interferometer results that profile the shape of the beams and the mass could then be inputted into FEA with the outcome likely to be closer to the measured results. These results ultimately indicate problems with the fabrication process.

7.3 Dynamic Electrical Characterisation

In this part of the chapter, the effect that the displacement of the structures has on the stress-induced electrical output of the Wheatstone bridges is studied.

For this characterisation, the sensors are glued and wirebonded in DIPs soldered onto Printed Circuit Boards (PCBs) together with potentiometers. The PCBs are then screwed to an aluminium frame which is in turn screwed onto a shaker. The output from the sensor is connected to a strain gauge bridge which is connected to an amplifier. From here the output is measured and visualised using an oscilloscope or spectrum analyser depending on the type of measurements being undertaken.

No results were obtained from the SMC designs and this chapter will only concentrate on the MultiMEMS Design. The reason for the lack of data from the SMC die is due to the faulty fabrication process of the sensors as discussed in Chapter 6. Resistivity measurements were performed between appropriate bond pads on various SMC chips and demonstrated that the chips were not electrically active. It was therefore decided not to proceed with these measurements.

A more detailed discussion of the preparation of the sensors and setup is now pre-

sented followed by the results obtained at a fixed frequency and for a broad spectrum of frequencies.

7.3.1 Measurement setup

The setup can be seen in Figure 7.10. The main component of the setup is the LDS V406 shaker suitable for frequencies of 5 to 9000 Hz [5]. The signal for the shaker was generated by a Farnell LFM4 sine square oscillator together with an amplifier. An Endevco 236 ISOBASE PZE accelerometer [6] was used to measure the output of the shaker together with a Bruel & Kjaer 2626 charge conditioning amplifier used for the calibration of the reference accelerometer [7]. The input and output signals were controlled and measured respectively using a strain gauge and the corresponding signals to and from the sensor were connected to the terminals of the strain gauge. The strain gauge was then connected to an amplifier for control of the voltage input and the bias. The output signal from this amplifier and the output signal from the reference sensor amplifier were then connected to a Tektronix TDS3014 oscilloscope via BNC cables [8].

A TDS3FFT FFT application module for the oscilloscope together with a Tabor 8550 modulated function/pulse generator capable of sweep operating mode were used for the spectrum measurements.

7.3.2 Sensor preparation

The next step for this characterisation was to find a way of fixing the sensors to the shaker securely to supply the input electrical signals and measure the output electrical signals generated. To achieve this the sensors were glued and wirebonded into DIPs. The generated DIPs were soldered onto PCBs employed to provide mechanical stiffness. On the PCBs, conductive tracks were patterned on the backside to provide the necessary electrical connections from the pins of the DIP socket to

the pads on the PCB. Into the PCB, holes were drilled for the placement of the DIP and the necessary components were then fixed in place by soldering. The use of a socket for the DIPs enables the measurement of several chip designs with the same platform. Photographs of a completed board can be seen in Figure 7.11.

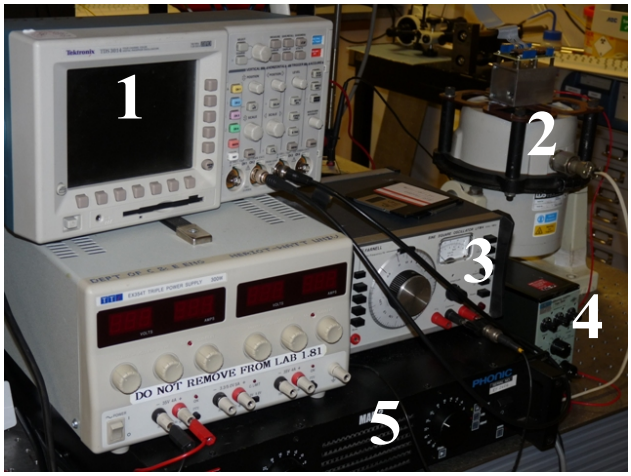

(a)

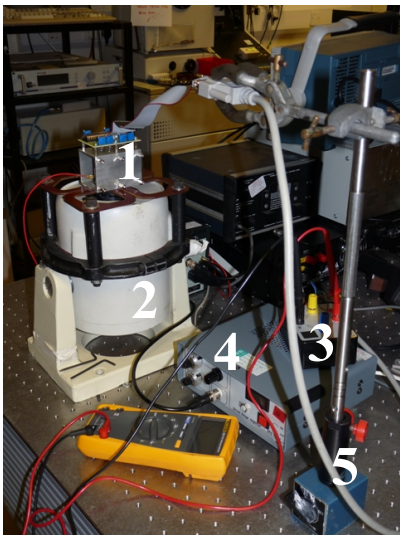

(b)

Figure 7.10: Photographs of the setup used to take the electrical measurements: (a) **(1)** oscilloscope, **(2)** shaker with the sensor mounted, **(3)** signal generator, **(4)** signal conditioning amplifier for the reference accelerometer, **(5)** amplifier; (b) **(1)** sensor with ribbon cable mounted on the shaker, **(2)** shaker, **(3)** strain gauge bridge, **(4)** strain gauge amplifier, **(5)** setup to isolate vibrations from the cable carrying the input and output sensor connections.

The components visible in Figure 7.11 are potentiometers used to balance the Wheatstone bridges across the terminals of the strain gauge. The resistance across each of the arms of the bridge was measured using a multimeter across the terminals of the strain gauge.

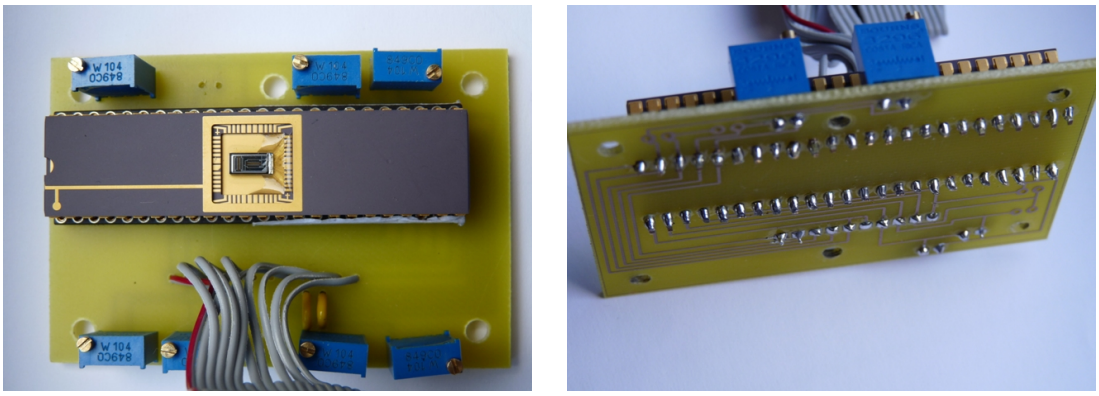

(a) (b)

Figure 7.11: Photographs of MultiMEMS sensors and associated components soldered onto PCBs from (a) the top side, and (b) the bottom-side.

A flexible short 25-way ribbon cable was chosen due to the vibration from the shaker. The ribbon cable was stripped at one end for soldering to the PCB. The other end was fitted with a female D-connector. A 25-way shielded cable with a male D-connector was employed for further connection to the setup from the PCB. The mated connectors were then suspended in the air using a magnetic stand to keep the cables from coming into contact with the common surface of the shaker as shown in Figure 7.10(b). The other end of this cable had its wires exposed and crimped with spade terminals for good connection to the strain gauge bridge terminals.

The sensor PCB was then fixed to the shaker using a machined aluminium frame as shown in Figure 7.12. The PCB was screwed in six places to pillars on the frame via drilled holes in the PCB to be securely fixed whilst also allowing the sensor under test to be simply changed. The aluminium frame was machined to allow the possibility for the board to be mounted on a different level on the frame to allow measurement of in-plane characteristics. Moreover, the fixture of a commercial accelerometer to

the frame was accommodated to act as a reference sensor to measure the acceleration from the shaker as shown in Figure 7.12(b).

Once the sensor PCB was fixed to the shaker, resistivity measurements were taken across the terminals of the strain gauge using a multimeter whilst the sensor was at rest. The potentiometers on the PCB were then adjusted accordingly to achieve matching resistivity. The amplifier, with full amplification, was then switched on and the bridge supply voltage increased whilst adjusting the offset until the maximum voltage, that still allowed for zero offset, had been reached.

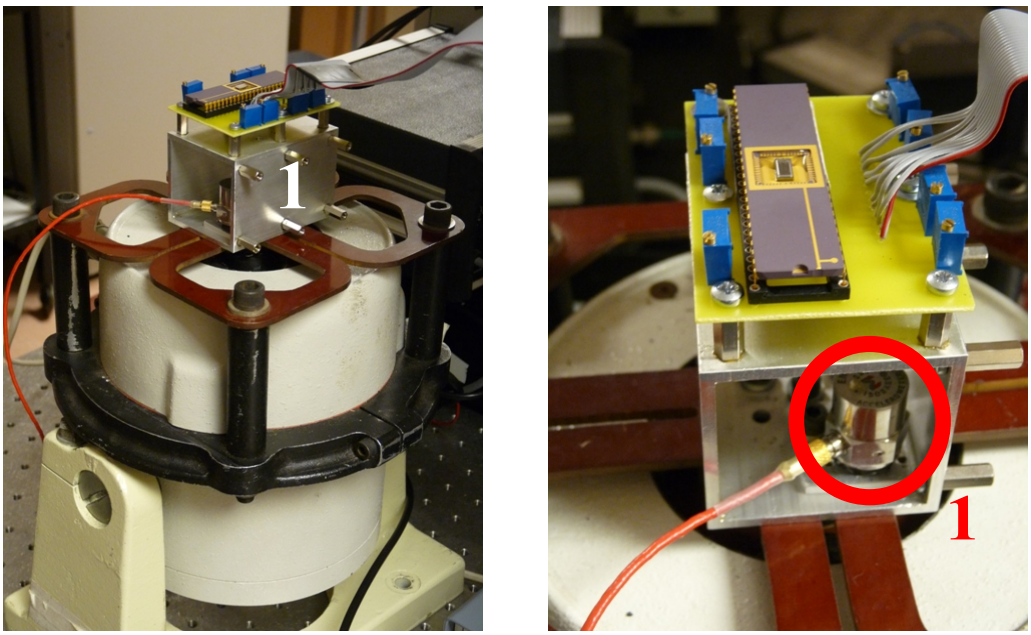

(a) (b)

Figure 7.12: Photographs of the (a) sensor mounted onto shaker **(1)**, and (b) the sensor fixed to frame with reference accelerometer **(1)**.

7.3.3 Fixed-frequency measurements

The sensor PCB was mounted onto the aluminium frame on the shaker in order to study the direction of excitation. The sensor was then balanced and the voltage supply and offset adjusted as discussed earlier. The necessary settings were then applied to the signal generator and the signal conditioning amplifier to power the

shaker at a chosen frequency. Using the oscilloscope, the amplifier for the shaker was adjusted until the desired acceleration was reached for each of the measurements.

Measurements were taken at frequencies of 100 and 1000 Hz at acceleration levels of 1, 5, 10, and 20 g. The largest value of 20 g for the acceleration was chosen because above this value an unwanted vibration was introduced by the test board mounting. Also, no measurements were taken at a resonance frequency because the frequency value of this is far beyond the intended operation of the sensor designs.

An example image captured from the oscilloscope can be seen in Figure 7.13. Note that the top waveform (in blue) is from the reference accelerometer and the bottom waveform (in green) is from the sensor being tested. To the right of these waveforms are the frequency and peak-to-peak voltage of each of the waveforms in their respective colour of text. 1 V output from the reference accelerometer was set to be equivalent to 1 g of acceleration and this holds for all of the oscilloscope plots in this chapter i.e. 20 V_{pk-pk} is equivalent to 20 g of acceleration.

MultiMEMS design out-of-plane acceleration sensing bridge

The voltage outputs from the reference accelerometer and the MultiMEMS design can be seen in Figures 7.13 and 7.14 for 20 g of acceleration at 1000 Hz and 20 g of acceleration at 100 Hz, respectively.

The peak-to-peak output values for all of the measurements have been collated in Table 7.3. These values are plotted for each frequency in Figure 7.15 with linear trend lines applied to each data set.

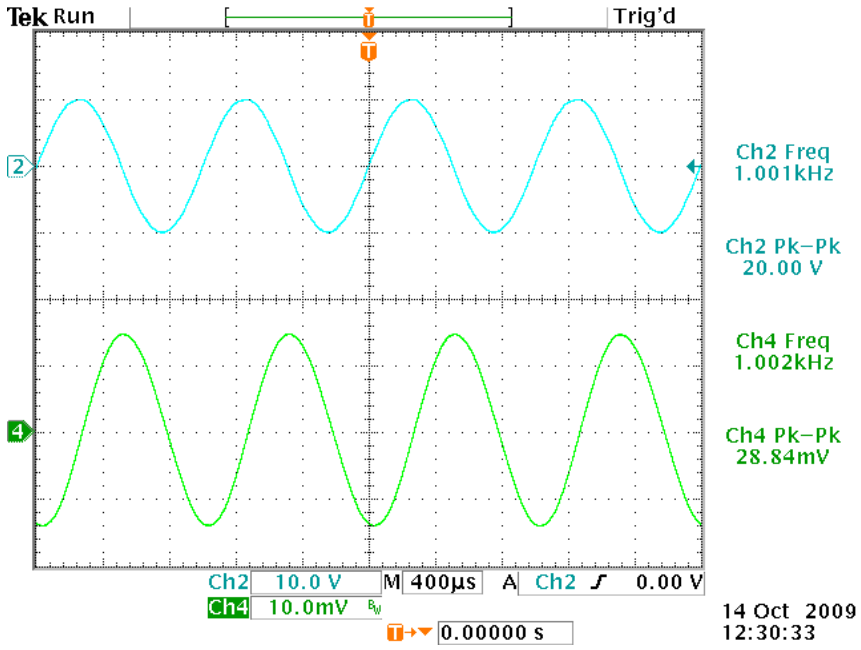

Figure 7.13: Voltage output from a MultiMEMS sensor out-of-plane acceleration sensing bridge for 20 g of acceleration at 1000 Hz.

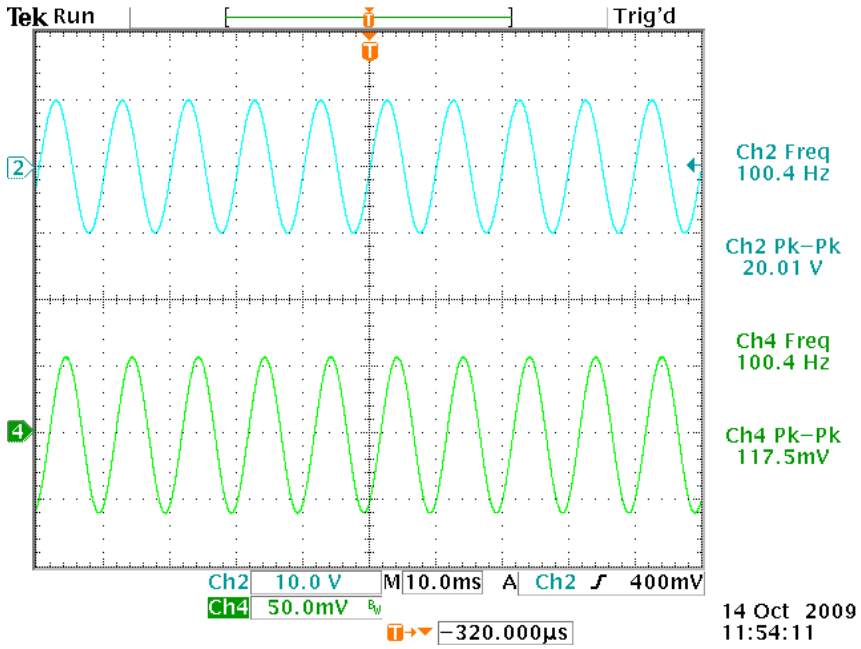

Figure 7.14: Voltage output from a MultiMEMS sensor out-of-plane acceleration sensing bridge for 20 g of acceleration at 100 Hz.

In Figures 7.13 and 7.14 it can be seen that the output of the sensor being tested lags from that of the reference accelerometer. It can be hypothesised that this is

as a result of the reference accelerometer not being mounted directly onto the PCB and as such the elastic behaviour of this board is not properly considered.

	Pk-Pk voltage output (mV)	
Frequency (Hz) / **Acceleration** (g)	**1000**	**100**
20	28.84	117.50
10	14.16	58.93
5	6.90	29.40
1	1.37	5.94

Table 7.3: Comparison of the voltage output measurements for different accelerations from a MultiMEMS sensor out-of-plane acceleration sensing bridge.

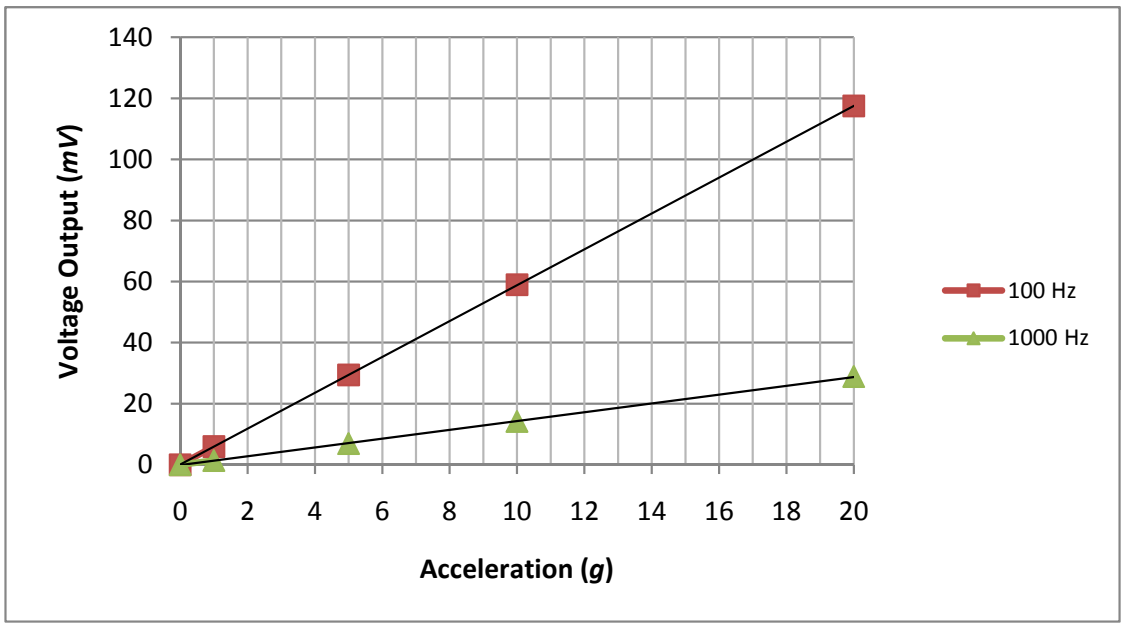

Figure 7.15: Plot of measured voltage outputs from Table 7.3 for the MultiMEMS out-of-plane sensing bridge.

The gradient of each of the trend lines in Figure 7.15 is 5.87 mV/g for a 100 Hz frequency and 1.45 mV/g for a 1000 Hz frequency. These values represent the sensitivity of the sensor to accelerations at these frequencies. The greater the value

of excitation frequency, the lower the sensitivity of the sensor to acceleration. This can be attributed to a damping effect that limits the displacement of the seismic masses. This results in a lower stress induced in the beams and therefore a smaller electrical output.

MultiMEMS design in-plane acceleration sensing bridge

The sensor PCB was removed from the top of the aluminium frame and then re-mounted onto the side. The outputs being wired into the strain gauge were the ones related to the pair of masses whose lengths are orientated in the direction of the acceleration.

As discussed in Chapter 4, the MultiMEMS design is not well suited to in-plane accelerations. This low sensitivity comes as a result of the shallow centre of gravity of the seismic masses caused by the fabrication process. The output signals are therefore considerably lower than those obtained from the out-of-plane sensing bridge.

The voltage outputs from the reference accelerometer and the MultiMEMS design can be seen in Figures 7.16 and 7.17 for 20 g of acceleration at 1000 Hz and 20 g of acceleration at 100 Hz, respectively.

The peak-to-peak output values for all of the measurements have been collated in Table 7.4. These values are plotted for each frequency in Figure 7.18 with linear trend lines applied to each data set.

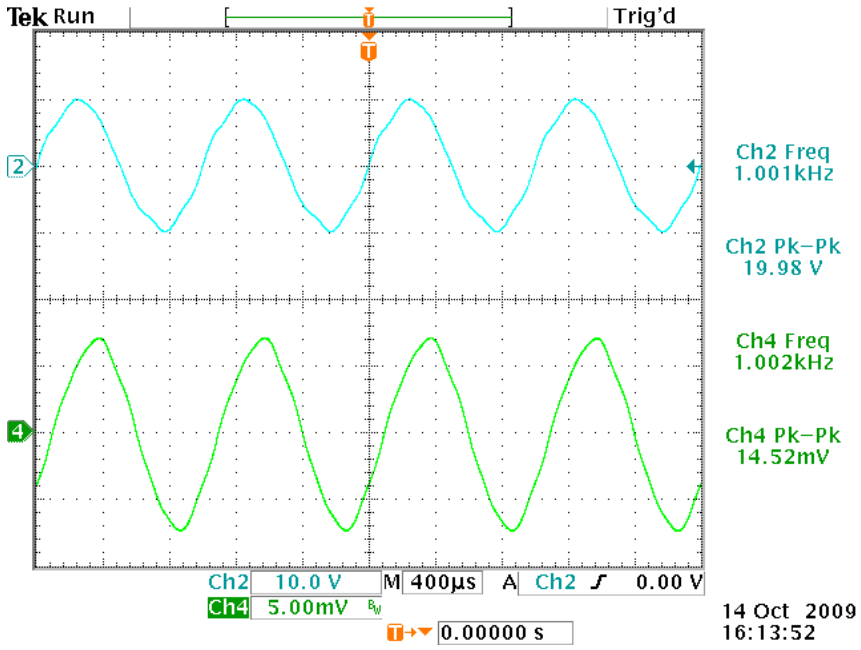

Figure 7.16: Voltage output from a MultiMEMS sensor in-plane acceleration sensing bridge for 20 g of acceleration at 1000 Hz.

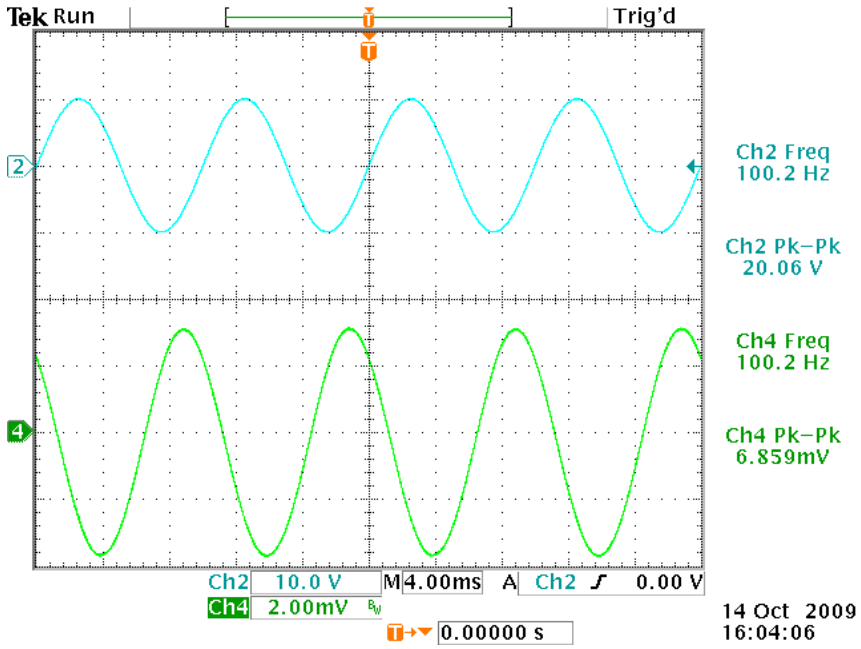

Figure 7.17: Voltage output from a MultiMEMS sensor in-plane acceleration sensing bridge for 20 g of acceleration at 100 Hz.

In Figure 7.16 it can be seen that the output signal is not a perfect sinusoid for excitation at a frequency of 1000 Hz and it is also possible to see that this is not the

case from the measurements at 100 Hz as demonstrated in Figure 7.17. This was the case for each of the other measurements taken at this frequency. This behaviour can also be seen with the output signal of the reference accelerometer which indicates that there may be an issue with the mounting for in-plane excitation. In addition it was difficult to increase the bridge supply voltage of the amplifier to the same level as that used for the out-of-plane sensing bridge whilst maintaining a zero offset. This could be attributed to some sort of leakage current effect or a larger resistivity due to the conductive tracks connecting the resistors or the crossing of the conductive paths.

	Pk-Pk voltage output (mV)	
Frequency (Hz) / **Acceleration** (g)	**1000**	**100**
20	14.52	6.86
10	11.04	3.50
5	4.90	1.78
1	0.64	0.41

Table 7.4: Comparison of the voltage output measurements for different accelerations from a MultiMEMS sensor in-plane acceleration sensing bridge.

As can be seen in Figure 7.18, a linear trend line only manages to fit the 100 Hz results well. The gradient for this trend line is calculated to be 0.34 mV/g and is the sensitivity of the sensor to accelerations at this frequency. In the case of the 1000 Hz trend, it can be seen that the voltage output for 20 g of acceleration is out of place. This could be attributed to an mistaken measurement or some kind of saturation behaviour. More effort needs to be applied to these measurements if and when the resources became available again to enable the setup necessary to do further measurements. However, due to these cost and time limitations it was not possible to perform consistent experimentation and as such it was only possible to

prove this as a concept for some first pass measurements.

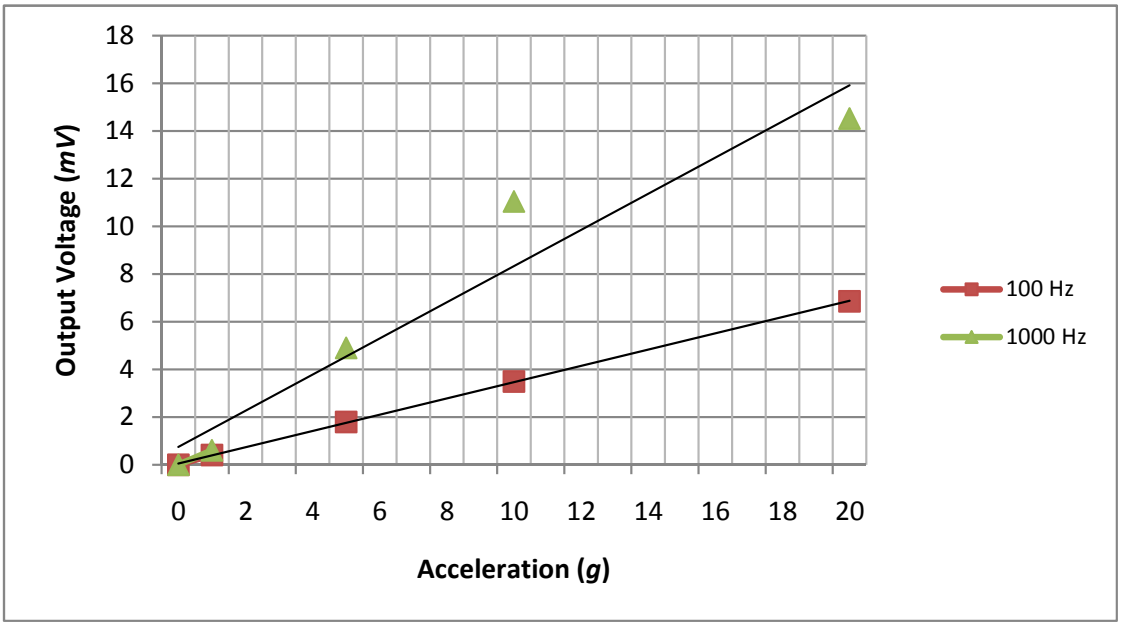

Figure 7.18: Plot of measured voltage outputs from Table 7.4 for the MultiMEMS in-plane sensing bridge.

7.3.4 Frequency spectrum measurements

This characterisation step was performed to identify the frequency of the first resonant mode of the beam-mass structures of the MultiMEMS design. This method is compared against the values obtained from the FEA results in Chapter 5 and later by the method using vibrometry introduced earlier in this chapter.

For these measurements, the same steps were followed as with the fixed-frequency measurement. The signal generator used for the fixed frequency measurements was replaced by one that was capable of sweeping frequencies and a Fast Fourier Transform (FFT) module was inserted into the oscilloscope to provide spectrum analysis capabilities.

When performing the measurements, the out-of-plane sensing bridge was connected for measurement because it is known from previous knowledge of the structures that

the first resonance results in out-of-plane deformation of each of the masses.

MultiMEMS Design

An example FFT waveform from the output of the out-of-plane sensing bridge can be seen in Figure 7.19 where the waveform in the lower half is an expanded version of the upper half. What is not possible to see clearly from this figure is the presence of two peaks close to each other in the upper waveform so the second peak is expanded in Figure 7.20. These peaks correspond to the resonance of each pair of masses. This behaviour is mirrored in previously reported dynamic mechanical studies.

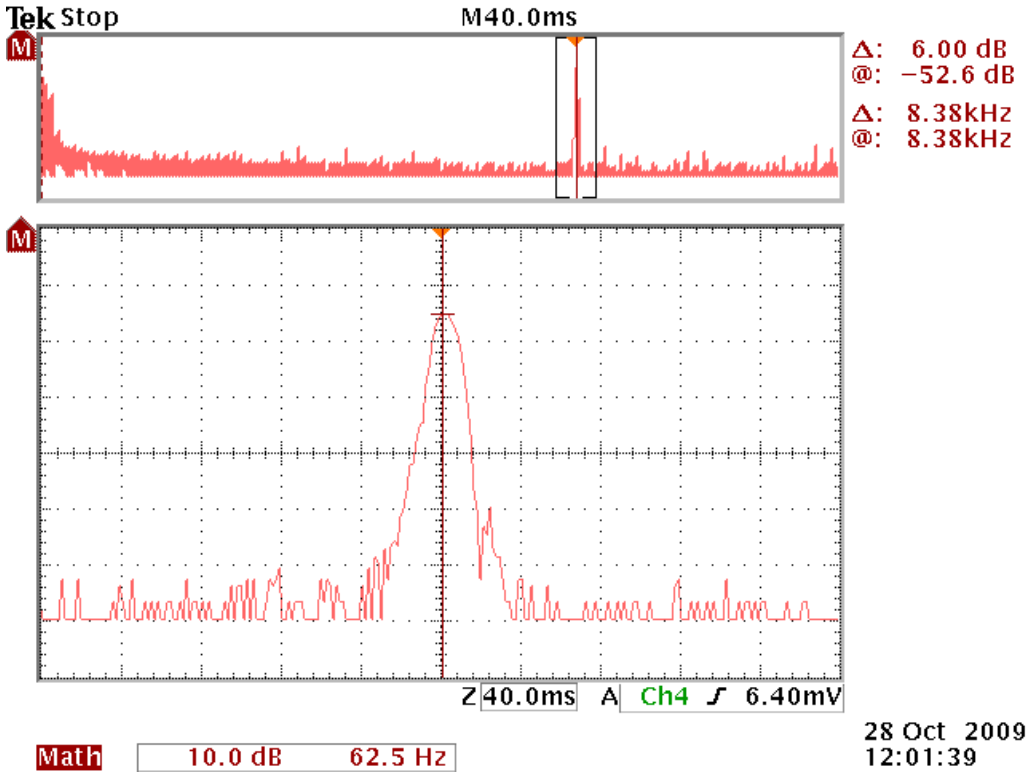

Figure 7.19: Results from frequency spectrum results of MultiMEMS Design showing the first resonance of one of the masses of the pair at 8.38 kHz.

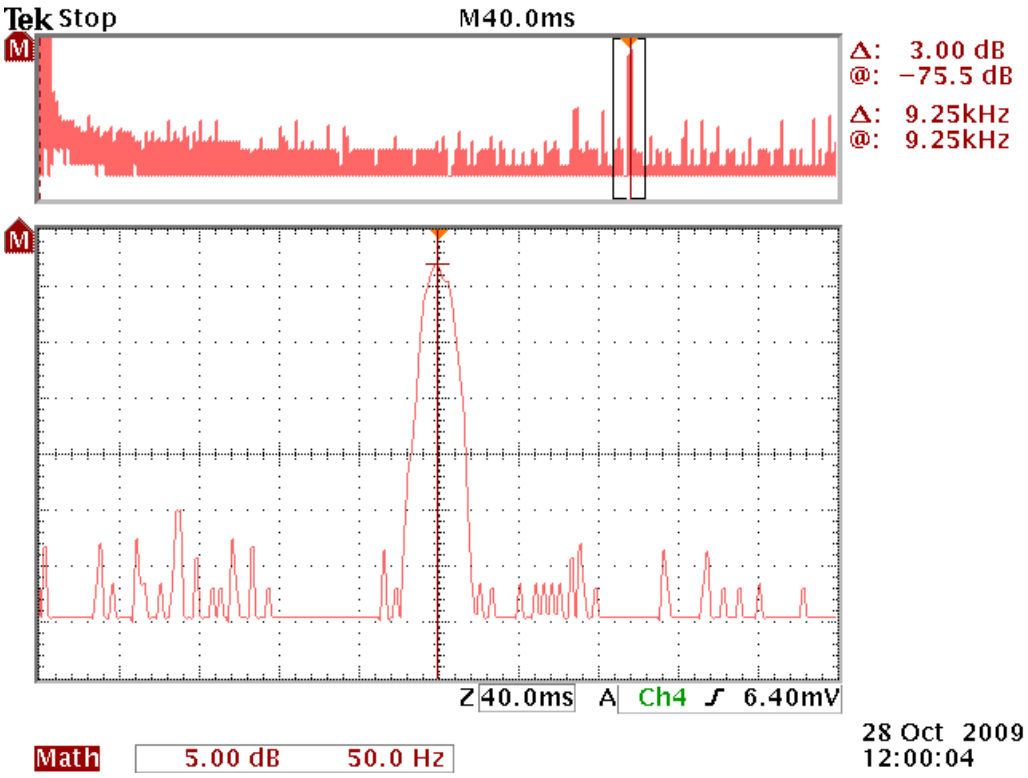

Figure 7.20: Results from frequency spectrum results of MultiMEMS Design showing the first resonance of the other mass at 9.25 kHz.

Method	**1^{st} Mode Frequency kHz**
FEA Simulation	7.366
Polytec 1	8.230
Polytec 2	9.020
Electrical 1	8.380
Electrical 2	9.250

Table 7.5: Comparison of the frequency values obtained from the ANSYS simulated results, the Polytec MSA results, and the electrical measurements for the 1^{st} mode of the MultiMEMS Design. N.B. A value quoted twice refers to each mass of the pair.

These measurements as well as the frequency obtained from the FEA simulations are presented in Table 7.5 and show good agreement. The main discrepancy with the FEA can be attributed to tolerances in the manufacturing process. Note that sensors other than those used in the dynamic mechanical studies have been employed

here.

7.4 Conclusions and Discussion

Results obtained using a Polytec Micro System Analyser have been presented in this chapter for the MultiMEMS Design and SMC Design 1. This characterisation tool incorporates vibrometry as well as stroboscopic techniques to measure out-of-plane and in-plane deformations, respectively. The sensor chips were fixed to PZE actuators to mechanically excite the free-standing structures. Double-sided adhesive tape was found to be the best option to fix the sensors in this instance. The actuator with the mounted sensor was then fixed to a movable stage and placed under the optical setup of the analyser.

The measured results from the MultiMEMS Design match up well with the FEA simulated results. Any variations can be attributed to fabrication variations where the structures have slight dimensional variations compared to the designed values.

For the SMC devices, large deviations between simulated and measured frequencies were obtained due to fabrication problems as described in Chapter 6. In one case the mode shape was even not the same.

It would be possible to break a mass from a die. The mass could then be placed in a SEM and the cross-section of the mass could be measured to give a better idea of the structure of the seismic mass following fabrication. These results together with interferometer results that profile the shape of the beams and the mass could then be inputted into FEA with the outcome likely to be closer to the measured results. These results ultimately indicate problems with the fabrication process.

The next part of the characterisation was performed by dynamically exciting the sensors using a shaker and measuring their electrical output. To achieve this, the sensors were glued and wirebonded into DIP's, placed into sockets, and soldered

onto PCB's together with potentiometers.

The boards were then fixed to an aluminium frame on the shaker. The electrical connections from off the boards were connected to a strain gauge bridge with the amplified output saved on an oscilloscope together with the signal from a commercial reference accelerometer also mounted onto the shaker.

By setting the frequency of the shaker via a signal generator and the amplitude of acceleration using the signal from the reference accelerometer, measurements were taken and presented for 1, 5, 10, and 20 g of acceleration at frequencies of 100 and 1000 Hz.

The experiments were only performed for the MultiMEMS design due to already discussed fabrication problems with the SMC designs. The sensors were first of all mounted on top of the aluminium frame for out-of-plane excitation and the corresponding wiring was connected to the strain gauge bridge. The sensor was then mounted to the side of the aluminium frame and the wiring changed accordingly to measure the output for in-plane excitation.

For the out-of-plane excitation, the results taken were in good agreement with those from the reference accelerometer. The results for each of the different values of acceleration fit well in a linear line and the sensitivities were calculated to be 5.87, and 1.45 mV/g for 100 and 1000 Hz, respectively. For the in-plane excitation the results were not of high quality and this was partly to be expected due to recognised issues which have already been mentioned. As discussed in Chapter 4, the sensitivity of the MultiMEMS design is limited due to the shallow centre-of-gravity of the seismic masses as limited by the thickness of the diffused n-Well. This meant that the signals had a considerably lower voltage. Only the 100 Hz frequency measurements fit fairly well onto a linear plot and this suggested a sensitivity of 0.34 mV/g. In the 1000 Hz measurements it is possible to see a non-perfect sinusoidal output from the reference accelerometer which is repeated in the output of the

measured sensor. This would suggest that there was something wrong with the fixation to the frame and makes the signal slightly unreliable.

The signal generator for the shaker was then replaced with one that was capable of sweeping frequencies and a FFT module inserted in the oscilloscope to take some spectrum frequency measurements. Two peaks were found at 8.380 and 9.250 kHz which represent the first resonance modes of each of the masses. These values were found to be in good agreement with the ones obtained using the vibrometer and from the FEA results.

Unfortunately only a limited time was available with the shaker. With more time the measurements could have repeated more often and different stimuli chosen to obtain further results to try to obtain more reliable data. However, the process for obtaining electrical measurements from dynamic excitation and the functioning of the MultiMEMS design was successfully proven. Because the SMC designs work with the same principle as the MultiMEMS design and in particular the placement and connection of the piezoresistors, with a better fabrication process it can be assumed that the same would hold for those designs and that a larger peak-to-peak voltage would be achieved due to the changes in the mechanical structures.

References

[1] Polytec MSA-500 Micro System Analyzer. http://www.polytec.com/eur/158_6392.asp (Accessed: 07 Oct 10).

[2] National Physical Laboratory website. http://www.npl.co.uk/ (Accessed: 07 Oct 10).

[3] Physik Instrumente UK website. http://www.physikinstrumente.co.uk/ (Accessed: 07 Oct 10).

[4] Polytec GmbH. 3-D vibration and motion analysis of microstructures. http://www.polytec.com/usa/_files/LM_AN_INFO_0105_E_Microstructures.pdf (Accessed: 07 Oct 10).

[5] LDS Test and Measurement website. http://www.lds-group.com/ (Accessed: 07 Oct 10).

[6] Endevco website. http://www.endevco.com/ (Accessed: 07 Oct 10).

[7] Bruel & Kjaer website. http://www.bksv.com/Products/TransducersConditioning/ConditioningAndAmps/ChargeConditioningAmplifiers/2635.aspx (Accessed: 07 Oct 10).

[8] Tektronix website. http://www.tek.com/products/oscilloscopes/tds3000c/ (Accessed: 07 Oct 10).

Chapter 8

Conclusions and Future Work

8.1 Summary and conclusions

This thesis has introduced the design, simulation, fabrication, packaging, characterisation and application of a miniaturised three-axis accelerometer to measure the heart wall motion of patients who have just undergone CABG surgery. The sensor, stitched directly to the heart wall enables the real-time monitoring of the heart during surgery and after convalescence. The sensor can give immediate warning of any deviation from normal heart motion which could be an indicator of the grafted bypass failure. Any detected problems can then be remedied quickly before the patient leaves the hospital which reduces risk and discomfort to the patient as well as reducing costs for the hospital.

This application requires the sensor to be sutured directly to the heart wall. This puts a strong emphasis on the miniaturisation of the device which MEMS technologies can enable. The required size of the sensor was $2{\times}5{\times}2$ $(W{\times}L{\times}H)$ mm^3. The small dimensions of the width and height compared to the length is due to the fact that the sensor is required to be pulled free from its stitches and out of the chest wall through a small hole.

As the sensor is to be operated *in-vivo* a biocompatible package made of silicone met the requirements. Beside its biocompatibility, the material is suitable for the necessary sterilisation and can be moulded into a smooth and rounded shape to avoid unnecessary skin tissue damage when the sensor is removed.

Feasibility studies have been carried out with the conclusion that three-axis ac-

celerometer sensors are indeed capable of measuring heart motion with good resolution. During measurements, it was possible to detect and identify patterns in the motion that could be an indication of heart circulation failure. To date this has been carried out using commercially available sensors, however these sensors were considered to be too large for the application and as such an in-house sensor design had to be carried out.

Many different sensing techniques are available to transduce acceleration into an electrical output. The transduction principle chosen in this thesis employs the piezoresistive effect, a well understood technique available from a variety of foundry services. In this technique, a free-standing structure is manufactured using etching process steps and is displaced when under acceleration. This acceleration induces stress into the thin supporting structures which can be measured by carefully implanting piezoresistors on the beam surface with different orientations. The main building block for the designs presented in this thesis was a seismic mass supported by two thin cantilever beams. To provide sensing of acceleration in three axes it was necessary to use four instances of this structure and to utilise four Wheatstone bridges so that the understood behaviour of the structures reaction to acceleration in each of the axes could be identified using the different outputs of the bridges.

A fabrication process through the MultiMEMS MPW was carried out and utilises the well established SensoNor foundry process. The main aspects of this process include 23 μm thick implanted n-wells to define the seismic masses, 3 μm thick epitaxial layer to represent the thin cantilevers into which stress-sensitive p-type piezoresistors were implanted. A backside wet anisotropic etch process step is combined with a p-n junction etch-stop to etch the p-type bulk silicon and stop on the n-type beam and mass membranes. A front-side dry etch is used to define the outline of and release the structures, and finally an anodic bond to form a hermetic glass-silicon-glass stacked structure with a bond pad area exposed for connection from inside the packaging to the outside world. Analytical calculations as well as FEA using

ANSYS software was used to decide on the size of the dimensions as defined by the design rules and to analyse the behaviour of the structures. The chips from this design iteration measured $3{\times}6{\times}1.5$ $(W{\times}L{\times}H)$ mm^3.

The yield obtained from this process was very good. This yield is fully attributed to the established process together with the suitable and concise design rules. However, a major limitation of the process is the thinness of the seismic masses. As the sensitivity of these structures to in-plane acceleration is dependent on the vertical centre of gravity of these masses the resulting sensors are not very sensitive. A design iteration to use the full wafer thickness to represent the seismic masses was unsuccessful due to complications with the backside etch.

DRIE was used instead of the wet anisotropic etch. Design of structures with deep near-vertical sidewalls was possible instead of the shallow angled sidewalls that occur as a result of the implanted n-wells. Together with SOI wafers and the selectivity of the etch to oxide, the 380 μm thickness of the silicon handle layer was used for the masses. Another benefit of this approach was that the vertical space was being utilised for maximum mass versus lateral space on the chip. The foundry process that was employed to fabricate these sensors originated from the SMC. In total four designs were submitted to this process and essentially all worked on the same principle of cantilever-mass structures with piezoresistive sensing. The structures of each version were designed for matching mechanical sensitivities to in-plane and out-of-plane accelerations. Further consideration of the stress profile along the length of the beam when subjected to out-of-plane accelerations led to one of the designs employing tapered beams. This cancelled the linear decrease in stress from the base of the beam when utilising rectangular beams. The out-of-plane acceleration sensing piezoresistors were placed in that region.

The yield from this process however was not good and serious complications occurred with the backside DRIE process step. This was mainly attributed to the variation of the thickness of the wafer and resulted in some areas of the wafer being over-etched

resulting in overly-fragile structures. Other areas were under-etched which resulted in structures that were not fully released. Effects stemming from residual stress resulted in fractured beams.

The packaging for these sensors was performed at chip-level rather than wafer-level as with the MultiMEMS process. As dicing of the wafer was not suitable due to the exposed free-standing structures, tabs were machined using the DRIE and were incorporated for each chip. The application of a small downward pressure was all that was required to break the tabs and free the sensors from the wafer. The actual bonding process was performed using an in-house low-temperature polymer, BCB, approach that allowed a bond directly over the surface metal tracks going out to the bond pad area and resulted in a glass-silicon-glass stacked structure. The resulting size of the chips was $2.5\times4\times1.5$ $(W\times L\times H)$ mm^3. This design layout included two sets of bond pads of which one set was for characterisation purposes. With this removed the overall size of the chip would be reduced to $2.5\times3.4\times1.5$ mm^3. When implementing the second generation packaging introduced in Section 6.4 and using the biocompatible encapsulation approach employed with the Kionix sensor solution, the resulting size of the biocompatibly packaged sensor would be $8.5\times6.4\times4.26$ mm^3 which compares to $11\times14.5\times5.2$ mm^3 for the biocompatibly packaged Kionix sensor.

To characterise the behaviour of the fabricated sensors, dynamic mechanical and electrical approaches were implemented. The results presented mainly focused on the MultiMEMS design. The mechanical approach used a MicroSystem Analyser from Polytec to measure the dynamic behaviour of the sensors when being excited by a PZE actuator. The equipment utilises vibrometry and stroboscopic techniques to measure out-of-plane and in-plane motions, respectively, and can be used to identify and study the different resonant modes of the structure. The results were compared to data obtained by FEA and were found to be in good agreement.

The electrical approach involved the use of a shaker. The die were prepared so that they could be attached to this shaker as well as being electrically connected to a

strain gauge and amplifier. A reference accelerometer was used to measure the output of the shaker which, in turn, was displayed on an oscilloscope together with the resulting output of the sensor being tested. The results ultimately showed that a good response was possible for out-of-plane accelerations but not for in-plane accelerations which was as expected. As well as performing fixed-frequency measurements it was also possible to perform measurements across a spectrum of frequencies by using a function generator with a sweep operating mode, and an oscilloscope using a FFT module. This made it possible to identify the first resonant frequency of the structures and this was found to be in good agreement when compared to the mechanical measurements and the FEA.

8.2 Future work

The most important consideration toward future work would be to develop or access a process that had a much better control of the backside DRIE. This would either involve getting access to another process that is based on more experience of such a process step or an iterative process to characterise the process step in much finer detail until an acceptable process has been attained and applied to the devices. Adjustments could be made to the layout of the structures near the centre of the wafer where structures are under-etched in comparison to the perimeter of the wafer where they are over-etched. This could involve, for example, making the etch trench widths narrower around the masses near the centre to try and increase the etch rate. Once this was achieved, a full process run could be completed and the work of characterising the sensors could be carried out in a similar manner to what was performed with the MultiMEMS sensors as well as some static/quasi-static response measurements. A more intensive approach would involve noise measurements, investigation of power consumption, stability/drift consideration, and cross-axis sensitivity measurements.

The sensor could be then biocompatibly packaged using silicone moulding and attached to a micro-ribbon cable, as demonstrated by the group with other sensors,

and then used in further animal and human studies to measure heart wall motion.

Further miniaturisation of the sensors could be investigated. The most obvious area to investigate further would be the packaging. Reducing the width of the bonding area alone could feasibly reduce the size of the overall chip to $2.25 \times 2.5 \times 1.5$ $(W \times L \times H)$ mm^3. One of the main benefits of using the polymer bonding with the SMC process was that the bond could be performed directly on top of the surface metal tracks due to the non-necessity for a planar surface. The bonding area for the SMC die was a minimum 300 μm from the boundary of the free-standing structures. Reducing this value would mean that the bond would be on top of metal tracks on three sides of the chip and further investigation would need to be done to ensure the quality of the bond. Another packaging consideration could be the utilisation of through-wafer interconnections in the packaging caps. This would remove the need for the bond pad area and reduce the overall length of the chip [1].

Another process modification could be to look at combining CMOS and MEMS technologies to embed CMOS signal processing circuitry on the masses of the seismic masses. This would increase the performance of the sensors and reduce overall real estate [2].

Further functionality could be attained in the areas of wireless communication of the sensor. This could allow the sensor to become a remote patient monitoring tool whilst being non-invasive and non-intrusive which better ensures the quality of life for the subject [3–5]. Battery powering, on-board memory [6] and energy harvesting [7] could also be investigated to achieve greater functionality.

With this extra performance and functionality, the sensor could be used for further applications in the medical field and beyond as discussed in Chapter 3.

References

[1] C-.W. Lin, H-.A. Yang, W.C. Wang, and W. Fang. Implementation of three-dimensional SOI-MEMS wafer-level packaging using through-wafer interconnections. *J. Micromech. Microeng.*, 17(6):1200–1205, 2007.

[2] H. Takao, H. Fukumoto, and M. Ishida. A CMOS integrated three-axis accelerometer fabricated with commercial submicrometer CMOS technology and bulk-micromachining. *IEEE Trans. Electron Devices*, 48(9):1961–1968, 2001.

[3] N. Najafi and A. Ludomirsky. Initial animal studies of a wireless, battery-less, MEMS implant for cardiovascular applications. *Biomedical Microdevices*, 6(1):61–65, March 2004.

[4] E. Jovanov, D. Raskovic, J. Price, A. Krishnamurthy, J. Chapman, and A. Moore. Patient monitoring using personal area networks of wireless intelligent sensors. *Biomed. Sci. Instrum.*, 37:373–378, 2001.

[5] Biotronik website. `http://www.biotronik.com/biohm/home` (Accessed: 07 Oct 10).

[6] J.P. Lynch, A. Partridge, K.H. Law, T.W. Kenny, A.S. Kiremidjian, and E. Carryer. Design of piezoresistive MEMS-based accelerometer for integration with wireless sensing unit for structural monitoring. *J. Aerosp. Engrg.*, 16(3):108–114, July 2003.

[7] S.P. Beeby, M.J. Tudor, and N.M. White. Energy harvesting vibration sources for microsystems applications. *Meas. Sci. Technol.*, 17(12):175–195, 2006.

Appendix A

Matlab Code Listings

The Matlab code for MultiMEMS Design 1 and SMC Design 1 are listed below in Sections A.1 and A.2, respectively.

A.1 MultiMEMS sensor design

```
%-------------------------------------------------------------
% Author:                Craig Lowrie
% Orgainsation:          Heriot-Watt University
% Title:                 MultiMEMS Design 1 Matlab File

% This code listing is to find the out-of-plane and
% in-plane stress values when the structure is subjected
% to different acceleration values.

% The structure is a rectangular mass supported by two
% rectangular beams.

% Note that dimensional units are in metres
%-------------------------------------------------------------

clc;
clear all;
close all;
```

```
20  ro = 2330;      % Silicon density

22  g = 2000;       % g's of acceleration
    acc = g*9.81;   % Acceleration
24
    %-------------------------------------------------------------
26  % Dimensions

28  % Note that the beams are represented by the epi-layer
    % and the masses by the implanted n-well and epi-layer
30
    %-----------------------------
32  % Beam

34  W_b = 44e-6;    % Width of the beam
    L_b = 34e-6;    % Length of the beam
36  H_b = 3e-6;     % Height of the beam

38  %-----------------------------
    % Mass
40
    W_m = 2050e-6;  % Width of the mass
42  L_m = 230e-6;   % Length of the mass
    H_m = 20e-6;    % Height of the mass
44
    alpha=(38)*(pi/180);    % Sidewall angle resulting from
46  % the nwell implant
```

```
48  %-------------------------------------------------------
    % Beam calculations
50
    zc_beam = H_b/2;        % Centre of mass of the beam in the
52  % direction of the thickness of the beam

54  disp(['zc_beam = ' num2str(zc_beam*1e6) '(um)'])

56  Ix_beam = (W_b*H_b^3)/12;       % Second moment of area
    % for a rectangular cross section
58
    disp(['Ix_beam = ' num2str(Ix_beam)])
60
    mass_beam = (L_b*W_b*H_b)*ro;   % Calculation for the mass
62  % of a single beam

64  disp(['Mass of single beam = ' num2str(mass_beam) '(kg)'])

66  %-------------------------------------------------------
    % Mass calculations
68
    %----------------------------
70  % n-well

72  mass_mass_nwell = H_m/3*ro*((4*H_m^2-3*H_m*L_m*...
    tan(alpha)-3*W_m*H_m*tan(alpha)+3*W_m*L_m*tan(alpha)^2)/...
74  tan(alpha)^2);  % Mass of the n-well representing each of
    % the seismic masses
76
```

```
disp(['Mass of the mass n-well = '...
num2str(mass_mass_nwell) '(kg)'])

zc_mass_nwell = ((H_m/2)*(6*H_m^2-4*H_m*W_m*tan(alpha)-...
4*L_m*H_m*tan(alpha)+3*L_m*W_m*tan(alpha)^2)/(4*H_m^2-...
3*H_m*W_m*tan(alpha)-3*L_m*H_m*tan(alpha)+3*L_m*W_m*...
tan(alpha)^2)); % Centre of mass in the direction of the
% thickness of the mass for the n-well representing each
% of the seismic masses

disp(['Centre of mass for the mass n-well = '...
num2str(zc_mass_nwell*1e6) '(um)'])

%-----------------------------
% Epi-layer

mass_mass_epi = (L_m*W_m*H_b)*ro;   % Mass of the epi-
% layer associated with each of the seismic masses

disp(['Mass of the mass epi-layer = '...
num2str(mass_mass_epi) '(kg)'])

zc_mass_epi = H_b/2;    % Centre of mass in the direction
% of the thickness of the mass for the epi-layer
% associated with each of the seismic masses

disp(['Centre of mass for the mass epi-layer = '...
num2str(zc_mass_epi*1e6) '(um)'])
```

```
106 %-----------------------------
    % Total
108
    mass_mass = mass_mass_nwell+mass_mass_epi;  % Total mass
110 % of each of the seismic masses

112 disp(['Total mass of the mass = ' num2str(mass_mass)...
    '(kg)'])
114
    zc_mass = (mass_mass_epi*zc_mass_epi+mass_mass_nwell*...
116 zc_mass_nwell)/(mass_mass); % Centre of mass in the
    % direction of the thickness of the mass of the seismic
118 % masses

120 disp(['Centre of mass of the mass = '...
    num2str(zc_mass*1e6) '(um)'])
122
    %-------------------------------------------------------
124 % Calculations of stress

126 x = 0;  % Distance along the length of the beam from
    % the base. The maximum stress is located at the base of
128 % the beam

130 mass_tot = (mass_mass+(2*mass_beam))/2; % Total mass
    % of the structure. Note that half the mass is used so
132 % that a single beam model can be used

134 %x = 0:1e-6:L_b;        % For plotting along entire beam
```

```
% length

yc_mass = L_m/2;    % Centre of mass in the direction of
% the length of the mass of the seismic masses

F = mass_tot*acc;   % Force acting on the mass

M_m = F*yc_mass;        % Bending moment of the mass for
% out-of-plane accelerations

M_b = F*(L_b-x); % Bending moment of the beam for
% out-of-plane accelerations

M_op = M_m+M_b; % Total bending moment

%-----------------------------
% Out-of-plane stress

stress_op_max = (M_op/Ix_beam)*zc_beam;
% Maximum out-of-plane stress

disp(['Out-of-plane stress = '...
num2str(stress_op_max/1e6) '(MPa)'])

%plot(x/1e-6,stress_op_max/1e6)
%axis([0  34  350  550])
%title('Stress Versus Distance From Base of Beam for...
%Out-of-Plane Acceleration')
%xlabel('x [microns]')
```

```
%ylabel('Stress [MPa]')
%hgsave('op_accel_plot')        % For plotting along
% entire beam length

x_L = 30e-6; % Distance from the base of the beam to the
% centre of the longitudinal resistors
x_T = 26e-6; % Distance from the base of the beam to the
% centre of the transversal resistors

M_b_L = F*(L_b-x_L);    % Bending moment of the beam for
% out-of-plane accelerations at the centre of the
% longitudinal resistors

M_b_T = F*(L_b-x_T);    % Bending moment of the beam for
% out-of-plane accelerations at the centre of the
% transversal resistors

M_tot_L = M_m+M_b_L;    % Total bending moment at the
% centre of the longitudinal resistors
M_tot_T = M_m+M_b_T;    % Total bending moment at the
% centre of the transversal resistors

stress_tot_L = (M_tot_L/Ix_beam)*(H_b-zc_beam);
% Out-of-plane stress at centre of longitudinal resistor

disp(['Longitudinal out-of-plane stress = '...
num2str(stress_tot_L/1e6) '(MPa)'])

stress_tot_T = (M_tot_T/Ix_beam)*(H_b-zc_beam);
```

```
% Out-of-plane stress at centre of transversal resistor

disp(['Transversal out-of-plane stress = '...
num2str(stress_tot_T/1e6) '(MPa)'])

%-----------------------------
% In-plane stress

r0 = zc_beam + zc_mass; % Distance between the centroid of
% the beam and the centre of mass of the mass

disp(['r0 = ' num2str(r0*1e6) '(um)'])

M_ip = F*r0;    % Bending
% moment for in-plane accelerations

stress_ip = (M_ip/Ix_beam)*zc_beam;     % In-plane stress.
% Note that this value is constant along the beam because
% just dependent on r0

disp(['In-plane stress = ' num2str(stress_ip/1e6) '(MPa)'])
```

A.2 SMC sensor design

```
%-------------------------------------------------------
% Author:               Craig Lowrie
% Orgainsation:         Heriot-Watt University
% Title:                SMC Design 1 Matlab File
```

```
% This code listing is to find the out-of-plane and
% in-plane stress values when the structure is subjected
% to different acceleration values.

% The structure is a triangular mass supported by two
% rectangular beams.

% Note that dimensional units are in metres
%------------------------------------------------------------

clc;
clear all;
close all;

ro = 2330;      % Silicon density

g = 500;        % g's of acceleration
acc = g*9.81;   % Acceleration

%------------------------------------------------------------
% Dimensions

% Note that the beams are represented by the device layer
% and the masses by the thickness of the SOI wafer

%-----------------------------
% Wafer

H_device    = 4e-6;     % Height of the device layer
```

```
H_box       = 0.5e-6;   % Height of the buried oxide layer
H_handle    = 380e-6;   % Height of the handle layer

%-----------------------------
% Beam

W_b = 60e-6;    % Width of the beam
L_b = 192e-6;   % Length of the beam
H_b = H_device; % Height of the beam

%-----------------------------
% Mass

L_m = 400e-6;   % Width of the mass
W_m = 2*L_m;    % Length of the mass
H_m = H_device+H_box+H_handle;  % Height of the mass

W_rie1 = 10e-6;         % RIE along the length of beams
W_rie2 = W_b+2*W_rie1;  % RIE around mass. This value is
% the same as the width of the backside DRIE, W_drie.

a = 380e-6;         % Width of recess in mass for
% beams
b = a-(2*W_b)-(4*W_rie1);% Width of mass between beams
D = b+W_b+(2*W_rie1);       % Distance between the centres
% of the beams
d = L_b-W_rie2;                 % Length of mass wrapped
% around the beams
```

```
64  %-----------------------------------------------------------
    % Beam calculations
66
    zc_beam = H_b/2;        % Centre of mass of the beam in
68  % the direction of the thickness of the beam

70  disp(['zc_beam = ' num2str(zc_beam*1e6) '(um)'])

72  Ix_beam = (W_b*H_b^3)/12;       % Second moment of area for
    % rectangular cross section
74
    disp(['Ix_beam = ' num2str(Ix_beam)])
76
    mass_beam = (L_b*W_b*H_b)*ro;   % Calculation for the mass
78  %of a single beam

80  disp(['Mass of single beam = ' num2str(mass_beam) '(kg)'])

82  %-----------------------------------------------------------
    % Mass calculations
84
    %----------------------------
86  % Triangular mass with no recesses

88  a_1 = (W_m*L_m)/2;      % Area
    m_1 = a_1*H_m*ro;       % Volume
90  yc_1 = 1/3*L_m;     % Centre of mass in the length of the
    % mass
92
```

```
%-----------------------------
% Outline of mass removed for both beams

a_2 = d*a;                      % Area
m_2 = a_2*H_m*ro;   % Volume
yc_2 = d/2;         % Centre of mass in the length of the
% mass

%-----------------------------
% Section of mass wrapped between the beams

a_3 = d*b;              % Area
m_3 = a_3*H_m*ro;       % Volume
yc_3 = yc_2;            % Centre of mass in the length of
% the mass

%-----------------------------
% Complete mass

mass_mass = m_1-m_2+m_3;
disp(['Mass of the mass = ' num2str(mass_mass) '(kg)'])

yc_mass = ((yc_1*m_1)-(yc_2*m_2)+(yc_3*m_3))/(mass_mass);
%Centre of mass of the mass in the length of the mass
disp(['Centre of mass of the mass in the direction of...
    the length of the mass = ' num2str(yc_mass*1e6) '(um)'])

zc_mass = H_m/2;    %Centre of mass of the mass in the
% direction of the thickness of the mass
```

```
122
    disp(['Centre of gravity of the mass in the thickness of...
124     the mass = ' num2str(zc_mass*1e6) '(um)'])

126 %-------------------------------------------------------
    % Calculations of stress
128
    x = 0;  % Distance along the length of the beam from
130 % the base. The maximum stress is located at the base of
    % the beam
132
    mass_tot = (mass_mass+(2*mass_beam))/2; % Total mass of
134 % the structure. Note that half the mass is used so that a
    % single beam model can be used
136
    F = mass_tot*acc;   % Force acting on the mass
138
    M_m = F*((yc_mass+W_rie2)-L_b); % Bending moment of the
140 % mass for out-of-plane accelerations

142 M_b = F*(L_b-x);    % Bending moment of the beam for
    % out-of-plane accelerations
144
    M_op = M_m+M_b; % Total bending moment
146
    %-----------------------------
148 % Out-of-plane stress

150 stress_op_max = (M_op/Ix_beam)*zc_beam;
```

```
% Maximum out-of-plane stress

disp(['Out-of-plane stress = ' num2str...
    (stress_op_max/1e6) '(MPa)'])

x_L = 30e-6; % Distance from the base of the beam to the
% centre of the longitudinal resistors
x_T = 30e-6; % Distance from the base of the beam to the
% centre of the transversal resistors

M_b_L = F*(L_b-x_L);    % Bending moment of the beam for
% out-of-plane accelerations at the centre of the
% longitudinal resistors

M_b_T = F*(L_b-x_T);    % Bending moment of the beam for
% out-of-plane accelerations at the centre of the
% transversal resistors

M_tot_L = M_m+M_b_L;    % Total bending moment at the
% centre of the longitudinal resistors
M_tot_T = M_m+M_b_T;    % Total bending moment at the
% centre of the transversal resistors

stress_tot_L = (M_tot_L/Ix_beam)*(H_b-zc_beam);
% Out-of-plane stress at centre of longitudinal resistors
disp(['Longitudinal out-of-plane stress ='...
    num2str(stress_tot_L/1e6) '(MPa)'])

stress_tot_T = (M_tot_T/Ix_beam)*(H_b-zc_beam);
```

```
% Out-of-plane stress at centre of transversal resistors
disp(['Transversal out-of-plane stress ='...
    num2str(stress_tot_T/1e6) '(MPa)'])

%-----------------------------
% In-plane stress

r0 = zc_beam+zc_mass;   % Distance between the centroid
% of the beam and the centre of gravity of the mass

disp(['r0 = ' num2str(r0*1e6) '(um)'])

M_ip = F*r0;    % Bending
% moment for in-plane accelerations

stress_ip = (M_ip/Ix_beam)*zc_beam;     % In-plane stress.
% Note that this value is constant along the beam because
% just dependent on r0

disp(['In-plane stress = ' num2str(stress_ip/1e6) '(MPa)'])
```

Appendix B

Other SMC Design Layouts

Only the layout and dimensions of SMC Design 1 are presented the main body of the thesis. In total, four designs were submitted for fabrication at SMC and the layout and dimensions of SMC Designs 2, 3 and 4 and presented below.

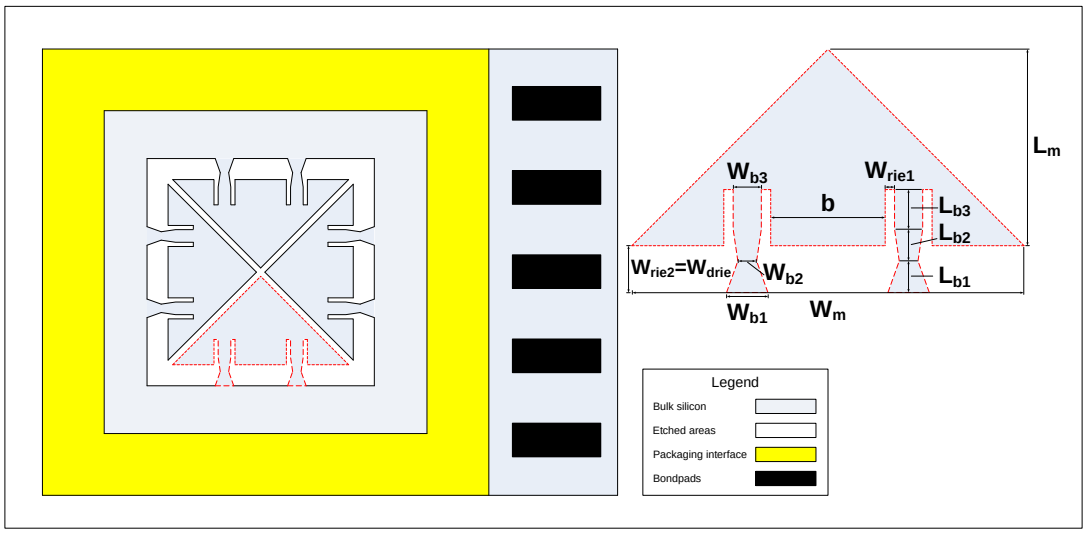

Figure B.1: Top view of SMC Design 2 chip layout with highlighted beam-mass structure.

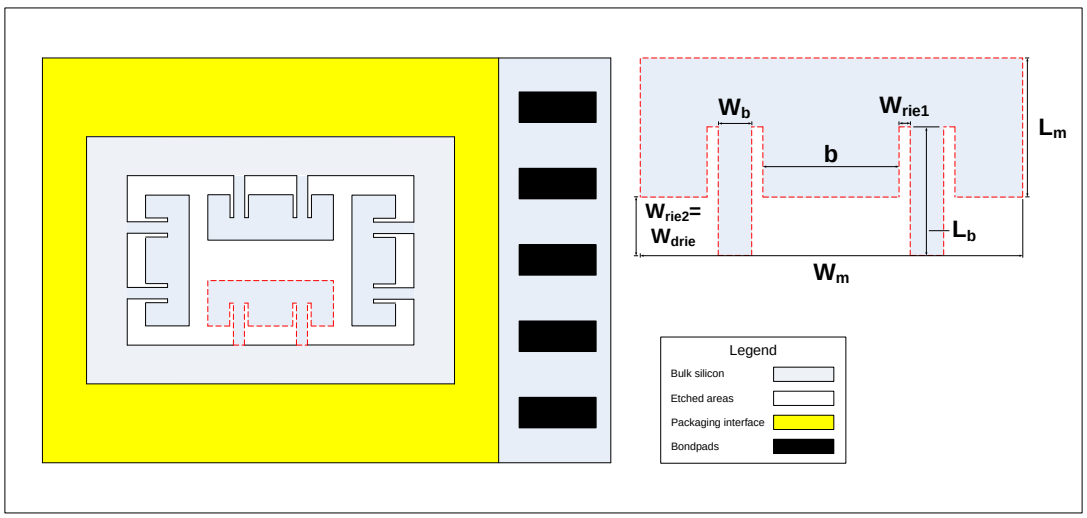

Figure B.2: Top view of SMC Design 3 chip layout with highlighted beam-mass structure.

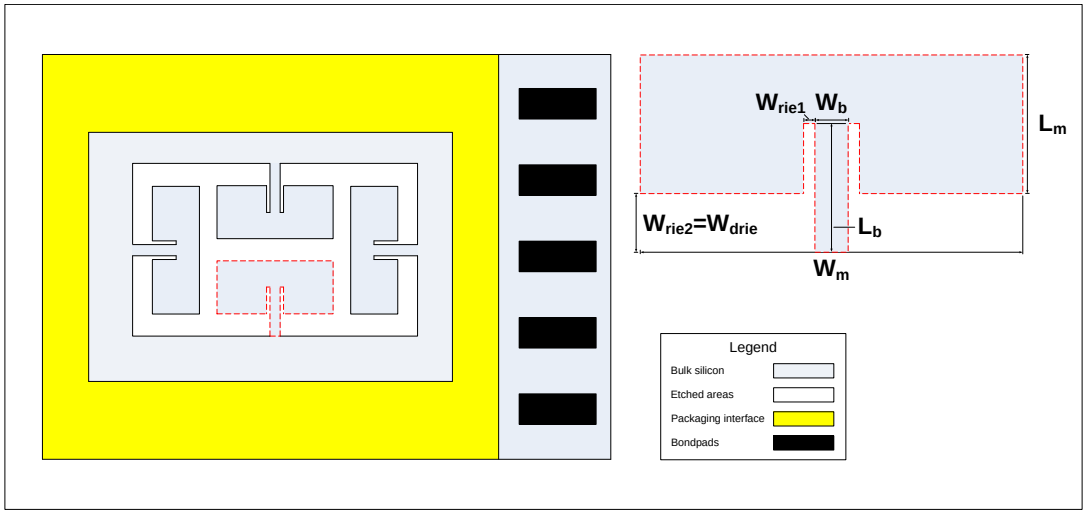

Figure B.3: Top view of SMC Design 4 chip layout with highlighted beam-mass structure.

Dimension	Abbreviation	Value (μm)
Length of the mass	L_m	400
Width of the mass	W_m	800
Width of the mass between the beams	b	220
RIE around the masses	W_{rie2}	80
DRIE around the masses	W_{drie}	80
RIE along the length of the beams	W_{rie1}	10
Length of beam section 1	L_b	50
Length of beam section 2	L_b	50
Length of beam section 3	L_b	92
Width of beam section 1	W_b	100
Width of beam section 2	W_b	70
Width of beam section 3	W_b	74

Table B.1: Structural dimensions for SMC Design 2. Refer to Figure B.1.

Dimension	Abbreviation	Value (μm)
Length of the mass	L_m	265
Width of the mass	W_m	700
Width of the mass between the beams	b	270
RIE around the masses	W_{rie2}	80
DRIE around the masses	W_{drie}	80
RIE along the length of the beams	W_{rie1}	10
Length of the beams	L_b	192
Width of the beams	W_b	60

Table B.2: Structural dimensions for SMC Design 3. Refer to Figure B.2.

Dimension	Abbreviation	Value (μm)
Length of the mass	L_m	225
Width of the mass	W_m	552
RIE around the masses	W_{rie2}	102
DRIE around the masses	W_{drie}	102
RIE along the length of the beams	W_{rie1}	10
Length of the beams	L_b	192
Width of the beams	W_b	82

Table B.3: Structural dimensions for SMC Design 4. Refer to Figure B.3.

Appendix C

ANSYS Code Listings

The ANSY code for MultiMEMS Design 1 and SMC Design 1 are listed below in Sections C.1 and C.2, respectively. The listings are done using ANSYS Parametric Design Language (APDL).

In each of these designs, a file hierarchy as shown in Figure C.1 is followed with each of the files instantiated in the top file with the title "Main".

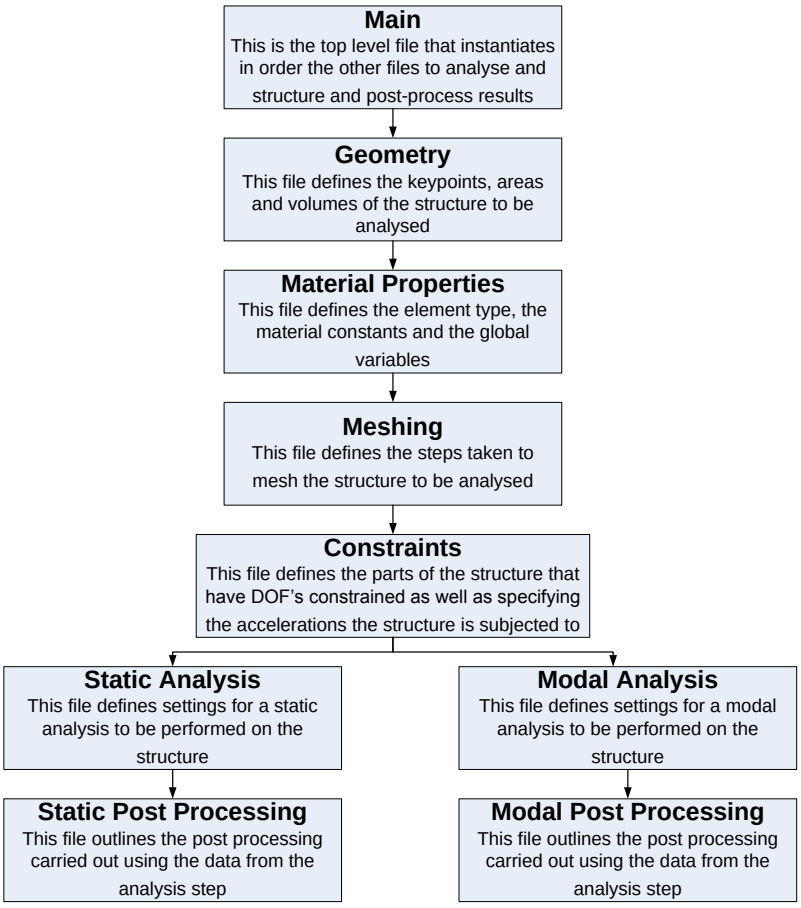

Figure C.1: ANSYS file hierarchy.

C.1 MultiMEMS sensor design

Main file

```
!-------------------------------------------------------------
! Author:       Craig Lowrie
! Organisation: Heriot-Watt University
! Title:        MultiMEMS Design 1 ANSYS File

! The structure is a rectangular mass supported by two
! rectangular beams.

! Note that dimensional units are in micrometres

!-------------------------------------------------------------

FINISH
/CLEAR

!-------------------------------------------------------------
! File hierarchy

/INPUT,geometry,txt
/INPUT,matprops,txt
/INPUT,constraints,txt
/INPUT,mesh,txt

! The static analysis or modal analysis are performed one at
! a time whilst the other analysis and associated post-
```

```
26  ! processing file are commented out

28  /INPUT,analysis_static,txt
    /INPUT,analysis_modal,txt
30
    /INPUT,post1_static,txt
32  /INPUT,post1_modal,txt
```

Geometry file

```
1   /PREP7
2
    !------------------------------------------------------------
4   ! Dimensions

6   !------------------------------
    ! Wafer
8
    H_epi = 3                       ! Height of the epi-layer
10  H_nwell = 20                    ! Height of the n-well

12  !------------------------------
    ! Mass
14
    Lm = 230                        ! Length of the mass
16  Wm = 2050                       ! Width of the mass
    Hm = H_epi+H_nwell              ! Height of the mass
18
```

```
!-----------------------------
! Beam

Lb = 34                          ! Length of the beam
Wb = 44                          ! Width of the beam
Hb = H_epi                       ! Height of the beam

!-----------------------------
! Support

Ls = 50                          ! Length of the support
Ws = Wm                          ! Width of the support
Hs = 50                          ! Height of the support

!-----------------------------
! Misc

Ldnwell = 25.6                   ! Lateral displacement of
! the n-well

!-------------------------------------------------------------
! Keypoints

!-----------------------------
! Half the mass

k,1,-Wm/2,Lb,0          ! Defines x,y,z coordinates of
! keypoint 1
k,2,-Wm/2,Lb+Lm,0
```

```
48  k,3,0,Lb+Lm,0
    k,4,0,Lb,0
50
    !-----------------------------
52  ! Single beam

54  k,10,-Bsp/2-Wb,0,0
    k,11,-Bsp/2-Wb,Lb,0
56  k,12,-Bsp/2,Lb,0
    k,13,-Bsp/2,0,0
58
    !-----------------------------
60  ! Half the support

62  k,20,-Wm/2,-Ls,0
    k,21,-Wm/2,0,0
64  k,22,0,0,0
    k,23,0,-Ls,0
66
    !------------------------------------------------------------
68  ! Areas

70  !-----------------------------
    ! Half the mass
72
    a,1,2,3,4               ! Defines area using keypoints 1,
74  ! 2,3 and 4

76  !-----------------------------
```

```
! Single beam

a,10,11,12,13

!-----------------------------
! Half the support

a,20,21,22,23

!-----------------------------

arsym,x,all     ! Generates a symmetry reflection of the
! previously defined areasaround the x-axis

aadd,1,4        ! Adds areas 1 and 4
aadd,3,6

!------------------------------------------------------------
! Volumes

!-----------------------------
! Mass epi-layer

vext, 7,,,,, -H_epi     ! Generates volume by extruding
! area 7 in the z-axis by the dimension H_epi

!-----------------------------
! Beams
```

```
106  vext,2,5,3,,, -Hb

108  !-----------------------------
     ! Support
110
     vext,1,,,,, -Hs
112
     !-----------------------------
114  ! Mass n-well

116  vext,3,0,,-Ldnwell,Ldnwell,-Hnwell      ! Extrude area 3
     ! with taper
118  vext,3,0,,-Ldnwell,-Ldnwell,-Hnwell
     vext,3,0,,Ldnwell,-Ldnwell,-Hnwell
120  vext,3,0,,-Ldnwell,Ldnwell,-Hnwell

122  vinv,5,6,7,8            ! Finds the intersection of
     ! volumes 5, 6, 7 and 8
124
     !-----------------------------
126
     aadd,27,28
128  aadd,24,25
     aadd,10,11
130  aadd,6,8
     aadd,57,59,60
132  aadd,34,62

134  vadd,1,9
```

```
136 vglue,all       ! Generates a new volume by gluing all
    ! previously generated volumes
138
    !-----------------------------------------------------------
140
    /EOF
```

Material properties file

```
 1  !-----------------------------------------------------------
 2  ! Define local element type

 4  et,1,SOLID92            ! SOLID92 defined which is a 3-D
    ! 10-node tetrahedral structural solid
 6
    !-----------------------------------------------------------
 8  ! Define linear material properties as a constant

10  mp,dens,1,2.33E-15      ! Mass density
    mp,ex,1,169E9*1E-6      ! Elastic moduli
12  mp,prxy,1,0.3           ! Major Poisson's ratio

14  !-----------------------------------------------------------
    ! Define variables
16
    G=9.80665E6             ! Gravity
18  AX=0*G                  ! Acceleration in x-axis
    AY=0*G                  ! Acceleration in y-axis
```

```
20  AZ=500*G                ! Acceleration in z-axis

22  !-----------------------------------------------------------

24  /EOF
```

Meshing file

```
1   !-----------------------------------------------------------
2   /PREP7          ! Enters the model creation preprocessor

4   vatt,1,,1,0                     ! Associates element
    ! attributes with the selected, unmeshed volumes
6
    vsel,s,loc,y,Lb,Lb+Lm   ! Selects volume by location
8   smrtsize,10             ! Specifies meshing
    ! parameters for automatic (smart) element sizing
10  vmesh,all               ! Specifies meshing
    ! parameters for automatic (smart) element sizing
12
    vsel,none
14  allsel,all

16  VSEL,S,LOC,Y,-Ls,Lb
    smrtsize,5
18  vmesh,all

20  vsel,none
    allsel,all
```

```
22
    asel,s,loc,x,-Bsp/2-Wb/2,-Bsp/2+Wb/2    ! Selects area
24  ! by location
    asel,a,loc,y,Bsp/2-Wb/2,Bsp/2+Wb/2
26  AREFINE,ALL,,,1                          ! Mesh refinement

28
    allsel,all
30
    !-----------------------------------------------------------
32
    finish                           ! Exits from processor
34
    /EOF
```

Constraints file

```
1   !-----------------------------------------------------------
2   /PREP7          ! Enters the model creation preprocessor

4   asel,none
    asel,all
6
    asel,s,area,,22,23,26,29        ! Areas selected
8
    da,all,all,0    ! All DOF constrained on
10  ! previously selected areas

12  asel,none
```

```
    allsel,all
14
    acel,AX,AY,AZ   ! Specifies the linear
16  ! acceleration of the entire structure

18  !-------------------------------------------------------

20  finish          ! Exits from processor

22  /EOF
```

Static analysis file

```
1   !-------------------------------------------------------
2   /SOLU           ! Specifies solution summary data per
    ! substep to be stored
4
    allsell,all
6
    antype,0        ! Specifies the analysis type: static
8
    solve           ! Starts solution
10
    save            ! Saves all current database information
12
    !-------------------------------------------------------
14
    finish          ! Exits from processor
16
```

```
/EOF
```

Modal analysis file

```
!------------------------------------------------------------
/SOLU           ! Specifies solution summary data per
! substep to be stored

allsel,all

antype,2        ! Specifies the analysis type: modal

modopt,lanb,4   ! Specifies modal analysis options: Block
! Lanczos extraction method, 4 modes to be extracted

solve           ! Starts solution

save            ! Saves all current database information

!------------------------------------------------------------

finish          ! Exits from processor

/EOF
```

Post processing file for the static analysis

```
!------------------------------------------------------------
/POST1                  ! Enters the database results
```

```
! postprocessor

!-------------------------------------------------------------
! Displays results as continuous contours

/title,MultiMEMS Design 1 - Von Mises Plot
! Sets the title

plnsol,s,eqv                              ! Displays
! equilavent stress as a continuous contour

/image,save,stresssmrtmesh5,png           ! Saves image

!-------------------------------------------------------------
! Animation of structure subjected to out-of-plane
! acceleration

anmode,100,0.06,,0                ! Produces animation
/anfile,save,stressanim,avi       ! Saves animation

!-------------------------------------------------------------
! Graph to show stress profile along length of a beam

path,beamlength,2,,L_b            ! Defines a path

ppath,1,,Bsp/2+Wb/2,0             ! Path defined by picking
! locations
ppath,2,,Bsp/2+Wb/2,Lb
```

```
32  pdef,stressx,S,x                ! Interpolates x-component
    ! stress onto path
34  pdef,stressy,S,y                ! y-component stress
    pdef,stressz,S,z                ! z-component stress
36
    /axlab,y,Stress (MPa)           ! Labels y axis on graph
38  /axlab,x,Dist from base to end beam (um)
    /title,MultiMEMS Design 1 - Stress Variation
40
    /color,curve,2,1                ! Specifies graph curve
42  ! colour
    /color,curve,7,2
44  /color,curve,12,3

46  /wait,5                         ! Delay until next command

48  plpath,stressx,stressy,stressz  ! Displays path items on a
    ! graph
50
    /image,save,stressdissmrtmesh5,png
52
    /wait,5
54
    prpath,stressx          ! Prints path items along path
56  prpath,stressy
    prpath,stressz
58
    save,stressy,txt        ! Saves all current database
60  ! information
```

```
!-------------------------------------------------------

/EOF
```

Post processing file for the modal analysis

```
!-------------------------------------------------------
/POST1                  ! Enters the database results
! postprocessor

!-------------------------------------------------------

set,first                       ! Defines the data set to
! be read from the results file

plnsol,u,sum                    ! Displays vector sum of
! the structural displacement as a continuous contour
/image,save,1stmode_sum,png     ! Saves image

anmode,20,0.1,,0                ! Prooduces animation
/anfile,save,1stmode_sum,avi    ! Saves animation

set,next                        ! Read the next data set

plnsol,u,sum
/image,save,2ndmode_sum,png

anmode,20,0.1,,0
```

```
/anfile,save,2ndmode_sum,avi

set,next

plnsol,u,sum
/image,save,3rdmode_sum,png

anmode,20,0.1,,0
/anfile,save,3rdmode_sum,avi

set,next

plnsol,u,sum
/image,save,4thmode_sum,png

anmode,20,0.1,,0
/anfile,save,4thmode_sum,avi

!-------------------------------------------------------------

/OUTPUT,Modal_Analysis,txt      ! Redirects text output to
! a file
SET,LIST

!-------------------------------------------------------------

/EOF
```

C.2 SMC sensor design

Main file

```
!-------------------------------------------------------------
! Author:       Craig Lowrie
! Organisation: Heriot-Watt University
! Title:        SMC Design 1 ANSYS File

! The structure is a triangular mass supported by two
! rectangular beams.

! Note that dimensional units are in micrometres

!-------------------------------------------------------------

FINISH
/CLEAR

!-------------------------------------------------------------
! File hierarchy

/INPUT,geometry,txt
/INPUT,matprops,txt
/INPUT,constraints,txt
/INPUT,mesh,txt

! The static analysis or modal analysis are performed one at
! a time whilst the other analysis and associated post-
```

```
! processing file are commented out

/INPUT,analysis_static,txt
/INPUT,analysis_modal,txt

/INPUT,post1_static,txt
/INPUT,post1_modal,txt
```

Geometry file

```
/PREP7

!-------------------------------------------------------
! Dimensions

!-----------------------------
! SOI wafer

H_device = 4    ! Height of the device layer of the SOI wafer
H_box = 0.5     ! Height of the BOX layer of the SOI wafer
H_handle = 380  ! Height of the handle layer of the SOI wafer

!-----------------------------
! Mass

Lm = 400                        ! Length of the mass
Wm = 2*Lm                       ! Width of the mass
Hm = H_device+H_box+H_handle    ! Height of the mass
```

```
20  !-----------------------------
    ! Beam
22
    Lb = 192                        ! Length of the beam
24  Wb = 60                         ! Width of the beam
    Hb = H_device                   ! Height of the beam
26
    !-----------------------------
28  ! Support

30  Ls = 50                         ! Length of the support
    Ws = Wm                         ! Width of the support
32  Hs = 50                         ! Height of the support

34  !-----------------------------
    ! Misc
36
    Wrie1 = 10                      ! RIE along the length of
38  ! the beams
    Wdrie = Wb+(2*Wrie1)            ! DRIE around masses and
40  ! in beam recess
    a = 380                         ! Distance between far
42  ! edges of beam recesses
    b = a-(2*Wdrie)                 ! Mass between beam
44  ! recesses
    c = b+(2*Wrie1)                 ! Distance between near
46  ! edges of beams
    Bsp = b+Wdrie                   ! Distance between centres
```

```
48  ! of beams
    d = Lb-Wdrie                        ! Length of recess in mass
50
    !-------------------------------------------------------------
52  ! Keypoints

54  !-----------------------------
    ! Half the mass
56
    k,1,0,0,0       ! Defines x,y,z coordinates of keypoint 1
58  k,2,0,Lm,0
    k,3,Wm/2,0,0
60
    !-----------------------------
62  ! Single beam recess in the mass

64  k,10,0,0,0
    k,11,0,d,0
66  k,12,a/2,d,0
    k,13,a/2,0,0
68
    !-----------------------------
70  ! Half the mass between the beams

72  k,20,0,0,0
    k,21,b/2,0,0
74  k,22,b/2,d,0
    k,23,0,d,0
76
```

```
!-----------------------------
! Single beam

k,30,c/2,-Wdrie,0
k,31,c/2+Wb,-Wdrie,0
k,32,c/2+Wb,d,0
k,33,c/2,d,0

!-----------------------------
! Half the support

k,40, 0,-Wdrie-Ls,0
k,41, Ws/2,-Wdrie-Ls,0
k,42, Ws/2,-Wdrie,0
k,43, 0,-Wdrie,0

!------------------------------------------------------------
! Areas

!-----------------------------
! Half the mass

a,1,2,3         ! Defines area using keypoints 1,2 and 3

!-----------------------------
! Single beam recess in the mass

a,10,11,12,13
```

```
!----------------------------
! Half the mass between the beams

a,20,21,22,23

!----------------------------
! Single beam

a,30,31,32,33

!----------------------------
! Half the support

a,40,41,42,43

!----------------------------

asba,1,2        ! Subtracts area 2 from area 1

arsym,x,all     ! Generates a symmetry reflection of the
! previously defined areasaround the x-axis

aadd,1,3,6,8    ! Adds areas 1,3,6 and 8
aadd,5,7

!------------------------------------------------------------
! Volumes

!----------------------------
```

```
! Mass

vext,9,,,,,-Hm  ! Generates volume by extruding
! area 9 in the z-axis by the dimension Hm

!-----------------------------
! Beams

vext,2,4,2,,,-Hb

!-----------------------------
! Support

vext,1,,,,,-Hs

!-----------------------------

aadd,16,17
aadd,32,33
aadd,29,30

VGLUE,ALL       ! Generates a new volume by gluing all
! previously generated volumes

!------------------------------------------------------------

/EOF
```

Material properties file

```
1  !-----------------------------------------------------------
2  ! Define local element type

4  et,1,SOLID92            ! SOLID92 defined which is a 3-D
   ! 10-node tetrahedral structural solid
6
   !-----------------------------------------------------------
8  ! Define linear material properties as a constant

10 mp,dens,1,2.33E-15      ! Mass density
   mp,ex,1,169E9*1E-6      ! Elastic moduli
12 mp,prxy,1,0.3           ! Major Poisson's ratio

14 !-----------------------------------------------------------
   ! Define variables
16
   G=9.80665E6             ! Gravity
18 AX=0*G                  ! Acceleration in x-axis
   AY=0*G                  ! Acceleration in y-axis
20 AZ=2000*G               ! Acceleration in z-axis

22 !-----------------------------------------------------------

24 /EOF
```

Meshing file

```
!-----------------------------------------------------------
/PREP7          ! Enters the model creation preprocessor

vatt,1,,1,0                     ! Associates element
! attributes with the selected, unmeshed volumes

vsel,all                        ! Selects all volumes

smrtsize,1                      ! Specifies meshing
! parameters for automatic (smart) element sizing


vmesh,all                       ! Generates nodes and
! volume elements within volumes.

asel,s,loc,x,c/2,c/2+Wb         ! Areas selected by
! location
asel,a,loc,x,-c/2,-c/2-Wb
arefine,all,,,1                 ! Mesh refinement

allsel,all

!-----------------------------------------------------------

finish                          ! Exits from processor

/EOF
```

Constraints file

```
!-----------------------------------------------------------
/PREP7          ! Enters the model creation preprocessor

asel,none
asel,all

asel,s,loc,y,-Wmretch-Ls,-Wmretch       ! Areas selected
! by location on the mass support

da,all,all,0    ! All DOF constrained on
! previously selected areas

asel,none
allsel,all

acel,AX,AY,AZ   ! Specifies the linear
! acceleration of the entire structure

!-----------------------------------------------------------

finish          ! Exits from processor

/EOF
```

Static analysis file

```
!-----------------------------------------------------------
```

```
/SOLU           ! Specifies solution summary data per
! substep to be stored

allsell,all

antype,0        ! Specifies the analysis type: static

solve           ! Starts solution

save            ! Saves all current database information

!-------------------------------------------------------

finish          ! Exits from processor

/EOF
```

Modal analysis file

```
!-------------------------------------------------------
/SOLU           ! Specifies solution summary data per
! substep to be stored

allsel,all

antype,2        ! Specifies the analysis type: modal

modopt,lanb,4   ! Specifies modal analysis options: Block
! Lanczos extraction method, 4 modes to be extracted
```

```
12  solve           ! Starts solution

14  save            ! Saves all current database information

16  !-----------------------------------------------------------

18  finish          ! Exits from processor

20  /EOF
```

Post processing file for the static analysis

```
1   !-----------------------------------------------------------
2   /POST1                  ! Enters the database results
    ! postprocessor
4
    !-----------------------------------------------------------
6   ! Displays results as continuous contours

8   /title,SMC Design 1 - Von Mises Plot    ! Sets the title

10  plnsol,s,eqv                            ! Displays
    ! equilavent stress as a continuous contour
12
    /image,save,stresssmrtmesh5,png         ! Saves image
14
    !-----------------------------------------------------------
16  ! Animation of structure subjected to out-of-plane
```

```
! acceleration

anmode,100,0.06,,0              ! Produces animation
/anfile,save,stressanim,avi     ! Saves animation

!-------------------------------------------------------
! Graph to show stress profile along length of a beam

path,beamlength,2,,L_b          ! Defines a path

ppath,1,,D_1/2,-W_rie_front     ! Path defined by picking
                                ! locations
ppath,2,,D_1/2,L_b-W_rie_front

pdef,stressx,S,x                ! Interpolates x-component
! stress onto path
pdef,stressy,S,y                ! y-component stress
pdef,stressz,S,z                ! z-component stress

/axlab,y,Stress (MPa)           ! Labels y axis on graph
/axlab,x,Dist from base to end beam (um)
/title,SMC Design 1 - Stress Variation

/color,curve,2,1                ! Specifies graph curve
! colour
/color,curve,7,2
/color,curve,12,3

/wait,5                         ! Delay until next command
```

```
46
   plpath,stressx,stressy,stressz  ! Displays path items on a
48 ! graph

50 /image,save,stressdissmrtmesh5,png

52 /wait,5

54 prpath,stressx          ! Prints path items along path
   prpath,stressy
56 prpath,stressz

58 save,stressy,txt        ! Saves all current database
   ! information
60
   !------------------------------------------------------------
62
   /EOF
```

Post processing file for the modal analysis

```
1  !------------------------------------------------------------
2  /POST1                  ! Enters the database results
   ! postprocessor
4
   !------------------------------------------------------------
6
   set,first                       ! Defines the data set to
8  ! be read from the results file
```

```
plnsol,u,sum                    ! Displays vector sum of
! the structural displacement as a continuous contour
/image,save,1stmode_sum,png     ! Saves image

anmode,20,0.1,,0                ! Prooduces animation
/anfile,save,1stmode_sum,avi    ! Saves animation

set,next                        ! Read the next data set

plnsol,u,sum
/image,save,2ndmode_sum,png

anmode,20,0.1,,0
/anfile,save,2ndmode_sum,avi

set,next

plnsol,u,sum
/image,save,3rdmode_sum,png

anmode,20,0.1,,0
/anfile,save,3rdmode_sum,avi

set,next

plnsol,u,sum
/image,save,4thmode_sum,png
```

```
anmode,20,0.1,,0
/anfile,save,4thmode_sum,avi

!-----------------------------------------------------------

/OUTPUT,Modal_Analysis,txt      ! Redirects text output to
! a file
SET,LIST

!-----------------------------------------------------------

/EOF
```